Imperial College London

Design of toughened composite sandwich structures

by

George Irven

Department of Mechanical Engineering
Imperial College London

A thesis submitted for the degree of
Doctor of Philosophy of Imperial College London
and the Diploma of Imperial College

June, 2023

Declaration of originality

I hereby declare that the work presented in this thesis is my own and that any contributions from others included in this thesis are fully acknowledged and appropriately referenced. No part of the present work has been submitted to any other university or institution for any other degree or qualification.

Copyright declaration

The copyright of this thesis rests with the author. Unless otherwise indicated, its contents are licensed under a Creative Commons Attribution-Non Commercial 4.0 International Licence (CC BY-NC).

Under this licence, you may copy and redistribute the material in any medium or format. You may also create and distribute modified versions of the work. This is on the condition that: you credit the author and do not use it, or any derivative works, for a commercial purpose.

When reusing or sharing this work, ensure you make the licence terms clear to others by naming the licence and linking to the licence text. Where a work has been adapted, you should indicate that the work has been changed and describe those changes.

Please seek permission from the copyright holder for uses of this work that are not included in this licence or permitted under UK Copyright Law.

Abstract

Composite sandwich structures are used across a wide range of industries due to their exceptional stiffness and strength-to-weight ratios. These structures are brittle in nature and their failure is often more complex than the materials they replace. This research project considers methods aimed at increasing the damage resistance of these structures. Specifically, the work presented in this thesis shows that the impact performance of composite sandwich structures can be improved in a systematic manner.

Initial impact tests were carried out to evaluate the resulting damage types. Following this, each aspect of the sandwich structure, the core, the skin, and the skin-core bond, was considered in an isolated manner. For each component, alterations aimed at improving the performance of the sandwich structure were devised. These toughening alterations were then tested under static conditions. The most successful alterations were a 3 wt% core shell rubber toughened skin matrix, a 2.5 parts per hundred resin 0.75 mm aramid fibre-reinforced foam core, and 1.5 mm deep 3 mm wide 13 mm spacing grid of grooves in the foam core. These alterations were then combined in sandwich structures that were subject to further impact testing. The result was a 26.5% improvement in back face deflection from 13.2 mm to 9.7 mm. Furthermore, an aramid fibre-reinforced foam core sandwich structure completely resisted perforation in a test where the control panel only absorbed 74.2% of the projectile energy. The key findings are that the toughness of all constituents and interfaces are important when considering the damage tolerance of a sandwich structure. If one element is toughened more than another, damage will likely be experienced in another element of the structure. An optimised structure will distribute damage in such a way as to maximise post-impact strength. It is considered that the techniques developed are very appropriate in optimising composite sandwich structures for transport, wind energy, and other applications.

Throughout this thesis, further studies were carried out to gain a more complete understanding of the materials used. Epoxy foams were investigated over a range of densities, as a result, a transition in fracture performance has been identified. Architected polymers were studied with systematically varying bulk polymer properties. The outcome of this work has informed the design of toughened epoxy foams. Tensile testing of composite laminates was carried out to investigate the effect of adding toughening on the tensile properties. Novel strain measurement techniques allowed micro cracks and small damage areas to be investigated. Toughening were found to reduce the extent of these cracks and damage areas.

Acknowledgements

Foremost, I would like thank my supervisor, Prof. John P. Dear, and sponsor, Dr. Alex Fergusson, for giving me this PhD opportunity and for the guidance and knowledge they have both shared throughout. I would also like to thank Dr. Declan Carolan, my industrial supervisor. His day-to-day input, support, and guidance were crucial to the success of this project.

Thanks to Jun Liu for his assistance in carrying out impact testing. Thanks also to Ruth and Suresh for help in the labs throughout the project. I am also grateful for the hard work and contributions of Aaron Duncan, Adam Whitehouse, and Catherine Folkson. I would also like to thank everyone from FAC Technology, for the provision of the project materials, and to every colleague, past and present, for all the help with manufacturing equipment and machinery.

Lastly, thank you Issie for the incredible support.

Table of contents

Declaration of originality **2**

Copyright declaration **3**

Abstract **4**

Acknowledgements **6**

Table of contents **7**

List of figures **11**

List of tables **20**

List of publications **21**

Nomenclature **23**

1 Introduction **26**

1.1 Background 26

1.2 Project aim 28

1.3 Thesis structure 29

2 Literature review **31**

2.1 Introduction 31

2.2 Impact of composites 32

2.3 Rubber-toughening of epoxy polymers 34

2.4 Fibre-reinforcements of foam 35

2.5 Foam properties over a range of densities 37

2.6 Skin-core debonding 39

2.7 Laminate tensile testing . . . 43
2.8 Concluding remarks . . . 44

3 Experimental methods **45**
3.1 Introduction . . . 45
3.2 Mechanical testing . . . 45
3.2.1 Bulk polymer uniaxial tension . . . 45
3.2.2 Foam uniaxial tension . . . 46
3.2.3 Bulk polymer uniaxial compression . . . 48
3.2.4 Foam uniaxial compression . . . 48
3.2.5 Single edge notch bending . . . 48
3.2.6 Double cantilever beam test . . . 51
3.2.7 Single cantilever beam test . . . 53
3.2.8 Laminate tensile testing . . . 54
3.3 Impact testing . . . 55
3.4 Imaging . . . 59
3.4.1 Scanning electron microscopy . . . 59
3.4.2 Photography . . . 61
3.5 Concluding remarks . . . 62

4 Impact response with toughened epoxy matrices **63**
4.1 Introduction . . . 63
4.2 Materials & Manufacturing . . . 63
4.3 Microscopy . . . 66
4.4 Bulk tensile properties . . . 67
4.5 Fracture properties . . . 68
4.6 Impact study . . . 71
4.7 Concluding remarks . . . 77

5 Toughening of fibre-reinforced epoxy foam **81**
5.1 Introduction . . . 81
5.2 Materials & Manufacturing . . . 81
5.3 Microscopy . . . 82
5.3.1 Polished aramid-reinforced foam . . . 82
5.3.2 Polished carbon-reinforced foam . . . 84
5.4 Compression . . . 85
5.5 Density . . . 86

5.6 Fracture properties . . . 87
5.6.1 Fracture energy: Aramid-reinforced foam . . . 87
5.6.2 Fracture morphology: Aramid-reinforced foam . . . 88
5.6.3 Fracture energy: Carbon-reinforced foam . . . 91
5.6.4 Fracture morphology: Carbon-reinforced foam . . . 91
5.7 Concluding remarks . . . 96

6 Fracture properties of epoxy foam over a range of densities 98
6.1 Introduction . . . 98
6.2 Materials & Manufacturing . . . 98
6.3 Microscopy & Morphology . . . 99
6.4 Mechanical properties: strength and modulus . . . 104
6.5 Fracture properties . . . 110
6.6 Concluding remarks . . . 119

7 Skin-core debonding 121
7.1 Introduction . . . 121
7.2 Materials & Manufacture . . . 122
7.3 CSR and silica modified matrices . . . 123
7.3.1 Failure modes . . . 123
7.3.2 Data reduction method . . . 125
7.3.3 Results . . . 129
7.4 Grooved foam cores . . . 130
7.4.1 Results . . . 131
7.5 Fibre-reinforced foam . . . 134
7.5.1 Results . . . 134
7.6 Concluding remarks . . . 137

8 Impact response with combined toughening mechanisms 138
8.1 Introduction . . . 138
8.2 Results . . . 139
8.2.1 Displacement test . . . 140
8.2.2 Perforation test . . . 143
8.3 Concluding remarks . . . 148

9 Digital image correlation analysis of laminate tensile tests 150
9.1 Introduction . . . 150

9.2 Results . . . 151
9.2.1 Mechanical properties 0° and 90° . . . 151
9.2.2 Mechanical properties ± 45° in-plane shear . . . 154
9.3 DIC . . . 156
9.4 Concluding remarks . . . 165

10 Conclusions and future work **167**
10.1 Conclusions . . . 167
10.1.1 Impact response with toughened epoxy matrices . . . 168
10.1.2 Toughening of fibre-reinforced epoxy foam . . . 170
10.1.3 Fracture properties of epoxy foam over a range of densities . . . 171
10.1.4 Skin-core debonding . . . 172
10.1.5 Impact response with combined toughening mechanisms . . . 173
10.1.6 DIC of laminate tensile testing . . . 174
10.1.7 Final remarks . . . 176
10.2 Recommendations for future work . . . 177

References **179**

Appendix A Fracture performance of architected polymers **194**
A.1 Introduction . . . 194
A.2 Materials & Manufacturing . . . 195
A.2.1 Hole arrangements . . . 195
A.3 Results . . . 200
A.3.1 Simple holes . . . 200
A.3.2 Regular arrays . . . 204
A.3.3 Random arrays . . . 209
A.4 Concluding remarks . . . 215

List of figures

1.1 A schematic of a sandwich panel compared to an I-beam. 27
1.2 An example of the structural efficiency of sandwich panels in terms of weight. 27
1.3 A schematic of a Boeing 787 Dreamliner detailing the use of composites and other materials in its structure. Adapted from [8]. 28
1.4 A photograph of a Swedish Visby-class corvette showing the carbon fibre sandwich hull and superstructure. [9] 28

2.1 Schematics of SCB and DCB skin-core debonding specimens. (a): SCB specimen. (b): DCB specimen. Adapted from [102] 40

3.1 Type 1BA specimen geometry for tensile tests. Dimensions are in mm. 46
3.2 Foam tension. (a) Foam tensile test specimen geometry showing specimen bonded to load blocks. Dimensions are in mm. (b) Example image used in DIC measurement showing both virtual extensometers. 47
3.3 SENB test specimen geometry. 49
3.4 SENB testing rig geometry. 50
3.5 DCB specimen dimensions. Dimensions are in mm. 52
3.6 SCB test schematic. 53
3.7 Example picture taken during an SCB test. 54
3.8 Laminate tension. (a) Laminate test specimen geometry. Dimensions are in mm. (b) Example image from the DIC analysis showing full field major strain and the extensometer used to calculate specimen tensile strain. 55
3.9 Schematic of the gas gun apparatus and high speed camera positioning. 57
3.10 Examples of the back face of composite panel samples. (a): First round of impact testing. (b): Second round of impact testing. 57

3.11 Still photographs from Photron high speed cameras. (a) and (b): Example calibration images. (c) and (d): Example test images. 59
3.12 (a): Example of two 19 × 19 pixel facets 16 pixels apart. (b): Example full field out-of-plane displacement colour map (left camera). . . . 60
3.13 Example photographs taken of a sectioned sandwich panel. Also showing an intact panel and the location of the sectioned plane. . . . 62

4.1 Fracture surfaces of bulk SENB samples containing (a): 6 wt% CSR at a lower magnification. (b): 9 wt% CSR and 17.2 wt% silica nanoparticles. Fracture surfaces of CFRP composites with matrices containing (c): 9 wt% CSR and (d): 3 wt% CSR and 5.9 wt% silica nanoparticles. 67
4.2 Tensile properties of the bulk epoxy polymers. (a): Modulus versus CSR content with the dashed lines representing Halpin-Tsai predictions. (b): Ultimate tensile strength versus CSR content. 69
4.3 Fracture energies versus wt% of CSR. (a): Bulk epoxy polymers. (b): Propagation - initiation for CFRP laminates. 71
4.4 Fracture energies versus wt% of CSR. (a): Initiation for CFRP laminates. (b): Propagation for CFRP laminates. 72
4.5 DCB example fracture energy versus crack length curve. 73
4.6 (a): R-Curve length versus wt% CSR. (b): SEM image of fracture surface of 9 wt% CSR CFRP. 74
4.7 Digital photograph of a typical DCB specimen during a test showing the extent of fibre-bridging and the maximum bridging distance. . . 74
4.8 Centre point displacement and velocity versus time for all sandwich structures. The times of perforation and rear face contact are indicated by green lines. 75
4.9 Deflection at time intervals for the vertical centre section of the sandwich structure with an unmodified matrix. Left: Up to maximum displacement. Right: Return from maximum to minimum displacement. 76
4.10 (a): Maximum out-of-plane displacement versus wt% CSR. (b): Delamination extent within the front skin versus wt% CSR. (c): Extent of back face debond versus wt% CSR content. 76
4.11 Example digital photograph of the impact site of a sandwich panel showing how front skin delamination is measured. 77

4.12 Examples of the differentiating failure modes of core cracking and skin core debonding. 77
4.13 Typical images of sandwich structure cross sections with blue resin reservoir on top. For scale, sandwich core thickness is 30 mm. (a) Unmodified matrix. (b) 3 wt% (c) 6 wt% (d) 6 wt% zoomed image (e) 9 wt% CSR modified matrix. 78

5.1 SEM images of polished aramid foam samples. (a): Control (b): 0.75 mm 2.5 PHR (c): 3 mm 0.5 PHR. (d): 6 mm 1 PHR. 83
5.2 SEM images of polished aramid foam samples. (a): Large void in 6 mm 1 PHR. (b): Epoxy covered fibres in 0.75 mm 2.5 PHR. 83
5.3 SEM images of polished carbon foam samples. (a): Milled fibre 2.5 PHR. (b): 1.5 mm 1 PHR. (c): 3 mm 1 PHR. (d): 6 mm 1 PHR. . . 84
5.4 Compressive yield versus fibre loading for aramid fibre-reinforced foams. 85
5.5 Compressive yield versus fibre loading for carbon fibre-reinforced foams. 86
5.6 Fracture energy versus fibre loading for Aramid fibres. 87
5.7 Load-displacement curves for the SENB testing of aramid 6mm and control. 88
5.8 SEM images of SENB fracture surfaces. (a): Control sample. (b): 6 mm 1 PHR aramid sample showing exposed aramid fibres up to 1 mm in length. 89
5.9 SEM images of SENB fracture surfaces with 0.75 mm Aramid. (a): Fibres exposed after pull-out and fracture. (b): Fibres exposed after surrounding matrix failure. 90
5.10 SEM images of SENB fracture surfaces with 6 mm aramid. (a): Fibre pulled out with epoxy remaining on the end. (b): Image showing how long aramid fibres fray when broken. 91
5.11 Photos of 6 mm carbon foam SENB samples. (a): Zoomed in image of the front of a sample during a test. The crack can be seen to initially cross the path of fibres, fracturing them, then deflect to follow a path between aligned fibres within the foam. (b): Fracture surface of a sample showing a crack that has been deflected multiple times and fractured fibres protruding from the fracture surface. 92
5.12 Load-displacement curves for the SENB testing of carbon 6 mm and control. 94

5.13 SEM images of SENB fracture surfaces of carbon foams. (a): Empty fibre track from a 3 mm fibre. (b) Example of both a pulled out and fractured 3 mm fibre. (c): Example of two 6 mm fibres pulled out. . . 95
5.14 SEM images of SENB fracture surfaces of carbon foam. (a) 3mm fibres bridging after epoxy has fractured off. (b): 1.5 mm fibre pulled out with epoxy remaining. (c): Pair of 6 mm fibres pulled out coated with epoxy. 95
5.15 SEM image of a SENB fracture surface showing milled carbon fibres pulled out. Note the relatively clean surfaces of the milled fibres. . . . 96
5.16 SEM image of a 6 mm fibre below the surface of a fractured node having been loaded. 96

6.1 Examples of SEM images and their respective processed images.(a): 0.25 PHR blowing agent – high density foam and (b): 2.00 PHR blowing agent – low density foam. 99
6.2 SEM micrographs of polished foam samples. (a): 0.25 (b): 0.50 (c): 0.75 (d): 1.00 PHR of blowing agent. 100
6.3 SEM micrographs of polished foam samples. (a): 1.25 (b): 1.50 (c): 1.75 (d): 2.00 PHR of blowing agent. An example of cell coalescence is highlighted by a red circle. An example of small cells in close proximity is highlighted by a green circle. 101
6.4 Cumulative distribution plot of cell characteristic length for all of the foams with different amounts of blowing agent (0.25 – 2 PHR). 101
6.5 Box plot of cell aspect ratio for each foam (at least 220 cells were measured for each foam and the blue rectangular box contains median as red line and first quartile either side). 102
6.6 Box plot of cell areas for each foam (at least 220 cells were measured for each foam and the blue rectangular box contains median as red line and first quartile either side). 103
6.7 Normalised histogram of the angle of cell maximum diameter for foams 0.75-2.0 PHR blowing agent. 105
6.8 Representative compressive stress versus strain for each foam and for the cases with 0.25 and 1.25 PHR blowing agent, the 0.2% Yield and ASTM Yield points are added. 106

6.9 Normalised compressive and tensile strength of all foams versus normalised density including two models taken from Gibson and Ashby [16] (Normalised density of 0.16 corresponds to 2 PHR blowing agent and 0.43 corresponds to 0.25 PHR blowing agent). 107
6.10 Normalised compressive and tensile modulus for all foams versus normalised density including both open cell and closed cell models from Gibson and Ashby [16] (Normalised density of 0.16 corresponds to 2 PHR blowing agent and 0.43 corresponds to 0.25 PHR blowing agent).108
6.11 SEM micrographs of the fracture surfaces of foam SENB samples. (a): 0.25 (b): 0.50 (c): 0.75 (d): 1.00 PHR of blowing agent. 110
6.12 SEM micrographs of the fracture surfaces of foam SENB samples. (a): 1.25 (b): 1.50 (c): 1.75 (d): 2.00 PHR blowing agent. 111
6.13 Representative load versus displacement data from SENB testing. Lines of constant fracture energy are plotted as dashed lines. Examples of small load dips are circled in red. 112
6.14 Normalised fracture energy versus normalised density. (Normalised density of 0.16 corresponds to 2 PHR blowing agent and 0.43 corresponds to 0.25 PHR blowing agent). 113
6.15 Normalised fracture toughness versus normalised density including two models from Gibson and Ashby [16]. (Normalised density of 0.16 corresponds to 2 PHR blowing agent and 0.43 corresponds to 0.25 PHR blowing agent). 114
6.16 Normalised fracture toughness versus normalised density including the Gibson and Ashby model [16] and a Sigmoid fit. 116
6.17 Normalised fracture energy versus normalised density including a calculated Gibson and Ashby line and fracture energy calculated from the Sigmoid fit of fracture toughness. 118

7.1 Example images of SCB specimens mid-test. (a): 3 wt% displaying sub-interface foam failure (b): 6 wt% displaying interface failure. . . . 123
7.2 Representative laminate side fracture surfaces of 0 wt%, 3 wt%, 6 wt% and 9 wt% CSR samples. 124
7.3 Typical load versus displacement curves from SCB testing. Raw data is in black with the valid fracture regions in red. (a): Typical stable fracture curve. (b): Typical unstable stick/slip fracture curve 124

7.4 Load versus displacement curve from the SCB testing of a 6 wt% CSR specimen exhibiting both fracture mechanisms. On the right hand side is the corresponding laminate side fracture surface showing the transition between unstable and stable fracture. 125
7.5 Schematic of an SCB with an elastic foundation. 127
7.6 Load versus displacement curves plotted from numerical results based on elastic foundation (EF) and built-in (BI) models. (a): Examples plotted based on a core modulus, E_c, of 1 MPa. (b) Examples based on the real core modulus of 90 MPa 128
7.7 Fracture energy versus wt% CSR for SCB specimens with CSR and silica modified matrices. The transition in failure mode is labeled. . . 129
7.8 Photograph of the polished side of a 1.5 mm deep grooved specimen. 131
7.9 Representative mid-test photographs of the side of SCB specimens showing the fracture paths in grooved foams. From top to bottom the groove depth is 0 mm, 0.75 mm, and 1.50 mm. 132
7.10 Load versus displacement curves and crack length curves for the SCB testing of two specimens. (a): 9 wt% CSR. (b): 9 wt% CSR with 1.5 mm deep grooves with 13 mm spacing. 133
7.11 Load versus displacement curves for the SCB testing of a control and a 2.5 PHR 0.75 mm aramid specimen 134
7.12 Side view images taken during the SCB testing of a control and a 2.5 PHR 0.75 mm aramid specimen showing exposed fibres in the aramid sample. 135
7.13 SCB skin side fracture surface. (a) Digital photograph. (b) SEM image.136
7.14 SEM image showing the edge of a machined sample of aramid foam showing exposed fibres on the surface. 136

8.1 Bar chart displaying maximum displacement recorded during the displacement test and energy absorbed during the perforation testing of sandwich structures with a control foam core. 140
8.2 Control foam core sandwich structure cross sections from the displacement test. 141
8.3 Aramid foam core sandwich structure cross sections from the displacement test. 142

8.4 Centre point displacement and velocity versus time for sandwich structures with an aramid-reinforced foam core. The times of perforation and rear face contact are indicated by green lines. 144
8.5 Control foam core sandwich structure cross sections from the perforation test. 145
8.6 Aramid foam core sandwich structure cross sections from the perforation test. Note the Aramid-0 panel was not perforated by the projectile. 146

9.1 Tensile modulus versus wt% CSR. (a) 0° direction. (b) 90° direction. . 153
9.2 (a) Example stress versus strain data from the tensile testing of a control and a 9 wt% CSR sample, 0° direction. (b) Average percentage area of the 90° samples with a major strain over 3.75%. 154
9.3 (a) Shear modulus versus wt% CSR, 45° direction. (b) Example shear stress versus shear strain including the 0.2% offset line and strength and the 5% strength. 155
9.4 (a) Shear strength at a 0.2% offset versus wt% CSR, 45° direction. (b) Shear strength at a shear strain of 5% versus wt% CSR, 45° direction. 156
9.5 Example DIC of tensile specimens high strain region analysis at 1.5% global tensile strain. A standard colour map is shown followed by the corresponding binary colour map where the threshold strain is 3.75%. An example specimen from each wt% CSR is then shown. (Specimens and test direction are orientated horizontally across the page) 158
9.6 Example DIC analysis of a 3 wt% CSR tensile specimen with 90° tows on the surface. A standard colour map image is shown of the entire specimen showing where zoomed images are taken from. The black line on the colour maps represents a section where numerical values of strain have been output and plotted periodically at 0.25% increments of global tensile strain. 159
9.7 Example tensile strain graphs similar to the graph in Figure 9.6. The sections used to output the strain data were chosen to include a particularly high strain region. The strain is plotted periodically at 0.25% increments of global tensile strain. 161

9.8 Example DIC analysis of a 3 wt% CSR tensile specimen with 0° tows on the surface. A standard colour map image is shown with the corresponding topographical projection below which reveals the position of the tows in the ply below. Zoomed images show cracks between tows on the surface due to damage in the ply below. 162
9.9 Example DIC analysis of a 6 wt% CSR tensile specimen with 0° tows on the surface. Standard colour map images are shown for three strains just prior to failure as severe damage development occurs. An image of the failed specimen is included. A zoomed image shows cracks along a failing tow on the surface and stress shielding. 163
9.10 Example tensile stress versus strain graphs for the Section, 2 mm wide area, 4 mm wide area, and Whole specimen strain. (a) The 3 wt% CSR shown in Figure 9.8. (b) The 6 wt% CSR shown in Figure 9.9 . 164

A.1 Hole configurations drilled into bulk epoxy material for SENB testing. Simple hole configurations followed by regular arrays and random arrays of holes. Area fraction values represent the proportion of bulk material remaining. 197
A.2 Schematic of hexagonal circle packing. 199
A.3 Fracture energy versus hole spacing for SENB samples with simple hole arrangements ahead of the starting hole. 14 mm spacing represents a sample with no further holes drilled in addition to the crack starting hole. 200
A.4 DIC strain colour-map of SENB samples with no further holes drilled (14 mm spacing). (a): 0% CSR (b): 3% CSR (c): 10% CSR. 202
A.5 ϵ_x versus distance along the section for SENB samples with no further holes ahead of the crack tip. 202
A.6 DIC strain colour-map of SENB samples with 7 mm spacing between hole centres. (a): 0% CSR (b): 3% CSR (c): 10% CSR. 203
A.7 DIC strain colour-map of SENB samples with 2.5 mm spacing between hole centres. (a): 0% CSR (b): 3% CSR (c): 10% CSR. 203
A.8 DIC strain colour-map of SENB samples with sharp cracks. (a): 0 wt% CSR (b): 10 wt% CSR. 204

A.9 Fracture energy versus area fraction for SENB samples with regular arrays of holes. (a) Apparent fracture energy measured up to the first load drop. The dashed lines represent the apparent fracture energy of samples with one hole (14 mm spacing). (b) Total fracture energy measured up to final ligament failure. (c) Total fracture energy minus the apparent fracture energy at first load drop. 205
A.10 Load versus displacement for the SENB testing of 10 wt% CSR and 0 wt% CSR samples with regular arrays of holes. (a): Area fraction 0.39 (b): Area fraction 0.48 (c): Area fraction 0.65. 206
A.11 DIC strain colour-map of SENB samples with regular arrays of holes, 0.39 area fraction. (a): 0% CSR (b): 3% CSR (c): 10% CSR 207
A.12 DIC strain colour-map of SENB samples with regular arrays of holes, 0.65 area fraction. (a): 0% CSR (b): 3% CSR (c): 10% CSR 207
A.13 ϵ_x versus distance along the section for SENB samples with a regular array of holes, 0.39 area fraction. 208
A.14 ϵ_x versus distance along the section for SENB samples with a regular array of holes, 0.65 area fraction. 209
A.15 Fracture energy versus area fraction for SENB samples with random arrays of holes. (a) Fracture energy measured up to the first load drop, apparent fracture energy. (b) Total fracture energy measured up to final ligament failure. (c) Total fracture energy minus the apparent fracture energy. 210
A.16 Fracture energy versus area fraction for SENB samples with random arrays of holes showing the value for individual hole configurations. Dashed lines represent the values for regular arrays of holes. (a) Area fraction 0.39 (b) Area fraction 0.48 (c) Area fraction 0.65 210
A.17 DIC strain colour-maps of random SENB samples. 0.65 area fraction arrangement 3. Top three images: 0 wt% CSR. Bottom two images: 10 wt% CSR. Letters correspond to load drops in Figure A.18 (a) . . 212
A.18 Load versus displacement for the SENB testing of 10 wt% CSR and 0 wt% CSR samples with 0.65 area fraction. (a) Arrangement 3 (b) Arrangement 1. 213
A.19 DIC strain colour-maps of random SENB samples. 0.65 area fraction arrangement 1. Top two images: 0 wt% CSR. Bottom five images: 10 wt% CSR. Letters correspond to load drops in Figure A.18 (b). . . 214

List of tables

4.1 Tensile properties of the bulk epoxy polymers. 69
4.2 Measured fracture energies of both the bulk epoxy polymers and the CFRP laminates. 70
4.3 A summary of the data collected from the impact study. 72

5.1 Measured properties of aramid reinforced foam. 87
5.2 Measured properties of carbon reinforced foam. 92

6.1 Density, Modulus, Strength and Fracture data for all foams with varying amounts of blowing agent (0.25 to 2.0 PHR). 104

7.1 Results of the SCB testing of CSR and silica modified matrices. . . . 129
7.2 Results of the SCB testing of grooved foam cores. 131
7.3 Results of the SCB testing of fibre-reinforced foam cores 135

8.1 Results of the impact testing of sandwich structures with combinations of toughening mechanisms 139

9.1 Tensile test results for the 0° and 90° samples. 152
9.2 Tensile test results for the in-plane shear samples. 154

A.1 Tensile properties and fracture energy of the bulk polymers used in this chapter. 200

List of publications

Journal papers

[1] G. Irven, A. Duncan, A. Whitehouse, D. Carolan, A. D. Fergusson, J. P. Dear. Impact response of composite sandwich structures with toughened matrices. *Materials & Design*, 203:109629, 5 2021.

[2] G. Irven, D. Carolan, A. D. Fergusson, J. P. Dear. Fracture performance of epoxy foam: Low density to bulk polymer. *Polymer*, 261:125420, 11 2022.

[3] G. Irven, D. Carolan, A. D. Fergusson, J. P. Dear. Fracture performance of fibre-reinforced epoxy foam. *Composites Part B: Engineering*, 250:110433, 2 2023.

[4] G. Irven, D. Carolan, A. D. Fergusson, J. P. Dear. Digital image correlation of cross-ply laminates in tension to reveal micro cracking. *Composite Structures*, 319:117148, 9 2023.

[5] G. Irven, A. Whitehouse, D. Carolan, A. D. Fergusson, J. P. Dear. Toughening of face-sheet core bonds in sandwich structures. *Engineering Fracture Mechanics*, 290:109498, 9 2023.

In draft, to be submitted.

G. Irven, C. Folkson, D. Carolan, A. D. Fergusson, J. P. Dear. Fracture performance of architected polymers.

G. Irven, J. Liu, D. Carolan, A. D. Fergusson, J. P. Dear. Design of impact resilient composite sandwich structures.

Conference papers.

[6] G. Irven, A. Duncan, E. Rolfe, D. Carolan, A. D. Fergusson, and J. P. Dear. Impact response of composite sandwich structures with toughened epoxy matrices. In *International Conference on Composite Materials 22*, pages 1895–1906, Melbourne, 2019. Engineers Australia.

G. Irven, D. Carolan, A. D. Fergusson, and J. P. Dear. Impact response of composite sandwich structures . In *International Conference on Composite Materials 23*, Belfast, *2023*.

Nomenclature

Abbreviations

.tiff	Tagged image file format
2D	Two-dimensional
3D	Three-dimensional
ASTM	American Society for Testing and Materials
CBT	Corrected beam theory
CFRP	Carbon fibre-reinforced polymer
CNC	Computer numerical control
CSR	Core-shell rubber
DCB	Double cantilever beam
DGEBA	Diglycidyl ether of bisphenol-A
DSLR	Digital single-lens reflex
FEG-SEM	Field-emission gun scanning electron microscopy
ISO	International Organization for Standardization
LEFM	Linear elastic fracture mechanics
PHR	Parts per hundred resin
PTFE	Polytetrafluoroethylene
PVC	Polyvinyl chloride
RCP	Randomly close-packed
RSA	Random sequential adsorption
SCB	Single cantilever beam
SEM	Scanning electron microscopy
SENB	Single edge notch bending
UTS	Ultimate tensile strength
wt%	Weight percentage

English Alphabet

a	Crack length
A_0	Original cross-sectional area
a_0	Initial debond length
$a_{\max}$	Maximum debond length
B	Specimen thickness
b	DCB and SCB width
C	Compliance
E	Young's modulus
E_{c}	Core modulus
E_{f}	Particulate modulus
E_{f}	Skin flexural modulus
E_{t}	Composite modulus
E_{t}	Matrix modulus
E_{t}	Tensile modulus
E_{C}^{*}	Foam compressive modulus
E_{s}	Bulk material compressive modulus
E_{T}^{*}	Foam tensile modulus
F	Large displacement correction
G_{Ic}	Fracture energy
$G_{\mathrm{Ic,init}}$	Initiation fracture energy
$G_{\mathrm{Ic,prop}}$	Propagation fracture energy
$G_{\mathrm{Ic,prop\text{-}init}}$	Propagation - initiation fracture energy
G_{Q}	Provisional fracture energy
G_{Ic}^{*}	Foam fracture energy
G_{sIc}	Bulk material fracture energy
h	DCB and SCB beam thickness
K_{Ic}	Fracture toughness
K_{Q}	Provisional fracture toughness
K_{Ic}^{*}	Foam fracture toughness
K_{sIc}	Bulk material fracture toughness
$K_{\max}$	Maximum fracture toughness
$K_{\min}$	Minimum fracture toughness
$L_{\mathrm{b,min}}$	Minimum intact specimen length
L	Specimen length

ΔL	Change in length
L_0	Original length
N	Load block correction
P	Load
S_{c}	Core shear modulus
$S_{\mathrm{xz,f}}$	Skin shear modulus
t_{c}	Core thickness
t_{f}	Skin thickness
V_{f}	Particulate volume fraction
W	Specimen width
f/#	Aperture

Greek Alphabet

Δ	Crack length correction
δ	Displacement
ε	True strain
ε_x	SENB opening strain
ε_{E}	Engineering strain
ζ	Shape factor
ν	Poisson's ratio
Φ	Energy calibration factor
ρ^*	Foam density
ρ_{s}	Bulk material density
σ	True stress
σ_{E}	Engineering stress
σ_{t}	Tensile true strength
σ_{yt}	Tensile true yield strength
σ_{ys}	Bulk material yield strength
$\sigma^*_{0.2C}$	Foam 0.2% offset yield strength
σ^*_{YC}	Foam compressive yield strength
σ^*_{pl}	Foam plastic collapse strength
σ^*_{FT}	Foam tensile fracture strength

Chapter 1

Introduction

1.1 Background

A composite material is the result of combining two or more materials together such that better properties than those of the individual components can be achieved [7]. Composite materials exist all around us in both natural and man-made forms. For example, wood is a composite material consisting of cellulose fibres bound together by a lignin matrix. The modern advanced composites considered in this research consist of a strong and stiff fibre reinforcement and a polymer matrix. The main advantages of composite materials are their high strength and stiffness compared to a metallic part of equivalent weight. A composite sandwich structure consists of two strong, stiff composite skins separated by a lightweight core. Composite sandwich structures are used extensively in the aerospace and naval sectors due to their extremely lightweight construction and high stiffness and strength-to-weight ratios [7]. The basic concept of a sandwich structure is that the skins carry the tension and compression loads, while the core transmits the shear loads between the skins. In this way, sandwich structures are analogous to steel I-beams used in the construction industry. A diagram comparing these structures is included in Figure 1.1. The separation of the skins by the core increases the moment of inertia of the panel with little increase in weight producing an efficient structure for resisting bending and buckling loads. Figure 1.2 shows illustratively the flexural stiffness and strength advantage of sandwich panels compared to solid panels using typical beam theory with typical values for skin and core density.

More recently, composite sandwich structures have been used in critical load bear-

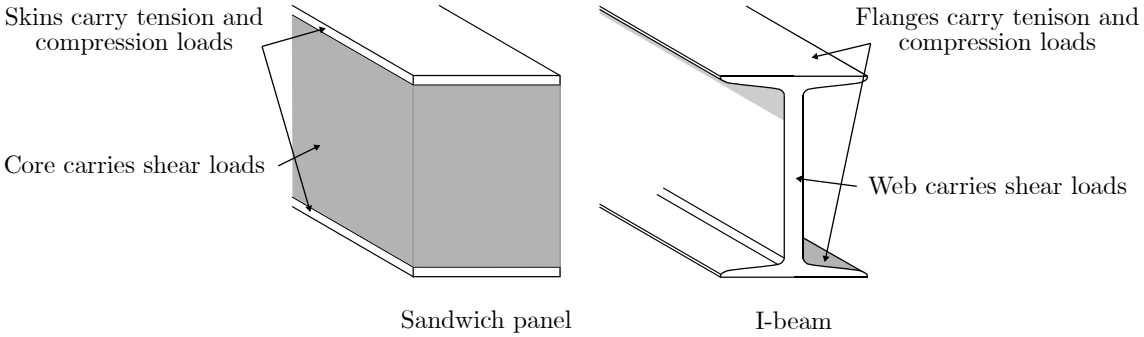


Figure 1.1: A schematic of a sandwich panel compared to an I-beam.

	Solid skin	Core thickness t	Core thickness 3t
	t	2t	4t
Bending stiffness	1	7.0	37.0
Flexural strength	1	3.5	9.2
Weight	1	1.03	1.06

Figure 1.2: An example of the structural efficiency of sandwich panels in terms of weight.

ing applications such as primary aircraft structures and naval vessel structures. Examples of these are the Boeing 787 Dreamliner, a schematic of which is displayed in Figure 1.3, and the Swedish Visby-class corvette pictured in Figure 1.4. As composite sandwich structures are adopted in critical load bearing functions, understanding how they respond to damage events becomes ever more important. Despite the numerous benefits composite materials provide over the use of metals, they are often more brittle and fail in a more complex manner. The behaviour of metals is well understood and can be predicted using analytical and/or finite element models with relative ease. On the other hand, the properties of composites such as their anisotropy and innumerable interfaces both microscopic (fibre-matrix) and macroscopic (skin-core) make effective modelling a more complex undertaking. The complex failure of composites and the difficulty surrounding the prediction of these failures, can lead to the substantial overdesign of composite structures. Unfortunately, these high safety factors detract from the very reason they are first considered, namely their high specific stiffness and strength.

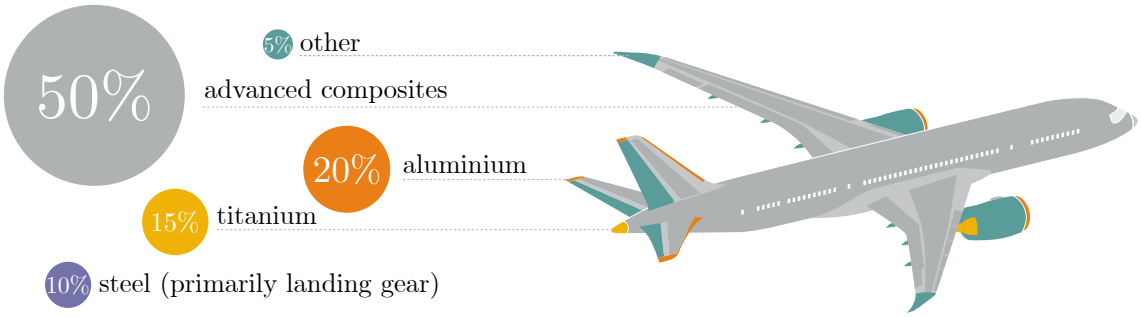


Figure 1.3: A schematic of a Boeing 787 Dreamliner detailing the use of composites and other materials in its structure. Adapted from [8].



Figure 1.4: A photograph of a Swedish Visby-class corvette showing the carbon fibre sandwich hull and superstructure. [9]

1.2 Project aim

This research project considers the damage resistance of composite sandwich structures. In order to allow structural designers to be more confident with these materials, their damage resistance must be improved. In this way, designs can be conceived to allow for certain amounts of damage to occur while knowing that the structure will not fail catastrophically. This is the design approach taken with many metallic based designs, i.e. allowable damage [10]. Due to the soft nature of the lightweight foam core, concentrated transverse loads such as impact loads are of particular concern when employing composite sandwich structures. The ability of a composite sandwich structure to withstand increased impact loading will depend on improving the properties of the individual components and the means by which these compo-

nents co-operate together in the overall structure to dissipate energy. Toughness is a crucial material property when considering energy absorption during a damage event. The toughness of materials is well understood, however, the toughness or energy absorbing ability of a composite sandwich structure during an impact event is far more complex. The aim of this research project will be to evaluate and improve the toughness of individual sandwich components and the sandwich structure as a whole. The aspects of the sandwich structure to be improved are the skin, the core, and the skin-core interface. This project will address all of these aspects in an attempt to improve the impact performance of a sandwich structure. It will be vital to assess how changing the properties of one sandwich component affects the resulting damage response of the sandwich structure. Damage will occur where the least resistance exists, therefore, ensuring that there are no low damage resistant paths will be vital to reducing overall damage in the sandwich structure.

1.3 Thesis structure

This thesis is divided into ten chapters. Each chapter can be briefly summarised as follows:

Chapter 2 gives a literature review on subjects relevant to the present study. This includes a brief introduction to the impact testing of composite sandwich structures. The toughening mechanisms present in foams and bulk epoxy will also be briefly discussed.

Chapter 3 describes the experimental methods used to evaluate the materials and structures in this research. The methods used for the impact testing of composite sandwich structures are described in detail. Microscopy and photography methods are also outlined.

The main results of this thesis are presented in Chapters 4 - 9. Chapter 4 describes the results of the first of two rounds of impact testing. The first round of impact testing evaluates whether applying a standard rubber toughening technique to the matrix of the skins of the sandwich structure improves the impact performance.

Chapter 5 presents the outcome of reinforcing epoxy foams with short fibres. Chapter 4 revealed that core cracking was a major damage type resulting from the partic-

ular impact testing and sandwich structures used in this research. As such, toughening the core became a significant aim of the project. The literature suggests that short fibres are an effective method for toughening epoxy foams. This chapter characterises the effect of fibre reinforcement on the fracture performance of low density epoxy foams.

Chapter 6 presents a study on the fracture properties of epoxy foam over a range of densities. This chapter follows on from chapter 5 after the importance of core fracture performance was established in chapter 4. How foam fracture properties and morphology change with foam density are described in detail. A link between a transition in foam fracture performance and cell morphology is discovered.

Chapter 7 presents a series of tests evaluating the toughness of the skin-core bond of a sandwich structure. The impact testing of chapter 4 revealed that skin-core debonding was a major damage type. As a result, a series of tests were carried out to evaluate this failure mode in a static manner. Furthermore, various methods for improving the toughness of the skin-core bond were designed and evaluated.

Chapter 8 presents the results of a second round of impact testing. This second round of impact testing includes sandwich structures employing a combination of successful toughening mechanisms established in the previous chapters. The effectiveness of these toughening mechanisms are evaluated under impact loading having previously been proven in static conditions.

Chapter 9 presents the results of a series of tensile tests conducted in laminates with toughened matrices. A surprising relationship between matrix toughness and laminate modulus is discussed. Digital image correlation (DIC) techniques are used to identify damage in a novel way.

Lastly, Chapter 10 presents the overall conclusions of this thesis, and gives recommendations for future work within the scope of this project.

Chapter 2

Literature review

2.1 Introduction

In this chapter, a brief review of the literature relevant to this research is given. In the present study, composite sandwich structures are tested under impact loads and a number of toughening mechanisms are employed to reduce damage and back face deflection. This chapter provides a summary of available literature considering impact testing of composite sandwich structures and the methods used to improve the performance of these structures under impact loading. Impact testing is often carried out with dissimilar equipment and so no direct quantitative comparison between different studies can be made.

The second section of this chapter provides a brief summary of the literature surrounding the rubber toughening of epoxy used in this research. The main energy absorbing mechanisms will be described.

The third area of literature that will be summarised in this chapter relates to the fibre-reinforcement of epoxy foams. Literature specifically regarding epoxy foam is limited and so other more common foams have been considered. Due to the effect on viscosity, it is difficult to manufacture low-density fibre-reinforced epoxy foam. As something which was a key objective of this research, it was important to consider the densities of the foams in the current literature. Achieving a favourable dispersion of reinforcing particles is challenging. A poor dispersion can lead to reinforcing particles having a detrimental effect on mechanical properties, as such, any reference to dispersion in the literature has been carefully considered.

The forth section presented in this chapter is in the area of epoxy foam characterisation over a range of densities. More specifically, the fracture performance of these materials and how it varied with density was of particular interest. However, no extensive literature exists on the fracture performance of epoxy foam over a range of densities. Therefore, other foams other than epoxy based foams have been considered. The transition from low-density foam through to bulk epoxy polymer will be a key theme.

The fifth section of literature presented in this chapter will focus on the testing of composite sandwich skin-core bonds. More specifically it will concern the mode-I critical strain energy release rate of these bonds. Much of the focus will be on the work done to standardise tests in this field.

The sixth section of literature will concern the tensile testing of cross-ply fibre-reinforced composite laminates. In particular, the focus of this section will be on the crack density in the plies perpendicular to the test direction. How these cracks effect laminate modulus will be discussed.

2.2 Impact of composites

Plantema [11], Allen [12], and Zenkert [13] have summarised the literature, theory, and practical aspects of sandwich structures. The combination of high specific strength, corrosion resistance and low radar signature make composite sandwich structures an attractive structural choice for many applications including in the naval, aerospace, and, energy sectors [14, 15]. However, the brittle nature of composite materials can lead to substantial overdesign of sandwich structure components, counteracting their weight and cost savings benefits. Failure modes of sandwich panels under quasi-static flexural loading are well researched and have been described in detail by both Gibson and Ashby [16] and Steeves and Fleck [17, 18].

Critical to the viability and reliability of sandwich structures are concentrated loads such as impact loads [19–24]. During the service life of aircraft composite structures, they may encounter impacts such as dropped tools and runway debris, furthermore, the damage caused by such events is often very difficult to inspect [24, 25]. Moreover, the residual strength of composite sandwich panels is reduced by an impact

event [26], therefore, the study of impacts of these structures is critical. There has been considerable recent interest in understanding the response of composite sandwich panels to impact loading such as the studies presented in these papers [27–30]. These studies mainly concentrated on developing finite element models of impact and penetration to match the companion experiments. Huo et al. [30] noted that the impactor shape could have a significant influence on damage dissipation mechanisms and that incorporating a multi-layer core could greatly increase damage dissipation within the composite sandwich panel. Feng and Aymerich [31] examined the influence of core density on sandwich panel response and found that this was strongly correlated with skin layup. They attributed this to skin responses dominated by either global bending or local shear rigidity. However, they did not explicitly consider the role of damage dissipation in either the skin or the core or at the interface between them. Zhu and Sun [32] developed an analytical model to partition the energy absorbed during an impact into various consecutive phases. They did so via a fracture mechanics approach, considering the role of the fracture toughness of each location where damage is likely to occur. However, their model does not allow for transitions in failure mode, for example, where the extent of damage may increase in, for instance, the core due to toughening of the skins, or skin-core interface. In their comprehensive analysis, Zhou et al. [33] investigated the behaviour of foam-based sandwich panels under low-velocity impact loading, highlighting the important role of foam core properties and geometric parameters in determining the panels' resistance to impact damage. The study conducted by Wang et al. [34] provided a comprehensive investigation into the influence of core material on the response of sandwich structures subjected to medium-velocity impact. Their experimental and numerical analysis highlighted the significance of core material selection in determining factors such as deformation behaviour, energy absorption, damage mechanisms, and penetration resistance, offering important observations for the design and optimisation of toughened composite sandwich structures. Anderson [35] explored the application of single degree of freedom models for analysing the impact response of sandwich composites subjected to large mass impact. The study investigated the accuracy and limitations of single degree of freedom models in predicting the dynamic behaviour and failure modes of sandwich composites under impact loading, providing insights into the design and analysis of such structures. Feraboli and Kedward [36] presented a novel program for assessing the impact performance of composite structures. The study introduced a comprehensive methodology that combined analytical models, experimental data, and numerical simulations to eval-

uate the impact response and damage tolerance of composite sandwich structures, offering meaningful contributions to the design and evaluation of toughened composite sandwich structures with enhanced impact resistance capabilities. Buitrago et al. [37] successfully correlated experimental and numerical results to determine the ballistic limit of carbon laminate aluminium honeycomb core composite sandwich structures. Their modelling approach, combined with energy absorption analysis, provides valuable insights into the design and optimisation of sandwich structures for applications requiring high-velocity impact resistance.
To improve the ability of a composite sandwich structure to withstand impact loading will depend on improving the properties of the individual components and the means by which these components co-operate together in the overall structure to dissipate energy. Energy absorption mechanisms in laminate impacts include delaminations and matrix cracking [38]. A critical parameter for a composite structure to withstand impact loading is the damage resistance of the structure, this can be improved by improving the toughness of the individual components of the sandwich structure.

2.3 Rubber-toughening of epoxy polymers

Epoxy polymers find uses across a range of industries as the matrix in fibre-reinforced composites. The highly crosslinked polymer possesses good mechanical properties and thermal stability. The high level of crosslinking results in an inherently brittle material. As a result, toughening of epoxy polymers is a long established technique. Preformed core-shell rubber (CSR) particles have been used extensively [39–45]. The two main toughening mechanisms are plastic shear band yielding and cavitation and subsequent plastic void growth [46–49]

Plastic shear band yielding is identified as a major toughening mechanism occurring in rubber modified epoxy polymers [49]. Rubber particles in epoxy act as stress concentrations. In a well dispersed system, these stress concentrating particles induce intense plastic shear strains in narrow regions of material between them. These regions are known as shear bands. The plastic deformation of this material can absorb a significant amount of energy. This increased energy absorption leads to a higher fracture energy [49]. This mechanism was successfully modelled using 2D finite element analysis by Huang and Kinloch [49]. The method was also observed using optical microscopy as demonstrated by Pearson and Yee [50].

Cavitation of rubber particles is caused by large hydrostatic stresses ahead of the crack tip. This cavitation leads to the formation of voids within the epoxy. The cavitation process itself does not absorb a substantial amount of energy, however, it is critical in relieving the stress triaxiality ahead of the crack tip [51]. This delays further crack propagation by inducing the surrounding matrix around the void to undergo more plastic deformation, thus absorbing plastic energy and enhancing toughness.

2.4 Fibre-reinforcements of foam

Toughness is a crucial property for foams as in tension they fail by the propagation of a single crack [16]. Marsavina and Linul [52] recently conducted a comprehensive review of the fracture toughness of polymer foams including reinforcement methods. Reinforcement of epoxy foam has experienced attention from two groups of researchers in recent years, Song et al. [53] produced short carbon fibre-reinforced epoxy foams via mechanical frothing and achieved an increase in toughness of up to 113% at densities ranging from 362-475 kg/m^3. Alonso et al. [54] synthesised short fibre-reinforced epoxy foam with both glass and aramid fibres at a density of approximately 300 kg/m^3. However, individual foam densities were not given. This is a shortcoming of this and other works in the literature. The density of a foam can have a massive influence on the fracture performance, see chapter 6 for a detailed discussion on this topic. Improvements in shear and compressive strength were substantial, especially in the foam rise direction. Due to the foaming process, bubbles often manifest as either oblate or prolate spheroids aligned with the foam rise direction depending on the density [16]. Alonso et al. highlighted the importance of using a suitable coupling agent between fibre and matrix to ensure effective strengthening. They also worked on modelling of the compressive properties of glass fibre-reinforced epoxy foam using a statistical approach [55]. The foams ranged from 250-550 kg/m^3 and the variables that were studied were density, fibre weight fraction, and fibre length. They noted that more variables such as fibre aspect ratio and stiffness could have been included for increased accuracy. The omission of these parameters from the model does not lend confidence in their model as these fibre properties are critical in determining the overall properties of a reinforced material or foam.

Fibre modification of polymer foams has been the subject of research since at least the late 1970s. An early seminal work by Cotgreave and Shortall [56–58] investigated polyurethane foams reinforced with chopped glass fibres. Increases in tensile strength were moderate, up to 22%, while increases in toughness were more pronounced, up to 45%. Fibres were found to lie within struts and shown to arrest or deflect cracks propagating through the foam matrix causing fibre pull-out to occur. They found that individual filaments well distributed within the foam were more effective than fibre bundles. Carling [59] tested polyurethane foams reinforced with 7 mm glass fibres at a density of 80 kg/m^3. Limited gains in fracture energy were realised, however, modulus and critical stress intensity factor were improved. It was noted that improvements in mechanical performance were limited due to the fibres being bundled together as opposed to being individually distributed throughout the foam. Significant work has been carried out on fibre-reinforced phenolic foams [60–63], improvements in compressive, tensile, shear, and friability properties were substantial. In addition, the failure mode of skin-core debonding from a fibre-modified foam was analysed by Shen et al. [63]. They reported a seven-fold increase in peel resistance with the addition of 3 weight percent (wt%) 6.4 mm aramid fibres in phenolic foam.

Compared to the use recorded in foams, fibre toughening is more commonly utilised in bulk polymers and continuous fibre-reinforced composites. The toughening mechanisms of short fibres in these composites is the subject of many research studies [64–67]. The main toughening mechanisms in bulk polymers and fibre-reinforced composites are briefly summarised here. Crack deflection is a toughening mechanism whereby a rigid particle forces a crack front to deviate from its main plane. The result is the tilting or twisting of the crack. The originally mode-I crack is then subjected to local mixed-mode loading. The energy release rate increases due to the increased fracture toughness associated with the mixed mode failure of most materials. Fibre bridging is a toughening mechanism whereby fibres bridge across the two faces in the wake of the crack. Fibre bridging occurs when the interface between the fibres and the bulk material is strong enough for stress transfer, yet weak enough for the partial debonding of the fibre [66]. Stress is transferred to the fibres bridging the crack and they are deformed elastically. As the crack progresses, the strain energy in the bridging fibres increases, in this way they resist crack growth. Fibre pull-out occurs as loaded fibres are completely debonded from the matrix. A significant amount of energy can be absorbed during pull-out due to interfacial

frictional sliding. Longer fibres are more likely to fracture before experiencing pull-out. The sum of the bonding forces maintaining the fibre in place increase with length. The longer fibres are expected to fracture at the crack plane where the fibre is bridging the crack due to the increased stress at this location [68]. In this case, pull-out should not occur. However, the variability in strength along the length of the fibre can allow fibre fracture within the matrix [67].

2.5 Foam properties over a range of densities

Gibson and Ashby [16] provided an extensive study of foam material mechanical properties and proposed micromechanical models thereof. These models relate foam mechanical properties to the mechanical properties of the bulk polymer and the relative density of the foam. Later, these models will be compared to the experimental data within this research. There are numerous other models available covered by Mills [69], however, these models are for specific cell geometries and are often very complex relying on specific finite element modelling results. As a result, Mills models are not often used in the literature. Modulus, strength and fracture toughness will be compared to the Gibson and Ashby models with a focus on fracture toughness and how this relates to fracture energy. Currently, no adequate models exist for directly predicting the fracture energy of cellular solids. Fracture toughness of foams, especially used as core materials, is important. Core cracking often leads to cracks propagating parallel to the skin leading to debonding of the skins from the core [69]. Marsavina [70] presented a summary specifically of micromechanical models for foam fracture. The models relate the fracture toughness of the foam to the fracture strength of the bulk material, the relative density, and various lengths such as cell size and edge thickness. Marsavina and Linul [52] recently conducted a comprehensive review of the fracture toughness of rigid polymeric foams. They concluded that linear elastic fracture mechanics (LEFM) can be applied to rigid polymer foams. Furthermore, in another study, Marsavina et al. [71] showed that fracture toughness does not overly depend on the size or shape of specimens. Specimens were tested with widths ranging from 5 mm to 226 mm, only the 5 mm specimens began to deviate from the results of the other specimens.

With regard to conducting fracture tests on polymer foams over a range of densities, early work was conducted by McIntyre and Anderton [72] on polyurethane foams. They found a linear relationship between K_{Ic} and density below 200 kg/m^3,

however, they reported a non-linear relationship beyond this density. When G_{Ic} was calculated from these toughness values, interesting transitions were observed as modulus varied with density at a different rate to K_{Ic}. Zenkert and Bäcklund [73] conducted tests on polyvinyl chloride (PVC) foam of nominal density 200 kg/m^3 and found that the fracture toughness decreased slightly with increasing mean cell diameter. They also confirmed that the difference between linear elastic fracture mechanics and non-linear analyses were small such that K_{Ic} and G_{Ic} could be used. Viana and Carlsson [74] tested a range of PVC foams from 36 to 400 kg/m^3 though a different grade of foam was used for the densest foam. They found a linear relationship between K_{Ic} and density up to 300 kg/m^3. However, the 400 kg/m^3 foam falls considerably below this relationship. They also found a minimum specimen thickness of 12.8 mm was required before further increases in thickness had no effect.

Few studies exist on the effects of density on the mechanical properties of chemically blown epoxy foam. Stefani et al. [75] conducted compression tests on fifteen chemically blown epoxy foams from 200–550 kg/m^3. The modulus and strength of the tested foams follow power law relationships as observed in this research. The results are lower than those that will be presented in this research, most likely due to differences in the foaming resin giving different bulk material properties. Wang et al. [76] manufactured epoxy foam using expandable microspheres from 450–1000 kg/m^3. Once again, the modulus and strength follow power law relationships. In fact, the densest foam in the current research matches precisely with the lower end of the results obtained by Wang et al. [76]. More recently, epoxy foams have been manufactured in small 50 ml batches via a mechanical whipping process by Jalalian et al. [77]. The compressive strengths achieved are consistent with the current research. The modulus is much lower, this could be due to the high proportion of non-curing surfactant or the 10 mm height of the compression samples. The machined top and bottom surfaces on thin compression samples result in a high ratio of broken cells causing a low measured modulus.

Bureau and Kumar [78] investigated the fracture toughness of microcellular polycarbonate foams with relative densities between 0.7 and 0.9. Such high relative density materials are rarely considered foams, Gibson and Ashby [16] referred to an upper limit of 0.3 relative density when describing foam. They found that while the fracture toughness of the 0.7 relative density foam was 37% less than the bulk polymer, the fracture energy was increased by 12% due to a reduction in modulus of 66%. A

selection of other researchers have studied the toughening effects of microvoids in bulk epoxy [79–83]. Huang and Kinloch [79] tested epoxy with 17% volume 0.7 µm voids. They found that the combination of an increase in K_{Ic} and a reduction in modulus gave rise to a significant increase in fracture energy G_{Ic}. It should be noted that the voids in a chemically blown foam, such as the ones that will be discussed in the main body of this thesis, are several orders of magnitude larger than these voids. Bagheri and Pearson [81–83] studied epoxy containing a range of hollow latex particles acting as voids. The particles ranged in size from 0.2-40 µm. They found that conventional rubber modifiers and the hollow particles toughened the epoxy in the same manner. They show that the materials go though a brittle-to-tough transition as the inter-particle distance decreases, and that the critical distance is related to the particle size. The evolution from a plane strain to plane stress state is the major factor in this transition. Kim and Kim [80] used a mechanical stirring technique to develop 80 µm voids within epoxy. However, this is an average value and the scanning electron microscopy (SEM) micrographs clearly show voids over 100 µm. They found considerable increases in fracture energy, G_{Ic}, with void volume fractions between 15% and 28%. They also suggest that void inter-particle distance is key in the brittle-to-tough transition. It is clear that voids can toughen epoxy polymers in a similar manner to conventional rubber modifiers.

Further to the investigations surrounding conventional foam, the appendix of this thesis will cover structures consisting of bulk material with holes drilled in to mimic a foam on a 2D plane. This body of work was inspired by work carried out by Liu et al. [84] on "micro-architectured" materials. They machined holes in aluminium blocks and carried out fracture toughness testing. They found that a structure can be 50% lighter than the bulk material while maintaining the same fracture toughness. Furthermore, fracture toughness was found to increase with relative density. The key mechanisms described are crack-blunting and hole-hole interaction. These mechanisms are also prevalent in conventional foam fracture, as such, this research provides an insight into the design of tough foams.

2.6 Skin-core debonding

The failure mode of skin-core debonding can cause significant decreases in the structural integrity of sandwich panels. Once a debond occurs, the skins of a sandwich can no longer transfer shear stresses between each other. The skins then act as in-

dividual thin flexible beams and lose the high bending stiffness of the thick singular structure.

Unlike the other quasi-static tests that will be carried out in this research, there is no standard test for evaluating skin-core bond toughness. As with the fracture toughness testing of most common materials and structures, failure due to mode-I loading is of the most interest. Furthermore, the mode-I fracture toughness is lower than the mode-II or III toughness for most common materials. Testing the most conservative value for failure is prudent. Finally, the skin-core debonding experienced in this research was the rear face peeling off the core during an impact event. This is a mode-I failure, as such, a mode-I failure test was sought to quantify this interface toughness.

A large number of test methods have been used to evaluate mode-I skin-core debonding [85–101]. These methods all include a sandwich structure with a section of pre-crack or debond included along one skin-core interface. They can be grouped in to two main categories as displayed in Figure 2.1, double cantilever beam (DCB) and single cantilever beam (SCB). They were summarised by Ratcliffe [102].

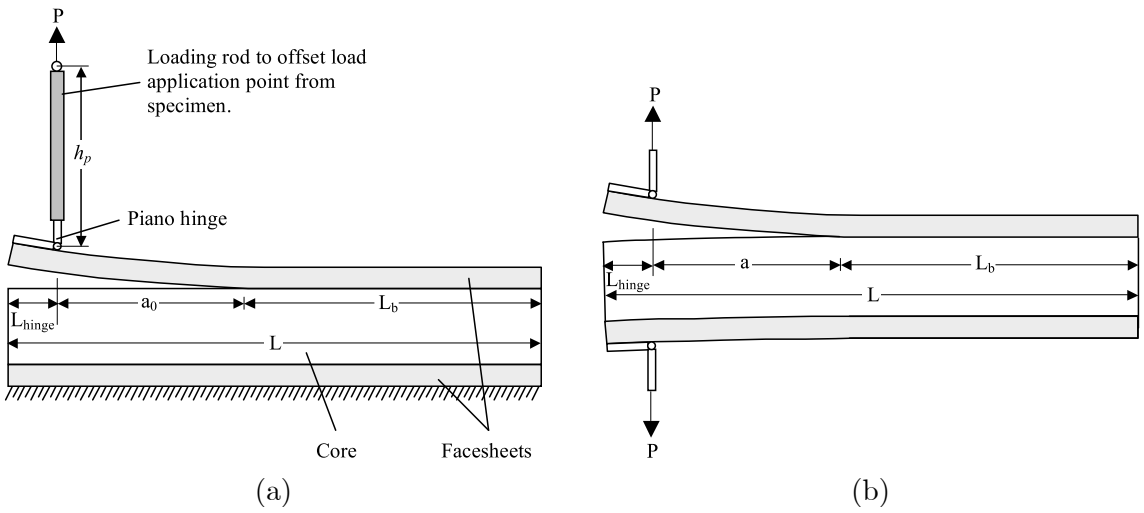


Figure 2.1: Schematics of SCB and DCB skin-core debonding specimens. (a): SCB specimen. (b): DCB specimen. Adapted from [102]

Ratcliffe favoured the SCB for the development of a testing standard, specifically, the SCB test design in Figure 2.1 (a). He notes that in DCB specimens, the bending moment is applied below the unbonded portion of the specimen, leading to tensile stresses in the core. Examples have demonstrated a tendency for the crack to kink

into the core due to these tensile stresses [97].

Ratcliffe also carried out a sizing study which proposes an algorithm based on limitations of the material used to determine appropriate dimensions for SCB specimens [102, 103]. Dimension limitations such as sizing the initial debond length to ensure bending is the dominant deformation mode of the loaded face sheet are outlined in a step-by-step manner.

The two most important dimensions are the initial debond length and the skin thickness. The initial debond length, a_0, is sized such that bending is the dominant mode of deformation in the skin.

$$a_0 \geq \sqrt{\frac{30 E_\mathrm{f} t_\mathrm{f}^2}{S_{\mathrm{xz,\,f}}}} - 0.59 L_{\mathrm{b,min}} \tag{2.1}$$

where $L_{\mathrm{b,min}}$ is the minimum length of the intact specimen, and E_f and $S_{\mathrm{xz,f}}$ are the skin flexural modulus and shear modulus respectively.

The skin thickness is first calculated to prevent flexural failure of the skin. The required thickness for this is small, the more stringent requirement is sizing the skin to ensure small deformation to allow a linear analysis as follows.

$$t_\mathrm{f} \geq t_\mathrm{f}^{\text{small disp}} = \left[\frac{a_{\max}}{\left(\frac{3 a_{\max}^2 E_\mathrm{f}}{200 S_\mathrm{c}}\right)^{\frac{1}{4}} - \left(\frac{t_\mathrm{c} E_\mathrm{f}}{3 E_\mathrm{c}}\right)^{\frac{1}{4}}} \right]^{\frac{4}{3}} \tag{2.2}$$

where $a_{\max}$ is the maximum crack length. E_c, S_c, and t_c are the core modulus, shear modulus, and thickness, respectively.

It must be noted that there are problems with measuring pure mode-I fracture properties of an interface between dissimilar materials, indeed the measured mode is often mixed [104]. The difference of elastic properties between, in this instance, the skin and core, will disrupt the symmetry even if the geometry and loading are symmetric. The mismatch in modulus will couple the normal and shear deformations ahead of the debond front [102]. However, it is expected that the mode-mixity for the SCB test used in this research is minimal. Adams et al. [105, 106] conducted

finite element analyses to evaluate the mode-mixity of various face-sheet debonding test methods. They found that the SCB test method was the most appropriate for minimising bending stresses in the core, eliminating crack kinking, and minimising any mode-II component at the crack tip to below 5%. In fact, they found that the mode-I component is over 98% for the sandwich configurations evaluated.

Considering the significant effort within the literature to devise test methods to evaluate skin-core debonding, there are relatively few instances of researchers attempting to improve the performance of this bond. Gholami et al. [107] investigated sandwich panels with grooves almost the depth of the entire core thickness. During DCB testing these grooves were shown to split open and so are of limited practical use. However, the grooves served to arrest crack propagation and gave rise to stick-slip behaviour. Stick-slip behaviour in a test describes a scenario where the load drops are sudden and intermittent. These sudden load drops correspond to large instantaneous increases in crack length. This behaviour is in contrast to the normal scenario where continuous and smooth crack growth and load drop occur over the course of the test. The grooves employed by Yokozeki and Iwamoto [108] were more effective. They combined both perforations and grids of grooves to achieve a 36% improvement in fracture energy as measured in DCB testing. Truxel et al. [109] machined grooves in both balsa and PVC cores. The grooved specimens performed poorly due to the starvation of resin from the surrounding interface. However, the grooved specimens showed locally high fracture resistance and temporary crack arrest at the sites of the grooves. Hirose et al. [110] studied the effect of a singular 10 mm diameter semi-cylindrical groove. As the crack approached the groove the fracture energy increased, it then dropped after passing through the resin filled grooved. Miao et al. [111] shear tested sandwich structures with slits in the core. They found that panels with core slits that were filled or partially filled had a higher fracture resistance than intact cores or cores with empty slits. Hu et al. [112] constructed sandwich structures with stitches passing through the skin and partially into the core. The holes of the stitched fabric then filled with resin during the infusion process. The stitches formed columns of resin and fibre that were pulled out from the core during testing. With a sufficiently small gap between stitches, this pull-out gave rise to significant R-cure behaviour. In fact, they were unable to measure a steady state propagation fracture energy for some samples. Longer specimens would have been required to measure this. As mentioned in Section 2.4, Shen et al. [63] reported increases in the peel resistance of aramid fibre-reinforced phenolic foams.

2.7 Laminate tensile testing

When CFRP cross-ply laminates are subjected to mechanical loading, four major damage mechanisms can occur as described by Berthelot [113]: 'transverse matrix cracking in 90° plies, delamination at the interface between 0° and 90° plies, axial splits in the 0° plies in the direction of the loading, and fibre fracture in the 0° plies. In the case of uniaxial loading, the early stage of damage is dominated by transverse matrix cracking in 90° plies. Matrix cracks develop across the width of the specimen starting from the free edges. The analysis of transverse matrix cracking is important since it reduces the effective strength and stiffness of the laminate. Transverse cracks induce local stress concentrations at crack tips and can involve significant inter-laminar delamination between 0° and 90° plies, according to the nature of cross-ply laminates. Longitudinal matrix cracking and fibre fracture in 0° plies are induced only for high loads in the case of monotonic loading or for large cycle numbers in the case of fatigue loading. Garett and Bailey [114] observed a decrease in laminate stiffness following the first signs of transverse cracks. They were investigating a glass/polyester composite, however, the analysis of the laminate serves to show the possible effect of transverse cracks in other composites. Bailey et al. [115] also carried out work on carbon/epoxy laminates and found the effect of transverse cracks on modulus is reduced for carbon/epoxy compared to glass/epoxy. The reason being the ratio of Young's Moduli of transverse over longitudinal plies are larger in the glass/epoxy laminates. As a result, the transverse plies carry a substantial load which is reduced when transverse cracks occur. Talreja [116] carried out research on tensile loaded cross-ply carbon laminates. Contrary to Bailey et al. [115], he found that as the density of transverse cracks increases, the decrease in the Young modulus is not significant, however, the decrease in Poisson's ratio is. Talreja [116] found the transverse crack density increased with strain but tends to a saturation value. Further work by Talreja [117] on the effect of a toughened matrix on transverse cracking is of particular to this research project. He found that increasing the matrix resin toughness increases the axial strain at which the onset of transverse cracking occurs. Furthermore, the density of microcracks at a given axial strain is reduced in the toughened system. The density of these microcracks correlates with a reduction in Poisson's ratio but does not cause a reduction in stiffness as measured with strain gauges. Subramanian et al. [118] characterised the laminate stiffness of samples with varying fibre-matrix interphases. They found that the laminate stiffness could be increased by 21% by simply changing the sizing on the

carbon fibres. They rule out explanations such as the sizing causing a degradation of the fibres and conclude that the sizing controls the load transfer between the matrix and the fibres. Ineffective load transfer causes the fibre load carrying capacity to not be fully utilised and results in a reduction in the laminate stiffness. Other researchers reported similar effects, Madhukar and Drzal [119, 120] reported a 15% increase in modulus for a laminate after doubling the single-fibre-matrix interfacial shear strength. Various models have been developed to predict the development of transverse cracking during static tests, they are summarised by [113] and consist of stress based [114, 121–124] fracture mechanics based [125–133] and mixed models [134].

2.8 Concluding remarks

This chapter has presented a review of the literature relevant to the topics that will be covered in this thesis. The impact testing of composite structures, fibre-reinforced foams, foam properties over a range of densities, skin-core debonding, and laminate tensile testing have been discussed. In the next chapter, the experimental methods used in this study are presented.

Chapter 3

Experimental methods

3.1 Introduction

This chapter describes the experimental procedures used to determine the mechanical and fracture properties of the bulk epoxy polymers, foams, and full carbon fibre-reinforced polymer composite sandwich structures. The procedure for carrying out impact testing of the sandwich structure will also be detailed. Several microscopy techniques and image analyses were also used to fully characterise these materials and these are also briefly described.

3.2 Mechanical testing

3.2.1 Bulk polymer uniaxial tension

Uniaxial tensile tests were carried out in accordance with the International Organization for Standardization (ISO) 527-1 [135] test standard to determine the tensile modulus, E_t, and tensile true strength, σ_t, values of the bulk epoxy polymers. Dumbbell shaped specimens of type 1BA were used with the dimensions outlined in Figure 3.1. These were machined from 3 mm thick plates using a pillar drill with a router bit and jig.

Tensile tests were performed using an 'Instron 3366' universal testing machine fitted with a 10 kN load cell, at a constant displacement rate of 1 mm/min. The strain was measured using an 'Epsilon 3442' extensometer attached to the specimen with at a gauge length of 10 mm. At least five replicate specimens were tested for each

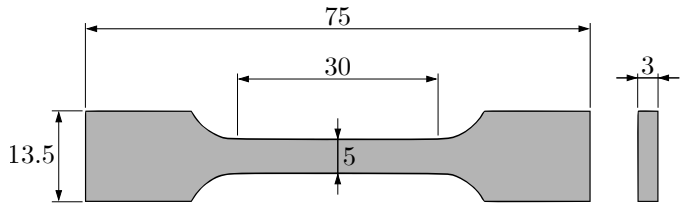


Figure 3.1: Type 1BA specimen geometry for tensile tests. Dimensions are in mm.

bulk epoxy formulation.

The engineering stress, σ_{E}, and engineering strain, ε_{E}, were calculated using:

$$\sigma_{\mathrm{E}} = \frac{P}{A_0} \qquad \varepsilon_{\mathrm{E}} = \frac{\Delta L}{L_0} \tag{3.1}$$

where P is the load, A_0 is the original cross-sectional area, ΔL is the change in length, and L_0 is the original gauge length. These values were subsequently converted to true stress, σ, and true strain, ε, using:

$$\sigma = \sigma_{\mathrm{E}}(1 + \varepsilon_E) \qquad \varepsilon = \ln(1 + \varepsilon_{\mathrm{E}}) \tag{3.2}$$

The tensile true strength, σ_{t}, was taken as the stress at the first local maximum during the tensile test [135]. In all cases a yield point was visible, as such, the tensile true strength is defined as the tensile yield strength, σ_{yt}, i.e. $\sigma_{\mathrm{t}} = \sigma_{\mathrm{yt}}$. Strain softening occurs after yield, where the stress decreases with increasing strain. The tensile modulus, E_{t}, was defined according to the standard [135] as:

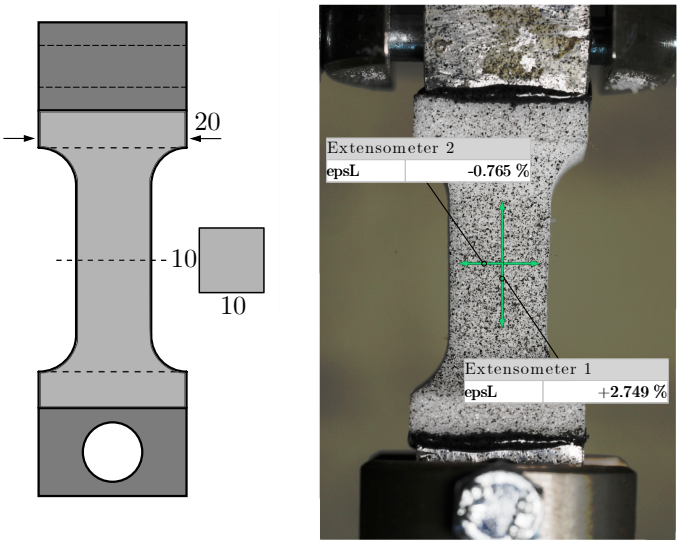
$$E_{\mathrm{t}} = \frac{\sigma_2 - \sigma_1}{\varepsilon_2 - \varepsilon_1} \tag{3.3}$$

which is the slope of the true stress-true strain curve in the strain interval between $\varepsilon_1 = 0.0005$ and $\varepsilon_2 = 0.0025$.

3.2.2 Foam uniaxial tension

Uniaxial tension tests were carried out to determine the tensile strength and tensile modulus of the foam. The specimens tested were a combination of type A and type B from the American Society for Testing and Materials (ASTM) standard [136]. Limitations on the amount of material available prevented type A specimens from being used and type B specimens do not provide a failure strength. Dumbbell

specimens bonded to aluminium load blocks were used with dimensions outlined in Figure 3.2. These were machined from 40 mm foam blocks using a pillar drill with a router bit and jig. Tests were carried out parallel to the foam rise direction. Load blocks were applied at orthogonal directions to allow for misalignment corrections in both directions.



(a) (b)

Figure 3.2: Foam tension. (a) Foam tensile test specimen geometry showing specimen bonded to load blocks. Dimensions are in mm. (b) Example image used in DIC measurement showing both virtual extensometers.

The foam specimens were sprayed with a black speckle as displayed on the specimen in Figure 3.2 (b). Photographs were taken at two second intervals throughout the test with a 'Canon EOS 5D Mark IV' digital single-lens reflex (DSLR) camera equipped with a 100 mm macro lens. The images were recorded with a resolution of 2240 $\times$ 3360 pixels. The field of view was approximately 60 mm tall resulting in a resolution of approximately 0.02 mm/pixel. The specimens were well lit. An aperture of f/8 was used alongside an exposure time of 1/40 s and an ISO speed of ISO-100. GOM Correlate DIC software was then used to calculate strain both parallel and perpendicular to the test direction with gauge lengths of 15 mm and 8 mm respectively. DIC will be discussed in detail in Section 3.3.

3.2.3 Bulk polymer uniaxial compression

Uniaxial compression tests were carried out in accordance with the ASTM D695 [137] test standard to determine compressive yield strength. The tests were performed on a 'Shimadzu' universal testing machine fitted with a 250 kN load cell at a constant displacement rate of 0.5 mm/min. All specimens exhibited a distinct yield point before strain softening occurred. Specimens of dimensions $14 \times 14 \times 28$ mm^3 were compressed between two stainless steel platens. The top platen was self-orienting to ensure the load was applied parallel to the top face of the sample. Both platens were lubricated with molybdenum grease prior to the test. This was in order to reduce the influence of friction at the platen sample interface [138].

3.2.4 Foam uniaxial compression

Uniaxial compression tests were carried out in accordance with the ASTM D1621 [139] test standard to determine compressive yield strength and compressive modulus of all foam samples. Specimens of dimensions $30 \times 30 \times 30$ mm^3 were cut from foam panels with a diamond tipped saw. Specimens were tested parallel to the foam growth direction. The variation in foams tested resulted in a wide range of loads. As a result, depending on the foam strength, the tests were either performed on a 'Shimadzu' universal testing machine fitted with a 250 kN load cell or an 'Instron 3366' universal testing machine fitted with a 10 kN load cell at a constant displacement rate of 2 mm/min. Compressive yield strength was calculated from the maximum stress within a strain of 10% as defined in the ASTM standard [139]. A number of the foams did not exhibit a distinct yield point within the initial 10% strain. As a result, a 0.2% offset strength was also calculated to better enable the comparison of the results with existing models. This is calculated by translating the modulus of elasticity line along the strain axis from the origin by 0.2% and recording the stress at which this line intersects the stress-strain curve [140]. Prior to testing, the compression samples were also used to calculate density. The samples were measured and weighed with an electronic balance. Measuring multiple samples allowed for variations in density across a foam panel to be monitored.

3.2.5 Single edge notch bending

Of both the foams and bulk epoxy plates, the fracture toughness, K_{Ic}, and fracture energy, G_{Ic}, were determined using single edge notch bending (SENB) tests in

accordance with the ASTM D5045 [141] test standard. This standard is aimed at testing bulk plastics. However, multiple studies have confirmed the SENB specimen to be suitable for fracture toughness testing of foam [74, 142]. Test specimens were cut according to the ratios outlined in Figure 3.3, where W, L and B are the test specimen width, length, and thickness respectively.

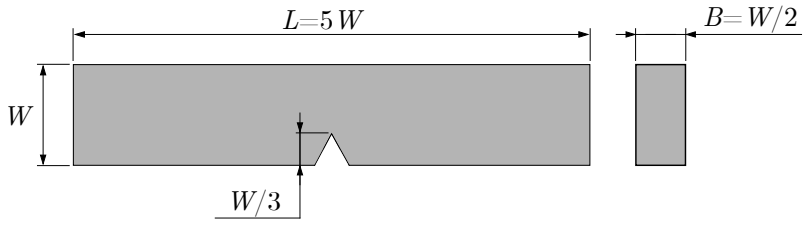


Figure 3.3: SENB test specimen geometry.

For the bulk epoxy polymers, specimens of dimensions 80 × 16 × 8 mm^3 were cut from the bulk plates. A V-notch 5.3 mm deep was then cut at the mid-length using a V-notch router bit in a pillar drill. For the foams, specimens of dimensions 140 × 28 × 14 mm^3 were cut, and a V-notch 9 mm deep was milled at the mid-length. Foam specimens were larger to ensure plane strain conditions during the SENB tests.

For the bulk epoxy polymers, a chilled razor blade was carefully tapped into the notch to produce a sharp pre-crack of length a that satisfies $0.45W < a < 0.55W$ [141], see Figure 3.4. The foam specimens were cut to a depth of 14 mm with a razor blade held in a custom device that was fixed to a drill press, allowing a consistent pre-crack depth to be achieved. Razor blades are frequently used in a similar way in the literature to create pre-cracks in foam fracture toughness specimens [58, 59, 73, 74, 143]. This method was the best available, however, determining whether this creates a 'sharp crack' in the foam would constitute future work. Carling [59] remarks that the sharpness of the crack would be limited by the diameter of a cell and that as long as the razor notch was clean and did not cause surrounding damage, the razor method would be sufficient. The tests were performed using an 'Instron 3366' universal testing machine at a constant displacement rate of 1 mm/min in three-point bending with a support span of 64 mm for the bulk epoxy and 112 mm for the foams.

After testing, the crack lengths were measured using a pixel counter in ImageJ software using images captured with a digital camera.

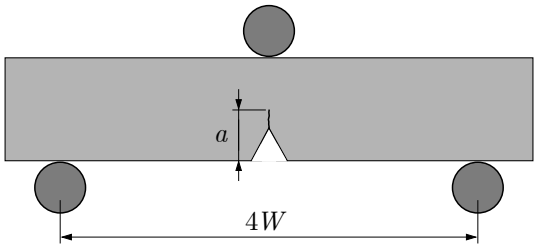


Figure 3.4: SENB testing rig geometry.

The provisional fracture toughness, K_{Q}, was calculated using [141]:

$$K_{\mathrm{Q}} = \left(\frac{P}{B\sqrt{W}} \right) f\left(x\right) \tag{3.4}$$

where P is the load at crack growth initiation, and $f\left(x\right)$ is the geometry calibration factor for SENB specimens [141]:

$$f\left(x\right) = 6x^{\frac{1}{2}} \frac{1.99 - x\left(1-x\right)\left(2.15 - 3.93x + 2.7x^2\right)}{\left(1+2x\right)\left(1-x\right)^{\frac{3}{2}}} \tag{3.5}$$

where $x = \frac{a}{W}$. The provisional fracture energy, G_{Q}, can be calculated by two different methods. The first method uses LEFM, and converts K_{Q} to G_{Q} via the relationship:

$$G_{\mathrm{Q}} = \frac{\left(1-\nu^2\right) K_{\mathrm{Q}}^2}{E} \tag{3.6}$$

where ν is the Poisson's ratio and E is the elastic modulus. However, due to the visco-elastic nature of polymers, E must be obtained at the same time and temperature conditions, and will therefore introduce uncertainties [141]. It is hence preferable to determine G_{Q} by directly integrating the area under the load versus displacement curve to determine the energy at crack growth initiation. This was achieved via the following relation [141]:

$$G_{\mathrm{Q}} = \frac{U}{BW\Phi\left(x\right)} \tag{3.7}$$

where U is the corrected energy at crack growth initiation, and $\Phi\left(x\right)$ is the energy calibration factor [141]:

$$\Phi = \frac{A + 18.64}{\mathrm{d}A/\mathrm{d}x} \tag{3.8}$$

where:

$$A = \frac{16x^2}{(1-x)^2}(8.9 - 33.717x + 79.616x^2 - 112.952x^3 + 84.815x^4 - 25.672x^5) \quad (3.9)$$

and:

$$\frac{\mathrm{d}A}{\mathrm{d}x} = \frac{16x^2}{(1-x)^2}(-33.717 + 159.232x - 338.856x^2 + 339.26x^3 - 128.36x^4)$$
$$+16\frac{[2x(1-x)+2x^2]}{(1-x)^3}(8.9-33.717x+79.616x^2-112.952x^3+84.815x^4-25.672x^5) \quad (3.10)$$

The energy under the load displacement curve was corrected for system compliance, loading-pin indentation, and sample compression. The integrated area used for the correction was measured using the load displacement curve of an unnotched sample and a loading span as short as possible.

Both the LEFM and energy methods were used and compared, and provided consistent results. The provisional fracture toughness and fracture energy are valid if the test specimens satisfy the following size criteria:

$$B, a, (W-a) > 2.5\left(\frac{K_{\mathrm{Q}}}{\sigma_{\mathrm{yt}}}\right)^2 \quad (3.11)$$

The linearity criterion of the load displacement curve was checked for all SENB samples. The maximum load achieved in the test was compared against the intersection of the 0.95x gradient line with the load-displacement curve measured, as described in ASTM D5045 [141]. If these criteria are met, the test is deemed valid, and thus the provisional values, K_{Q} and G_{Q}, are taken as the fracture toughness and energy values, K_{Ic} and G_{Ic}, respectively. At least five valid tests were performed for each bulk epoxy and foam formulation.

3.2.6 Double cantilever beam test

DCB tests were used to measure the composite mode-I fracture energy in accordance with the ISO 15024 [144] standard. Test specimens were cut according to the ratios outlined in Figure 3.5 from composite plates. A 12 µm thick Polytetrafluoroethylene

(PTFE) crack starter film of length 50 mm was used to ensure an appropriately sharp starter crack.

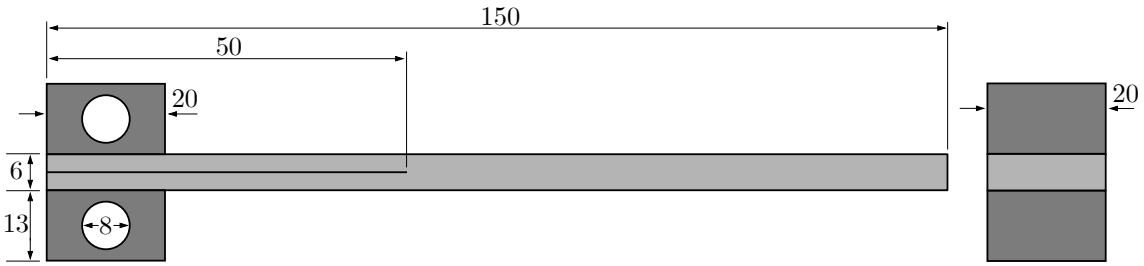


Figure 3.5: DCB specimen dimensions. Dimensions are in mm.

The corrected beam theory (CBT) method was employed to calculate both the mode-I initiation interlaminar fracture energy, $G_{\mathrm{Ic,init}}$, and the steady-state propagation fracture energy, $G_{\mathrm{Ic,prop}}$ of the composites. The initiation value used for DCB specimens was the point of the first load drop. This coincided with a visual increase in the crack length for all samples. The interlaminar fracture energy was calculated via:

$$G_{\mathrm{Ic(init,prop)}}(\mathrm{comp}) = \frac{3P\delta}{2b(a+|\Delta|)}\frac{F}{N} \tag{3.12}$$

where P is the load δ is the displacement, b is the width, a is the crack length and Δ is the crack length correction. F is the large displacement correction and N is the load block correction given by:

$$F = 1 - \frac{3}{10}\left(\frac{\delta}{a}\right)^2 - \frac{3}{2}\left(\frac{l_1\delta}{a^2}\right) \tag{3.13}$$

$$N = 1 - \left(\frac{l_2}{a}\right)^3 - \frac{9}{8}\left[1 - \left(\frac{l_2}{a}\right)^2\right]\frac{l_1\delta}{a^2} - \frac{9}{35}\left(\frac{\delta}{a}\right)^2 \tag{3.14}$$

where l_1 and l_2 are dimensions related to the load block. The crack length correction, $|\Delta|$, accounts for deflections and rotations at the crack tip due to the low shear modulus of the matrix. $|\Delta|$ can be obtained as the x-intercept of a plot of $C^{1/3}$

against crack length, where C is the compliance of the beam given by:

$$C = \frac{8a^3}{Ebh^3} \tag{3.15}$$

The tests were conducted at a constant crosshead displacement rate of 2 mm/min using a 'Instron 3366' universal testing machine fitted with a 10 kN load cell. The loads and displacements were recorded, and the crack lengths monitored using a travelling microscope. At least five replicate specimens were tested for each formulation of composite matrix. An R-curve was observed from the measured data, i.e. the value of the interlaminar fracture energy increased as the crack steadily propagated through the carbon fibre-reinforced polymer (CFRP) DCB test: from value for the onset, or initiation, of crack growth until an upper limit, steady-state value of the interlaminar fracture energy for crack propagation was attained. Thus, an initiation value, $G_{\mathrm{Ic,init}}$, for the onset of crack growth and a value for steady-state propagation, $G_{\mathrm{Ic,prop}}$, could be defined, as described in ISO-15024 [144].

3.2.7 Single cantilever beam test

To investigate the skin-core bond fracture energy of sandwich structures, SCB mode-I fracture tests were carried out. The chosen SCB method was based on tests done by Glaessgen et al. [98]. A schematic for the test is included in Figure 3.6. This method provides the closest loading to mode-I at the crack tip.

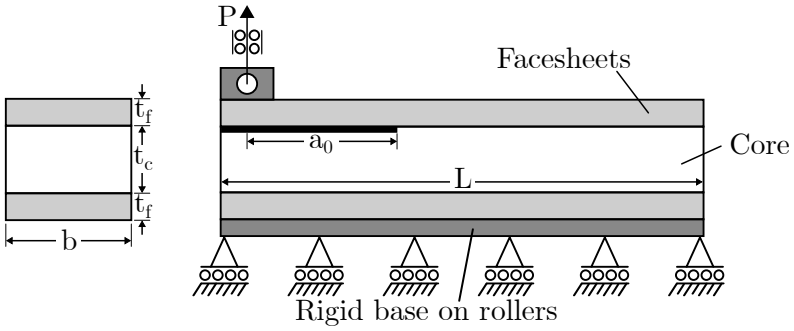


Figure 3.6: SCB test schematic.

Ratcliffe [102, 103] developed a sizing method for SCB specimens as described in Section 2.6. Following this sizing method using the properties of the skin and core used in this research, the resulting sandwich dimensions are as follows: $t_c = 10$ mm, $t_f = 3.2$ mm, $L = 185$ mm, and $a_0 = 55$ mm. The skin is made up of layers of dry fabric infused with resin, furthermore, the skin lay up must be balanced and sym-

metric. As a result, there are discrete gaps between achievable skin thicknesses. As a result, the skin thickness used in experiments was the smallest achievable thickness greater than the minimum required by the sizing equations. The specimens were fixed to a rigid moving carriage using clamps on the bottom skin. The bottom skin was sufficiently thick such that the specimen could be clamped with considerable force without damaging the sample.

High resolution photographs were taken at intervals throughout the tests to allow crack lengths and failure modes to be recorded. These images were also used to check that the specimens did not slip in the clamps. An example image is included in Figure 3.7.

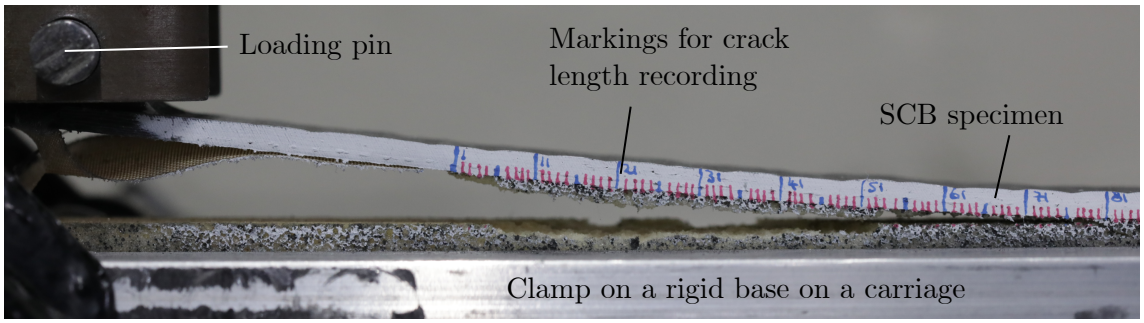


Figure 3.7: Example picture taken during an SCB test.

The tests were conducted at a constant crosshead displacement rate of 1 mm/min using a 'Instron 3366' universal testing machine fitted with a 10 kN load cell. The loads and displacements were recorded, and the crack lengths monitored using a high resolution digital camera. At least five replicate specimens were tested for each composite. The data reduction scheme for this test will be described in chapter 7 as it was developed for this research project and forms an integral part of the chapter.

3.2.8 Laminate tensile testing

Laminate tensile tests were conducted in accordance with ASTM D3039 [145]. In-plane shear laminate tensile tests were conducted in accordance with ASTM D3518 [140]. From each of the tensile panels to be tested, three smaller panels were cut in the 0°, 90° and 45° directions. The panels then had glass fibre reinforced polymer tabs adhered to each grip section using 'Araldite 2014' epoxy adhesive, the tabs were 50 mm long and had a 45° bevel. Each panel and tab section was prepared with grit blasting equipment prior to bonding the tabs to ensure a good bond. Each panel was

then cut into five 25 × 250 mm^2 samples with a diamond edged saw. The specimen geometry can be seen in Figure 3.8 (a). The specimens width and thickness were measured three times with a digital vernier caliper. The specimens were then spray painted matte white and speckled with fine black ink using an airbrush attached to an air compressor set to 0.1 Bar. The tests were performed on an 'Instron' universal testing machine fitted with a 250 kN load cell at a constant displacement rate of 4 mm/min. Pneumatic grips were used to secure the samples.

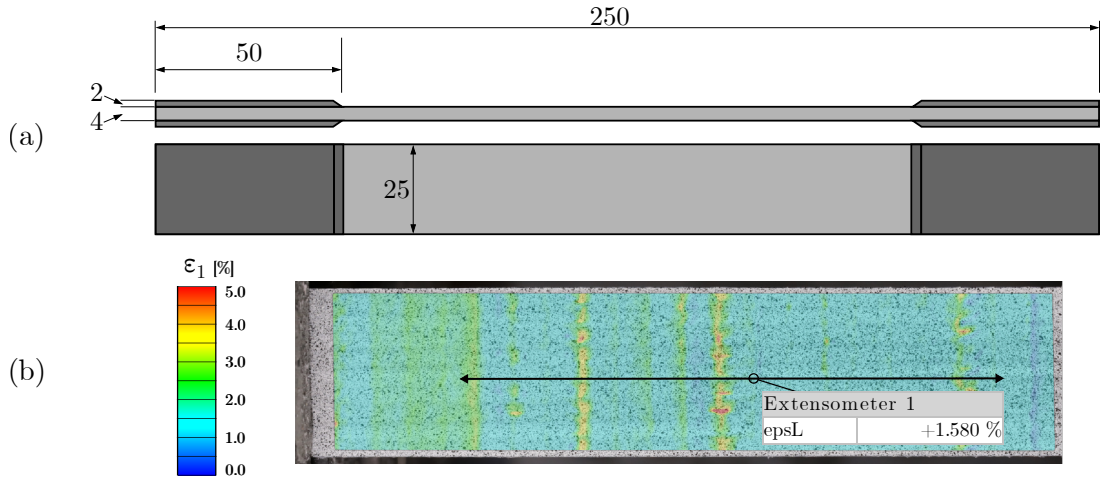


Figure 3.8: Laminate tension. (a) Laminate test specimen geometry. Dimensions are in mm. (b) Example image from the DIC analysis showing full field major strain and the extensometer used to calculate specimen tensile strain.

A 'Canon EOS 5D Mark IV' DSLR camera was setup perpendicular to the sample to take images at 3 s intervals, 2D DIC full field strain data was obtained from the images using GOM Correlate. An example full field major strain colour map output from GOM Correlate is displayed in Figure 3.8. Figure 3.8 also shows the 80 mm virtual extensometer used to calculate tensile strain. From the GOM Correlate software it is possible to output numerical values of strain along a section drawn within the full field output. Strain data from the DIC was matched with the load data from the load cell which was recorded at 10 Hz.

3.3 Impact testing

To investigate the impact performance of the composite sandwich panels, experiments were performed using a gas gun apparatus. The projectile used was 6082T6 aluminium with a hemispherical tip. The projectile had a nominal diameter of

24.9 mm and length of 25.45 mm. The first round of impact testing used projectiles with a weight of 28.5 g while the second round of impact testing used projectiles with a weight of 28 g due to different machining batches. For the first round of impact testing, an impact velocity of 130 m/s was selected as this would lead to projectile kinetic energies of 241 J. This impact energy was chosen as it caused significant damage to the panels without causing perforation, allowing the back face displacement to be measured. Back face displacement of perforated panels cannot be measured due to the risk of damaging expensive camera equipment. Due to slight changes in the behaviour of the gas gun apparatus, the same pressure in the gas gun resulted in a higher velocity of 135 m/s for the second round of impact testing. This resulted in an impact energy of 255 J. The control of the gas gun was not sufficiently fine such that the velocities of the two rounds of impact testing could be matched exactly. Consequently, the results of the two rounds of testing will not be directly compared. However, both rounds of impact testing contain a 'control' panel. A 'control' panel contains an unmodified epoxy foam core with unmodified skin matrices.

The second round of impact testing also included perforation tests for each panel type. The velocity chosen for this testing was 173 m/s, this resulted in a kinetic energy of 419 J, a 64% increase over the back face displacement test. The end of the gas gun barrel and the sandwich panels were contained within a transparent safety box constructed from thick polycarbonate panels, steel panels, and extruded aluminium frames. The projectiles were accelerated along the 3 m long barrel and the velocity was measured using two pairs of infrared sensors just before the barrel exit connected to an oscilloscope. A schematic of the setup is displayed in Figure 3.9

The composite panels measured 230 $\times$ 230 $\times$ 34 mm^3 and were bolted into a steel frame using 12 M8 bolts as displayed in Figure 3.10. In order to record the deflection of the panels under impact, two high speed cameras were synchronised and located behind the target outside the chamber. To facilitate DIC, the panels were spray painted matt white and a random black speckle pattern was applied to the back surface of the panel with a black marker. An example of the pattern applied for each round of testing is presented in Figure 3.10.

During the first round of impact testing, two Phantom Miro M310 cameras were

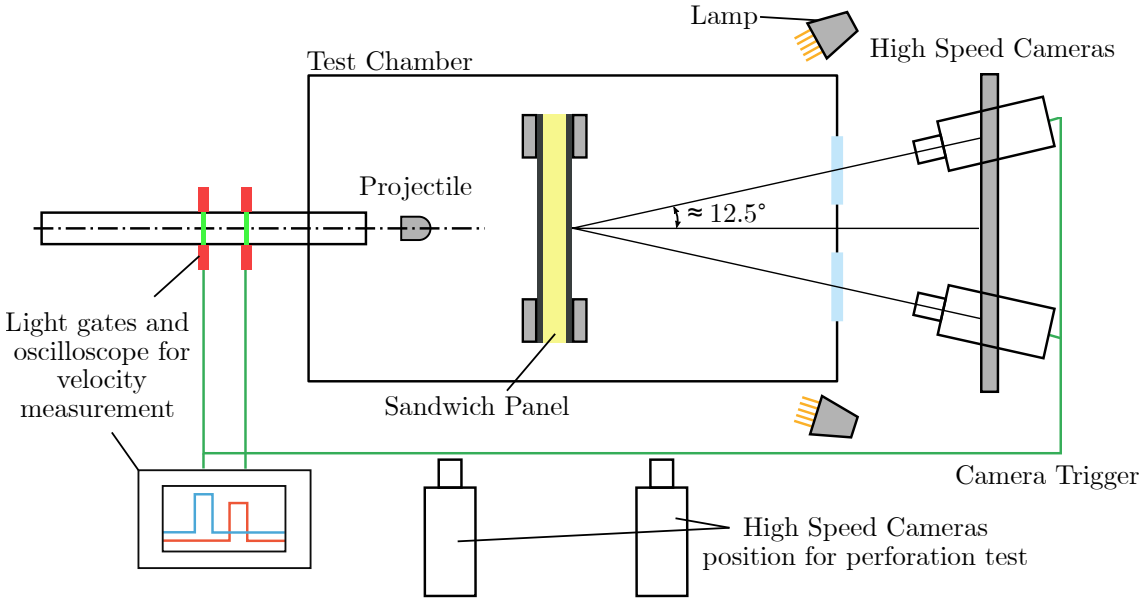


Figure 3.9: Schematic of the gas gun apparatus and high speed camera positioning.

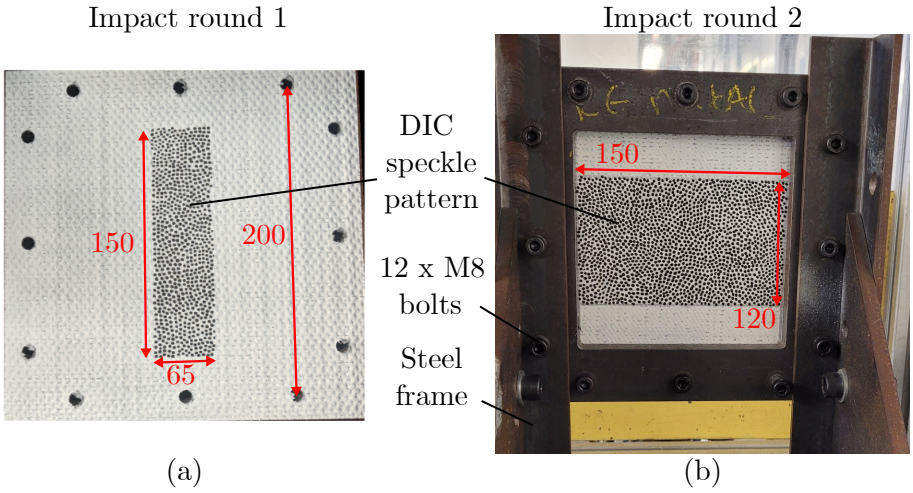


Figure 3.10: Examples of the back face of composite panel samples. (a): First round of impact testing. (b): Second round of impact testing.

used, recording at a frame rate of 28630 fps. The maximum resolution at this frame rate was 192 × 440 pixels, corresponding to a 65 × 150 mm^2 area on the back of the panels. During the second round of impact testing, two Photron Fastcam Mini AX200 cameras were used recording at a frame rate of 30000 fps. One of the Phantom cameras from the first round of testing became faulty and so this set could not be used in the second round of impact testing. The maximum resolution at this frame rate was 512 × 384 pixels, corresponding to a 150 × 120 mm^2 area on the back of the panels. The cameras were triggered by the signal from the infrared sensors, they were also connected by a cable to ensure time synchronisation.

Three-dimensional (3D) DIC was used to measure the back face displacement of the impacted panels. The camera setup was designed to be compatible with the GOM Correlate professional software [146]. The workflow consisted of setting up cameras with a 25° angle and focused on the centre of the measuring volume. The specific angle between the cameras allows for the triangulation of features on the panels. The camera sensors in this setup were 970 mm from the back face of the panel and 430 mm apart. The fixed focal length lenses were 50 mm. Once the cameras were focused, a calibration procedure was carried out to map the relative position of the cameras within the GOM software. To carry out calibration, a calibration object known to the GOM Correlate software is held in multiple orientations within the measuring volume and photographs are simultaneously taken using the two cameras. The calibration object presents a series of dots to the cameras, the location of the dots is known precisely within the software. From the image series, the location of the two cameras in 3D space is determined. A 120 × 96 mm un-coded calibration panel was used. Figure 3.11 (a) and (b) exhibit example calibration images from both the left and right camera taken simultaneously. Figure 3.11 (c) and (d) display example test still images used in the DIC measurements.

The test images are then exported in the tagged image file format (.tiff). These images are then imported into the GOM software along with the calibration file for the camera setup. The GOM software can then be used to form a series of 'facets', which together form a 'surface component'. A 'facet' is a square of pixels that is tracked between images to measure strain and movement, a pair of example facets are displayed in Figure 3.12 (a). The facets for the 3D DIC in this research were 19 pixels square and overlapped by 16 pixels. Each facet should contain a unique speckle pattern and should contain 3-4 speckles [146]. This results in a rec-

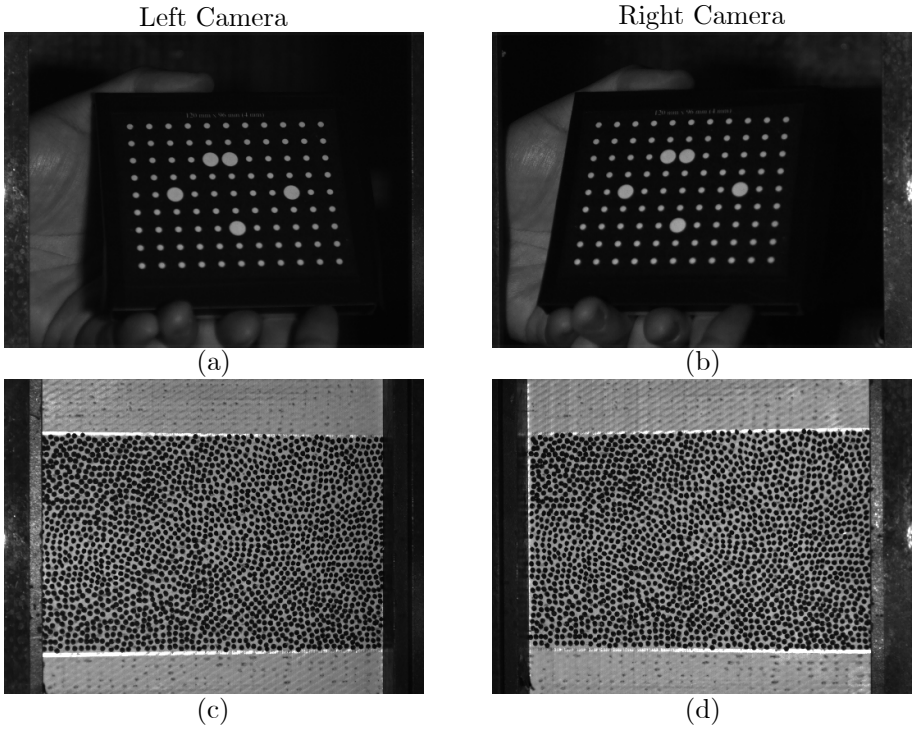


Figure 3.11: Still photographs from Photron high speed cameras. (a) and (b): Example calibration images. (c) and (d): Example test images.

ommended speckle size of 3-5 pixels. Once a surface component has been created, various measurements can be made such as full field out-of-plane displacement as shown in Figure 3.12.

For perforation testing, the velocity of the projectile before and after perforating the panel was measured by high speed cameras positioned perpendicular to the projectile path as shown in Figure 3.9. Once positioned and focused, a ruler was used to calibrate the mm/pixel value for each camera. Then the Photron software was used to measure the movement of the projectile between frames to calculate a velocity.

3.4 Imaging

3.4.1 Scanning electron microscopy

High resolution images of various samples were obtained using SEM. In particular, a 'Zeiss Ultra Plus' field-emission gun scanning electron microscopy (FEG-SEM) was used to obtain high-resolution images of the fracture surfaces of both the SENB and DCB samples in chapter 4. An accelerating voltage of between 3 and 5 kV was

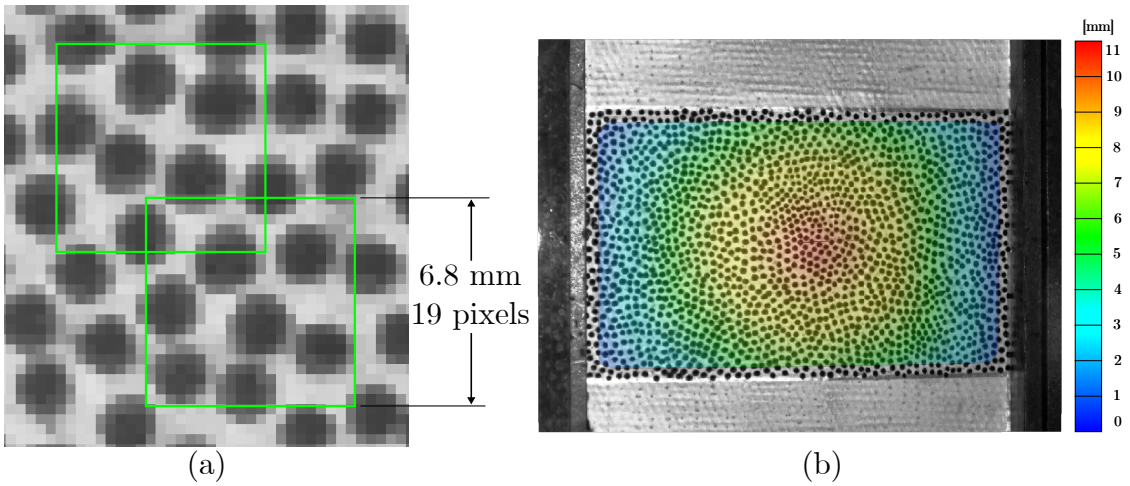


Figure 3.12: (a): Example of two 19 × 19 pixel facets 16 pixels apart. (b): Example full field out-of-plane displacement colour map (left camera).

applied. The samples for SEM were prepared by cutting out the SENB or DCB fracture surfaces using a hacksaw, these were then mounted on aluminium stubs using electrically-conducting pressure-sensitive carbon tabs. Conductive silver paint from RS Components, UK, was painted along the side of the sample to ensure an electrically conductive path from the fracture surface to the carbon tab. The samples were sputter coated with a 5 nm layer of gold–palladium prior to examination to prevent charging of the material. Images with a magnification of up to 50,000× were taken to identify the toughening mechanisms in each specimen. This magnification resulted in a resolution of 5.84 nm/pixel and allowed 20 nm particles to be readily identified within the epoxy matrix.

A 'Tescan Mira' conventional tungsten source SEM was used to examine the foams in chapter 5 and chapter 6. In chapter 5, SEM was primarily used to analyse toughening mechanisms related to short-fibre-reinforcement whilst allowing comments to be made about morphology. In chapter 6, SEM was used to enable measurements relating to morphology to be taken. In order to take these measurements a flat plane within the foam was required. Therefore, the foam samples were polished with standard wet grinding techniques up to 2000 grit. Some images with a magnification of up to 500× were taken to analyse toughening mechanisms. However, the majority of images were taken with a magnification in the region of 20× resulting in a resolution of 0.0045 mm/pixel. An accelerating voltage of 1 kV was applied with a low beam current of 100 pA. As a result, no coating was required to prevent charging of the material. These magnifications are achievable with optical microscopy, however the

translucent nature of the epoxy precludes any measurement of foam morphology.

3.4.2 Photography

Many of the tests described in this chapter were periodically photographed to record failure mechanisms and damage. Furthermore, specimens were often photographed after testing. The DSLR cameras used were a 8688×5792 50.6 mega pixel 'Canon EOS 5DS R' and a 6720×4480 30.4 mega pixel 'Canon EOS 5D Mark IV'. Using a 'Canon EF 100 mm f/2.8 USM Macro' lens, allows a 1:1 magnification ratio to be achieved. On the 36×24 mm senors in these cameras this magnification results in a maximum resolution of 0.00414 mm/pixel and 0.00536 mm/pixel for the 5DS R and 5D Mark IV, respectively. This resolution allows individual reinforcing fibres to be identified in foam in chapter 5.

The impact testing method described in Section 3.3 was designed to cause large amounts of damage within the sandwich structures to allow comparisons to be made between different toughening mechanisms. The numerical outputs of the test, namely back face displacement and energy absorbed in perforation tests do not provide information as to the damage types or quantities experienced within the panel. As such, the panels were examined visually after they were tested. The panels were first filled with a low viscosity epoxy resin that contained a blue dye. Figure 3.13 displays examples of photographs taken of a sectioned panel. At the top of the image the reservoir of blue dyed resin is visible.

This resin flowed into the cracks and damage caused by the impact and prevented any extra damage taking place during the sectioning of the panel. The impact tests to determine back face displacement often captured the projectile within the panel. The projectile could not be removed without causing extra damage to the panel. The blue resin was allowed to cure in an oven at 40°C for 12 hours. The panels were then carefully sectioned with a circular diamond tip saw to expose the center plane. This section was subsequently cleaned and polished with water and standard grit paper up to 2000 grit. Figure 3.13 shows the possible range of imaging available with the high-resolution DSLR cameras. In the full sectioned image, the damage types experienced by the panel are clear and these can be analysed and measured. While in the zoomed image, individual cells filled with resin during the infusion are visible along the sandwich skin, allowing the skin core debond to be analysed in detail.

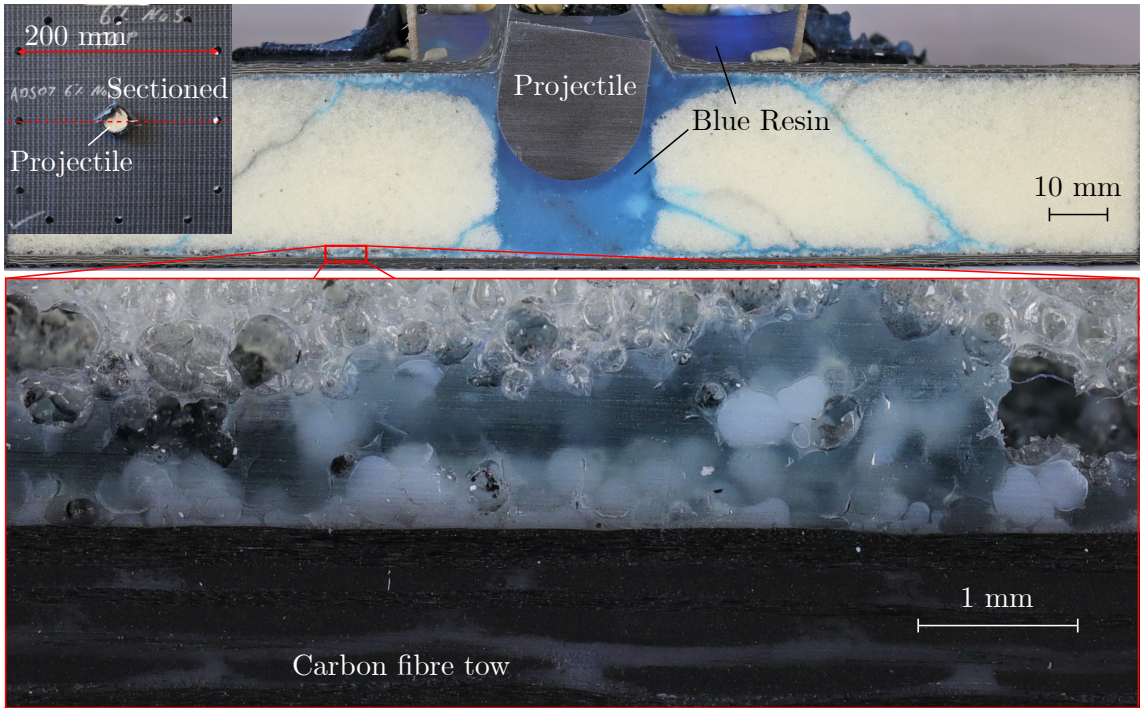


Figure 3.13: Example photographs taken of a sectioned sandwich panel. Also showing an intact panel and the location of the sectioned plane.

3.5 Concluding remarks

This chapter has detailed the experimental methods used to test and evaluate the materials and structures in this thesis. In the next chapter, the the first of two impact testing studies is presented.

Chapter 4

Impact response with toughened epoxy matrices

4.1 Introduction

This chapter details an investigation into the impact response of CFRP epoxy foam core sandwich structures. Previous research detailing the impact response of composite sandwich structures has demonstrated that by altering the layup of the individual plies in the composite skins, a significant increase in impact resistance of the structure can be obtained [19]. The research presented in this chapter extends this concept and details a systematic study of the effect of increasing the toughness of the matrix material in the CFRP skins on the impact resistance of a sandwich structure. The transfer of toughness from the bulk polymer which acts as the matrix, through to a carbon fibre laminate and finally into the composite sandwich structure will be a central theme. During this process it will be discovered that altering the properties of the skin matrix can cause transitions in failure modes during an impact event.

4.2 Materials & Manufacturing

An amine-cured epoxy system formed the basis of all the materials investigated in the current work. The resin was a standard diglycidyl ether of bisphenol-A (DGEBA) with an epoxide equivalent weight of 185 g/eq. This was cured with a stoichiometric amount of a difunctional primary amine (JEFFAMINE D-230) from Huntsman. The silica, SiO_2, nanoparticles were obtained at 40 wt% in DGEBA,

(Nanopox F400, Evonik). The silica nanoparticles used in the current work have a mean diameter of 20 nm [40]. The polysiloxane CSR particles were also obtained at 40 wt% in DGEBA (Albidur EP2240A, Evonik). The average diameter of the CSR nanoparticles is 160 nm [40].

Seven formulations of epoxy resin with systematically increasing amounts of CSR nanoparticles and silica nanoparticles were prepared. The DGEBA epoxy resin was mixed with the epoxy containing the silica nanoparticles and the epoxy containing the CSR particles. These constituents were thoroughly mixed and degassed in a vacuum. A stoichiometric amount of the curing agent was then added, mixed, and degassed again. Bulk polymer panels of each formulation were cast by pouring the resin mixture into silicone moulds to produce either 3 mm or 8 mm thick plates from which bulk specimen test samples could be machined. The plates were cured at 40 °C for 10 h, followed by a 12 h post-cure at 70 °C. CFRP composite panels and full sandwich structures were manufactured using resin infusion. The carbon fibre used was 385 gsm of H2550 fibres in 12k tows in a 0/90 non-crimp fabric. CFRP DCB panels adopted a layup of $[[[0/90]_4]_s]_s$ for a total of 16 plies and the impact sandwich structures used $[[0/90]_2]_s$ for 4 plies in each skin. The composite and sandwich structure panels were laid up on a flat, vacuum-assisted heated resin-infusion tool, and sealed using a vacuum bag. The infusion then took place over a period of 5-10 min depending on the viscosity and then cured under vacuum for 10 h at 50 °C. The panel was then post-cured at 70 °C for a further 12 h at atmospheric pressure. The impacted sandwich panels were 230 × 230 mm^2 in size and employed a 30 mm thick epoxy foam core.

The epoxy foam core used had a nominal density of 170 kg/m^3 and was manufactured using PB170 foaming epoxy resin and DM03 amine-based hardener sourced from Sicomin. The foaming took place in an open 300 × 300 mm^2 aluminium mould lined with a self-adhesive PTFE coated glass fabric. The mould was situated in a temperature-controlled environment at 21.5 °C and all foam was manufactured according to the manufacturer's guidelines. The foam was subsequently milled using a computer numerical control (CNC) milling machine to obtain flat faces and remove any skin formed at the mould surfaces during the foaming process.

Formulations for this chapter include a control polymer manufactured solely with DGEBA and hardener and modified epoxy polymers containing 3, 6, and 9 wt% of

CSR. These values of CSR wt% were chosen to match the CSR additions of previous work on similar epoxy formulations by Incerti et al. [147]. A key motivation for replicating the values used in this study was that it demonstrated a good increase in fracture properties across the full range of added toughener wt%. The addition of CSR reduces the modulus of the resin system [147]. The expected reduction in modulus was predicted using the Halpin-Tsai model, a semi-empirical model that allows the calculation of the modulus of a composite given the properties of the constituent phases [148]. The model calculates the tensile modulus, E_t, of a composite as follows:

$$E_\mathrm{t} = \frac{1 + \zeta\eta V_\mathrm{f}}{1 - \eta V_\mathrm{f}} E_\mathrm{m} \tag{4.1}$$

Where E_m is the modulus of the matrix, V_f is the volume fraction of the particulate phase, ζ is a shape factor and where:

$$\eta = \frac{E_\mathrm{f}/E_\mathrm{m} - 1}{E_\mathrm{f}/E_\mathrm{m} + \zeta} \tag{4.2}$$

The shape factor, ζ, has no direct physical significance, which is one of the major criticisms of this model. However, Halpin and Kardos [149] recommend a shape factor of $\zeta = 2$ for spherical particles, which is used for all the present predictions of the moduli of the nanocomposites.

The significant drop in modulus caused by the introduction of rubber into the matrix of a CFRP laminate will have an adverse effect on the matrix-dominated properties of the composite, such as out-of-plane stiffness. The current work explores whether the toughening benefits of CSR can be maintained whilst eliminating the reduction in modulus through the simultaneous addition of silica nanoparticles. To calculate the required wt% of silica, a modified Halpin-Tsai model as used by Carolan et al. [40] was employed. The cascaded application of a standard two-phase homogenisation procedure allows the calculation of a composite modulus containing two particulate phases. The modified model considers a system of unit volume containing a matrix of volume fraction, v_m, and two types of spherical inclusions, with volume fractions, v_1 and v_2 respectively. The first step separates the composite into two separate regions, A and B, such that each region contains a matrix phase, volume fraction v_m as in the original volume, and one type of particle, volume fraction $(1 - v_\mathrm{m})$. Each

of these regions can then be separately homogenised using the Halpin-Tsai model. The volume fractions to be use in the final homogenisation, v_A and v_B are dictated by conservation of volume as: $v_A(1 - v_m) = v_1$.

4.3 Microscopy

The imaging of fracture surfaces is described first to allow explanations of toughening mechanisms in the following sections to be better understood. Figure 4.1 displays micrographs of the fracture surfaces of two bulk epoxy SENB samples. Figure 4.1 (a) contains 6 wt% CSR and serves to demonstrate that the CSR particles are well-dispersed within the epoxy and that there were no problems with clustering of nanoparticles. Figure 4.1 (b) contains 9 wt% CSR and 17.2 wt% silica nanoparticles. The CSR particles are indicated as large voids whereas the silica nanoparticles can be observed as smaller white spots highlighted in green circles. It is clear from Figure 4.1 (b) that the diameters of the cavitated CSR particles are significantly larger than the original 160 nm average, the red circle in the scale bar represents the size of a 160 nm particle. This indicates that plastic void growth has taken place during the fracture of the sample, a well-established toughening mechanism in rubber modified epoxy [48]. Significant crack branching and feathering on the surface is clear in Figure 4.1 (b), unlike the smooth surface of an unmodified epoxy sample.

Figure 4.1 also shows the typical fracture surfaces of two CFRP DCB samples employing modified matrices. Figure 4.1 (c) is a fracture surface of a composite laminate and contains 9 wt% CSR particles which can be observed as white spots or voids in the matrix. This image (from left to right) contains a partially covered fibre, exposed fibre, and empty fibre track. The empty track exhibits how CSR particles can line up against the fibre surface and enable more fibre pull-out and bridging, thus increasing the toughness measured in a DCB test. Figure 4.1 (d) shows the space between two fibres of a 3 wt% CSR and 5.9 wt% silica nanoparticle sample. The image demonstrates the limited space between some fibres, as a result, there is less possibility for void growth and cavitation of the CSR particles. The cavitated CSR particles in this image, highlighted by green circles, are much smaller than those of the bulk epoxy in Figure 4.1 (a). The reduced space available for void growth partially limits the transferability of toughness from a bulk epoxy to

its corresponding CFRP laminate.

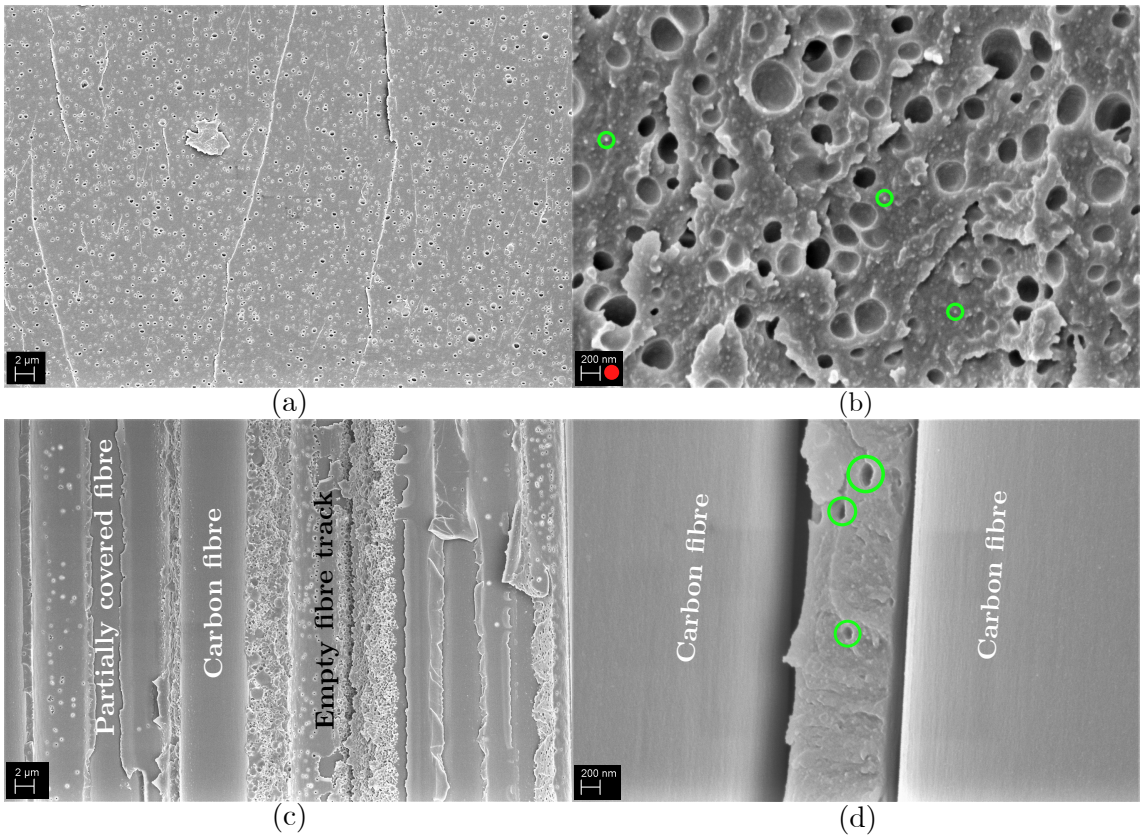


Figure 4.1: Fracture surfaces of bulk SENB samples containing (a): 6 wt% CSR at a lower magnification. (b): 9 wt% CSR and 17.2 wt% silica nanoparticles. Fracture surfaces of CFRP composites with matrices containing (c): 9 wt% CSR and (d): 3 wt% CSR and 5.9 wt% silica nanoparticles.

4.4 Bulk tensile properties

The tensile properties of the bulk epoxy polymers are summarised in Table 4.1. It can be seen from Figure 4.2 (a) that the addition of increasing CSR nanoparticles caused an approximately linear drop in the tensile modulus measured. The experimentally measured drop is consistent with that predicted by the Halpin Tsai model for this resin system. The addition of silica nanoparticles to the CSR modified bulk epoxy polymers was observed to cause an increase in measured modulus. As described in the materials section, the predicted modulus for the three silica and CSR modified systems were calculated to match that of the unmodified epoxy polymer. However, the measured moduli were found to be above that of the unmodified system, the model has under predicted the effect of silica on the modulus. A lower

silica wt% would be required to reach the modulus of the unmodified system. Similar disparities between model predictions and results were noted by Carolan et al. [40]. Regardless, the addition of silica nanoparticles reversed the loss in stiffness caused by the addition of the soft rubber particles.

An improved formulation of the hybrid composites in the current work could be used to produce a constant modulus as intended in this project. The Halpin Tsai equations are volume based, as such, it is essential to have suitable density values of all constituents to calculate accurate wt% for formulations. A more appropriate density value for the silica nanoparticles could be used when calculating the required wt% to recover stiffness loss. A value of 2650 kg/m3 was used for the density of silica nanoparticles, this value is widely accepted as the density of silicon dioxide [150]. However, silica nanoparticles pre-dispersed in DGEBA, as used in this project, are surface modified to prevent agglomeration and to increase their compatibility with the matrix [151]. As such, the equivalent density of the silica is lower than 2650 kg/m^3. A more representative value would be to calculate the density using the density of Nanopox F400, 1400 kg/m^3, and the density of DGEBA, 1160 kg/m^3, then considering that F400 is 40 wt% silica, the effective density of the silica is 1800 kg/m^3. This improved density value would result in lower wt% of silica being added to the matrix than those used here.

Figure 4.2 (b) displays the ultimate tensile strength properties of the bulk epoxy polymers. In all cases, the strength decreases approximately linearly with increasing CSR content, this is expected, and similar results were reported by [152]. On the other hand, the addition of silica nanoparticles has no further effect on the experimentally measured strength, this agrees with Sprenger [151] who reported that silica nanoparticles do not seem to increase tensile strength.

4.5 Fracture properties

The fracture energy, G_{Ic}, of each of the bulk polymers is given in both Figure 4.3 (a) and Table 4.2. The addition of CSR nanoparticles to the epoxy resin was found to greatly increase the toughness of the bulk resin. The subsequent addition of silica nanoparticles had a comparatively insignificant additional effect. Kinloch et al. [46], Carolan et al [39], Incerti et al. [147] and others have also noted that the

Table 4.1: Tensile properties of the bulk epoxy polymers.

wt% CSR	wt% SiO2	Experimental E_t [GPa]	Predicted E_t [GPa]	% Error	UTS [MPa]
0	0	2.96 ± 0.06	-	-	73.1 ± 0.005
3	0	2.76 ± 0.02	2.80	-1.8	62.8 ± 0.005
6	0	2.73 ± 0.02	2.66	2.3	59.6 ± 0.007
9	0	2.57 ± 0.02	2.52	1.6	52.0 ± 0.009
3	5.9	3.02 ± 0.08	2.96	2.0	63.8 ± 0.006
6	11.7	3.12 ± 0.07	2.96	-5.6	57.5 ± 0.013
9	17.2	3.16 ± 0.12	2.96	-6.8	51.8 ± 0.017

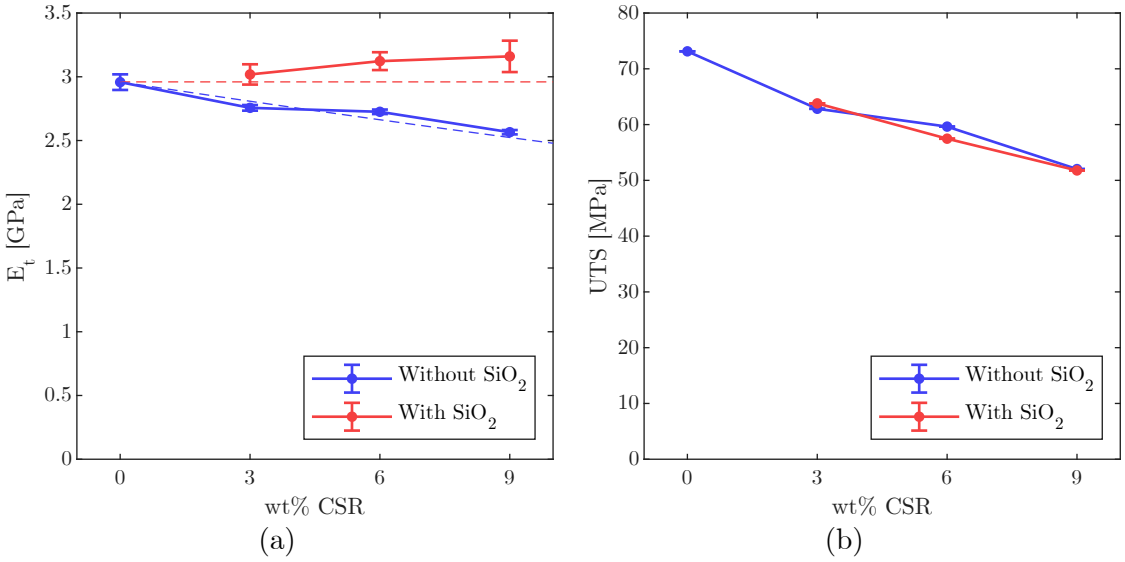


Figure 4.2: Tensile properties of the bulk epoxy polymers. (a): Modulus versus CSR content with the dashed lines representing Halpin-Tsai predictions. (b): Ultimate tensile strength versus CSR content.

toughness of epoxy polymers is greatly enhanced by the addition of rubber particles. Both Liang and Pearson [153] and Johnsen et al. [154] are amongst many who have reported on the toughening effects of nanosilica in epoxy. Johnsen et al [154] found an increase of 358 J/m^2 for an addition of 20.2 wt% nanosilica, and an increase of 240 J/m^2 for an addition of 11.1 wt% nanosilica, compared to a toughness of 103 J/m^2 for the unmodified epoxy.

The measured values of the mean mode-I initiation, $G_{\mathrm{Ic,init}}$(comp), and propagation, $G_{\mathrm{Ic,prop}}$(comp), inter-laminar fracture energies are also given in Table 4.2 and Figure 4.4 (a) and (b) respectively. The benefits of nano-modification of the composite

Table 4.2: Measured fracture energies of both the bulk epoxy polymers and the CFRP laminates.

wt% CSR	wt% SiO2	G_{Ic}(bulk) [J/m^2]	$G_{Ic,init}$(comp) [J/m^2]	$G_{Ic,prop}$(comp) [J/m^2]
0	0	188 ± 37	406 ± 61	996 ± 44
3	0	2695 ± 41	432 ± 33	1314 ± 169
6	0	2790 ± 318	613 ± 149	1534 ± 111
9	0	3221 ± 321	661 ± 112	1678 ± 104
3	5.9	2139 ± 408	537 ± 88	1411 ± 138
6	11.7	2922 ± 104	617 ± 130	1566 ± 49
9	17.2	3459 ± 145	670 ± 44	1643 ± 72

matrices can be clearly observed, as the CFRP composites with the modified epoxy matrices exhibit significantly higher values of both the initiation, $G_{Ic,init}$(comp) and the steady-state propagation, $G_{Ic,prop}$(comp), interlaminar fracture energies. From these tests, the transfer of toughness from the bulk polymer to the CFRP laminate is clear. However, there is a limit to the effectiveness of the toughening of a CFRP laminate as discussed by Carolan et al. [40] whereby the toughening mechanisms of the nanoparticles ahead of the crack tip, such as plastic zone formation, are restricted by the nearby fibres. For a 9 wt% CSR system, the values of G_{Ic} in the bulk polymer reach 3221 ± 321 J/m^2, whereas in the composite, the matrix dominated value of $G_{Ic,init}$(comp) only reaches 661 ± 112 J/m^2.

The values of $G_{Ic,prop}$(comp) - $G_{Ic,init}$(comp) are plotted in Figure 4.3 (b). Calculating the difference between propagation and initiation should remove the effect of matrix toughness, however, Figure 4.3 (b) shows an increase in $G_{Ic,prop}$(comp) - $G_{Ic,init}$(comp) for increasing CSR content. As a result, it can be concluded that the increasing presence of CSR particles increases the fibre-induced toughening mechanisms such as fibre-bridging. As discussed earlier, it can be seen from Figure 4.1 (c) that CSR particles often preferentially align along the empty fibre tracks on a DCB fracture surface. The presence of CSR reduces the area of matrix in contact with the fibre thus more easily allowing the fibre to be pulled out and form a bridge or fibre-bundle bridge. It can be seen, as with the bulk polymers, that the effect of CSR dominates that of the silica which has a comparatively insignificant effect.

Further analysis into fibre-induced toughening mechanisms revealed that the R-Curve length is also affected by CSR content. An example plot of fracture energy, G_{Ic}, versus crack length, a, is included in Figure 4.5 showing how $G_{Ic,init}$, $G_{Ic,prop}$,

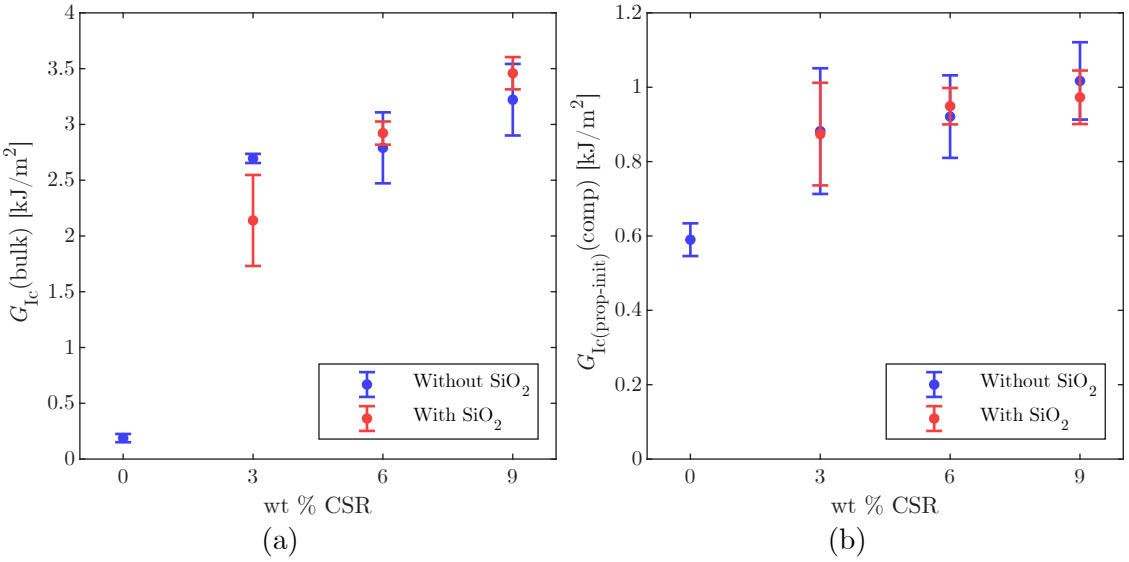


Figure 4.3: Fracture energies versus wt% of CSR. (a): Bulk epoxy polymers. (b): Propagation - initiation for CFRP laminates.

$G_{\text{Ic,prop-init}}$, and the R-curve length are extracted from a DCB specimen's test data. Figure 4.6 (a) displays the R-curve lengths versus wt% CSR values. While Figure 4.6 (b) exhibits a clear example of CSR particles lining an empty fibre track on a DCB specimen's fracture surface. Figure 4.7 is a typical example of DCB fibre-bridging with the fibre bridging extent and maximum distance annotated. The addition of CSR nanoparticles initially increases the length of the R-Curve, but further additions cause a downward trend. This suggests that the fibre-bridging extent, annotated in Figure 4.7, is reduced with large wt% of CSR. The same mechanisms that are promoting instances of fibre-bridging may be reducing the ability for fibres to bridge large distances as the fibres are held in place with a reduced force. This is assuming the fibres furthest from the crack tip are under the highest load. The angle between the fibres and the laminate increases with distance from the crack tip. Furthermore, it seems logical that the load is highest prior to the fibre-bridge breaking. Nevertheless, the fibre-induced toughening mechanisms are still increased with increasing wt% CSR content. An increase in the density of fibre bridging outweighs the reduction in fibre bridging extent.

4.6 Impact study

Table 4.3 displays a summary of the data from the impact study. Figure 4.8 shows the centre point out-of-plane displacement for all the panels under impact

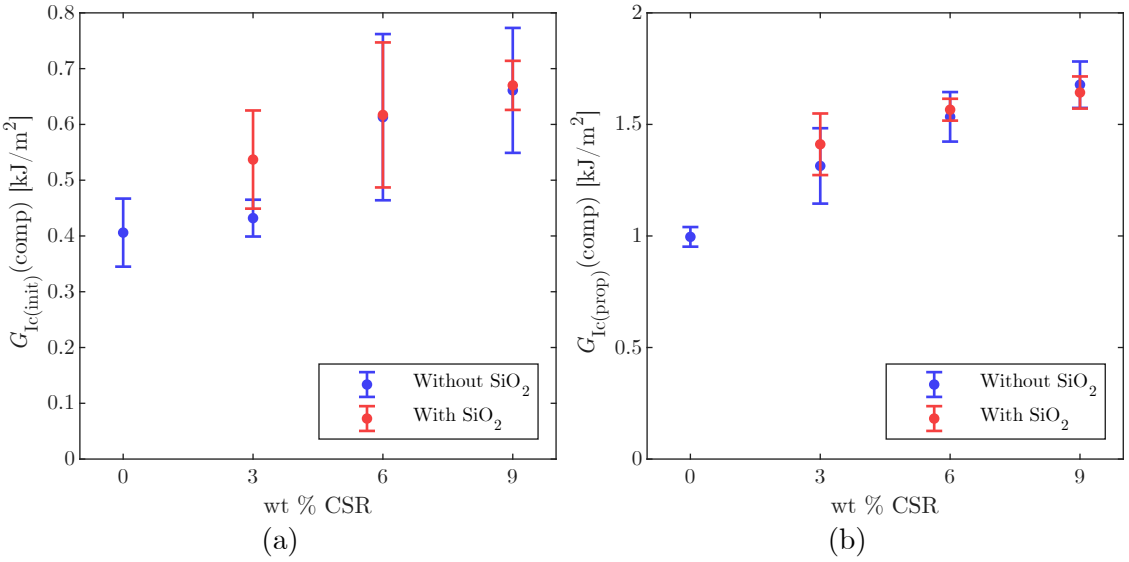


Figure 4.4: Fracture energies versus wt% of CSR. (a): Initiation for CFRP laminates. (b): Propagation for CFRP laminates.

at 130±3 m/s with a 28.5±0.1 g hemispherical aluminium projectile. Figure 4.8 also displays the back-face velocity versus time for all panels calculated from the out-of-plane displacement DIC data. The point where the front skin was perforated by the projectile can be clearly observed in Figure 4.8 and is marked by a vertical dashed green line. The perforation point is prominent when observing the velocity versus time graph as a peak, also indicated by a dashed green line. Perforation can also be viewed as the central section displacement in Figure 4.9 transitions from a smooth maximum displacement to a more angular maximum displacement as the projectile makes contact with the rear face.

Table 4.3: A summary of the data collected from the impact study.

wt% CSR	wt% SiO_2	Projectile Mass [g]	Projectile Velocity [m/s]	Maximum Displacement [mm]	Maximum Velocity [m/s]	Delamination Extent Within Front Skin [mm]
0	0	28.4	130	10.5	37.1	43.8
3	0	28.4	132	8.6	19.2	40.9
6	0	28.4	128	10.6	37.9	36.0
9	0	28.5	132	11.2	41.8	34.8
3	5.9	28.3	130	9.0	24.9	35.9
6	11.7	28.4	127	9.1	25.1	38.7
9	17.2	28.5	132	9.6	30.7	35.7

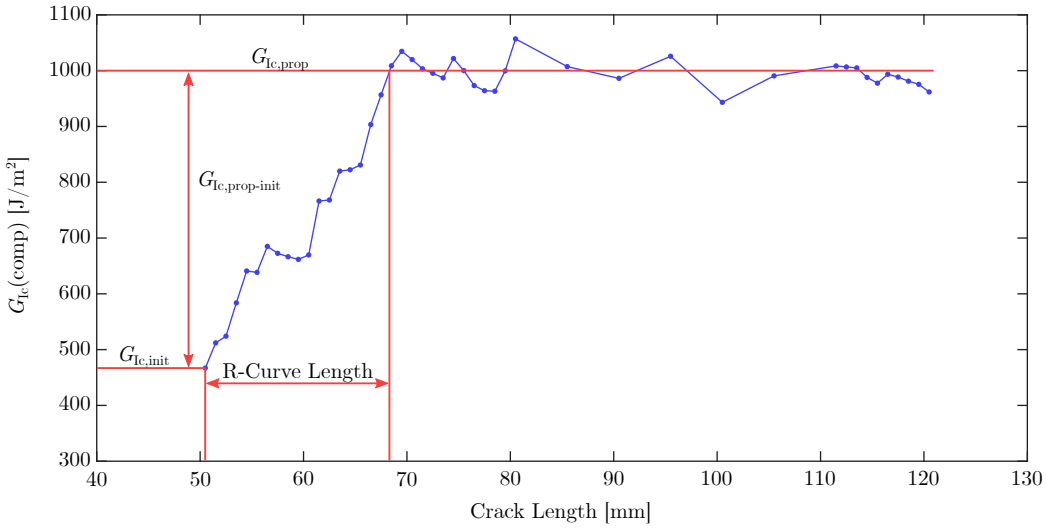


Figure 4.5: DCB example fracture energy versus crack length curve.

Figure 4.10 (a) displays the maximum displacement versus wt% CSR, the unmodified panel experiences a large displacement due to less energy being absorbed through skin damage. The 3 wt% CSR toughened panels have a lower displacement; however, further additions of CSR increase displacement. The subsequent addition of silica nanoparticles reduces the displacement to levels similar to that of the 3 wt% CSR modified panel. The 3 wt% panel exhibits the lowest displacement because of the complex interplay between different failure mechanisms. The untoughened panel does not absorb as much energy during front skin perforation and so has a greater rear-face displacement than the 3 wt% panel. However, the 6 and 9 wt% panels exhibit different failure mechanisms. Once the projectile contacts the rear face, the lower interface toughness allows widespread skin-core debonding. As a result, the rear face experiences large displacement.

Prior to perforation the panels behave uniformly, however, the initial dip in velocity, maximum velocity and maximum out of plane displacement allow for a more informative analysis. From Figure 4.8, a large dip in velocity prior to the projectile contacting the rear skin resulted in a greater maximum velocity and displacement of the rear skin overall. A possible explanation is that these panels provide less resistance to the projectile and transfer less load to the back skin, and so a large dip in velocity occurs prior to rear skin contact. These panels then undergo larger back face deflection as the projectile makes direct contact with the rear skin with a higher velocity.

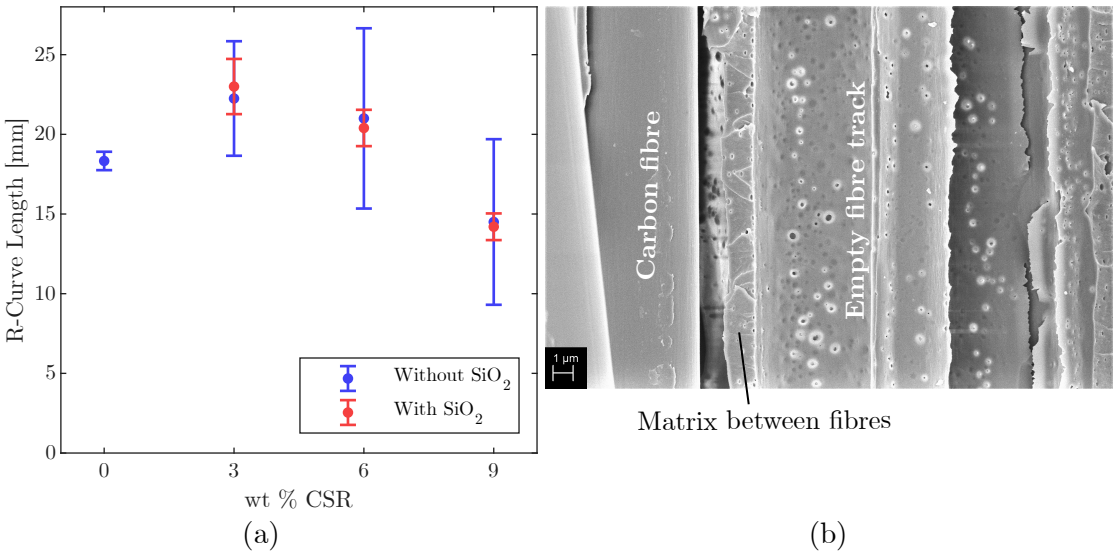


Figure 4.6: (a): R-Curve length versus wt% CSR. (b): SEM image of fracture surface of 9 wt% CSR CFRP.

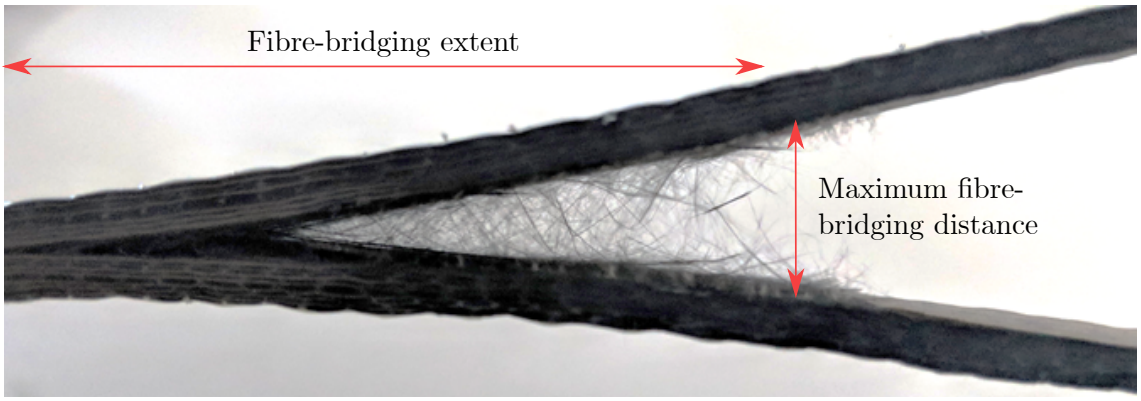


Figure 4.7: Digital photograph of a typical DCB specimen during a test showing the extent of fibre-bridging and the maximum bridging distance.

Figure 4.11 displays a section of the impact site of a panel and the damage types that take place during perforation of the front skin. The energy absorbed during perforation of the front skin occurs via four identifiable mechanisms: fibre breaking, delamination in the skin, debonding of the skin from the core and core crushing. Toughening of the matrix is most likely to affect the extent of delamination within the skin itself, as such, this was measured using high resolution images, the results are presented in Table 4.3 and Figure 4.10 (b). Increasing levels of CSR reduced the delamination within the skin as observed from the section cut. The subsequent addition of silica antiparticles presented no clear additional trend in the delamination extent measured within the front skin. Once the projectile has passed through the front skin, energy is then absorbed through further core-crushing and cracks and, in some cases, the debonding of the back face from the core. It is likely that the

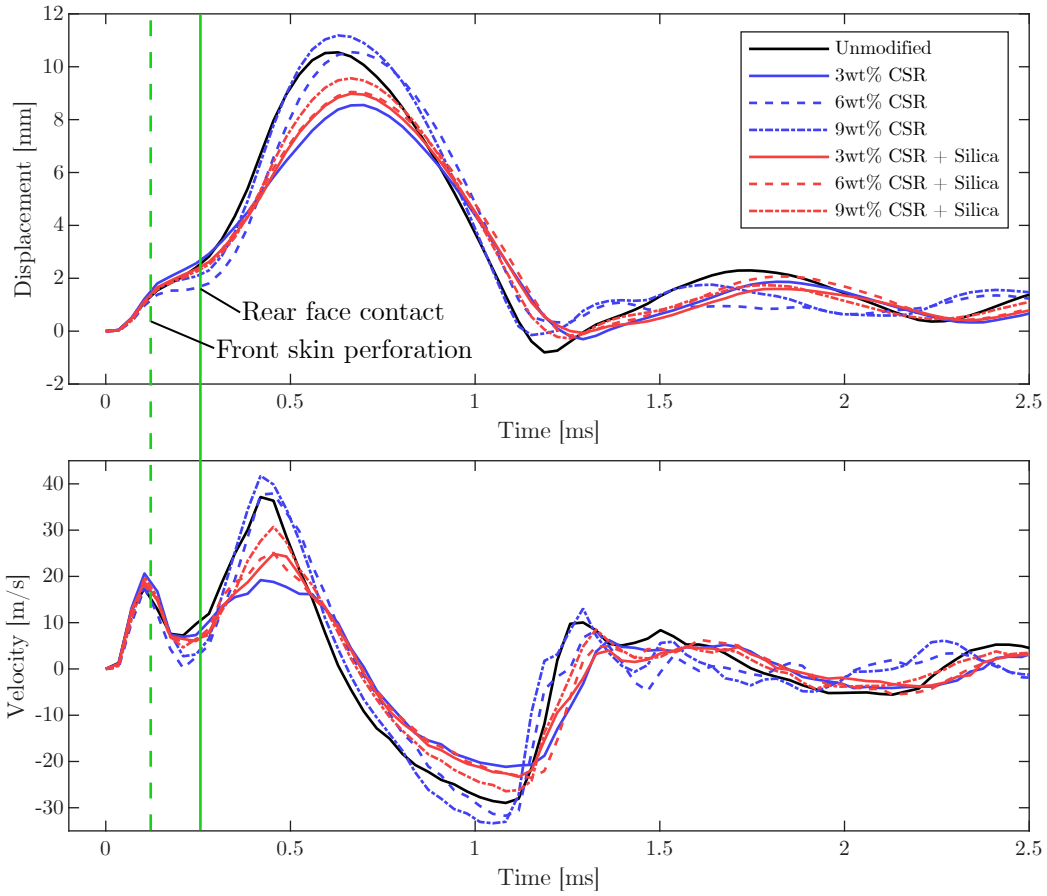


Figure 4.8: Centre point displacement and velocity versus time for all sandwich structures. The times of perforation and rear face contact are indicated by green lines.

cracks in the core furthest from the impact site are due to shear stresses experienced as the projectile impacts the front skin. In contrast, the core cracks closer to the projectile are likely caused by the projectile contacting the back face and applying a mode-I load component to the core and skin-core bond [155]. The two distinct damage modes caused by the projectile making contact with the rear face are shown in Figure 4.12.

Figure 4.13 shows the cross sections of the non-silica modified panels: the unmodified panel and the 3, 6 and 9 wt% CSR modified panels. It is clear that there is a transition in the skin-core bond failure between 3 and 6 wt% CSR. The 6 and 9 wt% CSR impact panels fail along the interface. On the other hand, the unmodified and 3 wt% CSR panels exhibited sub-interface failure of the foam. The interface in the less modified panels is tougher than in the highly CSR modified panels and so the crack is forced into the foam. The main observation from the images is that the 6 and 9 wt% CSR panels trade increased core cracking for widespread back face skin-core debonding. The debond was measured from high resolution images and

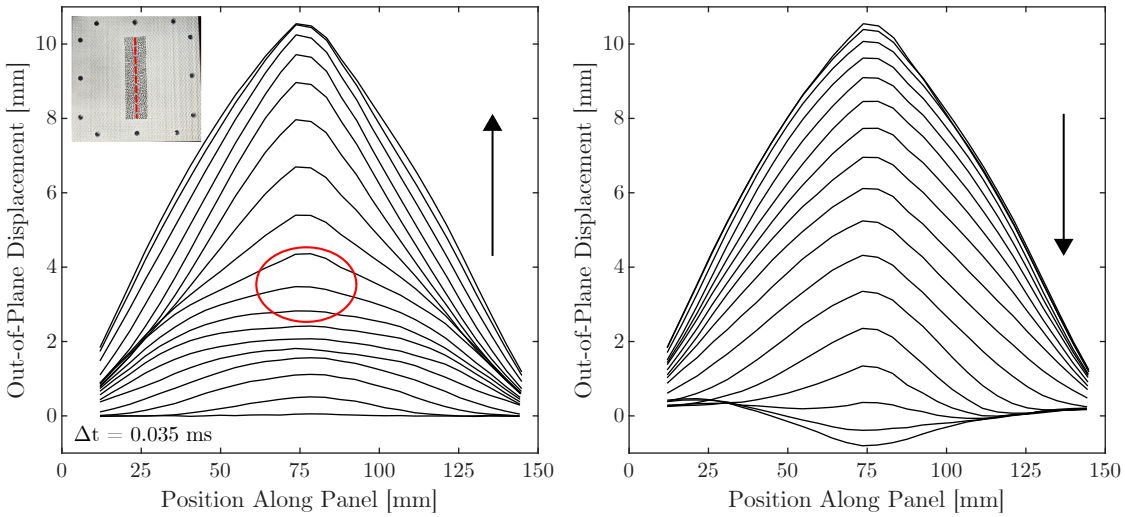


Figure 4.9: Deflection at time intervals for the vertical centre section of the sandwich structure with an unmodified matrix. Left: Up to maximum displacement. Right: Return from maximum to minimum displacement.

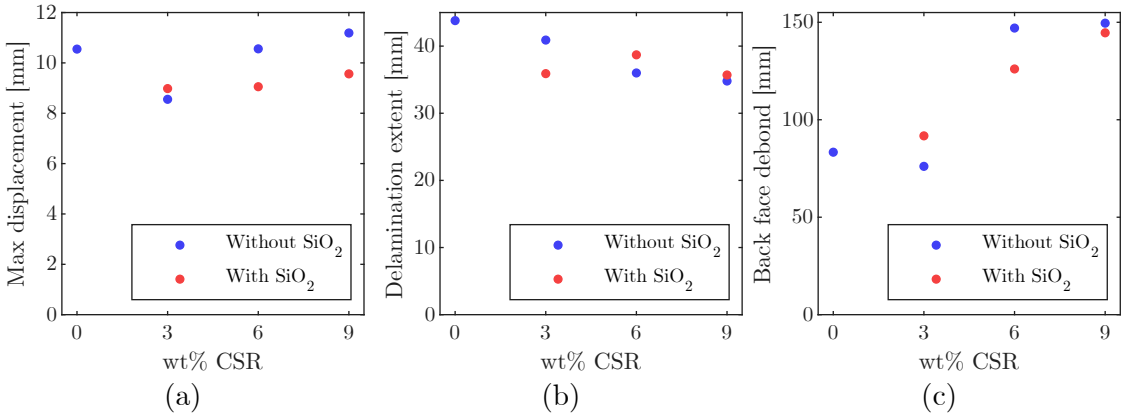


Figure 4.10: (a): Maximum out-of-plane displacement versus wt% CSR. (b): Delamination extent within the front skin versus wt% CSR. (c): Extent of back face debond versus wt% CSR content.

is plotted in Figure 4.10 (c). The unmodified and 3 wt% panel experience significantly less debonding, 80 mm compared to 150 mm for the 6 and 9 wt% CSR panels.

From the close-up image of the 6 wt% CSR panel back face debond in Figure 4.13, foam cells that were filled with white matrix resin during the infusion, are observed to have broken off from the skin. The failure of these matrix-resin-filled cells at the interface is widespread in the 6 and 9 wt% panels but not in the 3 wt% and unmodified panels. These cells fail sequentially in tension in order for the debond to propagate along the interface in the 6 and 9 wt% panels. The tensile testing of the bulk resin shows that CSR modification decreases the ultimate tensile strength

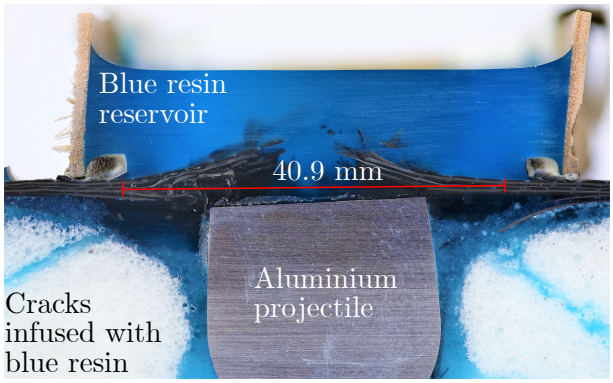


Figure 4.11: Example digital photograph of the impact site of a sandwich panel showing how front skin delamination is measured.

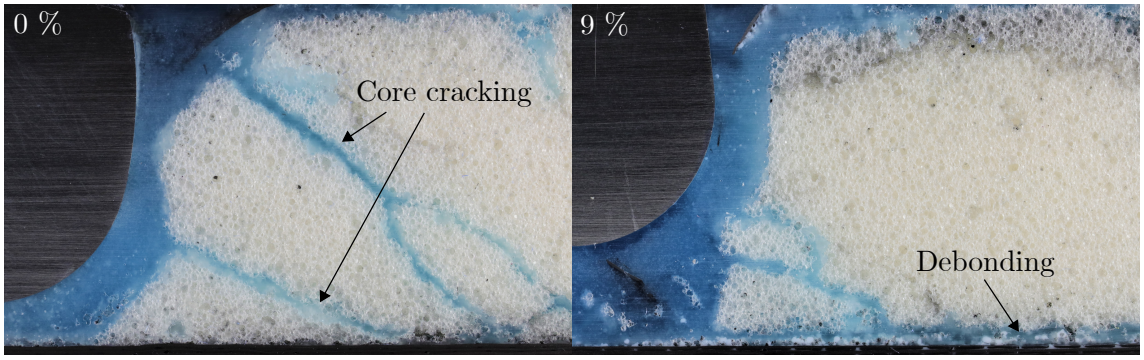


Figure 4.12: Examples of the differentiating failure modes of core cracking and skin core debonding.

(UTS) from 73.1 to 52.0 MPa for a 9 wt% modified resin. As a result, in the 3 wt% and unmodified panels, the matrix-resin-filled cells have a stronger connection to the skin. Consequently, the path of least resistance is different, and the cracks are forced into the foam. From these images and bulk resin tests, it appears significant differences between the modulus and UTS of the matrix resins affect the interfacial strength between the skin and core, indeed the results suggest that the strength and not the toughness of the resin is the dominating factor.

4.7 Concluding remarks

This chapter has investigated the impact performance of composite sandwich structures with CSR toughened epoxy matrices. A number of important conclusions can be drawn from this work, which can be summarised as follows:

The addition of CSR nanoparticles in the resin system used, caused a decrease in modulus similar to values anticipated by the Halpin-Tsai model. The silica nanopar-

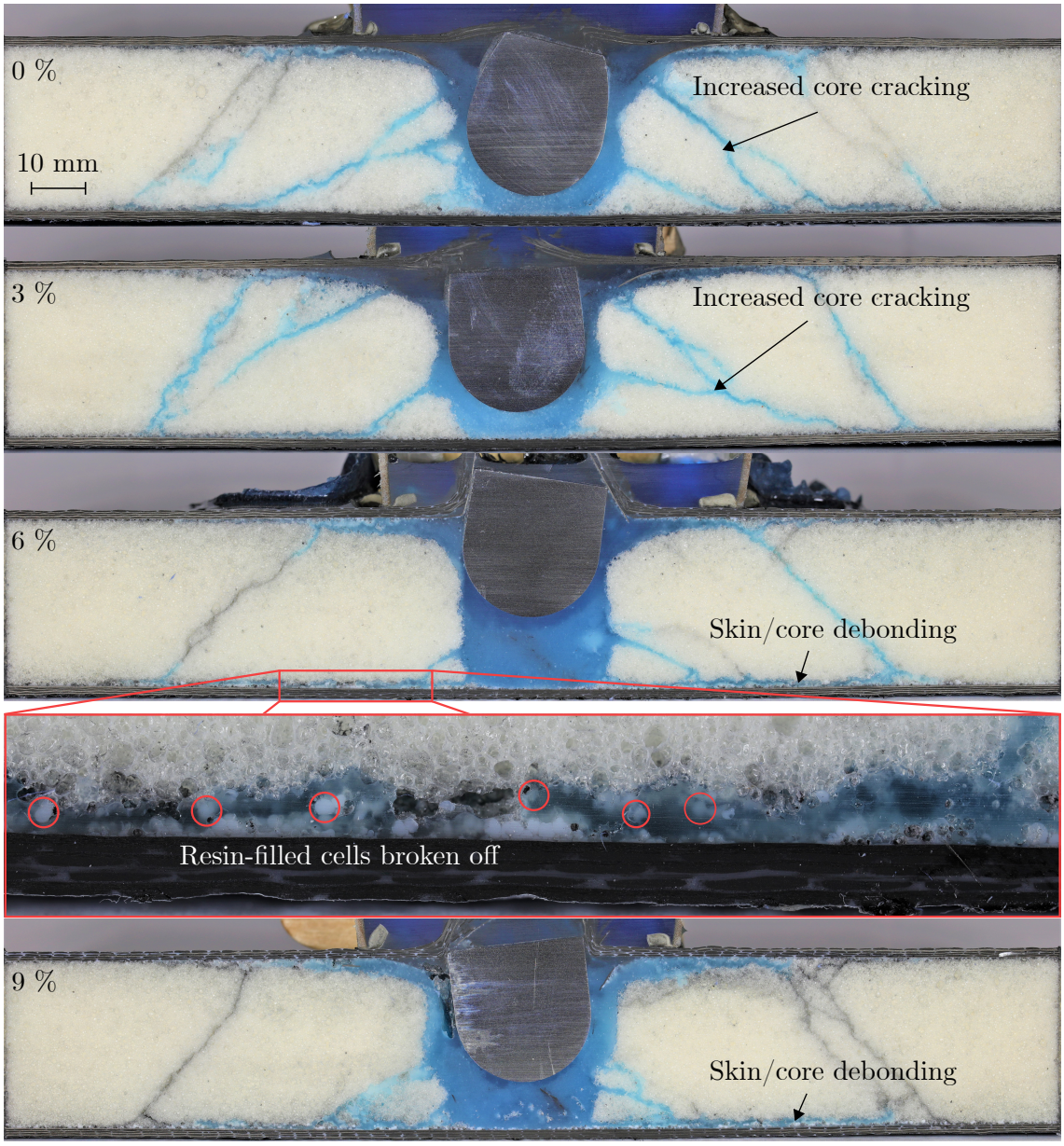


Figure 4.13: Typical images of sandwich structure cross sections with blue resin reservoir on top. For scale, sandwich core thickness is 30 mm. (a) Unmodified matrix. (b) 3 wt% (c) 6 wt% (d) 6 wt% zoomed image (e) 9 wt% CSR modified matrix.

ticles increased the modulus past that of the unmodified system due to the use of a non-optimal silica density value during calculations. The addition of CSR caused a drop in UTS while silica nanoparticles had little additional effect.

The addition of CSR nanoparticles caused a significant increase in the fracture energies of bulk epoxy polymers while silica nanoparticles had a comparatively insignificant additional effect.

The use of CSR modified matrices was demonstrated to significantly enhance the mode-I interlaminar fracture toughness of CFRP laminates. The transfer of toughness from the bulk epoxy polymers to the CFRP laminates in the form of initiation interlaminar fracture energies was limited due to space constraints between fibres. However, the steady-state propagation interlaminar fracture energies were enhanced through increasing CSR content as increased levels of fibre-bridging were induced.

A change in failure mode in the impacted panels is clear between 3 and 6 wt% CSR. Though the interface appears tougher in the low CSR wt% panels, the energy of the projectile must be absorbed, and so increased core cracking is observed. Were a tougher foam used, it may be possible to alter the location of this energy absorption back to the skin-core interface were such a failure mode desirable for panel performance. However, it is unlikely that skin-core debonding is an efficient failure mode for absorbing projectile energy when considering post-impact strength. Another set of tests would be required to ascertain this where the panels are not sectioned but instead strength tested post-impact.

The addition of 3 wt% CSR to the matrix of sandwich structures in the current work reduced back-face deflection and delamination within the front skin. Increasing to 6 and 9 wt% CSR caused increased deflection due to excessive drop in modulus and UTS outweighing toughening effects and rear face skin-core debonding. The subsequent addition of silica nanoparticles mitigated this drop in modulus and reduced deflection. Debonding failure occurring at the rear skin during impact has caused a higher back face deflection as the skin alone is less stiff than the skin with foam attached. As a result of the findings in this project, it is likely that the optimal loading of CSR is 3 wt% to ensure skin and core remain attached whilst also providing some skin toughening benefits.

It is likely that these results, such as the transition in failure mode between 3 and 6 wt% CSR are not widely applicable to any sandwich structure. Infusion manufacturing and the fracture toughness of the foam core being close to the interface toughness allowed this to occur. If a strong adhesive were used it is likely that sub-interface failure would be possible for all the matrix resins used in the current research. On the other hand, if a tougher or denser foam were used it is likely that interface failure would occur with all resin types.

The key findings are that mechanical properties can be tailored to dictate failure within the panel for a given impact event allowing maximum post-impact strength to be achieved. The toughness of all constituents and interfaces are important when considering the damage tolerance of a sandwich structure. If one element is toughened more than another, damage will be likely experienced in another element of the structure. An optimised structure will distribute damage in such a way as to maximise post-impact strength. It is considered that the techniques developed are very appropriate in optimising composite sandwich structures for transport, wind energy, and other applications.

The next chapter will detail an investigation into the short fibre-reinforcement of epoxy foams. Improving the fracture performance, as evaluated by SENB tests, will be the main aim.

Chapter 5

Toughening of fibre-reinforced epoxy foam

5.1 Introduction

During the impact testing of the epoxy-foam-core sandwich structures in chapter 4, extensive cracking within the core was found. As such, this chapter builds on this research further and details a systematic study of the effect of reinforcing epoxy foam with short-cut carbon and aramid fibres with the aim of increasing strength and toughness. The focus of this chapter will be on the fracture performance of these reinforced foams.

5.2 Materials & Manufacturing

A commercially sensitive epoxy based foaming resin formed the basis of the materials investigated in this chapter. The nominal density of the cured foam in this chapter is 170 kg/m^3. Short-cut para-aramid and carbon fibres were sourced from Barnet Europe. Aramid fibres had cut lengths of 0.75 mm, 3 mm, and 6 mm and an average diameter of 12 µm. Carbon fibres had cut lengths of 1.5 mm, 3 mm, and 6 mm and an average diameter of 8 µm. Manufacturing limitations prevented 0.75 mm carbon fibres being cut. Both short-cut fibre types were appropriately sized for use with epoxy. Milled carbon fibres were sourced from ELG Carbon Fibre with average length 0.6 mm and an average diameter of 7 µm. The milled fibres used were unsized prior to milling and were used as received. Reinforced epoxy foams

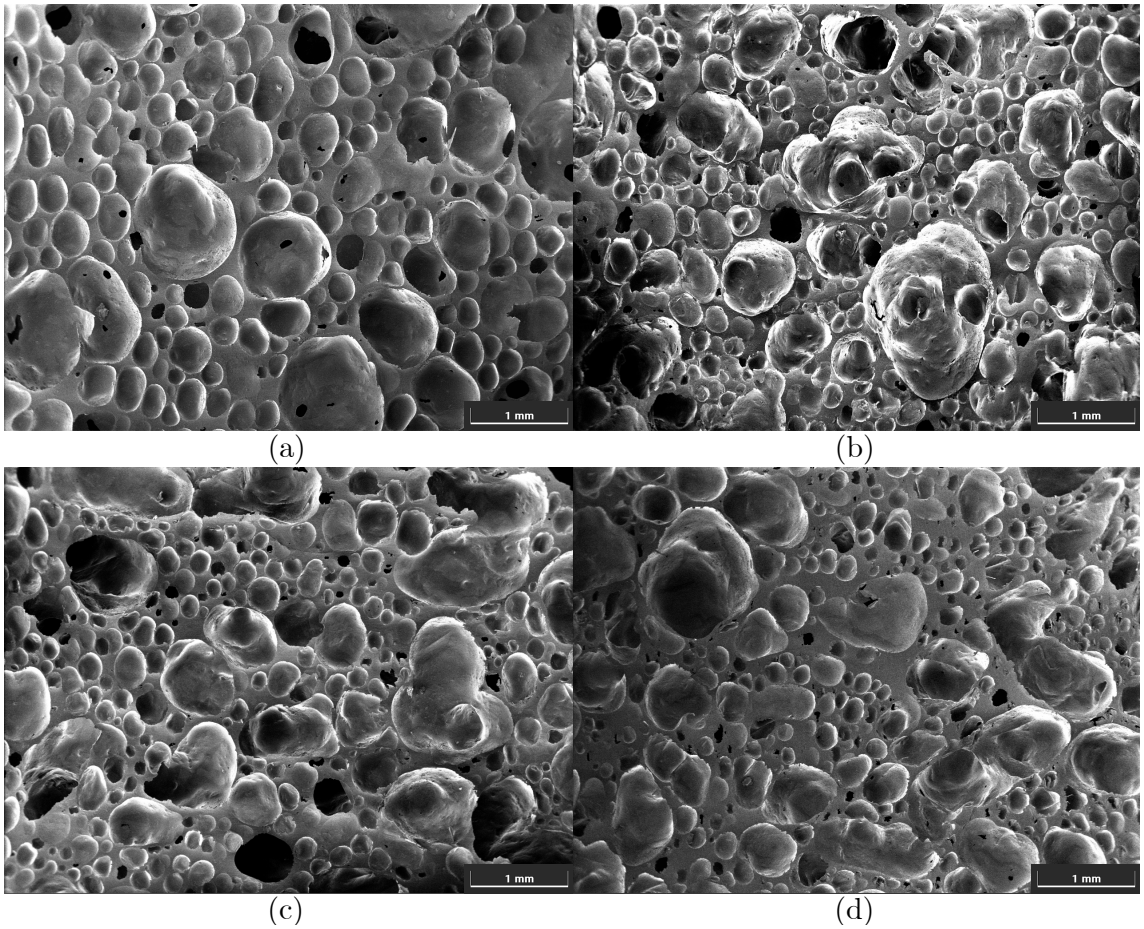
were synthesised using a high-speed mixer to disperse fibres in the foaming resin. A stoichiometric amount of hardener was then added, these constituents were then mixed thoroughly again. The mixture was then poured into a rectangular mould and cured at 21°C for 24 h, followed by a 24 h post-cure at 40°C. The long cure cycle at a precisely controlled temperature is required when manufacturing foams as the viscosity, particularly the thixotropic response, of the foam is critical to developing and maintaining an optimal microstructure at a target density. The fibre loadings used in parts per hundred resin (PHR) were 0.5, 1, 2.5, and 5. For 3 mm and 6 mm fibres, it was only possible to load the resin with 0.5 and 1 PHR, higher loading caused a drastic increase in viscosity and resulted in a poor-quality foam.

5.3 Microscopy

5.3.1 Polished aramid-reinforced foam

Each foam sample was cut and polished to give a smooth surface to image using an SEM. An SEM image of one foam containing each aramid fibre length is shown in Figure 5.1. The images show cells surrounded by nodes connected by cell walls. The images show the foams have bi-modal cell size distributions with many small cells surrounding fewer larger cells. The cell sizes do not appear to change significantly across the aramid fibre-reinforced formulations. However, the small cells in the aramid fibre-reinforced foams appear somewhat smaller than in the control foam. The images also show that there is a slight loss of spheroidicity in the cells between Figure 5.1 (a) and Figure 5.1 (b), (c), and (d). In the 3 mm and 6 mm aramid foams, very large voids could be found. This is shown clearly in Figure 5.2 (a). These voids could measure up to 6 mm across and were difficult to get an entire void within the field of view of the microscope. Large voids in fibre-reinforced foam with fibres of similar length have been previously reported in the literature [53, 59].

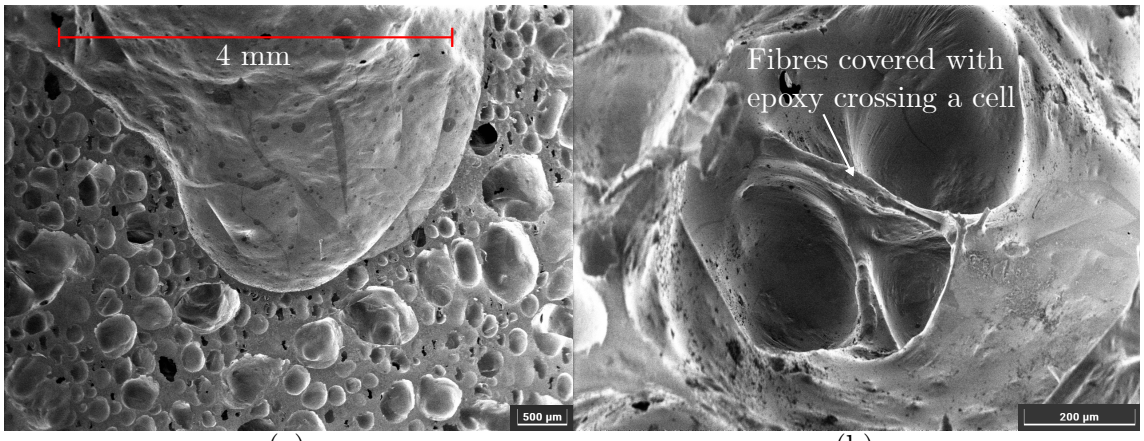
No exposed fibres can be seen in the SEM images of the polished aramid-reinforced foam. This is because during the manufacturing process of the foam, all fibres are completely wetted with liquid epoxy. Furthermore, the aramid fibres are sized appropriately for use in epoxy. As a result, the fibres in the finished foam are covered in epoxy. This is the case even if the fibres do not completely lie within a natural cell wall, epoxy will encapsulate the fibre and bridge to the cell wall, an example of this is shown in Figure 5.2 (b). Exposed fibres, with no epoxy sheath, are very rare



(a) (b)

(c) (d)

Figure 5.1: SEM images of polished aramid foam samples. (a): Control (b): 0.75 mm 2.5 PHR (c): 3 mm 0.5 PHR. (d): 6 mm 1 PHR.



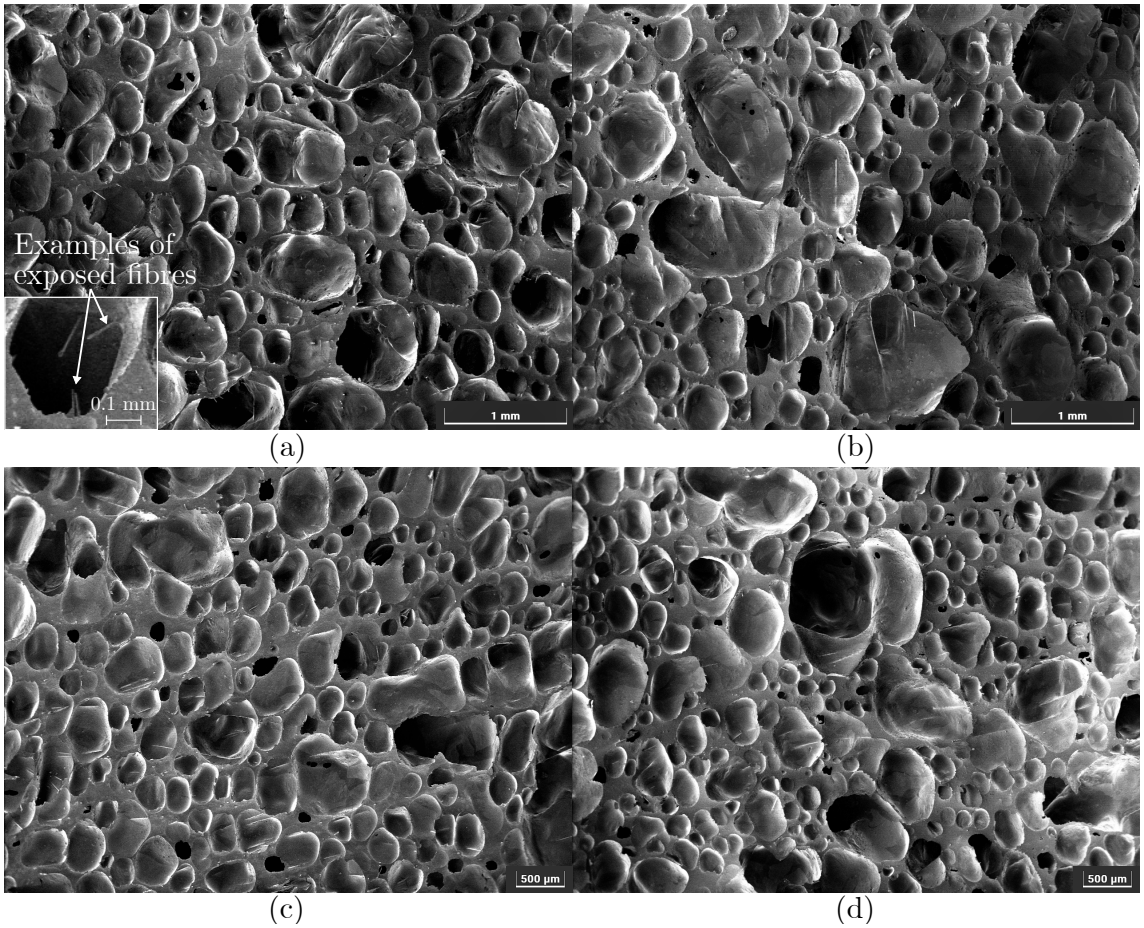
(a) (b)

Figure 5.2: SEM images of polished aramid foam samples. (a): Large void in 6 mm 1 PHR. (b): Epoxy covered fibres in 0.75 mm 2.5 PHR.

within the polished samples.

5.3.2 Polished carbon-reinforced foam

Figure 5.3 shows polished samples of foams containing each carbon fibre length. Again, there is a slight loss of spheroidicity in the cells between the control foam in Figure 5.1 (a) and the four foams in Figure 5.3. However, there appears to be less of a bi-modal distribution of cell sizes within the carbon-reinforced foams. As with the aramid foams, the 3 and 6 mm foams have some large voids which were avoided for these SEM images as the voids could measure up to 6 mm across. Similar to the chopped aramid fibre foams, the chopped carbon foams do not show exposed fibres when polished. However, some exposed fibres can be seen in the milled carbon fibre foam in Figure 5.3 (a), this is related to the lack of sizing on the milled carbon fibres.



(a) (b)

(c) (d)

Figure 5.3: SEM images of polished carbon foam samples. (a): Milled fibre 2.5 PHR. (b): 1.5 mm 1 PHR. (c): 3 mm 1 PHR. (d): 6 mm 1 PHR.

5.4 Compression

The compressive yield strengths of the aramid and carbon fibre-reinforced foams are presented in Table 5.1 and Table 5.2, and are plotted in Figure 5.4 and Figure 5.5 respectively. The compressive yield strength of the foam is increased by up to 10% by adding fibres. All aramid fibre lengths give rise to an increase in strength, however, adding 5 PHR 0.75 mm aramid fibre causes the compressive yield to drop below that of the control. A similar trend is observed when adding 0.6 and 1.5 mm carbon fibres, 5 PHR 0.6 mm causes strength to drop back to that of the control. It is clear that, to maximise compressive yield, approximately 2.5 PHR of the shortest fibre length is optimal for both fibre types. While short carbon fibres improve compressive yield, the 3 and 6 mm carbon fibres reduce the yield strength of the foam. A visual inspection reveals the 3 and 6 mm carbon fibre-reinforced foams have some large voids such as the one in Figure 5.2 (a). These large voids cause a drop in yield strength by reducing the total load bearing area of a foam sample. In contrast, short fibres do not reduce the quality of the foam in the same way. While the long aramid fibre-reinforced foams also display large voids, the increase in density of these foams prevents a potential drop in yield strength.

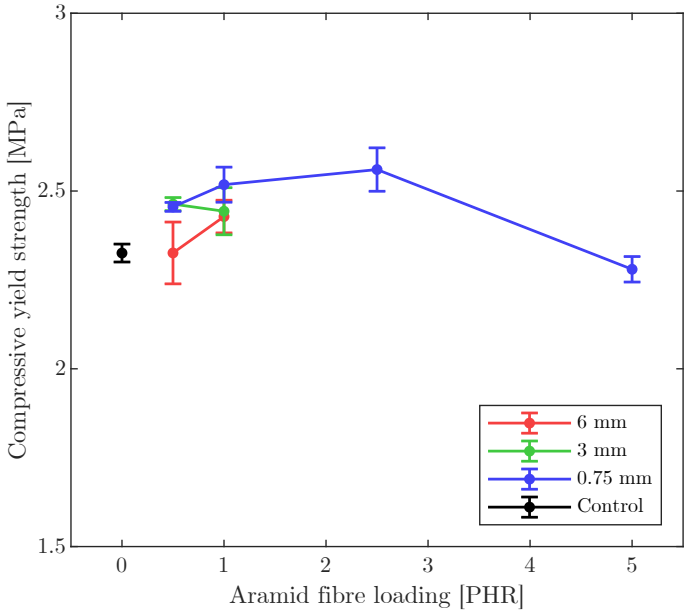


Figure 5.4: Compressive yield versus fibre loading for aramid fibre-reinforced foams.

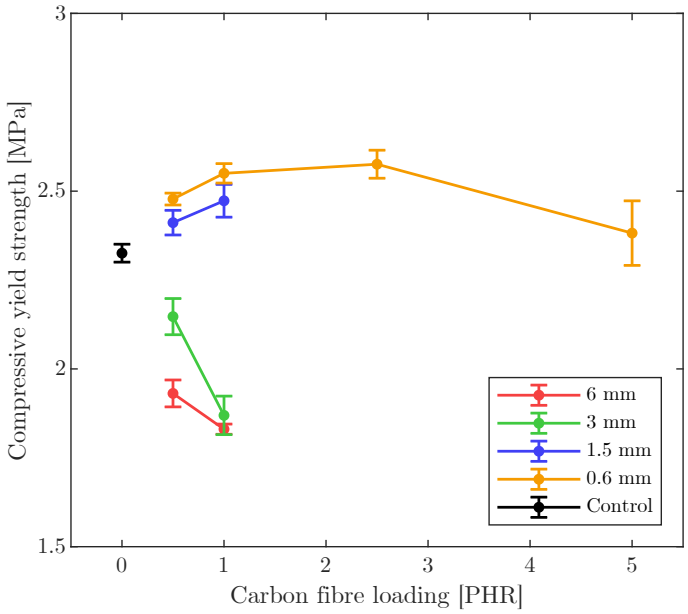


Figure 5.5: Compressive yield versus fibre loading for carbon fibre-reinforced foams.

5.5 Density

It is interesting to note the effect on density associated with each fibre type, length, and loading. The density of aramid and carbon fibre-reinforced foam can be found in Table 5.1 and Table 5.2 respectively. The addition of carbon fibres does little to increase the density of the foam, clearly a benefit in any potential application. However, the addition of aramid fibres moderately increases the density of the foam. The addition of 5 PHR 0.75 mm aramid fibre produces a foam of 200 kg/m^3, 14% denser than the control. However, this increase in density is far outweighed by the 107% increase in fracture energy. Furthermore, longer aramid fibres have an increased effect on the density with 1 PHR 6 mm producing a foam with a density of 203 kg/m^3. The increase in density is partially caused by the addition of the denser fibres. Both aramid and carbon fibres are denser than the epoxy polymer. The density is primarily affected by the inhibiting effect the fibres have on the foaming process due to the increased viscosity of the fibre resin mixture. It can be inferred that carbon fibres impede the foaming process significantly less than aramid fibres. In fact, the large voids in the 3 and 6 mm carbon fibre-reinforced foams have caused the overall density to be lower than the control. In these foams, the longer fibres have a tendency to mat together forming a barrier in the resin and effectively trap more gas during the foaming process than the resin would otherwise, forming large voids in the process.

5.6 Fracture properties

5.6.1 Fracture energy: Aramid-reinforced foam

Fracture energies for all the manufactured aramid fibre-reinforced foams are given in Table 5.1, all data shows the calculated average, standard deviation, and percentage difference to the control. The fracture energy, G_{Ic}, versus fibre loading of each of the aramid reinforced foams is shown in Figure 5.6.

Table 5.1: Measured properties of aramid reinforced foam.

Fibre Length [mm]	Fibre Loading [PHR]	Fracture Energy G_{Ic} [J/m^2]	% change	Compressive Yield Strength [MPa]	% change	Density [kg/m^3]	% change
-	-	124 ± 13	00	2.33 ± 0.03	00	175.1 ± 0.8	00
0.75	0.5	113 ± 14	- 08	2.46 ± 0.01	+ 06	187.8 ± 0.8	+ 07
	1	137 ± 25	+ 11	2.52 ± 0.05	+ 08	191.7 ± 1.4	+ 09
	2.5	208 ± 45	+ 68	2.56 ± 0.06	+ 10	199.6 ± 5.7	+ 14
	5	256 ± 30	+ 107	2.28 ± 0.04	- 02	200.1 ± 0.6	+ 14
3	0.5	133 ± 23	+ 07	2.46 ± 0.02	+ 06	189.8 ± 1.5	+ 08
	1	165 ± 28	+ 33	2.44 ± 0.07	+ 05	194.0 ± 1.1	+ 11
6	0.5	143 ± 31	+ 16	2.33 ± 0.09	00	190.6 ± 5.1	+ 09
	1	204 ± 44	+ 65	2.43 ± 0.05	+ 04	203.3 ± 3.5	+ 16

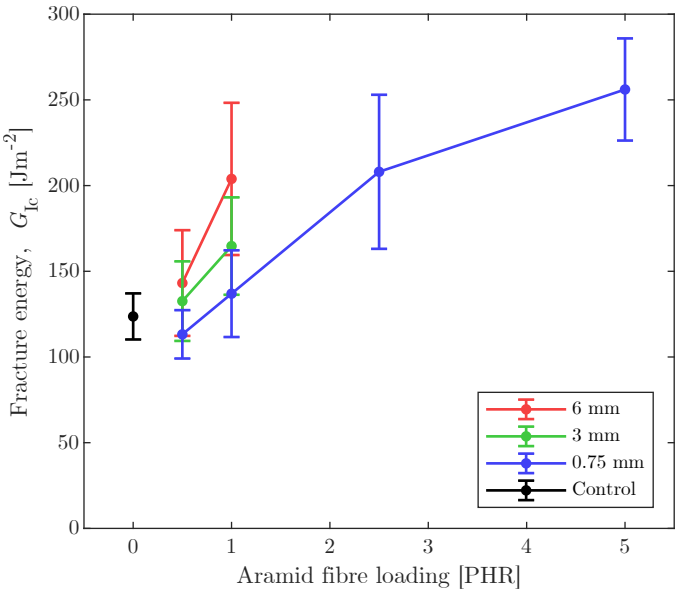


Figure 5.6: Fracture energy versus fibre loading for Aramid fibres.

The addition of aramid fibres was found to greatly increase the toughness of the foam from 124 J/m^2 to a maximum of 256 J/m^2. It is clear that, for a similar fibre loading, longer fibres induce a greater increase in toughness in the foam. For example, a loading of 1 PHR 6 mm aramid fibres produces a similar toughness to a loading of 2.5 PHR 0.75 mm aramid fibres. It was observed from SENB raw data curves that foams with long fibres failed in a progressive manner with fibres arresting the crack progression. In contrast, the control foam failed in a catastrophic manner, as displayed in Figure 5.7.

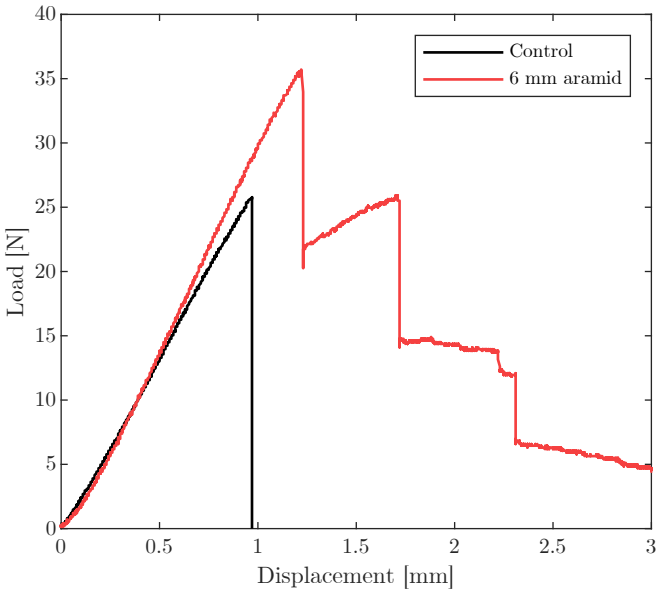


Figure 5.7: Load-displacement curves for the SENB testing of aramid 6mm and control.

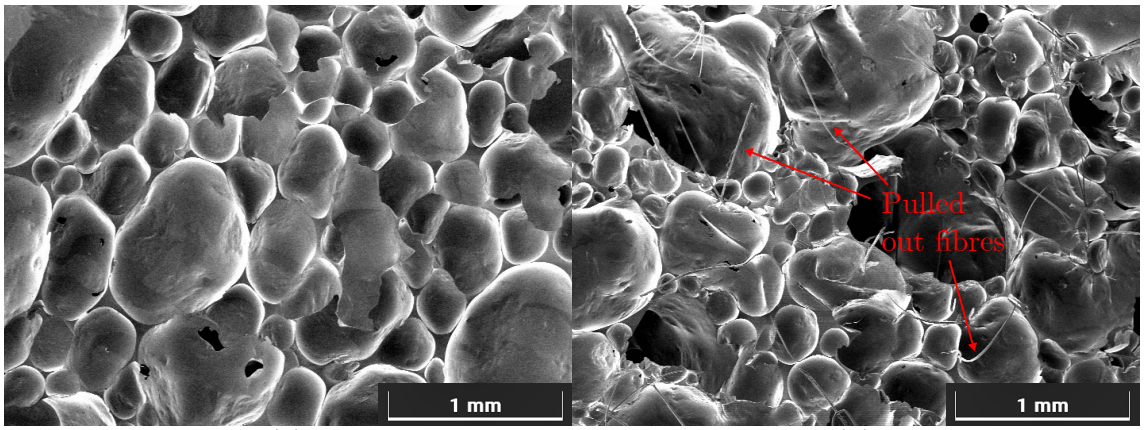
The progressive failure of the long fibre specimens does not affect the measured fracture energy; however, it is clearly a benefit for a material in service to fail in such a manner as the total energy absorbed during a complete failure of the foam is increased. Shen and Nutt [62] have also reported fibre bridging in aramid-reinforced sandwich core flexure tests. They noted a significant increase in load after initial failure, again this did not affect the measured property. However, they note the potential for fibre reinforcement to be used to avoid catastrophic failure of sandwich structures. This is otherwise achieved through increased safety factors leading to an increase in structure weight.

5.6.2 Fracture morphology: Aramid-reinforced foam

It can be seen in Figure 5.8 that the toughening mechanisms of aramid foams include fibre pull-out and fracture as well as crack deflection. The crack direction in all frac-

ture micrographs is from bottom to top. Figure 5.8 (a) shows the fracture surface of a control sample. The foam structure is clearly visible and not dissimilar to the polished samples examined in Figure 2. Moreover, the fracture surface was observed to have no significant deviations from the initial crack plane over the entire crack propagation length. Figure 5.8 (b) shows the fracture surface of a foam modified with 1 PHR 6 mm aramid fibres. Significant deviations from the initial crack plane were noted, indicating that the presence of the fibres in the foam caused the crack to deflect. In addition, many exposed fibres can be observed, up to 1 mm long. On the contrary, in the polished sample images, Figure 5.1, no exposed fibres were observed. Thus, the visible fibres in Figure 5.8 (b) are a consequence of the fracture process, i.e. they were pulled out of the opposite fracture surface. Fibre pull-out appears to be a principal toughening mechanism within all the aramid fibre-reinforced foams studied here.

The fibres shown in Figure 5.8 (b) are solitary fibres and appear well dispersed within the foam rather than manifesting as bundles or agglomerates. This represents a key development on fibre-reinforced foams previously reported in the literature where bundles of fibres are mentioned as a manufacturing issue and being less effective at improving mechanical and fracture properties [57, 59].

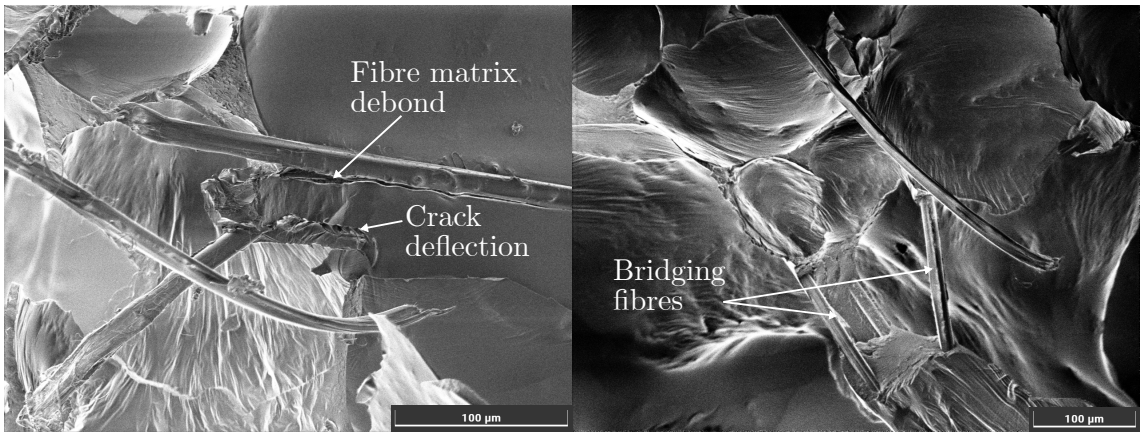


(a) (b)

Figure 5.8: SEM images of SENB fracture surfaces. (a): Control sample. (b): 6 mm 1 PHR aramid sample showing exposed aramid fibres up to 1 mm in length.

The 0.75 mm aramid fibres caused large increases in the fracture energy of the foam and allowed for a higher fibre loading than longer fibres. Figure 5.9 presents examples of fibres on SENB fracture surfaces, Figure 5.9 (a) demonstrates that fibres are pulled out but does not show significant amounts of epoxy left on the surfaces

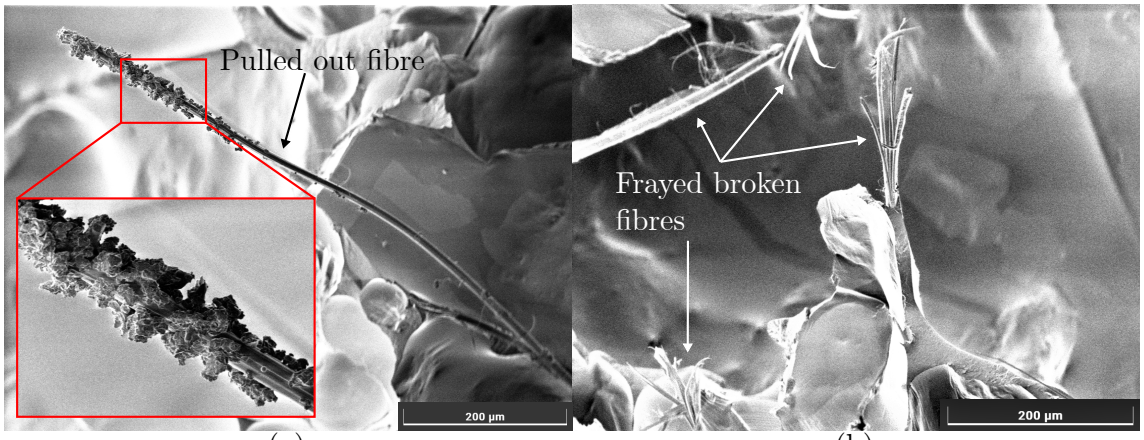
of the fibres. It can be seen that the crack is deflected by a fibre as it deviates from its main plane around the base of a pulled-out fibre. Figure 5.9 (a) exhibits a case where a microcrack is formed as a fibre debonds from the matrix. In Figure 5.9 (b) fibres are seen bridging across where a secondary crack has caused epoxy to fracture off around them. These images clearly demonstrate that the presence of the fibres causes the crack path to deflect and lengthen which requires additional energy to propagate [156] and for additional lesser cracks to form leading to an increase in fracture energy.



(a) (b)

Figure 5.9: SEM images of SENB fracture surfaces with 0.75 mm Aramid. (a): Fibres exposed after pull-out and fracture. (b): Fibres exposed after surrounding matrix failure.

Figure 5.10 (a) shows an image of a pulled-out fibre while (b) shows a series of fractured fibres, the bases of which are situated in nodes and cell walls. It is clear from Figure 5.10 (a) that, while the fibre is not completely encased in polymer, there is a significant amount of epoxy in small pieces remaining adhered to the end of the fibre. This contrasts with the clean exposed fibres shown in Figure 5.9. The cutting process to prepare the fibres is an aggressive process. It is probable that it affects the sizing of the virgin fibre, especially close to the cutting plane. The shorter 0.75 mm fibres will therefore be more affected by the cutting process than the longer fibres. The broken fibres in Figure 5.10 (b) have split and frayed upon fracture. Furthermore, some amount of pull-out has occurred before failure as the fibres are exposed. As the fibres are pulled out, they bridge the crack before failure. Sequential failure of groups of these fibres are responsible for the progressive load-displacement traces, such as the one shown in Figure 5.7.



(a) (b)

Figure 5.10: SEM images of SENB fracture surfaces with 6 mm aramid. (a): Fibre pulled out with epoxy remaining on the end. (b): Image showing how long aramid fibres fray when broken.

5.6.3 Fracture energy: Carbon-reinforced foam

The experimentally determined fracture energies for all of the manufactured carbon fibre-reinforced foams are given in Table 5.2. The addition of carbon fibres was found to greatly increase the toughness of the foam from 124 J/m^2 to a maximum of 245 J/m^2. All the carbon fibre-reinforced foams showed an increase in fracture energy over the unmodified foams. However, the link between fibre length and increase in fracture energy is not as clearly defined as with the foams modified with aramid fibres.

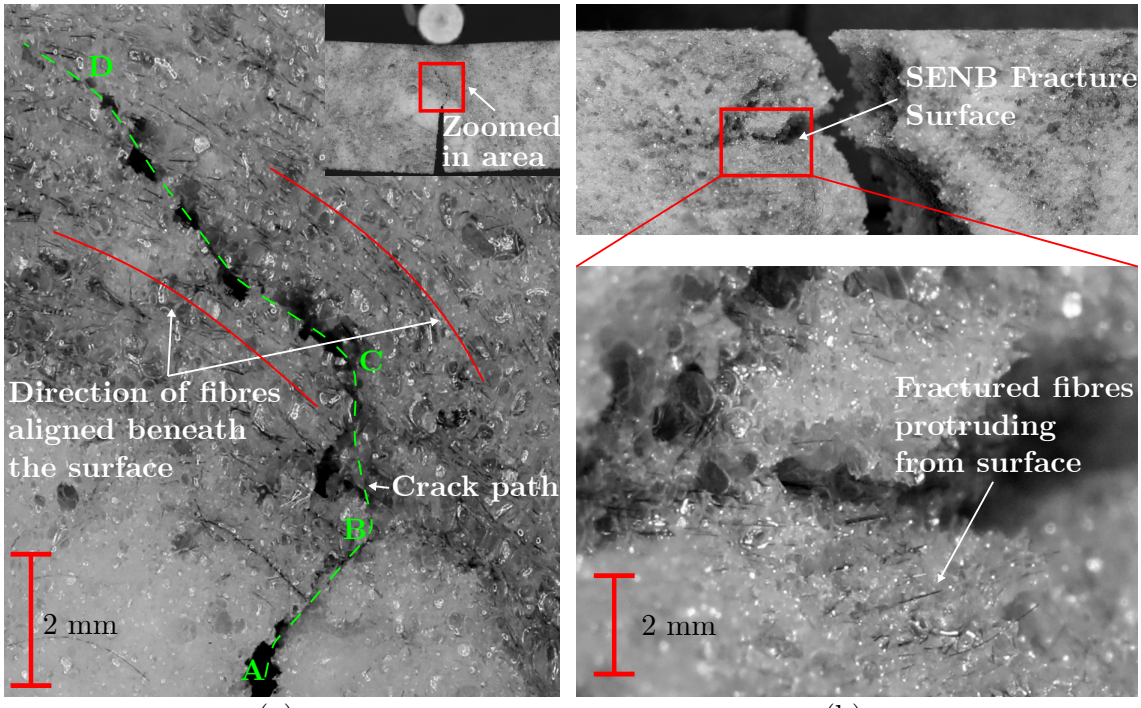
5.6.4 Fracture morphology: Carbon-reinforced foam

From fractographic analyses conducted on SENB samples, it can be seen that the toughening mechanisms for carbon fibre-reinforced foams also include fibre pull-out and fracture as well as crack deflection. Figure 5.11 shows high-fidelity photographs of two 6 mm carbon 1 PHR samples. Figure 5.11 (a) shows fibres aligned beneath the surface of the foam of one of the samples. These fibres are 6 mm long and span the whole width of the image. The process of manufacturing the foam involves mixing the resin and fibres together with a rotating blade. During this process, the fibres tend to align tangential to the tip of the mixing blade within the foam mixture. This is especially relevant for longer fibres.

As a result of the circular mixing motion and the subsequent step of pouring the mixture into a separate foaming and casting mould, there is no prevailing global di-

Table 5.2: Measured properties of carbon reinforced foam.

Fibre Length [mm]	Fibre Loading [PHR]	Fracture Energy G_{Ic} [J/m^2]	% change	Compressive Yield Strength [MPa]	% change	Density [kg/m^3]	% change
-	-	124 ± 13	00	2.33 ± 0.03	00	175.1 ± 0.8	00
0.6	0.5	161 ± 37	+ 30	2.48 ± 0.02	+ 07	175.4 ± 0.4	00
	1	168 ± 40	+ 36	2.55 ± 0.03	+ 10	176.2 ± 1.0	+ 01
	2.5	180 ± 33	+ 45	2.58 ± 0.04	+ 11	178.4 ± 0.8	+ 02
	5	245 ± 59	+ 98	2.38 ± 0.09	+ 02	184.5 ± 0.9	+ 05
1.5	0.5	140 ± 26	+ 13	2.41 ± 0.03	+ 04	176.5 ± 0.2	+ 01
	1	157 ± 33	+ 27	2.48 ± 0.05	+ 06	177.7 ± 0.5	+ 01
3	0.5	137 ± 16	+ 10	2.15 ± 0.05	- 08	172.5 ± 0.6	- 01
	1	201 ± 13	+ 62	1.87 ± 0.05	- 20	173.6 ± 1.2	- 01
6	0.5	159 ± 57	+ 29	1.93 ± 0.04	- 17	172.3 ± 1.4	- 02
	1	187 ± 43	+ 51	1.83 ± 0.01	- 21	176.7 ± 0.9	+ 01



(a) (b)

Figure 5.11: Photos of 6 mm carbon foam SENB samples. (a): Zoomed in image of the front of a sample during a test. The crack can be seen to initially cross the path of fibres, fracturing them, then deflect to follow a path between aligned fibres within the foam. (b): Fracture surface of a sample showing a crack that has been deflected multiple times and fractured fibres protruding from the fracture surface.

rection for these aligned fibres within the foaming and casting mould. The alignment of fibres is only local. However, since fracture initiation is a local process, this local alignment of fibres is critically important. In Figure 5.11 (a), the fracture initially progresses upwards from the initial crack tip from point A to point B, fracturing the fibres in its path. After approximately 2 mm of crack propagation, it straightens to progress mainly upwards to point C before deflecting again to progress upwards to point D, taking a less obstructive path between the aligned fibres within the foam. Figure 5.12 plots the raw load versus displacement data for this sample, as the load climbs from 20-35 N, small sharp dips in load are clearly visible. During this period of the test, cracking noises were heard, however, periodic imaging revealed no advancement of the main crack during this period. The control foam did not produce these cracking noises; therefore, the noises pre-failure in the fibre reinforced foams are attributable to the failure of the fibres. Based on the analysis of Figure 5.11 (a), Figure 5.12, the periodic imaging of the test, and the noises heard, the fibres fail before the crack advances. The failure strain of the carbon fibres is lower than that of the epoxy. As a result, when the sample is loaded and the area ahead of the crack is strained past the fibre failure strain, the fibres fail sequentially. When the epoxy failure strain is reached the broken fibres provide a path for the crack to travel through until intact fibres prevent further propagation in that direction. The crack then deflects along the aligned fibres and the sample fails suddenly. This deviation from the main plane of the crack will give rise to mode-II contributions and a resultant increase in fracture energy. The crack path in this sample is also longer than an unreinforced sample, again causing an increase in fracture energy.

The toughening mechanisms taking place within this sample depended greatly upon the state of fibre-reinforcement ahead of the crack tip, in this instance the arrangement of the fibres was conducive to a high fracture energy. Some samples did not have fibres positioned in such a way as to give as high a fracture energy. This fact explains the larger standard deviations in Table 5.1 and Table 5.2 for the fracture data of long fibre foams. Figure 5.11 (b) shows the fracture surface of a different sample, it is clear from the upper image that the crack path has been deflected. The lower image shows broken fibres protruding from the surface, the fibres appear to be individual and well dispersed. From these images it is clear that fibre breakage is a key toughening mechanism. Similar photographs are not shown for aramid foams as the yellow fibres are difficult to distinguish.

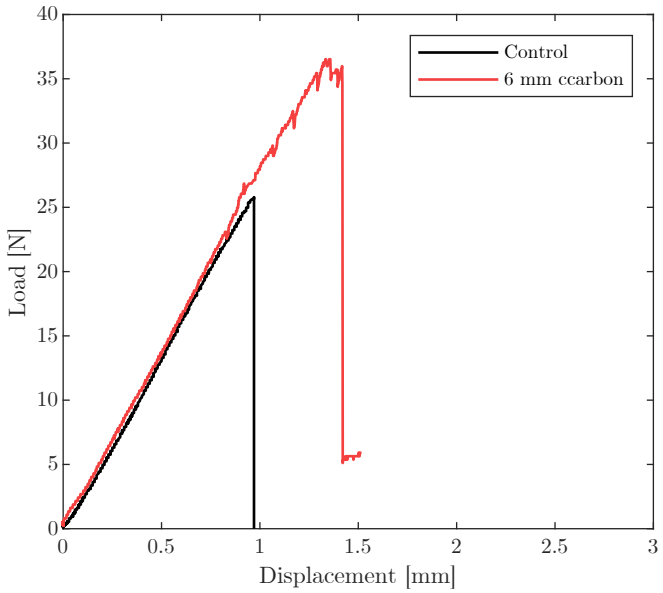
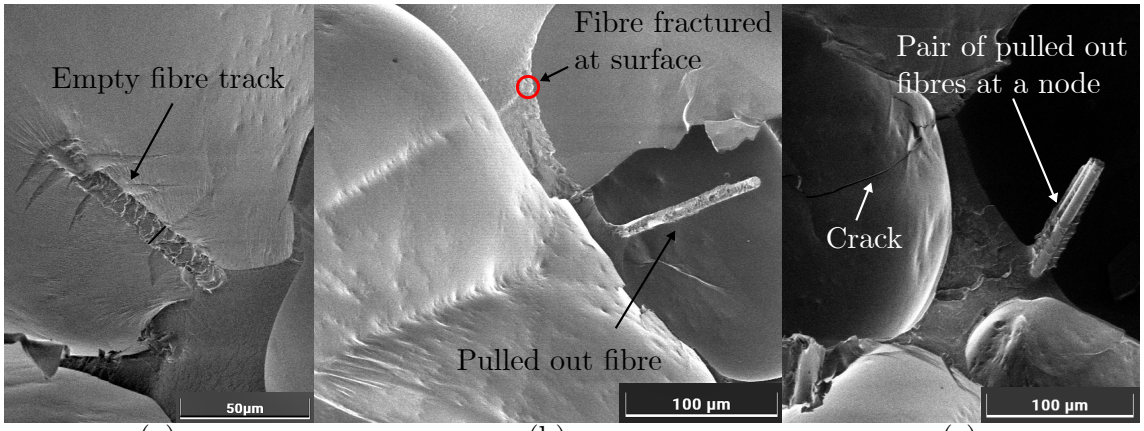


Figure 5.12: Load-displacement curves for the SENB testing of carbon 6 mm and control.

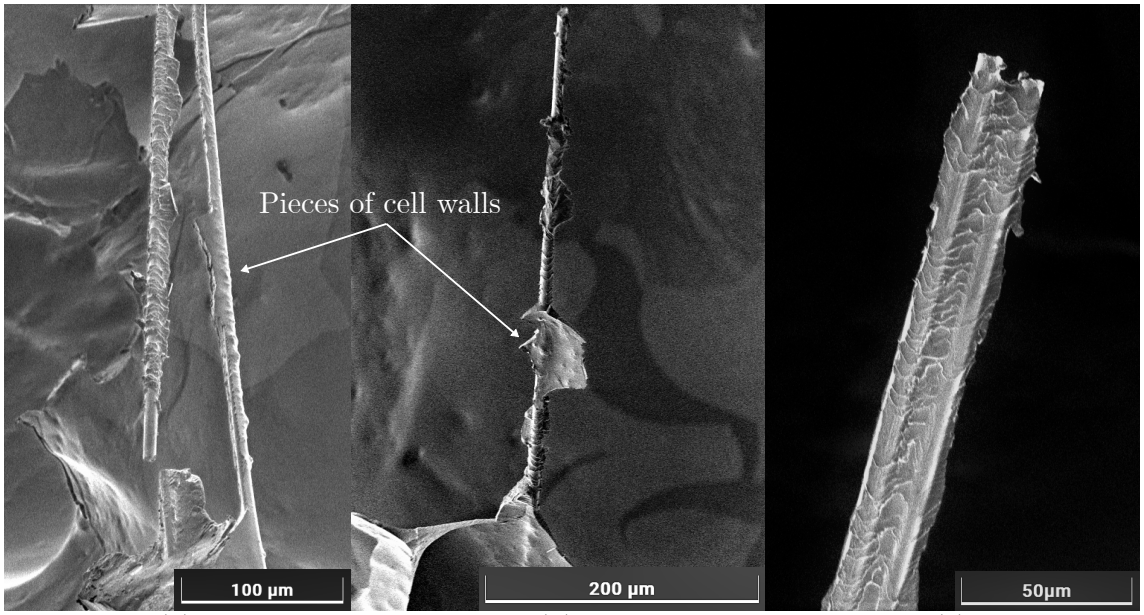
The toughening mechanisms in carbon fibre-reinforced foams are highlighted in Figure 5.13. Figure 5.13 (a) shows an empty fibre track, from where a fibre has been pulled during the fracture event. The fibre was encased in epoxy, this is evident as the track is 2 µm wider than the 8 µm diameter fibres. The rough surface of the fibre track reinforces this, a smooth track would indicate that the fibre was not well adhered. Figure 5.13 (b) demonstrates an example of how fibres can lie within a cell wall. One fibre is fractured at the crack plane while the second fibre has been pulled-out and is mostly encased in epoxy. Figure 5.13 (c) exhibits a pair of fibres lying within a node that have been pulled out and are also both encased in epoxy. Figure 5.14 (a) and (b) show long exposed fibres with significant parts of cell walls remaining after fracture. The extra fracture surfaces created by these fibres, and the associated energy absorption, represents a significant toughening mechanism. The main toughening from fibre pull-out is from the shear at the interface due to interfacial fictional sliding [68]. Figure 5.14 (c) shows a pair of fibres pulled out encased in epoxy showing clear signs of epoxy shear failure on the surface. While the aramid fibres were found by themselves, it was not uncommon to find longer carbon fibres in pairs such as in Figure 5.13 (c) and Figure 5.14 (a) and (c). Furthermore, while aramid fibres frayed and split when broken, carbon fibres exhibited clean fractures.

Figure 5.15 shows a series of milled fibres protruding from the fracture surface. A



(a) (b) (c)

Figure 5.13: SEM images of SENB fracture surfaces of carbon foams. (a): Empty fibre track from a 3 mm fibre. (b) Example of both a pulled out and fractured 3 mm fibre. (c): Example of two 6 mm fibres pulled out.



(a) (b) (c)

Figure 5.14: SEM images of SENB fracture surfaces of carbon foam. (a) 3mm fibres bridging after epoxy has fractured off. (b): 1.5 mm fibre pulled out with epoxy remaining. (c): Pair of 6 mm fibres pulled out coated with epoxy.

key difference between these fibres and the longer, chopped carbon fibres discussed earlier is the lack of epoxy polymer adhering to the fibre. The chopped fibres were originally sized for use with epoxy as the matrix and so are encased in epoxy when pulled out, whereas the milled fibres did not have any appropriate sizing and so pull out with a very clean surface, almost devoid of polymer. Despite this, the milled fibres provide benefit as the pull-out of clean fibres still absorbs energy through interfacial frictional sliding [68].

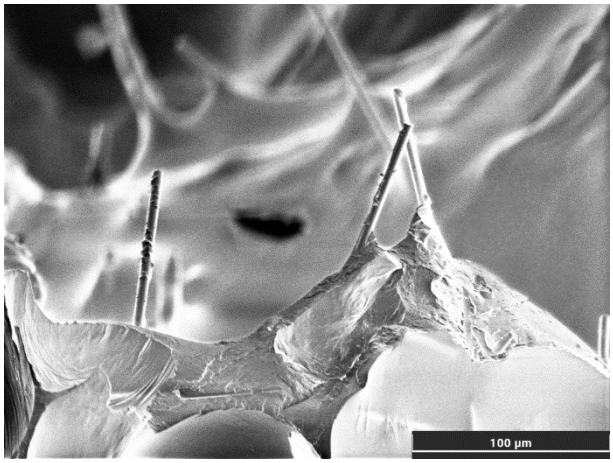


Figure 5.15: SEM image of a SENB fracture surface showing milled carbon fibres pulled out. Note the relatively clean surfaces of the milled fibres.

Figure 5.16 shows a carbon fibre below the surface of a fractured node from an SENB sample. From the striations leading to the cell wall and node, it is clear that the fibre and the surrounding polymer material was loaded as the crack passed along the main fracture plane, providing a stiffening effect. It is interesting to note that the fibres within the foam causing this stiffening effect and increasing constraint may well be reducing the fracture energy if they are not within the crack path triggering energy absorption mechanisms.

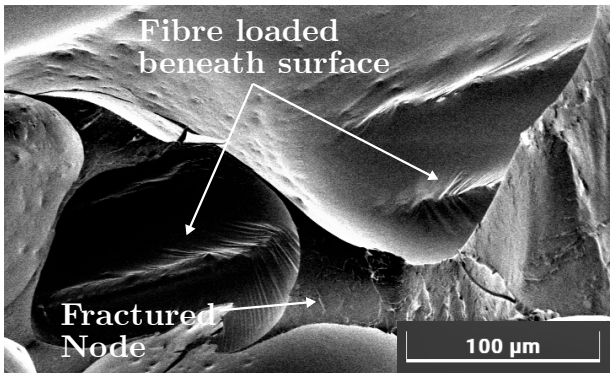


Figure 5.16: SEM image of a 6 mm fibre below the surface of a fractured node having been loaded.

5.7 Concluding remarks

In this chapter low density short carbon and aramid fibre-reinforced epoxy foams have been successfully synthesised for the first time in the literature. The effects of fibre type, length, and loading have been investigated. Compression and fracture

properties were measured and compared to an unreinforced foam.

Improvements in the fracture performance of epoxy foams have been achieved through the addition of short fibres. The incorporation of 5 PHR 0.75 mm aramid led to a maximum increase in fracture energy of 107% from 124 J/m^2 to 256 J/m^2. The main toughening mechanisms observed were fibre pull-out, fibre fracture and crack deflection and arrest. The addition of 2.5 PHR 0.75 mm aramid fibre and 0.6 mm carbon fibre both cause an increase in compressive yield strength of 10%, further additions cause a drop in strength. The addition of aramid fibre causes an increase in foam density of up to 16%, short carbon fibres only increased density up to 5% while 3 and 6 mm carbon fibres reduced density by up to 2%. This investigation has shown that fibre reinforced epoxy foams can outperform their unreinforced counterparts with few drawbacks other than a slight increase in density and increased manufacturing complexity. There are more gains to be realised if longer fibres can be used to manufacture low density foams without large voids which reduce compressive strength. Large voids will also cause increased resin uptake during a resin infusion or require more adhesive during bonded sandwich structure manufacture. For this reason, the most attractive option is to make use of short carbon and aramid fibres in epoxy foams.

The next chapter will investigate the effect of density on the fracture properties of epoxy foam. The transition from low density foam to bulk polymer will be discussed.

Chapter 6

Fracture properties of epoxy foam over a range of densities

6.1 Introduction

It has been established in chapter 4 that the fracture toughness of the foam core of a sandwich structure under impact loading is of critical importance. Chapter 5 focused on improving the fracture performance of epoxy foam using short fibre reinforcement. This chapter builds on this research further and details a systematic study of the effect of density on the fracture performance of epoxy foam. Material ranging from low-density foam through to the bulk polymer will be examined in detail.

6.2 Materials & Manufacturing

A commercially sensitive epoxy based foaming resin formed the basis of the materials investigated in this chapter. This resin was similar to the one used in Chapter 5 with some adjustments to enable a large variety of foam densities to be manufactured. Eight foams with varying densities from 183–506 kg/m^3 were manufactured. The resin mixture was kept constant while the amount of blowing agent was varied between 0.25 and 2.00 PHR in 0.25 PHR increments. Foams will be referred to within this research by the amount of blowing agent used in their manufacture. Epoxy foams were manufactured by mixing a stoichiometric amount of hardener into the foaming resin mixture with the blowing agent. The mixture was then poured into a rectangular mould and cured at 21°C for 24 h, followed by a 24 h post-cure

at 40°C. The long cure cycle at a precisely controlled temperature is required when manufacturing foams as the viscosity, particularly the thixotropic response, of the foam is critical to developing and maintaining an optimal microstructure at each density. Bulk epoxy plates were manufactured from a resin formulation that closely matches that of the foaming resin. This resin was first degassed in a vacuum. A stoichiometric amount of the curing agent was then added, mixed, and degassed again. Bulk polymer panels were cast by pouring the resin mixture into aluminium moulds to produce either 3 mm, 8 mm, or 14 mm thick plates from which bulk polymer test specimens could be machined. The plates were cured at 40 °C for 10 h, followed by a 12 h post-cure at 70 °C.

6.3 Microscopy & Morphology

Imaging of the polished foam samples revealed valuable information regarding the morphology and microstructure of the foams. ImageJ image processing software was used to analyse the SEM images of the polished foam. Figure 6.1 displays an example of two SEM images and their respective processed images using the ImageJ software.

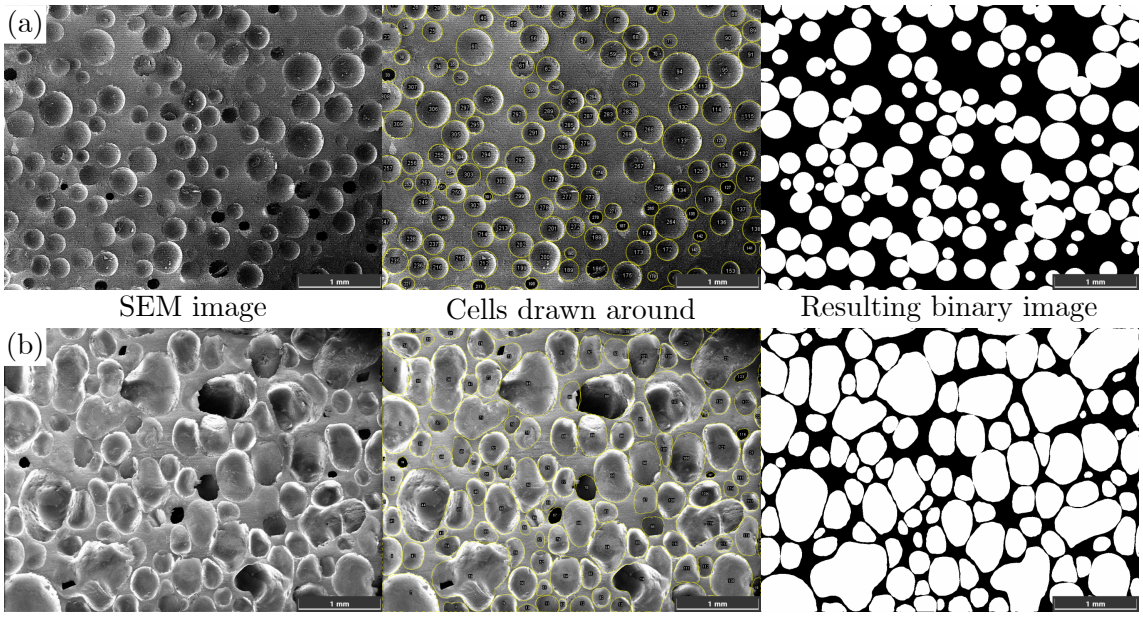


Figure 6.1: Examples of SEM images and their respective processed images.(a): 0.25 PHR blowing agent – high density foam and (b): 2.00 PHR blowing agent – low density foam.

Cells were manually drawn around using either the freehand or circle tools within the software. A stylus and a touchscreen were used to achieve accurate representa-

tions of the cells. Measurements of these elements could then be taken such as area, aspect ratio and angle of maximum diameter. At least 220 cells were measured for each foam, up to 1119 cells were analysed for some foams.

Example SEM images of foams 0.25 – 1.00 PHR blowing agent are exhibited in Figure 6.2, while images of foams 1.25 – 2.00 PHR blowing agent are displayed in Figure 6.3. The foam rise direction is from the bottom of the images to the top. The characteristic length of the cells of all the foams are plotted in a cumulative distribution plot in Figure 6.4.

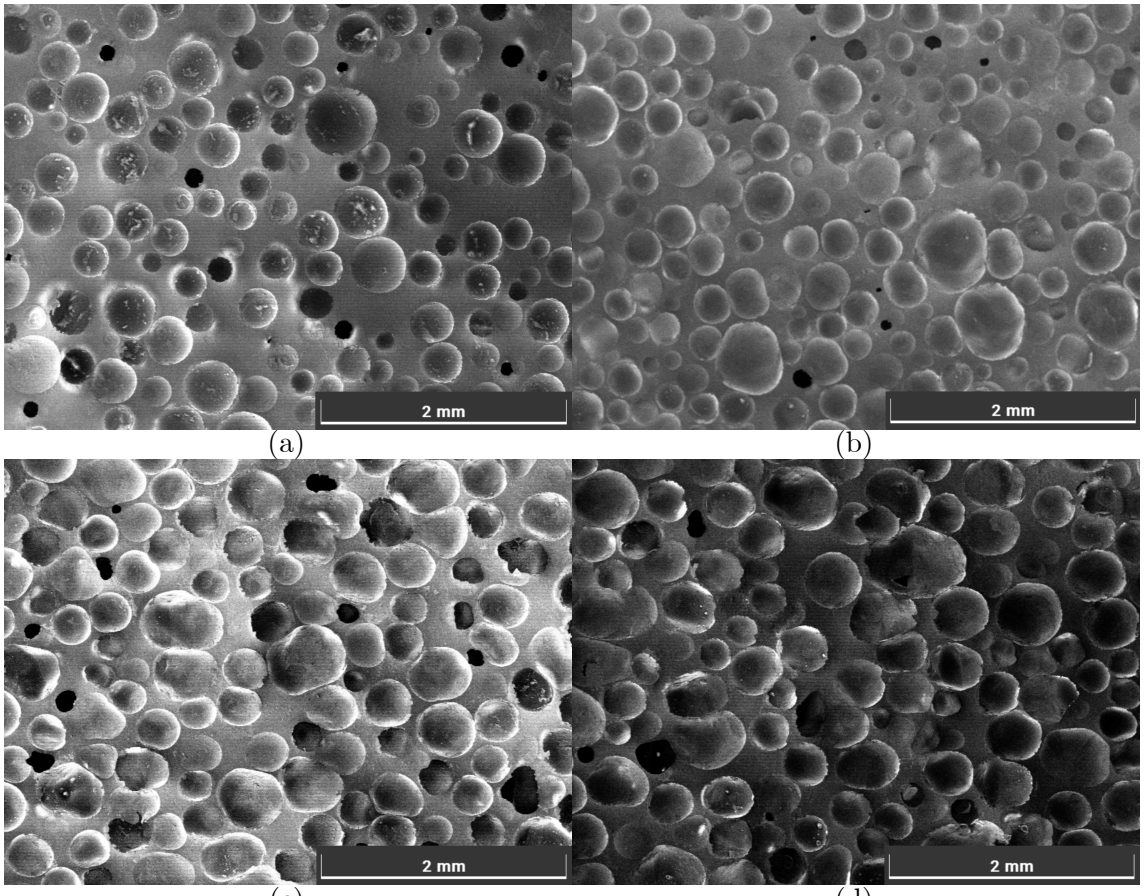


Figure 6.2: SEM micrographs of polished foam samples. (a): 0.25 (b): 0.50 (c): 0.75 (d): 1.00 PHR of blowing agent.

The characteristic length is calculated as four times the area over the perimeter, $4A/P$, which is simply the diameter for a cell appearing circular. The ImageJ software determines the cell aspect ratio by first fitting an ellipse to each cell. The aspect ratio is then calculated as the ratio of the major and minor axis of the fitted

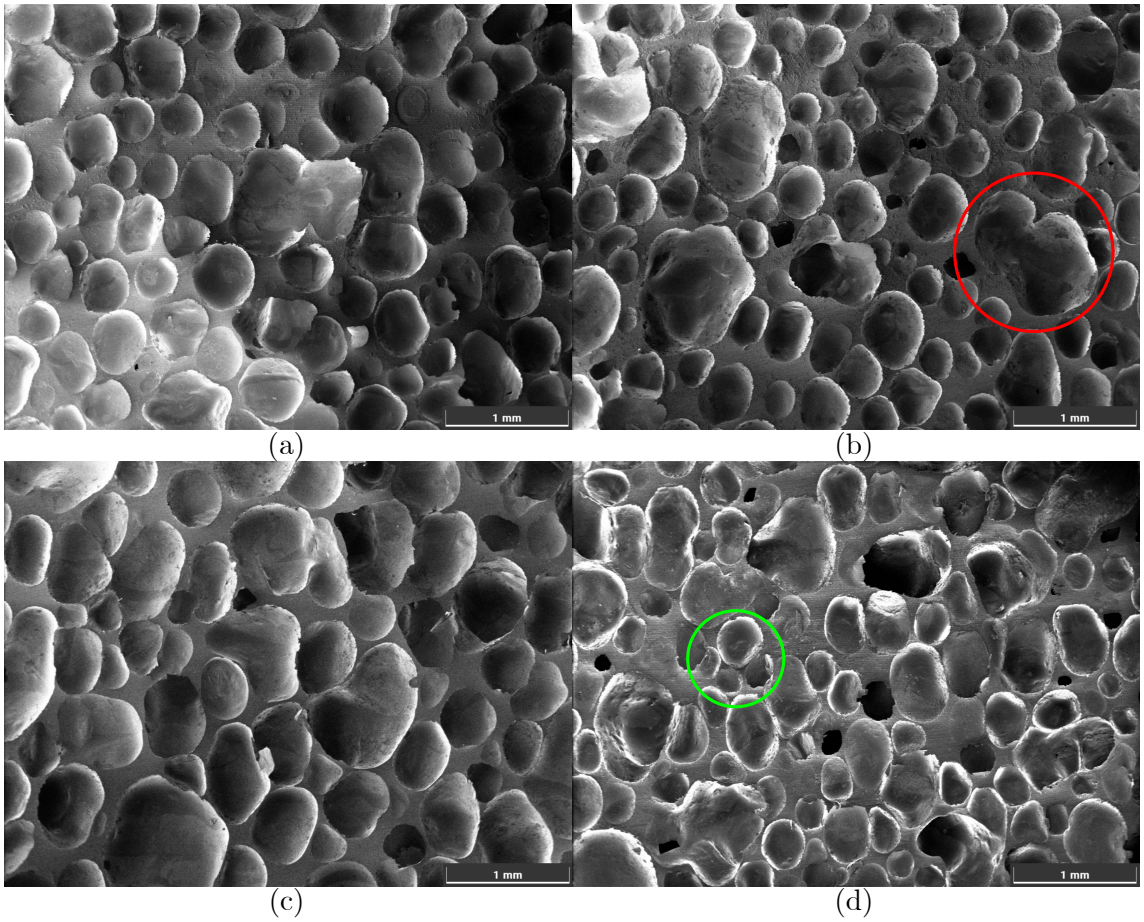


Figure 6.3: SEM micrographs of polished foam samples. (a): 1.25 (b): 1.50 (c): 1.75 (d): 2.00 PHR of blowing agent. An example of cell coalescence is highlighted by a red circle. An example of small cells in close proximity is highlighted by a green circle.

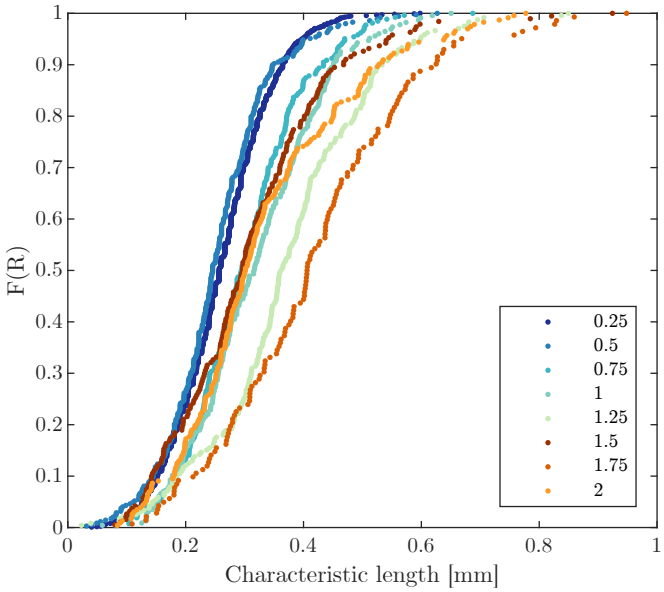


Figure 6.4: Cumulative distribution plot of cell characteristic length for all of the foams with different amounts of blowing agent (0.25 – 2 PHR).

ellipse. A box plot of cell aspect ratio is plotted in Figure 6.5. A box plot of the cell areas for each foam is plotted in Figure 6.6.

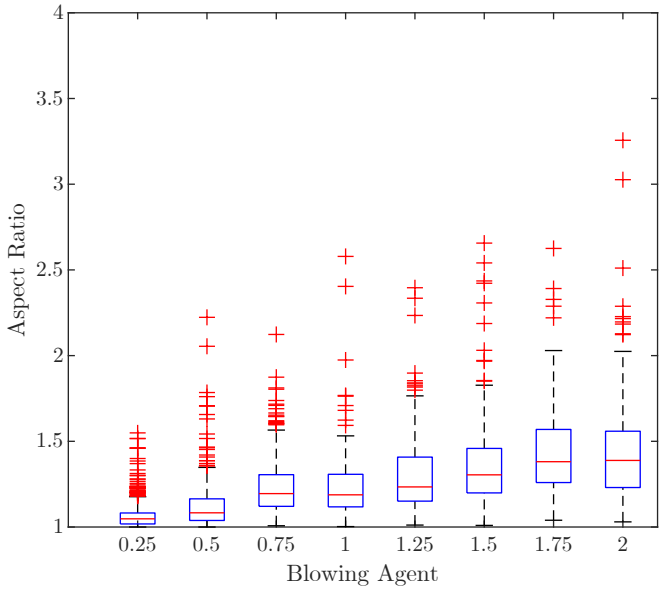


Figure 6.5: Box plot of cell aspect ratio for each foam (at least 220 cells were measured for each foam and the blue rectangular box contains median as red line and first quartile either side).

The blue rectangle on the box plots contains the median as a red line and the first quartile either side as the edges of the box. The whiskers extend to the last data point with a value within 1.5 times the interquartile range from the edge of the box. Red dots are data points that fall outside of the whiskers and are considered outliers. Data for each foam including the density and relative density is displayed in Table 6.1. The foam in this research is foamed by a chemical blowing agent within the resin. As bubbles nucleate, they initially manifest as spheres such as the cells found in Figure 6.2 (a). The bubbles that finally formed these cells lacked any interaction between neighbouring cells due to the sufficient space between them and therefore remained as spheres until the foam cured. The additional bubbles formed due to the increased addition of blowing agent begin to run out of space to grow without interacting with neighbouring bubbles. In fact, as the volume fraction of bubbles increases past 0.75 the bubbles necessarily deform each other [157]. A cell wall remains between these bubbles, and they begin to lose their spherical shape. Instead, they occupy the available space tending towards a polyhedral cell structure. This can be seen to happen as more blowing agent is added to the foams from Figure 6.2 (a) through to Figure 6.3 (d). It is interesting to note that the two densest

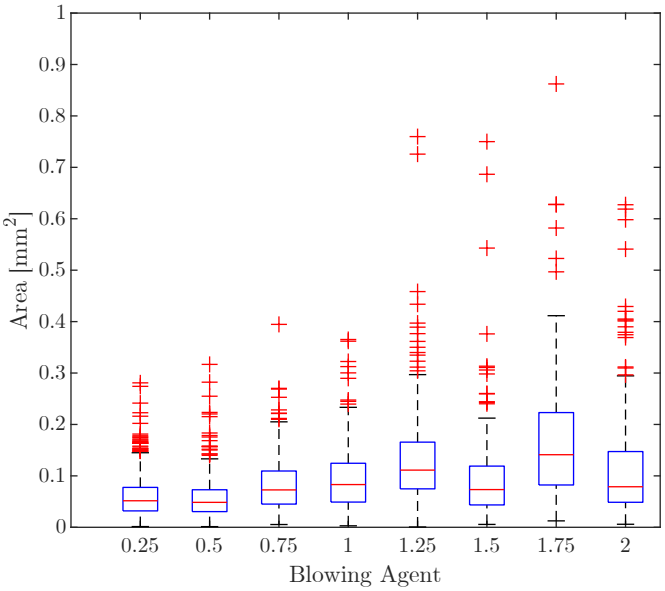


Figure 6.6: Box plot of cell areas for each foam (at least 220 cells were measured for each foam and the blue rectangular box contains median as red line and first quartile either side).

foams, with bubble volume fractions well below 0.75, exhibit extremely similar cell size distributions in Figure 6.4. The cells in these foams are spherical and rarely deform each other. The less dense of the two foams simply has more cells per unit volume resulting in a lower density albeit constructed of the same sized cells. The contrast between the cells in foams with the least and most blowing agent is clear in Figure 6.1. It shows the cells in the 0.25 foam as circles whereas the cells in the 2.00 foam are not circles and have deformed against each other. Figure 6.5 shows box plots of the aspect ratio of the cells of each foam. It is clear that the 0.25 and 0.5 foams have nearly perfectly spherical cells with aspect ratios very close to 1. As more blowing agent is added, the aspect ratio increases, and the cells become less spherical as they deform each other.

Two mechanisms that affect the lower density foams more significantly are drainage and cell wall rupture leading to coalescence [157]. These mechanisms do not affect the higher density foams as the cell walls are much thicker and so are less susceptible to rupture even if some liquid drains away during foaming. Examples of cells that are likely to have been created by at least two smaller cells coalescing can be found across the images in Figure 6.3, an example of this process has been circled in red in Figure 6.3 (b). From Figure 6.4, it can be seen that as more blowing agent is added to the foams the distribution of cell size shifts to ever larger values of characteristic length. However, all the foams still contain some small cells with characteristic

Table 6.1: Density, Modulus, Strength and Fracture data for all foams with varying amounts of blowing agent (0.25 to 2.0 PHR).

Blowing Agent [PHR]	Density [kg/m^3]	Relative Density [-]	Compressive Yield Strength [MPa]	Compressive Modulus [MPa]	Tensile Strength [MPa]	Tensile Modulus [MPa]	Fracture Energy G_{Ic} [J/m^2]	Fracture Toughness K_{Ic} [MPa m$^{1/2}$]
Bulk	1169	1.00	109.3 ± 2.0	-	96.8 ± 0.7	3844 ± 84	268 ± 23	0.98 ± 0.06
0.25	506	0.43	17.34 ± 0.47	516 ± 23	14.23 ± 1.47	936 ± 133	931 ± 353	0.79 ± 0.12
0.50	367	0.31	9.19 ± 0.53	300 ± 15	6.75 ± 0.40	347 ± 56	917 ± 171	0.60 ± 0.04
0.75	310	0.27	6.15 ± 0.12	233 ± 9	4.88 ± 0.35	302 ± 112	821 ± 67	0.42 ± 0.01
1.00	292	0.25	5.44 ± 0.13	217 ± 4	3.90 ± 0.54	324 ± 35	831 ± 119	0.41 ± 0.02
1.25	249	0.21	4.11 ± 0.03	173 ± 3	2.50 ± 0.40	204 ± 26	625 ± 62	0.30 ± 0.01
1.50	227	0.19	3.34 ± 0.04	131 ± 4	2.11 ± 0.29	196 ± 19	102 ± 6	0.13 ± 0.01
1.75	201	0.17	2.84 ± 0.03	105 ± 10	1.83 ± 0.12	148 ± 38	76 ± 13	0.10 ± 0.01
2.00	183	0.16	2.33 ± 0.02	86 ± 1	1.67 ± 0.22	113 ± 24	82 ± 15	0.10 ± 0.01

lengths of approximately 0.1 mm. This is also clear in the box plots of the cell areas in Figure 6.6. Figure 6.6 also reveals that while the average size of cells increases as more blowing agent is added, this increase is not drastic. However, the box plots show that the foams with 1.25 PHR blowing agent and above have a small number of much larger cells. It is likely that these cells are formed by smaller cells coalescing. The curves for the high-density foams in Figure 6.4 are smoothly varying, however, the curves for foams containing 1.75 and 2.00 PHR blowing agent contain steps in the collected data. The steps are distinct increases in characteristic length and show increments in the number of cells that have coalesced to form the measured cell.

Figure 6.7 presents histograms of the angle of the maximum diameter of cells for foams 0.75 – 2.0. Foams 0.25 and 0.5 have not been included as the cells appear circular and so this data has very little meaning. The histograms show that low density foam cells are predominantly elongated in the foam rise direction. In contrast, higher density foams 0.75 and 1.0 have cells laying perpendicular to the foam rise direction. The increase in the relative mass of liquid in the denser foams above each bubble causes the foam to collapse very slightly prior to curing fully.

6.4 Mechanical properties: strength and modulus

The compressive strengths and moduli of the epoxy foams are presented Table 6.1. Representative example stress versus strain curves for each of the foams is plotted in Figure 6.8. Also shown are examples of how both yield strengths have been calculated. Yield strength of rigid cellular plastics is defined by the ASTM standard

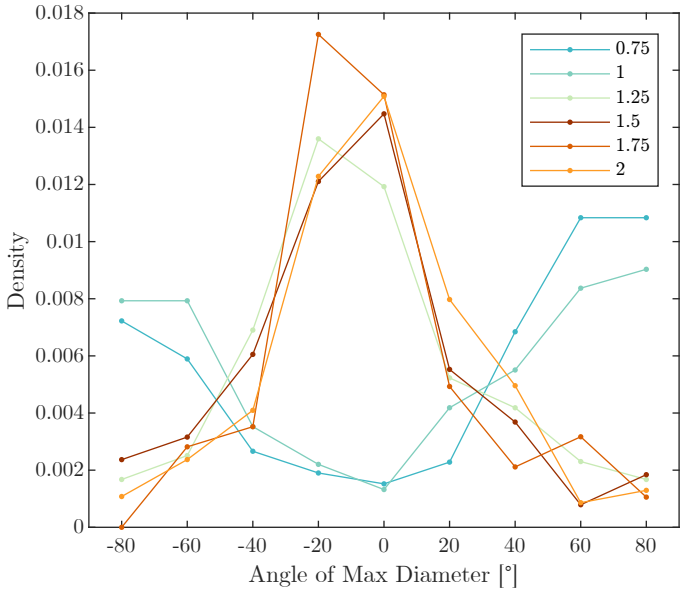


Figure 6.7: Normalised histogram of the angle of cell maximum diameter for foams 0.75-2.0 PHR blowing agent.

as the highest stress below a strain of 10% [139]. It is clear from Figure 6.8 that the location of this yield strength changes as the density of the foam changes. The lower density foams exhibit a distinct yield at approximately 5% strain after which the stress decreases before plateauing. On the other hand, the stress in the higher density foams either plateaus without such a distinct yield or continues to rise, such as with the highest density foam. In order to compare these results to models based on fundamental properties of foams, a 0.2% yield was also calculated for each foam. The ASTM yield strength for the 0.25 foam occurs at a point in the test with no significant change in response and so is unlikely to match with any model prediction. However, the 0.2% yield strength provides a value of strength just after the stress versus strain curve has deviated from an elastic response.

Gibson and Ashby [16] derived multiple models predicting the failure of foams in compression. These models were split into elastic collapse and plastic collapse. The elastic collapse models are not suited to structural foams such as the ones studied here. They were conceived to predict the plateau stress of elastomeric foams which recover fully from large strains. The plastic collapse models are based on a beam bending model and the formation of plastic hinges at the cell wall nodes. The plastic collapse models are split into an open cell and a closed cell model, shown in Equations 6.1 and 6.2, respectively, as:

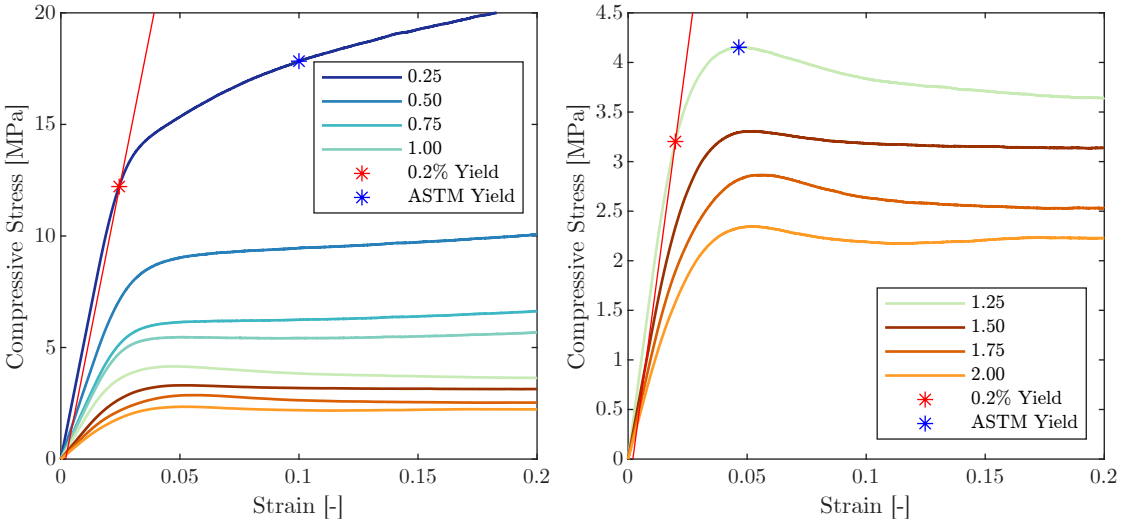


Figure 6.8: Representative compressive stress versus strain for each foam and for the cases with 0.25 and 1.25 PHR blowing agent, the 0.2% Yield and ASTM Yield points are added.

$$\frac{\sigma^*_{\mathrm{pl}}}{\sigma_{\mathrm{ys}}} = C_1 \left(\frac{\rho^*}{\rho_{\mathrm{s}}}\right)^{3/2} \quad \text{(open cell, } \rho^*/\rho_{\mathrm{s}} < 0.3\text{)} \tag{6.1}$$

$$\frac{\sigma^*_{\mathrm{pl}}}{\sigma_{\mathrm{ys}}} = C_2 \left(\phi\frac{\rho^*}{\rho_{\mathrm{s}}}\right)^{3/2} + C_2'(1-\phi)\left(\frac{\rho^*}{\rho_{\mathrm{s}}}\right) \quad \text{(closed cell, } \rho^*/\rho_{\mathrm{s}} < 0.3\text{)} \tag{6.2}$$

Where σ^*_{pl} is the plastic collapse stress of the foam and σ_{ys} is the yield strength of the bulk material. ρ^* and ρ_s are the density of the foam and bulk material, respectively, ρ^*/ρ_s will be referred to as the normalised density. For σ_{ys}, the bulk tensile yield strength is used as the model is based on beam bending. The constants, C_1, C_2, and C_2' are determined from fitting experimental data. For the closed cell model, ϕ is a parameter which represents the amount of solid polymer in the cell edges over the amount of solid in the faces. This takes a value of unity for an open cell foam. Gibson and Ashby state the largest applicable relative density for these models is 0.3 [16]. Above this density the cell wall aspect ratio reduces such that the beam bending model used is no longer suitable and they yield axially in compression or tension. As a result, the models were fitted to the six foams below 0.3 relative density. Gibson and Ashby found that a value of 0.3 for C_1 in Equation 6.1 showed the best fit for the available data for open cell foams. In addition, they found that the data for closed cell foams was also adequately described by the open cell Equation 6.1. The

values of compressive yield strength σ^*_{YC}, compressive 0.2% yield strength $\sigma^*_{0.2\mathrm{C}}$ and tensile fracture strength σ^*_{FT} are plotted alongside two models in Figure 6.9.

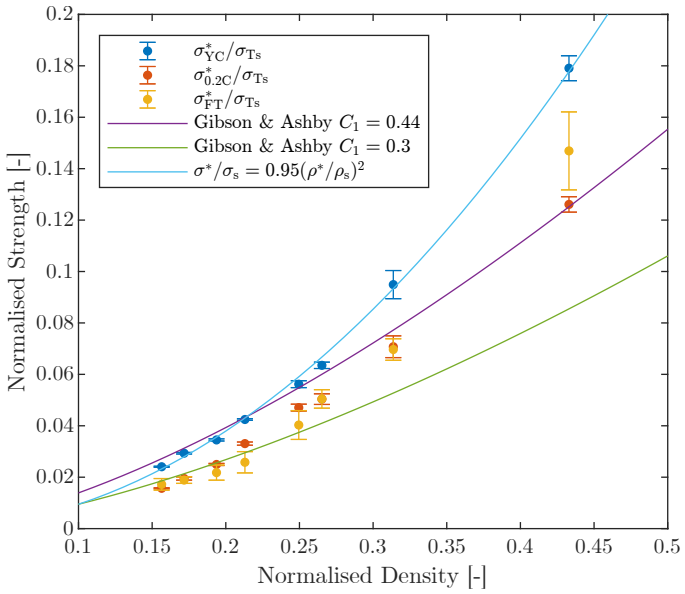


Figure 6.9: Normalised compressive and tensile strength of all foams versus normalised density including two models taken from Gibson and Ashby [16] (Normalised density of 0.16 corresponds to 2 PHR blowing agent and 0.43 corresponds to 0.25 PHR blowing agent).

This data is normalised against the tensile strength of the bulk polymer σ_{TS}. It is clear that as foam density increases the strength of the foam increases continuously. The values of tensile strength and 0.2% compressive yield strength match very well. The line for Equation 6.1 with C_1 equal to 0.3 is plotted in Figure 6.9. This model has some agreement with the 0.2% yield strength of the foams below 0.3 relative density. However, the best least squares agreement is between Equation 6.1 with C_1 equal to 0.44 and the ASTM yield strength. This line is also plotted in Figure 6.9 and can be seen to agree very well with the data for foams below 0.3 relative density. It is understandable that not all sets of data are effectively fitted by these models using the same constants. One of the mains reasons for this is that the measured properties of the bulk polymer will not be the same as the properties of the bulk material that is contained within the foam. The bulk material in the foam will have a different molecular structure and will also contain by-products from the foaming reaction. This applies throughout this research where bulk material properties are used in models to predict or fit foam properties.

When considering the closed cell model in Equation 6.2, the least squares difference

with the data below 0.3 relative density results in a value of unity for ϕ which recovers the open cell model. The foams in this research are closed cell. However, similarly to the data available to Gibson and Ashby, they are adequately represented by the open cell Equation 6.1. In reality, the proportion of material in the cell edges, ϕ, changes with density. As a result, for Equation 6.1 to accurately represent a large range of foam densities, a different exponent of the relative density term would be required. In fact, the complete set of strengths in the current research is fit better by a relative density exponent of 2 as opposed to the 3/2 in Equations 6.1 and 6.2. This best fit is plotted in Figure 6.9. The value of ϕ in Equation 6.2 can be adjusted so that the model matches the experimentally measured strength at each individual density value. When this is done, the value decreases with density from 1 for the four least dense foams to 0.56 for the densest foam. This suggests that more material is found in the cell walls as the foam becomes denser. However, from Figure 6.2 (a) and (b), it can be seen that the model of cell walls and edges is not appropriate for these dense foams which are better represented by a solid containing voids. Hence, the previously mentioned limitations of these models to less than 0.3 relative density is reasonable.

Tensile modulus E^*_T and compressive modulus E^*_C are plotted in Figure 6.10.

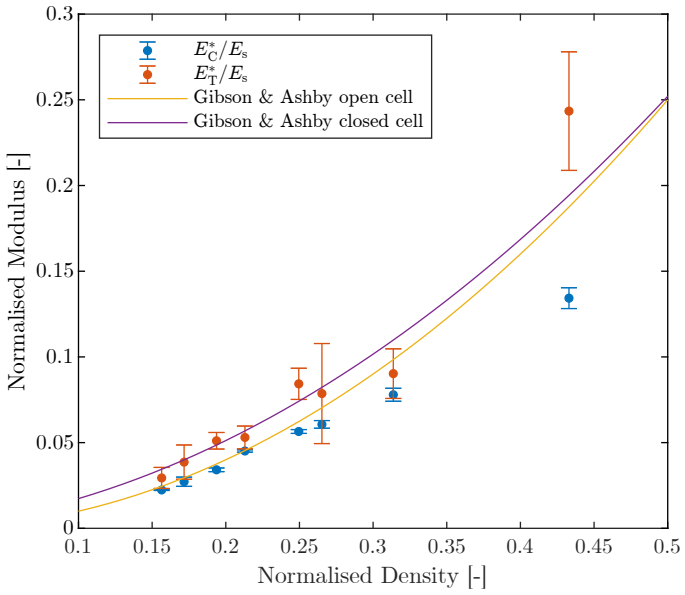


Figure 6.10: Normalised compressive and tensile modulus for all foams versus normalised density including both open cell and closed cell models from Gibson and Ashby [16] (Normalised density of 0.16 corresponds to 2 PHR blowing agent and 0.43 corresponds to 0.25 PHR blowing agent).

The compressive modulus of the foam increases continuously as the density increases. The tensile modulus also increases in a similar manner. The elastic modulus of a foam in tension is the same as that in compression [16]. The data for the tensile modulus is of lower quality and has a larger uncertainty due to the correspondingly smaller cross section of the tensile tests compared to the compression tests. However, the tensile modulus is likely closer to the real modulus of the foam due to the DIC method of strain measurement. It was not possible to use DIC for the compression tests in the current research. There are significant difficulties with accurately measuring strain in a compressive test of structural foam as discussed in detail by Rajput et al [158]. Primarily, parts of the sample can begin to fail and form a crush band, as a result, the strain throughout the sample can vary massively. Furthermore, when a foam sample is machined the top and bottom layer of cells are broken and are therefore very compliant. Consequently, the measured modulus will both be lower than the true modulus and it will be sample size dependent. Nevertheless, the tensile and compressive moduli behave as expected with the tensile modulus being consistently higher. Gibson and Ashby have also proposed models for predicting the modulus of both closed and open cell foam. These models are shown in Equations 6.3 and 6.4, respectively:

$$\frac{E^*}{E_\mathrm{s}} = C_3 \left(\frac{\rho^*}{\rho_\mathrm{s}}\right)^2 \quad \text{(open cell, all } \rho^*/\rho_\mathrm{s}\text{)} \tag{6.3}$$

$$\frac{E^*}{E_\mathrm{s}} = C_4\phi^2 \left(\frac{\rho^*}{\rho_\mathrm{s}}\right)^{3/2} + C_4'(1-\phi)\left(\frac{\rho^*}{\rho_\mathrm{s}}\right) \quad \text{(closed cell, } \rho^*/\rho_\mathrm{s} < 0.3\text{)} \tag{6.4}$$

where E^* and E_s are the modulus of the foam and the bulk polymer respectively. The constants C_3, C_4, and C_4' are determined from fitting experimental data. Gibson and Ashby found that the data for open cell foams was well fitted by taking C_3 as unity. They also found that data for closed cell foams was well fitted by taking C_4 and C_4' as unity also. It follows that the open cell model is valid through the full range of relative densities. The data in the current research also fits well with these constants as unity and so the models have been plotted as such in Figure 6.10. The remaining constant to determine is ϕ, the proportion of material within the cell edges. The modulus model was fitted over the full range of foam densities, therefore, the value for ϕ is different to the one found for the strength model. A value of 0.9

best satisfies a least squares fit between Equation 6.4 and the tensile moduli of the foam in this work.

6.5 Fracture properties

SEM micrographs of the fracture surfaces of foam SENB samples are displayed in Figures 6.11 and 6.12.

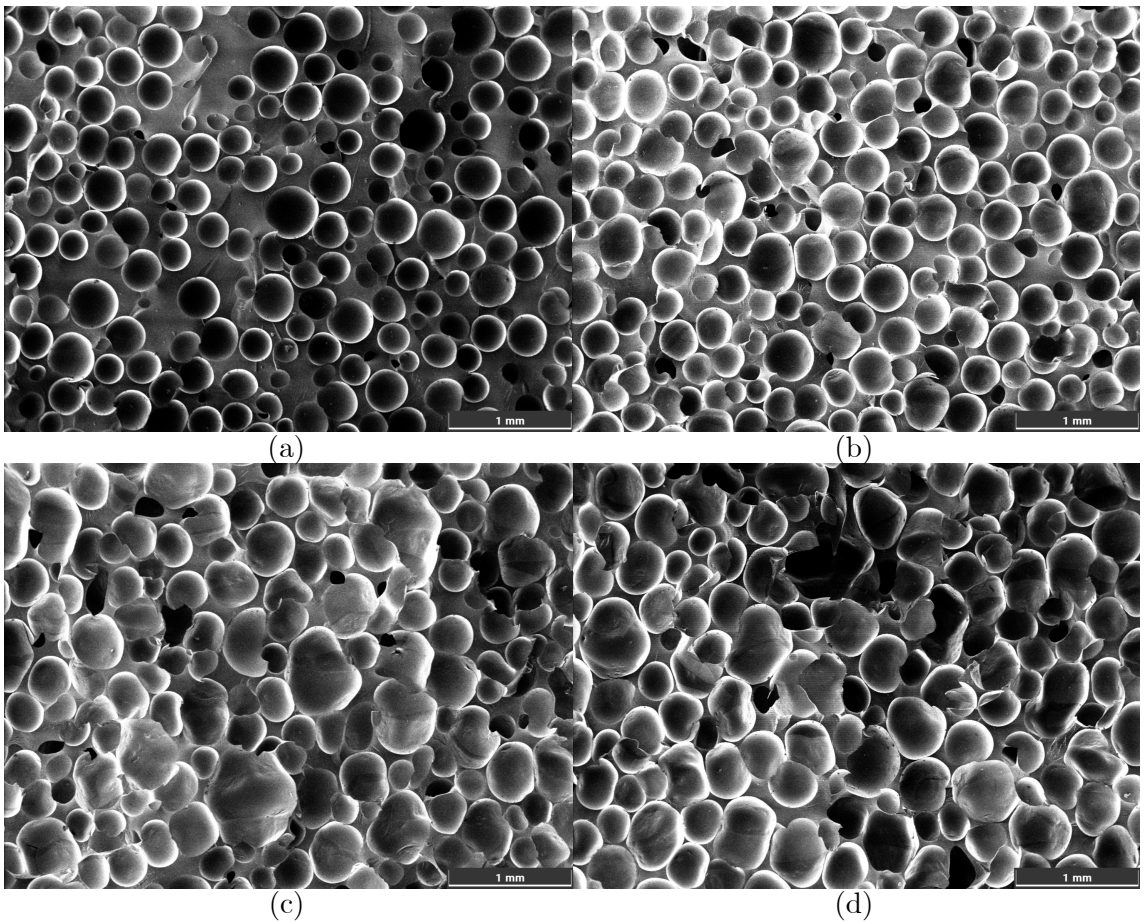


Figure 6.11: SEM micrographs of the fracture surfaces of foam SENB samples. (a): 0.25 (b): 0.50 (c): 0.75 (d): 1.00 PHR of blowing agent.

Large areas of bulk material fracture are visible in Figure 6.11 (a) compared to the other foams. It appears that the fracture surfaces show less bulk material than the polished samples. This is especially true when comparing the polished (Figure 6.3) and fractured (Figure 6.12) images of the low-density foams. During fracture a crack will take the path of least resistance, it then follows that this path will pass through the middle of large cells. As a result, the areas of bulk material seen on the polished

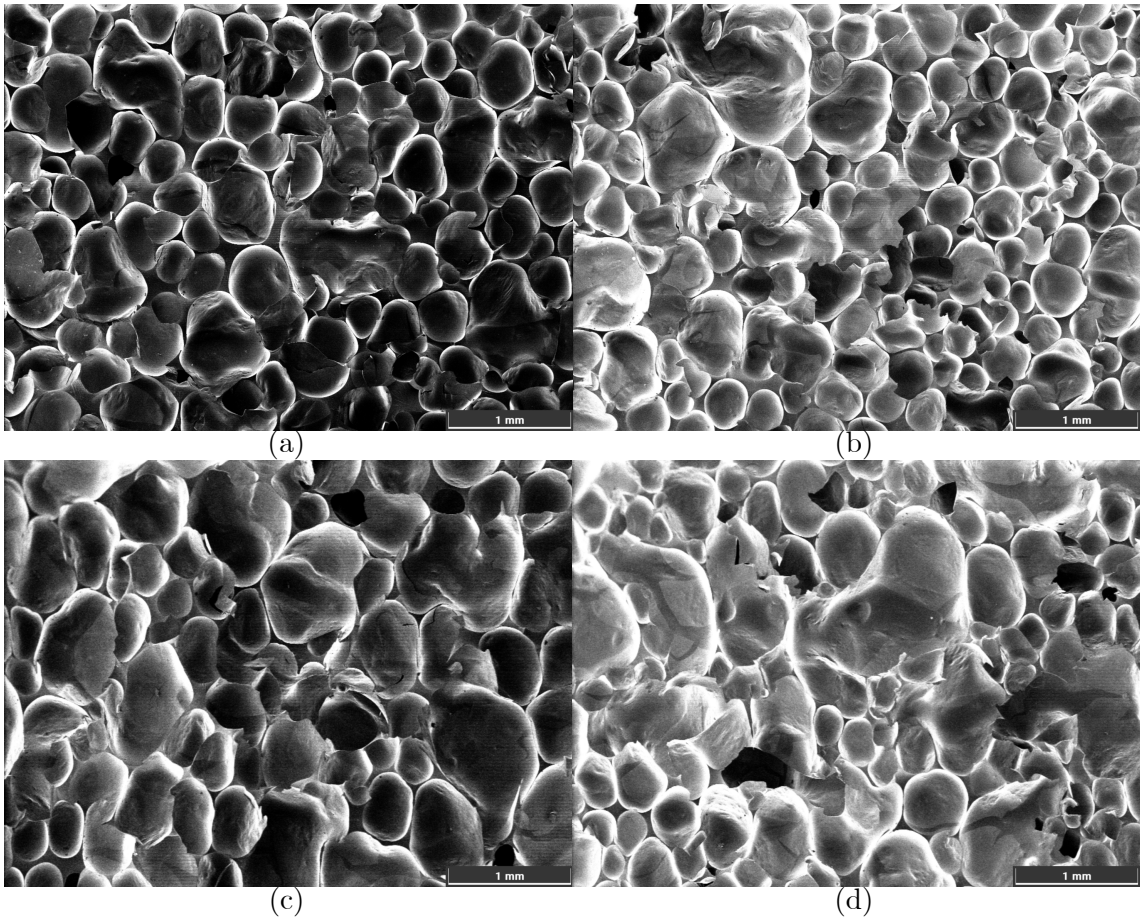


Figure 6.12: SEM micrographs of the fracture surfaces of foam SENB samples. (a): 1.25 (b): 1.50 (c): 1.75 (d): 2.00 PHR blowing agent.

samples of low-density foams are significantly smaller on the fracture surfaces of the same foams. On the other hand, the high-density foams which do not have any very large cells appear similar to the polished samples. There are no large cells to provide a significantly more favorable path that would reveal a difference between a polished and a fractured sample.

The fracture energy, G_{Ic}, and fracture toughness, K_{Ic}, of each foam and the bulk epoxy polymer are presented in Table 6.1. Representative load versus displacement graphs from SENB testing of each foam and the bulk epoxy polymer are plotted in Figure 6.13.

The foam samples have the same nominal dimensions, while the bulk sample load and displacement values have been appropriately scaled as if it had the same dimensions as the foam samples. When examining this plot, bear in mind that the crack lengths of each sample may vary slightly and that the plot is simply to demon-

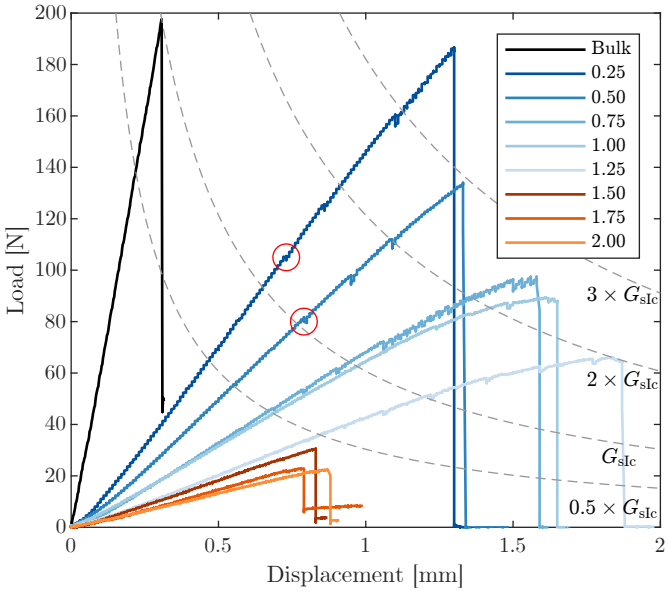


Figure 6.13: Representative load versus displacement data from SENB testing. Lines of constant fracture energy are plotted as dashed lines. Examples of small load dips are circled in red.

strate the varying responses of the samples. Furthermore, the 0.25 foam data has a particularly large spread and only one sample is plotted. For each sample, the load increases linearly as the displacement of the top roller of the three-point bend rig increases. The bulk epoxy polymer is the stiffest sample and also fails at the lowest displacement. The foams 1.5 – 2.0 fail in a catastrophic manner prior to 1 mm of displacement. There is then a dramatic change in response between foams 1.25 and 1.5. Foams 0.25 – 1.25 remain fully intact to a much larger displacement. Correspondingly there is a large increase in the measured fracture energy. The foam samples that fail at larger displacements show small dips in load which are quickly recovered. These dips suggest that small amounts of damage occurred within the sample, however, the foam withstood this damage without failing, i.e. the formation of a fracture process zone. These dips begin on the load versus displacement plot at approximately 0.75 mm. The foams that failed at lower displacements failed completely at a similar displacement suggesting they cannot withstand any microstructural damage without subsequently undergoing catastrophic failure. The normalised fracture energy (epoxy foam fracture energy / bulk epoxy polymer fracture energy) versus normalised density is plotted in Figure 6.14.

The transition in fracture energy is clear. The first three foams have a similar normalised fracture energy of approximately 0.5. There is then a sudden increase to three followed by a plateau. Interestingly, the densest foam has a large spread of

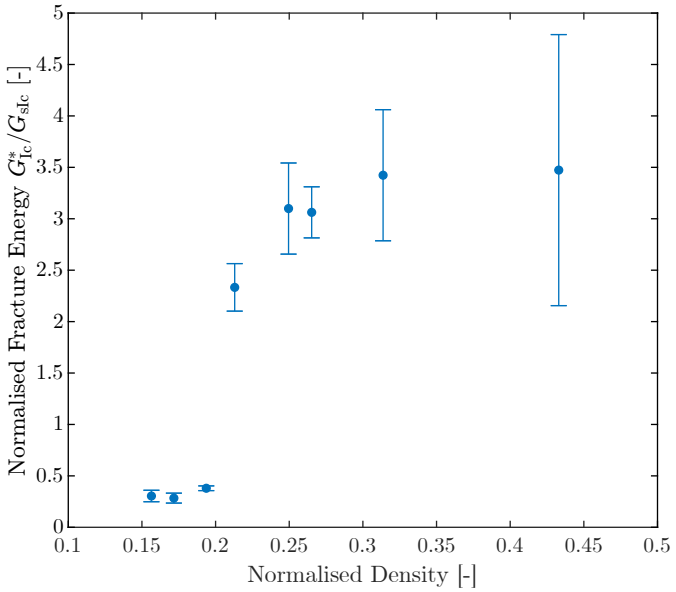


Figure 6.14: Normalised fracture energy versus normalised density. (Normalised density of 0.16 corresponds to 2 PHR blowing agent and 0.43 corresponds to 0.25 PHR blowing agent).

values. The size of the cells in both the 0.25 and 0.5 foams are similar, therefore, the inter-cell distance and the variance in inter-cell-distance in the 0.25 foam must be larger in order to achieve the higher density. Larger variation in inter-particle distance was found to be the main contributor to a larger variance in fracture strength of lower volume fraction syntactic foams by Carolan et al. [159]. Similar geometrically informed mechanisms are causing a large spread in fracture results here. The local density at the crack tip will determine whether the sample behaves like the bulk polymer or a foam. For example, the fracture surface of the foam shown in Figure 6.11 (a) shows large areas of bulk material. The results reflect this as some samples produced fracture energy values close to the bulk epoxy polymer while some other samples produced far higher fracture energies.

There is no simple explanation for the transition in fracture energy measured in this research. As discussed throughout this chapter, the other measured mechanical properties of the foam increase continuously with density without significant increases between samples. The foams were all manufactured using the same methodology, using the same base resin. Furthermore, at each density, all samples for all tests were taken from a single foam panel. In fact, a preliminary study was conducted with a different base resin and a similar transition in toughness was found.

To further investigate the transition in fracture energy the fracture toughness of each

sample was analysed. The normalised fracture toughness of each foam is plotted in Figure 6.15.

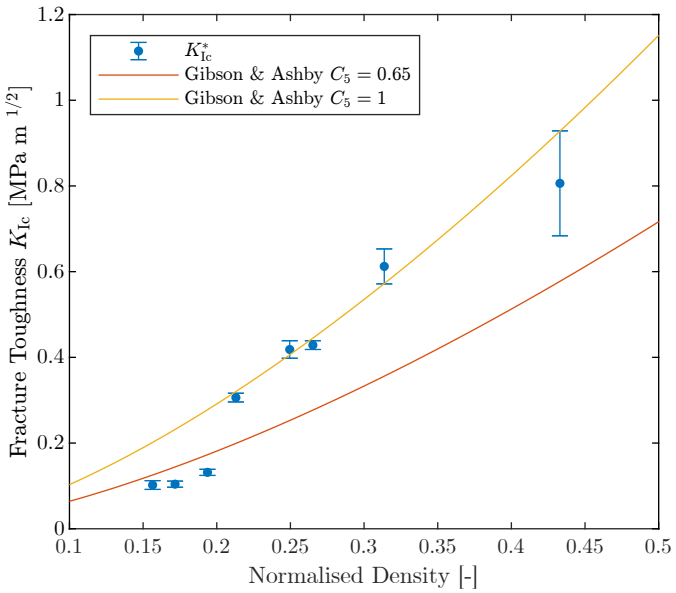


Figure 6.15: Normalised fracture toughness versus normalised density including two models from Gibson and Ashby [16]. (Normalised density of 0.16 corresponds to 2 PHR blowing agent and 0.43 corresponds to 0.25 PHR blowing agent).

While the fracture toughness, K_{Ic}, offers essential information about a material's resistance to crack propagation, it's crucial to be cautious when comparing similar materials with varying densities and thus different modulus values. This inherent change in material stiffness can influence the fracture behaviour, potentially making comparisons based on fracture toughness alone misleading.

The two models plotted are based upon the model for foam fracture toughness first reported by Ashby [160] and then by Maiti [161] and Gibson and Ashby [16]. The model is shown in Equation 6.5:

$$K^*_{Ic} = C_5 \sigma_{ys} \sqrt{\pi l} \left(\frac{\rho^*}{\rho_s} \right)^{3/2} \tag{6.5}$$

where C_5 contains all the constants of proportionality which was found to be 0.65 when compared with the data available to Maiti et al. [161], and l is the cell size of the foam. This is the only model proposed by Gibson and Ashby that explicitly considers the cell size of the foam. The model is based upon calculating the stress in

an equivalent linear-elastic continuum and comparing this to the fracture moment of an ideal cell. A cell size of 0.33 mm was used to plot and fit the models in Figure 6.15. This is the average cell size measured from SEM images. Although this value is different for each foam it is raised to the power of a half and so its effect on the model output is limited. A value of 0.65 for C_5 provides a reasonable agreement with the fracture toughness's of the three least dense foams. However, the four foams after the transition in fracture energy are better fit by a value of unity for C_5. The densest foam then fits between the two models. The model predicts that a larger cell size will produce a higher fracture toughness. Curiously, the three least dense foams have a slightly larger cell size than the denser foams, this can be seen in Figure 6.4. However, they have fracture toughness values less than the model values while the slightly smaller celled foams have higher fracture toughness values than the model values. The reason for this transitional behaviour is due to the cell size distribution. The less dense foams have larger cells on average and importantly also have a few very large cells. This distribution is clear from the box plots in Figure 6.6 where the transition between having, or not having, some very large cells occurs at the 1.25 foam. The transition in fracture energy occurs just before the 1.25 foam as well. Another important consideration is that all the foams have small cells. In theory all these measured small cells could be due to the measuring plane cutting a larger cell at either of its poles. However, it is not possible for this to be the case if three small cells are found close together, as is often the case with the foams in this research. An example of this is highlighted in Figure 6.3 (d). A foam having a large distribution of cell sizes will have a lower fracture toughness. Based on the Gibson and Ashby model of calculating the fracture moment of a cell edge, a foam containing smaller cells fails at a lower load. However, this model assumes that the cells along the crack front are the same size, and the load is equally distributed between each cell edge. A crack front containing small cells surrounded by larger cells will fail at a lower load as the larger cells are more compliant and are therefore carrying less load. As a result, the first failure in a foam with a wider cell size distribution will occur at a lower load and give a lower fracture toughness than a foam that has a tighter distribution of cell sizes. It follows that particularly large cells will exacerbate this problem if they are located along a crack front. A large cell will reduce the amount of cell edge material available to be loaded by reducing the local density at the crack tip. The cell edges of such a large cell would carry very little load due to the large compliance leading to premature failure of the cells either side of it. Furthermore, large cells result in a larger distance the crack can extend

before it contacts the next cell. The result of this is that for the fracture model in Equation 6.5 to accurately predict experimental data it must also consider the distribution of cell sizes within the foam. No mention of the limits of applicability of this model were found in the literature. However, the upward curve of the model does not intercept the value of the bulk toughness of 0.98 MPa $m^{1/2}$. In fact, it predicts a value of 2.02 MPa $m^{1/2}$ with $C_5 = 0.65$ and $l = 0.33$ mm. In order to predict the true value of a foam marginally less dense than the bulk, the cell size would need to be reduced to 0.077 mm. However, the cell size data collected in this study suggests that the cell size does not reduce as the relative density increases past 0.3. Instead, the number of cells simply decreases. This proposal is supported by research done by Wang et al. [162] who found cell size in chemically blown epoxy foam was approximately 0.3 mm diameter and unchanging between densities of 648 – 874 kg/m3. As established previously, the model proposed by Gibson and Ashby breaks down unless the crack front consists of foam cells with similar dimensions. In a material with a relative density of 0.4, such as the 0.25 PHR blowing agent foam, the crack front will begin to consist of significant proportions of solid material. This further suggests that the model is not suited to higher density foams.

In order to find a fit for fracture toughness covering the full range of data in this research, all of the normalised fracture toughness data points have been plotted against relative density in Figure 6.16.

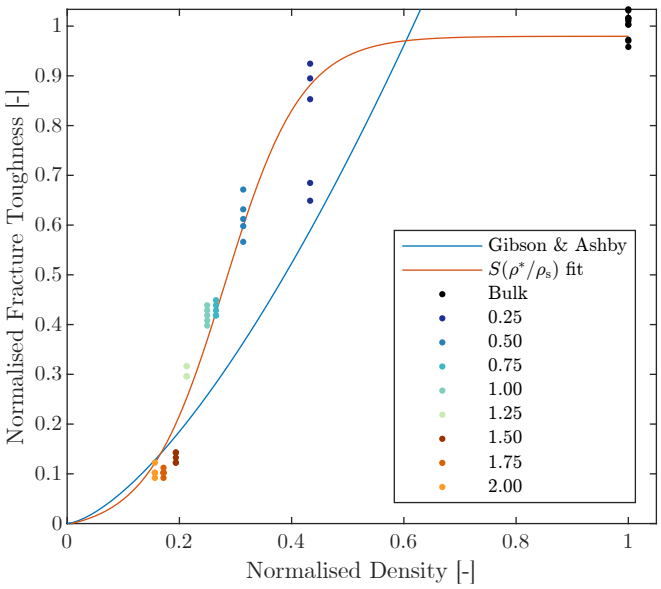


Figure 6.16: Normalised fracture toughness versus normalised density including the Gibson and Ashby model [16] and a Sigmoid fit.

The fracture toughness of the 0.25 foam at a relative density of 0.43 is already approaching the toughness of the bulk polymer. As a result, any proposed fit must flatten out across the range of densities 0.4-1.0. Furthermore, the fit must pass through the origin and also increase sharply through the 0.2-0.4 relative density range. A sigmoid function can satisfy these requirements and fit the data well. The form of the proposed empirical fit is shown in Equation 6.6:

$$\frac{K^*_{\mathrm{Ic}}}{K_{\mathrm{sIc}}} = S\left(\frac{\rho^*}{\rho_{\mathrm{s}}}\right) = K_{\min} + \frac{(K_{\max} - K_{\min})}{(1 + 10^{m(\rho_{50} - \rho^*/\rho_s)})} \tag{6.6}$$

$$\frac{K^*_{\mathrm{Ic}}}{K_{\mathrm{sIc}}} = S\left(\frac{\rho^*}{\rho_{\mathrm{s}}}\right) = -0.017 + \frac{(0.979 - (-0.017))}{(1 + 10^{6.3(0.28 - \rho^*/\rho_{\mathrm{s}})})} \tag{6.7}$$

Where $K_{\min}$ and $K_{\max}$ are the values which the function will tend to at $-\infty$ and $+\infty$ respectively and in this fit are close to 0 and 1. ρ_{50} is the normalised density value resulting in $(K_{\max} + K_{\min})/2$, and m is the gradient at this relative density value. This function was fit to all of the fracture toughness data with the additional requirement of passing through the origin. The resulting function is Equation 6.7. This function is plotted in Figure 6.16 and shows very good fitting to the experimental data. Aside from providing a reasonable fit to the available experimental data, the choice of a sigmoid function seems physically rational as it is commonly used to provide physical context to percolating phenomena, e.g., in the design of electrically conductive polymers [163–165]. In these cases, the electrical percolation threshold is defined as the volume fraction of conductive material in the polymer that causes a sharp increase in the electrical conductivity of the material. More recently, He et al. [166] have hypothesised the concept of a structural percolation effect for the case of carbon fibres embedded within a syntactic foam matrix. They noted an initial loss in strength with a small volume fraction of included fibres, which thereafter recovered sharply to give improved behaviour of the composite. They argue that above a critical threshold of fibres the direct fibre to fibre stress functions as a percolated network whereas below this threshold, they act as individual particles. In the case of foams, it is the interactions between voids, which do not transmit any stress, that is important. At very high densities we have voids which are remote from each other. Thus, their impact on the fracture toughness remains low. Once the voids begin to get closer to each other they begin to interact and the sharp drop

in fracture toughness is noted. In the lower (or foam) region, further decreases in density is not brought about by any of the individual voids becoming ever closer, but through void coalescence. Thus, no significant increase in stress interactions would be expected in this region.

It remained to be seen whether this fit for the fracture toughness would result in a calculated fracture energy fit that would agree with the experimental data. Fracture energy can be calculated from fracture toughness assuming a linear elastic response using Equation 3.6. A suitable model for E has already been established in Equation 6.3. ν is Poisson's ratio which was found to be 0.33 from the DIC of tension tests, in agreement with Gibson and Ashby [167]. A G^*_{Ic} fit can then be calculated by substituting Equation 6.7 and Equation 6.3 into Equation 3.6, this fit is plotted in Figure 6.17.

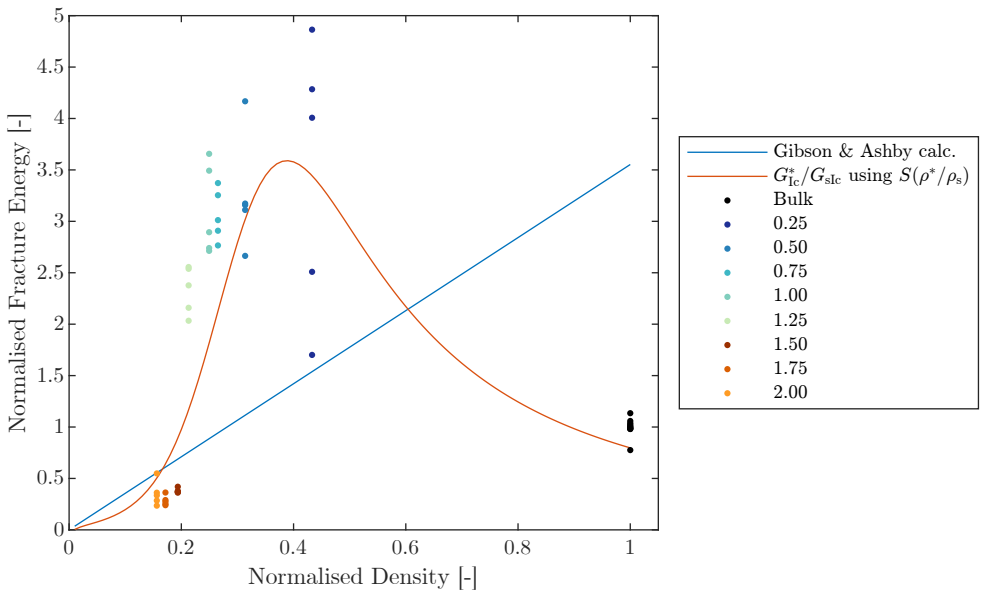


Figure 6.17: Normalised fracture energy versus normalised density including a calculated Gibson and Ashby line and fracture energy calculated from the Sigmoid fit of fracture toughness.

The shape of the fit is a reasonable representation of the experimental data. Using the Gibson and Ashby K^*_{Ic} model in Equation 6.5, another G^*_{Ic} fit can be calculated. This results in a straight line due to the relative density powers used for each model cancelling out. It may seem plausible that a measure of energy per unit area such as fracture energy may increase linearly since the area of bulk material fractured within the foam increases linearly with relative density. However, this does not reflect the data in this study well. The data in this study is better fit using the

sigmoid fit for fracture toughness in Figure 6.16 and the resulting fit for fracture energy in Figure 6.17.

This investigation has attempted to answer the question of how the fracture energy of a foam might vary with relative density. Consider the SENB load versus displacement curves in Figure 6.13 and that the fracture energy is directly proportional to the area under these curves using Equation 3.7. Iso-fracture energy lines relative to the bulk polymer fracture energy are also plotted in Figure 6.13. These iso-fracture energy lines are based on the nominal dimensions of the SENB samples in this research. The lines cover a range of sample compliances which can be achieved through varying the modulus or crack length of a sample. The crack lengths in this research are nominally the same. Therefore, in order to travel along the lines, the modulus of the sample must change. For example, if a foam sample had a lower modulus but the same fracture energy as the bulk polymer it would fail at a point on the G_{sIc} line with a higher displacement than the bulk polymer sample. It becomes clear why the foams with intermediate relative densities have fracture energies far greater than either the bulk material or very low-density foams. The maximum load does not fall proportionally with the extra displacement achieved by these high fracture energy foams. From Equation 3.6 we can see that if fracture toughness (proportional to the highest load achieved) falls at a slightly slower rate than modulus, the fracture energy of that material will increase. For example, in this research we have manufactured a foam with a normalised fracture toughness of 0.6, which has a normalised modulus of less than 0.1 and results in a normalised fracture energy over 3.

6.6 Concluding remarks

In this chapter the variation in fracture energy of an epoxy foam has been studied as a function of the density of the foam. A critical foam density has been identified, above which the fracture energy is significantly higher than that of the base epoxy polymer. At densities lower than this, the fracture behaviour of the foam is consistent with the models proposed by Gibson and Ashby. The critical foam density for this epoxy polymer was identified as a relative density, ρ^*/ρ_s of 0.28. The tensile and compressive modulus and strength were found to be reasonably well described by Gibson and Ashby models across their recommended validity ranges. Notably, the

transition from Gibson and Ashby behaviour to toughened behaviour occurs over a small density range. The data shows that the behaviour of the fracture toughness as a function of density, K^*_{Ic} is well described by a sigmoidal function over the entire density range, including the bulk polymer. The relative density of the transition in fracture properties coincides with changes in foam morphology observed by SEM. Lower density foams, below the transition in fracture toughness, displayed evidence of a few large cells and a wider cell size distribution. This wider cell size distribution appears to be the cause of the transition in fracture properties. Larger cell size distributions caused the premature failure of smaller cells at the crack front as larger cells are more compliant and do not carry a proportional amount of load. Larger cells also allow for cracks to propagate through low resistance paths within the foam. Interestingly, the tensile and compressive properties are not affected by cell morphology in the same way. It is proposed for applications where energy absorbing capabilities of the foam are critical, denser foams may be a more optimal choice, sacrificing a small gain in weight for a considerable gain in damage resilience.

The next chapter will investigate the failure mode of skin core debonding. Quasi-static tests will be used to discuss the transition in failure mode between 3 and 6 wt% CSR. Skin-core bond toughening mechanisms will also be investigated.

Chapter 7

Skin-core debonding

7.1 Introduction

The failure mode of skin-core debonding can cause significant decreases in the structural integrity of sandwich panels. In an infusion manufactured sandwich structure, the matrix resin forms the bond between the skin and the core. As the mechanical properties of the matrix resin in chapter 4 were modified the behaviour of the skin-core bond was affected. A transition in failure mode was identified between 3 and 6 wt% CSR. As a result, a series of skin-core debonding tests were proposed in order to study the transition in failure mode that is caused by changing the toughness of the matrix in the skins in an isolated manner. Understanding this failure mode and the point of transition is key to optimising the matrix resin toughness, modulus and UTS. The results of chapter 4 revealed that over toughening the matrix resin with rubber particles, causing a drop in UTS and modulus, could cause an unacceptable decrease in the performance of the skin-core bond.

Furthermore, this chapter investigates methods of improving the performance of the skin-core bond. Analysing images of skin-core debonding in chapter 4, it is clear that the crack can propagate through the foam below the interface. In chapter 5, the foam was reinforced with short fibres which resulted in an improved fracture performance. As such, it can be expected that any improvement in foam fracture performance caused by the addition of short fibres would translate to an improvement in interface toughness measured via SCB. Other skin-core bond toughness improvement techniques in the literature include using grooves [108], as discussed in chapter 2. Consequently, grooves of increasing depth were machined into epoxy

foam cores to assess the possibility of improving the toughness of the skin-core bond.

This chapter will be split into three main sections. The first section will detail the investigation into how toughening the matrix resin affects the skin-core bond. Secondly, the effects of machining grooves into the core will be summarised. Finally, the response of fibre-reinforced foam cores will be outlined. It will become clear that different data reduction approaches are necessary to extract useful results for design.

As discussed in chapter 2, it is difficult to measure pure mode-I failure of an interface between dissimilar materials. Consequently, the measured critical strain energy release rate will not be referred to as mode-I, G_{Ic}, but G_{c} and should be considered as a fracture energy that is mode-I dominant but not pure mode-I.

7.2 Materials & Manufacture

CFRP composite sandwich panels were manufactured for SCB testing. The carbon fibre used was 385 gsm of H2550 fibres in 12k tows in a 0/90 non-crimp fabric. The SCB sandwich panels used $[[0/90]_4]_s$, giving a total of 8 plies in each skin. An amine-cured epoxy system was used to infuse the fibres comprising the skin of the SCB panels. The resin was a standard DGEBA with an epoxide equivalent weight of 185 g/eq. This was cured with a stoichiometric amount of a difunctional primary amine (JEFFAMINE D-230) from Huntsman, UK. The foam cores were 10 mm thick and were CNC machined flat on both faces prior to infusion of the skins. The composite sandwich panels were laid up on a flat release-coated aluminium plate and sealed using a vacuum bag. Resin was drawn through the foam fibre layup under vacuum. Infusion of the liquid matrix into the fibres took place over a period of 5-10 min and was then cured under vacuum for 10 h at 40°C and 10 h at 55°C.

- The resins used for the CSR and Silica modified matrices were identical to the systems used in chapter 4. The foam cores were also made using Sicomin PB170 and DM03 hardener.
- The matrix resin system used in the grooved foam core study was a 9 wt% CSR resin. This resin has the lowest UTS and so would be expected to promote interface rather than foam failure in an SCB test. This would allow the interface toughening mechanisms to be best analysed. The grooves were CNC

machined 3 mm wide and 13 mm center to center. The grooves were only machined perpendicular to crack growth and were not machined in the pre-crack area of the samples. Two different groove depths were machined to 1.5 mm and 0.75 mm, respectively.

- The foam core used for the fibre-reinforced SCB study was a 2.5 PHR 0.75 mm aramid fibre-reinforced foam. The foaming resin was identical to that used in chapter 5. No tougheners were used in the skin matrix resin.

7.3 CSR and silica modified matrices

7.3.1 Failure modes

The results of the SCB debonding tests of the CSR and silica modified samples manifested as more than a simple comparison of G_c values for different matrix resin systems. A sample of each of the two main types of failure observed during the test are shown in Figure 7.1.

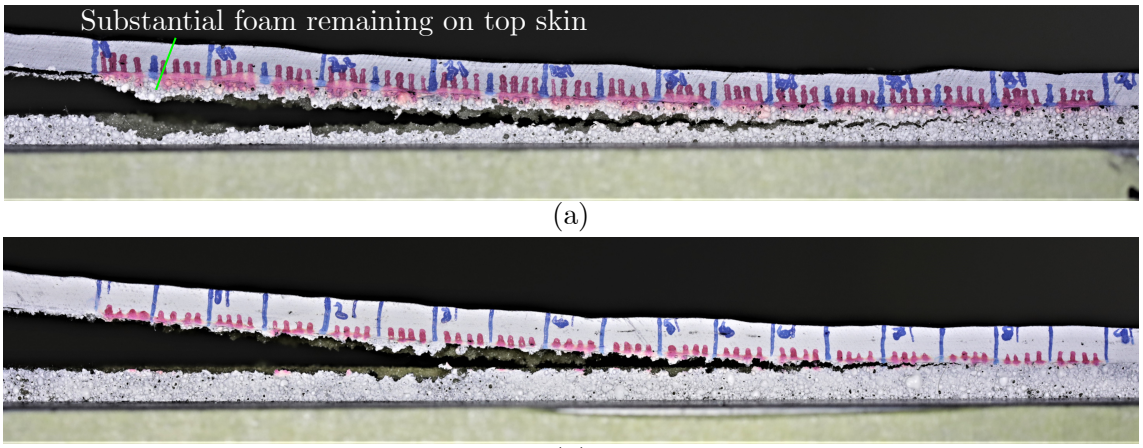


Figure 7.1: Example images of SCB specimens mid-test. (a): 3 wt% displaying sub-interface foam failure (b): 6 wt% displaying interface failure.

Figure 7.1 (a) shows a sample with 3 wt% CSR, it is clear that the crack has propagated through the foam in a sub-interface manner. Samples that failed in this way exhibited a stick/slip load-displacement curve. Figure 7.1 (b) shows a sample with 6 wt% CSR, the crack in this sample propagated mostly along the interface with the carbon skin being exposed but also with some pieces of foam remaining attached. Samples that failed in this manner, displayed a more stable

load-displacement curve. Representative fracture surfaces of the laminate for each CSR loading are shown in Figure 7.2. The amount of foam attached to the laminate clearly shows the transition in failure mode between 3 and 6 wt% CSR.

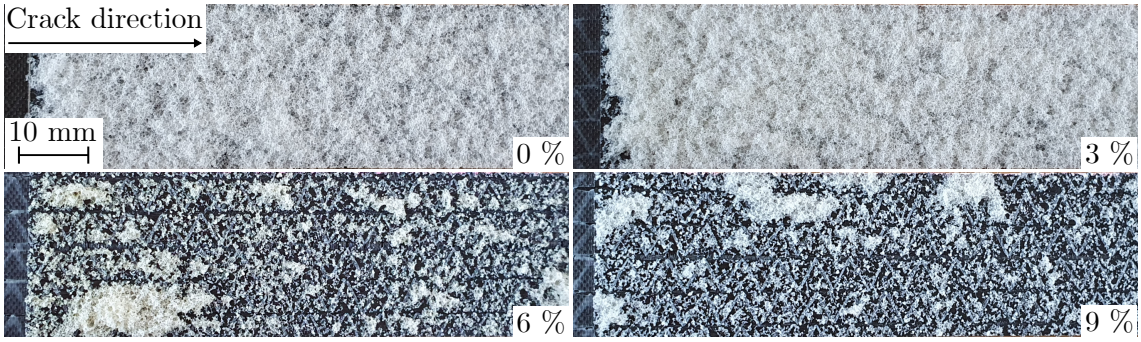


Figure 7.2: Representative laminate side fracture surfaces of 0 wt%, 3 wt%, 6 wt% and 9 wt% CSR samples.

Figure 7.3 shows typical load-displacement curves of the two failure modes highlighting the difference between (a) interface failure with stable crack growth and (b) sub-interface stick/slip failure.

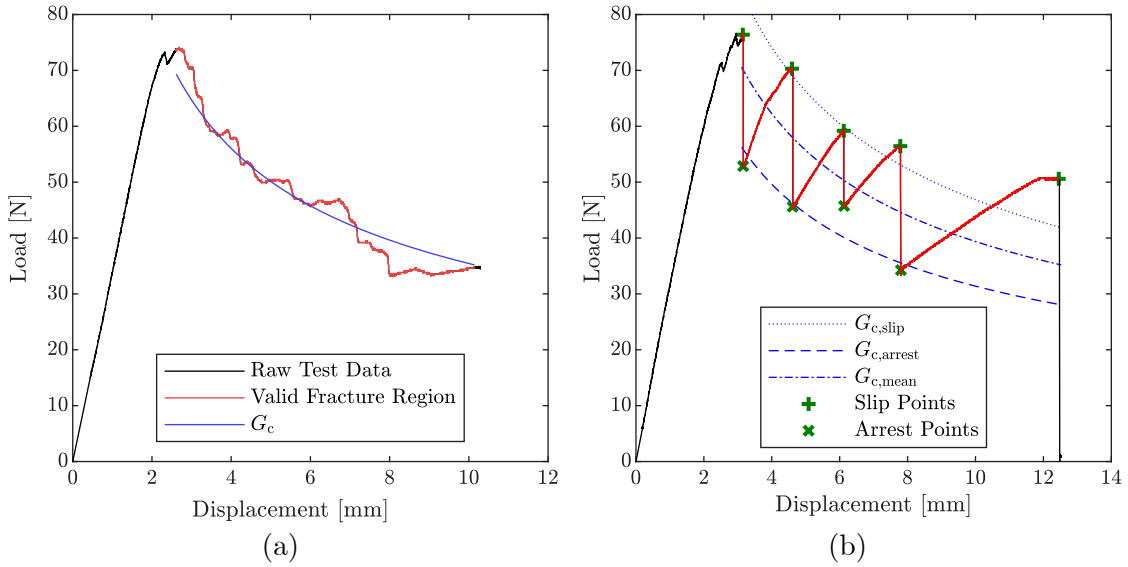


Figure 7.3: Typical load versus displacement curves from SCB testing. Raw data is in black with the valid fracture regions in red. (a): Typical stable fracture curve. (b): Typical unstable stick/slip fracture curve

Having established that a transition in SCB failure mode takes place between 3 and 6 wt% CSR, it is interesting to note that two of the 6 wt% samples exhibited mixed behaviour as seen in Figure 7.4. By comparing the crack growth, Δa, measurements with the fracture surface of the laminate it is again clear that unstable crack growth

occurs within the core, i.e. between points A and B, and stable crack growth occurs at the interface. However, all of the 3 wt% CSR SCB samples tested exhibited completely unstable crack growth. These results suggest that the transition point in fracture behaviour lies closer to a CSR content of 6 wt% rather than 3 wt%.

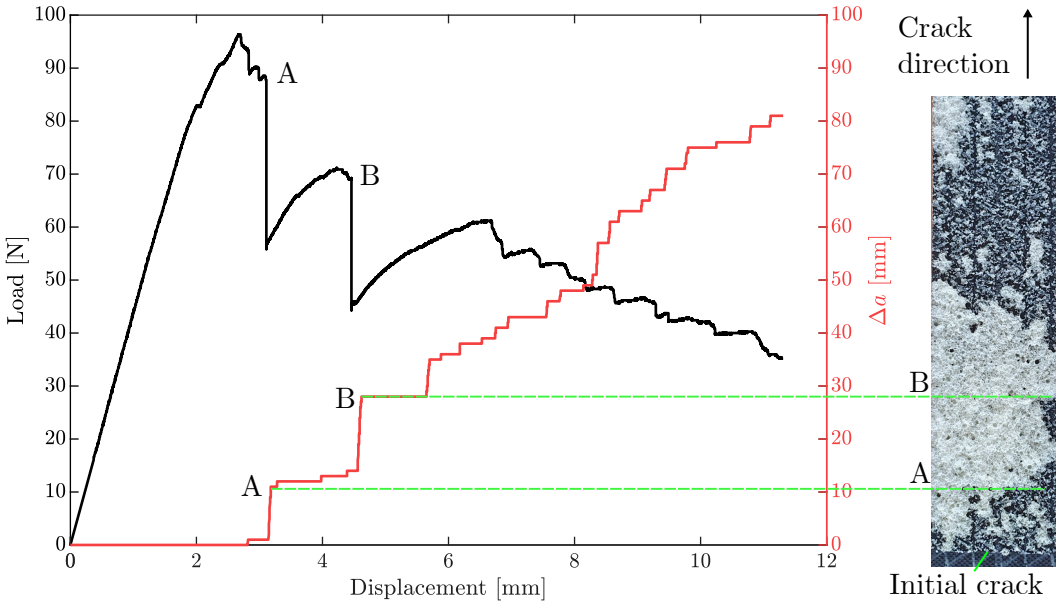


Figure 7.4: Load versus displacement curve from the SCB testing of a 6 wt% CSR specimen exhibiting both fracture mechanisms. On the right hand side is the corresponding laminate side fracture surface showing the transition between unstable and stable fracture.

7.3.2 Data reduction method

The standard data reduction method for a test such as this involves calculating G using LEFM, in a similar manner to a DCB, from the following relationship.

$$G_{\mathrm{c}} = \frac{P^2}{2b}\frac{\mathrm{d}C}{\mathrm{d}a} \tag{7.1}$$

where the derivative $\mathrm{d}C/\mathrm{d}a$ is evaluated from the compliance/debond length relationship measured during the test. However, this data reduction method is less suitable for the stick/slip failure modes found in the current work. The compliance/debond length relationship is complicated by there being multiple load and displacement values for a single debond length between slip points and multiple debond lengths for a single displacement value during a slip. As a result, an analyt-

ical model of the test was developed to allow load, P, to be expressed as a function of G and displacement, δ. This allows lines of constant G for a given system to be plotted on a load versus displacement axis and directly compared with the raw test data of load and displacement. The fracture toughness for each sample was taken as the G value which gave the least-squares fit between the model and raw data. It is noted that no significant toughening mechanisms that would contribute to R-curve behaviour were observed experimentally, which would invalidate this method of analysis.

The analytical representation of the test was first developed using a beam built-in at the crack tip as the basis for the model. The end displacement for a given load for such a beam is:

$$\delta = \frac{4Pa^3}{Ebh^3} \tag{7.2}$$

The compliance is then:

$$C = \frac{\delta}{P} = \frac{4a^3}{Ebh^3} \tag{7.3}$$

Differentiating with respect to debond length and substituting into Equation 7.1 yields:

$$G_\mathrm{c} = \frac{6P^2a^2}{Eb^2h^3} \tag{7.4}$$

Rearranging Equation 7.3 for a, substituting into Equation 7.4 and subsequently rearranging for P gives:

$$P = 2b\left(\frac{G_\mathrm{c}^3h^3E}{216}\right)^{0.25}\delta^{-0.5} \tag{7.5}$$

To plot the lines of constant G using Equation 7.5, a value for modulus must be calculated by rearranging Equation 7.2 and inputting test load and displacement data from the initial linear loading portion of the test. A check of these modulus, E, values showed they were not in the expected range of approximately 70 GPa for the skin flexural stiffness, instead they were much lower at approximately 20 GPa. This demonstrates that a built-in beam is not an accurate representation of the SCB

system. The low modulus of the foam core is ignored in the built-in model and so would produce inflated G_c values. As a result, a model based on a beam cantilevered from an elastic foundation was used instead as shown in Figure 7.5.

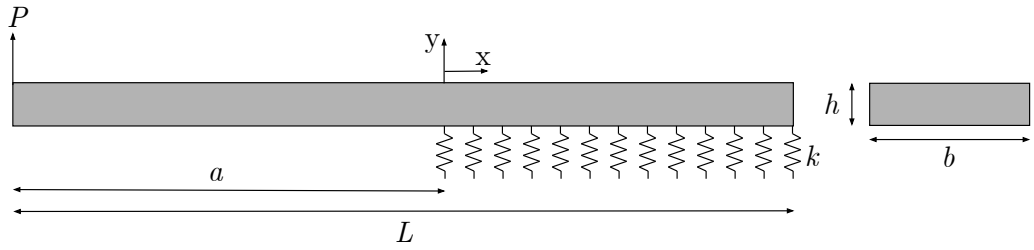


Figure 7.5: Schematic of an SCB with an elastic foundation.

The governing equation for the deflection of a beam on an elastic foundation is a fourth order differential equation as demonstrated by Kanninen [168] when proposing an improved model for a DCB test. The expression for compliance resulting from the solution of the model proposed by Kanninen is as follows:

$$C = \frac{2}{Eb\lambda^3 h^3}\left(2\lambda^3 a^3 + 6\lambda^2 a^2 A_1 + 6\lambda a A_2 + 3A_3\right) \tag{7.6}$$

where,

$$\lambda^4 = \frac{3k}{Ebh^3} \tag{7.7}$$

and,

$$k = \frac{E_c b}{t_c} \tag{7.8}$$

In Equation 7.6, A_1, A_2, and A_3 are hyperbolic functions of the crack length and k is the stiffness of the elastic foundation and relates to the modulus and thickness of the core material, E_c and t_c, respectively. This compliance equation can be differentiated and substituted into Equation 7.2 to give G as a function of P and a. However, unlike for the built-in model, a cannot be isolated from Equation 7.6, to allow P to be expressed purely as function of δ and G as for the built-in model in Equation 7.5. As a result, a numerical approach to solving this set of equations was adopted. A sweep of feasible values of a and δ are selected. For every value of a, the compliance and its derivative are subsequently calculated. Next, for every combination of a and δ, the load is calculated using the relation $P = \delta/C(a)$, and the energy

release rate is calculated using Equation 7.1. Rounding the resultant G values gives an array of points of P and δ for each value of G allowing curves of constant energy release rate to be plotted on a load versus displacement axis. Model predictions for three G values have been plotted in Figure 7.6. To highlight the importance of the elastic foundation model versus the built-in model on the fracture region, the curves in Figure 7.6 (a) have been calculated using an artificially reduced core modulus of 1 MPa, in reality the core has a modulus of 90 MPa as used in Figure 7.6 (b). Figure 7.6 (b) describes the significant effect of the elastic foundation model on the initial loading region of the test. As the compliance value for the specimen is taken from the initial loading portion of the test, the use of the elastic foundation model is essential due to the large error in the built-in model.

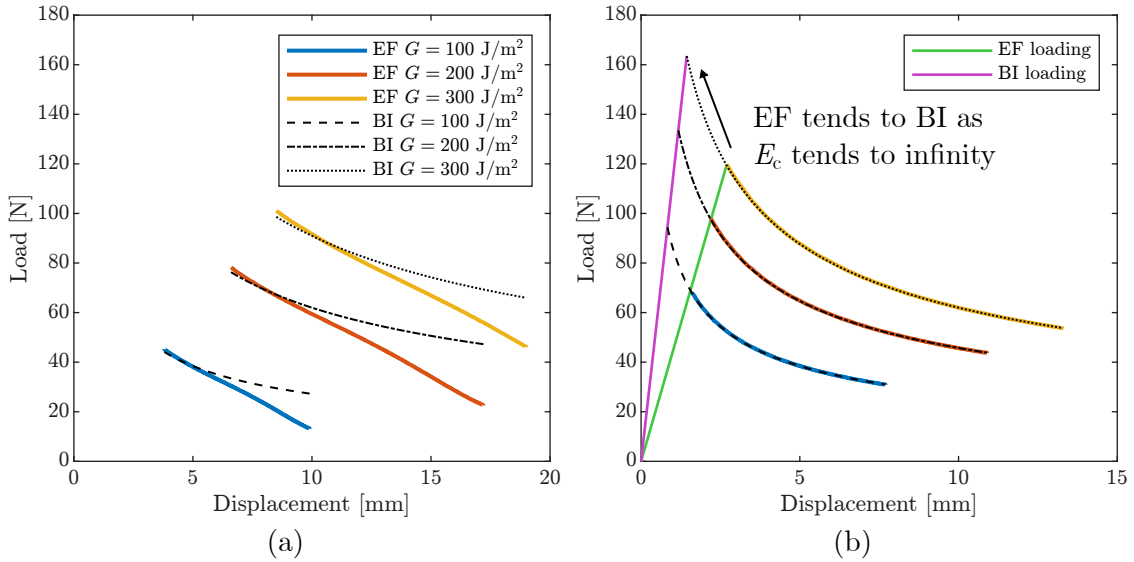


Figure 7.6: Load versus displacement curves plotted from numerical results based on elastic foundation (EF) and built-in (BI) models. (a): Examples plotted based on a core modulus, E_c, of 1 MPa. (b) Examples based on the real core modulus of 90 MPa

This data reduction method, based on a beam on an elastic foundation, allowed the slip and stick points to be analysed separately whilst also providing a robust method of analysing a stable failure sample as shown in Figure 7.3. The values of G for stick and slip were calculated using all the stick and slip points observed experimentally.

7.3.3 Results

The values of G obtained from the SCB testing can be found in Table 7.1, these values are plotted in Figure 7.7.

Table 7.1: Results of the SCB testing of CSR and silica modified matrices.

wt % CSR	wt % SiO_2	G_c stable [J/m^2]	G_c slip [J/m^2]	G_c stick [J/m^2]	G_c slip/G_c stick
0	0	-	227 ± 15	110 ± 17	2.06
3	0	-	202 ± 16	100 ± 18	2.02
6	0	186 ± 16	-	-	-
9	0	170 ± 17	-	-	-
3	5.9	-	259 ± 28	121 ± 21	2.14
6	11.7	137 ± 11	-	-	-
9	17.2	151 ± 5	-	-	-

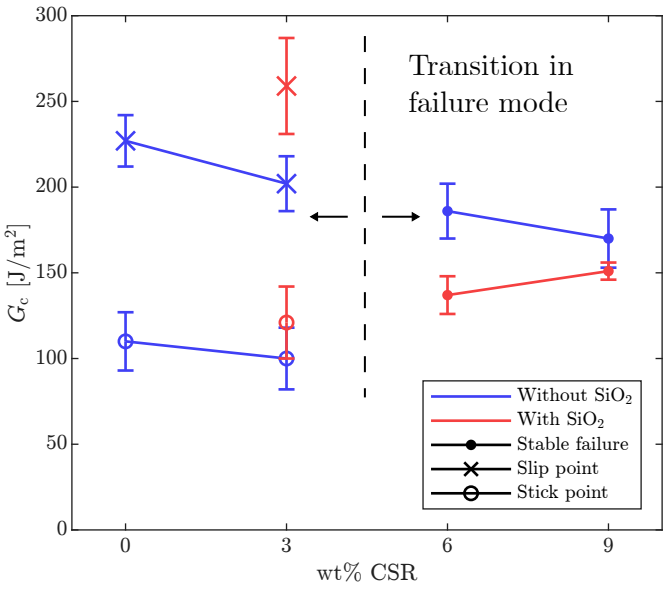


Figure 7.7: Fracture energy versus wt% CSR for SCB specimens with CSR and silica modified matrices. The transition in failure mode is labeled.

The results of the SCB testing clearly show a transition in failure mode, as a result, the direct comparison of fracture values either side of the transition is ambiguous.

The effect of this change in failure mode is that the G_c values obtained from the SCB testing of the 0 and 3 wt% panels are dominated by fracture of the foam. On the other hand, the values from 6 and 9 wt% are a result of the true interface toughness and how the matrix resin interacts with the foam surface. This transition in failure mode precisely replicates the behaviours described in chapter 4. The impacted panels displayed a larger amount of skin-core debonding in the panels with 6 and 9 wt% CSR and more core cracking was evident in the unmodified and 3 wt% CSR panels. Here the same phenomenon has been shown. The lower UTS of the highly modified matrices results in a lower toughness skin-core bond. This is despite the high fracture energy of these matrices which appears to have no further benefit on the fracture performance of the interface.

It is interesting to note that were failure to occur along the interface of the less modified panels, the corresponding toughness value would likely be higher than that achieved for the SCB samples that did fail in this manner. However, the foam used in this research prevents the necessary load from being reached, as such, it is not possible to force the crack into the interface with unmodified and 3 wt% CSR matrix resin using the SCB approach. Were a tougher or denser foam used, the true interface toughness for all matrix resin types could be directly compared.

7.4 Grooved foam cores

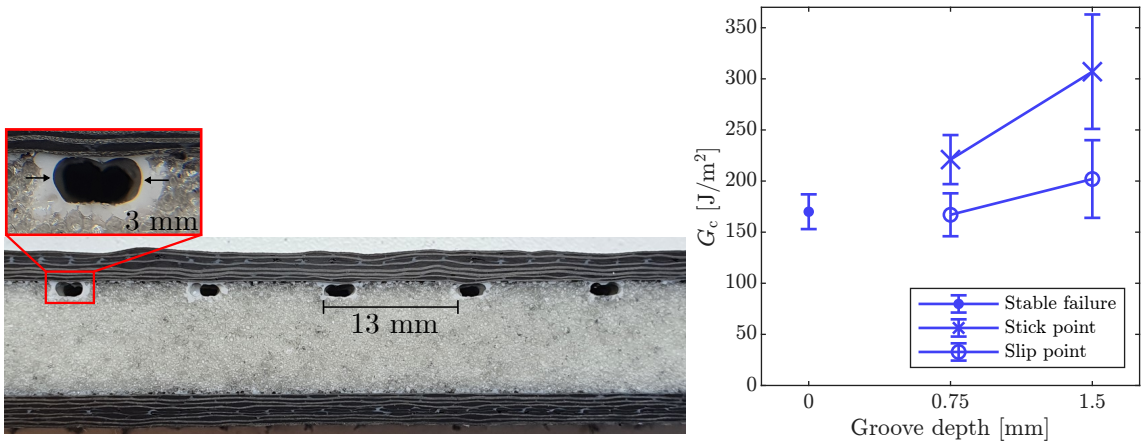
This section presents the results of the grooved foam core SCB tests. The resin used on the skin of these tests was a 9 wt% CSR formulation. Without any grooves, this formulation always results in a stable skin-core debond at the interface. However, the presence of grooves in the core results in a stick/slip response, i.e. a change in fracture mechanism. The results presented in Table 7.2 include the result of a resin formulation manufactured with no toughenners. This is to allow a comparison to be made between stick/slip values with and without grooves.

The infusion manufacturing process of the sandwich panels resulted in the matrix resin lining the grooves as displayed in Figure 7.8 (a). It is possible to carry out an infusion that would result in grooves filled with the matrix resin. A more flow restricted outlet or 'resin break' would assist with this. However, this process would also make it difficult to regulate the thickness of the laminates. The liquid resin cannot exit the panel during the infusion, as a result, the exact amount of liquid

Table 7.2: Results of the SCB testing of grooved foam cores.

wt % CSR	Groove Depth [mm]	G_c stable [J/m^2]	G_c slip [J/m^2]	G_c stick [J/m^2]	G_c slip/G_c stick
0	-	-	227 ± 15	110 ± 17	2.06
9	-	170 ± 17	-	-	-
9	0.75	-	221 ± 24	167 ± 21	1.32
9	1.5	-	307 ± 56	202 ± 38	1.52

resin required to fill the empty space within the infusion must be calculated and allowed to flow into the infusion. Furthermore, this process would also add weight to the panel. All of the grooved panels in this study were manufactured to have lined, empty grooves. No significant research effort was expended in controlling the thickness of these linings.



(a) (b)

Figure 7.8: Photograph of the polished side of a 1.5 mm deep grooved specimen.

7.4.1 Results

The results presented in Table 7.2 and plotted in Figure 7.8 (b) demonstrate that adding grooves to the core improves the fracture energy of the skin-core bond. The improvement is minor for the 0.75 mm deep grooves, an increase from 170 ± 17 J/m^2 to 194 ± 21 J/m^2, but increases with groove depth within the range tested. The 1.5 mm grooves result in a considerably higher fracture energy of 255 ± 47 J/m^2. Figure 7.9 displays pictures taken during fracture testing of SCB specimens with grooves. The panel with no grooves failed along the interface. The panel with 0.75

mm grooves failed partially along the interface between the grooves. The crack can be seen to deviate around the grooves, it is initially deflected downwards into the foam core causing local mixed-mode fracture within the foam. The crack then propagates within the foam below the groove before turning upward to travel diagonally toward the skin. The resin lined groove breaks off from the core and remains attached to the skin. This deviation causes a longer length of crack. The increase in toughness can be explained by this increase in length alongside the occurrence of local mixed mode fracture. For the 1.5 mm deep grooved panel, as the crack travels back toward the skin after propagating under the groove, the distance the crack has to travel back to the interface is further and so more foam is observed adhered to the laminate side of the SCB. Furthermore, the existence of multiple terminated crack fronts can be clearly observed between the grooves. These secondary crack fronts dissipate extra energy resulting in an observed increased in the measured G.

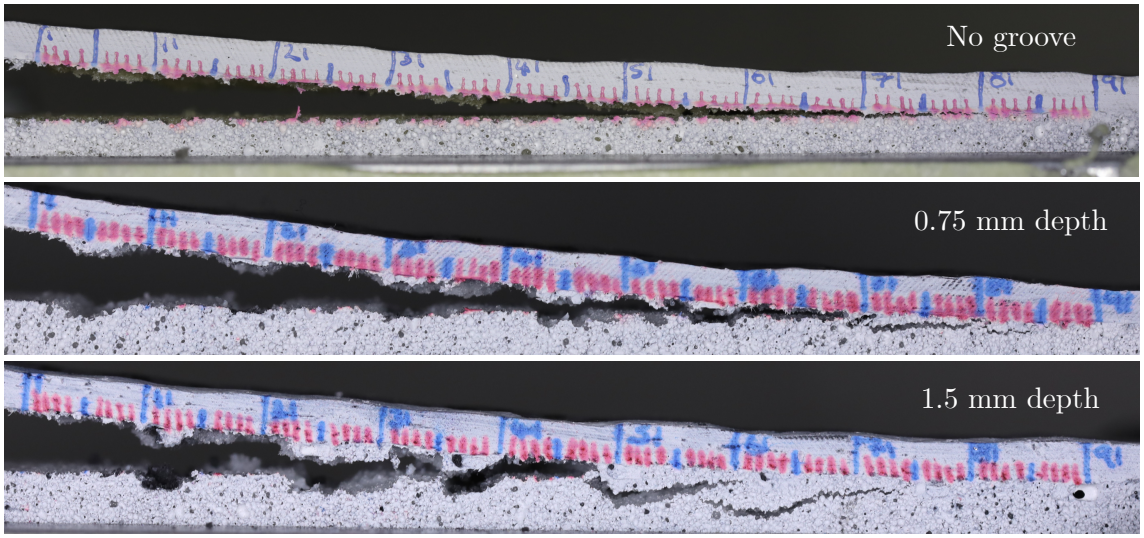


Figure 7.9: Representative mid-test photographs of the side of SCB specimens showing the fracture paths in grooved foams. From top to bottom the groove depth is 0 mm, 0.75 mm, and 1.50 mm.

Figure 7.10 displays two graphs of load versus displacement from the SCB testing of a specimen without grooves in (a) and a specimen with 1.5 mm grooves in (b). The plots also include the advancement of the crack, Δa on the right side axis with the crosshead displacement on the x-axis. The initiation point has been circled on both graphs. It is interesting to note that both the initiation points are at approximately the same load and displacement, thus resulting in similar initiation fracture energies. Until this point in the test the specimens are essentially identical,

there are no grooves in the pre-crack area and there is no groove immediately ahead of the pre-crack front. However, after this point in the test, the responses of the two specimens deviate considerably. The ungrooved sample continues to fail in a stable manner as described previously. The load in the grooved sample rises as soon as the debond encounters the first groove. Once the load increases enough to pass the first groove, the load then drops suddenly in a stick/slip manner as the debond advances. The debond advances rapidly to the next groove, this is clearly demonstrated by considering that the distance between crack jumps in Figure 7.10 (b) is approximately 13 mm, the same as the spacing of the grooves.

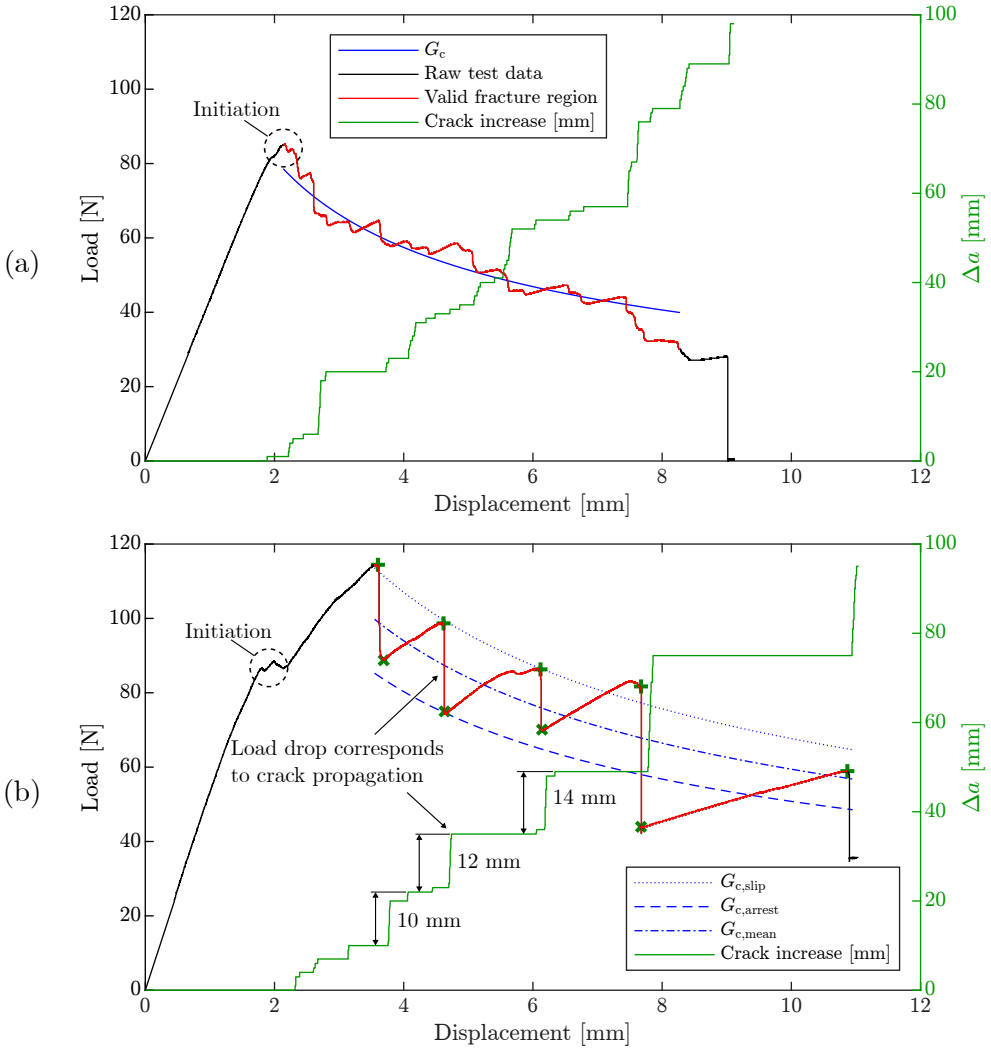


Figure 7.10: Load versus displacement curves and crack length curves for the SCB testing of two specimens. (a): 9 wt% CSR. (b): 9 wt% CSR with 1.5 mm deep grooves with 13 mm spacing.

7.5 Fibre-reinforced foam

This section presents the results of the fibre-reinforced foam core SCB tests. The foam used in this section is reinforced with 2.5 PHR 0.75 mm aramid fibres. This combination of fibres and fibre loading was chosen as it performed well in both fracture and compression testing as outlined in chapter 5. Furthermore, this foam had good manufacturability and produced a 'good quality' foam with no large voids.

7.5.1 Results

The results of this SCB testing can be found in Table 7.3. An example of a load versus displacement plot for each sample is shown in Figure 7.11. After examining the test data for these samples it became clear that the data reduction method used for the previous SCB samples would not be suitable. The addition of the fibres had changed the shape of the load versus displacement plot and had caused R-curve behaviour. As a result, a corrected beam theory method, similar to the one used in Section 3.2.6 was used. This was possible as the failures of these samples were stable and not stick/slip.

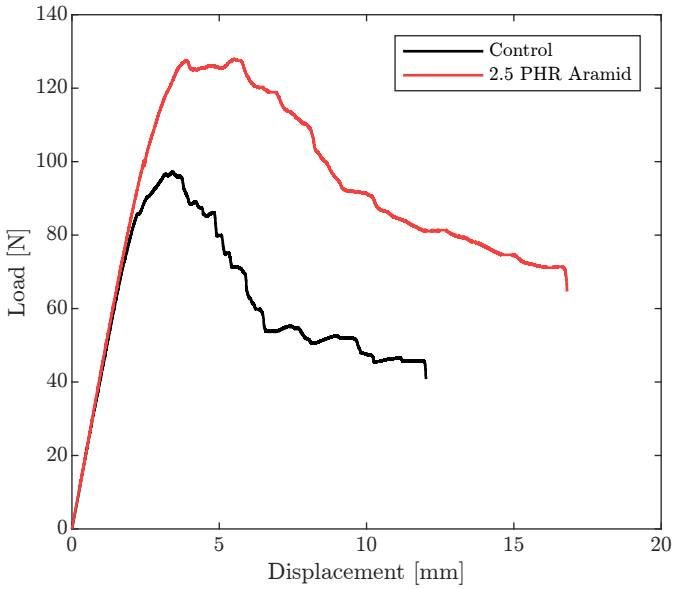


Figure 7.11: Load versus displacement curves for the SCB testing of a control and a 2.5 PHR 0.75 mm aramid specimen

Adding 0.75 mm 2.5 PHR aramid fibres to the foam core of the sandwich structures in this research increases skin-core propagation fracture energy by 50% and initiation fracture energy by 30%. Figure 7.12 displays images taken of the side of both types

Table 7.3: Results of the SCB testing of fibre-reinforced foam cores

Fibre Length [mm]	Fibre Loading [PHR]	Initiation G_c [J/m^2]	% change	Propagation G_c [J/m^2]	% change	Prop – Init G_c [J/m^2]	% change
-	-	231 ± 43	-	277 ± 38	-	46 ± 7	-
0.75	2.5	301 ± 52	+ 30	416 ± 24	+ 50	115 ± 54	+ 150

of SCB samples during testing. The images clearly show that foam is fractured off the core and remains on the skin surface. As a result, it is expected that similar toughening mechanisms observed in SENB foam fracture have caused the increase in the fracture energy of this interface. These mechanisms are further elucidated in skin-side fracture surface images, in Figure 7.13 (a) and (b). Exposed fibres that have been pulled out of the foam are clear in both photographs and SEM images. There is an increase in the difference between the propagation and initiation fracture toughness with the addition of the aramid fibres. This increase suggests an increase in the R-curve behaviour. This is due to material, mainly the fibres, bridging the gap behind the crack tip. As the aramid foam fractures, the fibres are often pulled out as seen in the side-on image in Figure 7.12, and also in the photograph and SEM micrograph of the fracture surfaces in Figure 7.13. The fibres are being pulled out of the foam behind the crack tip, therefore causing an increase in R-curve behaviour and a large increase in the difference between propagation and initiation fracture toughness.

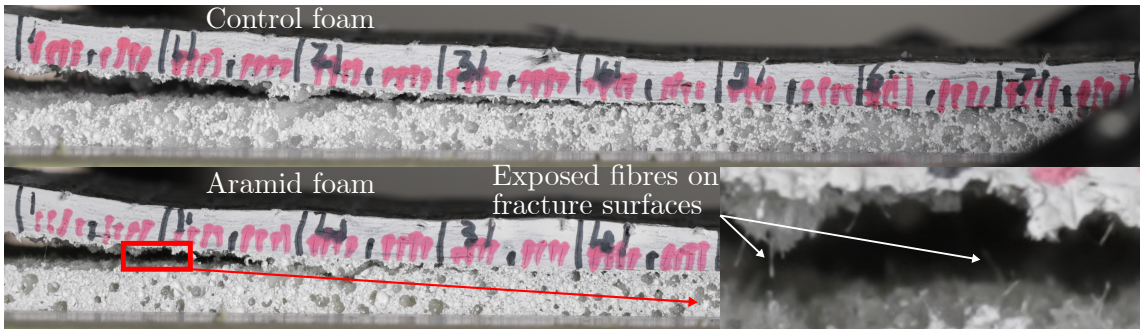
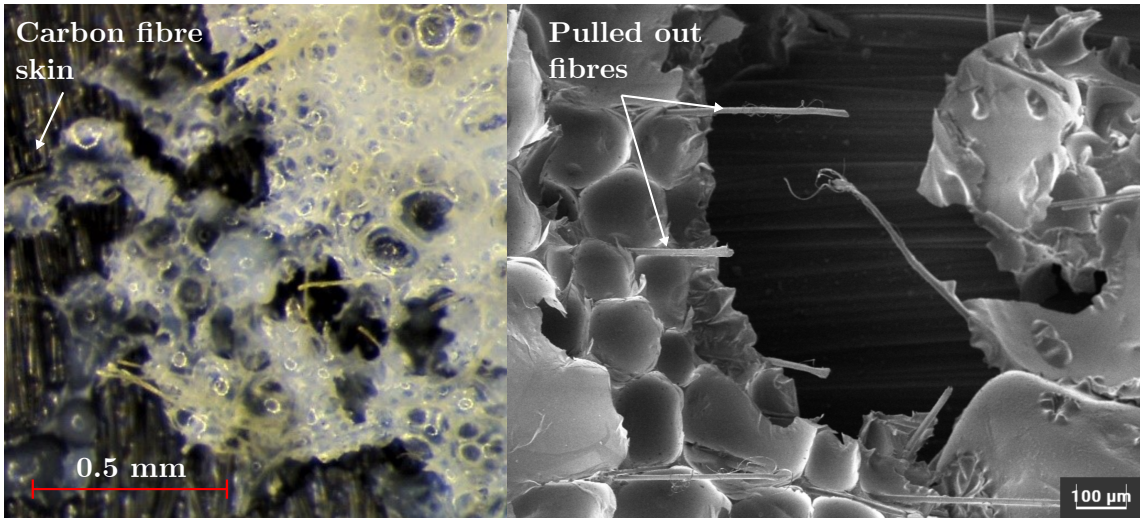


Figure 7.12: Side view images taken during the SCB testing of a control and a 2.5 PHR 0.75 mm aramid specimen showing exposed fibres in the aramid sample.

To further demonstrate the role of fibre bridging on improving the toughness of the skin-core interface, a side-on micrograph was taken using an SEM of the surface of an 'as-machined' foam. This is shown in Figure 7.14. Exposed fibres on the surface can be clearly observed. This is the surface that the skin is ultimately infused upon. The aramid fibres are much tougher and more difficult to machine than the rela-



(a) (b)

Figure 7.13: SCB skin side fracture surface. (a) Digital photograph. (b) SEM image.

tively friable polymer foam structure. As a result, during the machining process, they tend to deflect under the cutting blade and bounce back once the blade has passed over. Fibres exposed during foam machining leave an ideal surface for the skin matrix resin to bond to, i.e. via a z-pinning type mechanism [169].

Control foam samples showed failure partially within the foam. The original hypothesis of this work was that making the foam tougher would drive the failure mode of the SCBs back to the interface and that no sub-surface fracture of the foam core would be observed. However, it is clear from the results presented here, that in adding fibres to the foam, the toughness of the interfacial bond between the skin and the foam core has also been improved as well as the bulk toughness of the foam core. This is due to the exposed fibres on the surface.

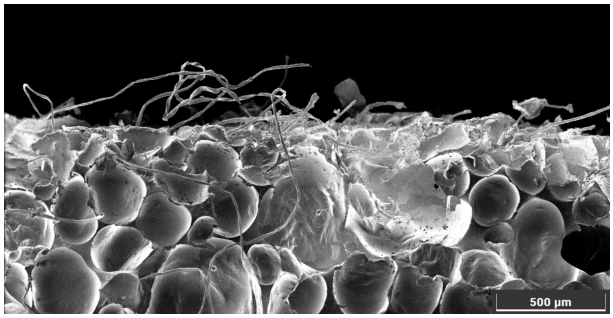


Figure 7.14: SEM image showing the edge of a machined sample of aramid foam showing exposed fibres on the surface.

7.6 Concluding remarks

In this chapter the fracture energy of the skin-core bond has been measured using an SCB specimen for a variety of different composite sandwich structures. A novel method of fitting test data to idealised fracture energy curves on a load versus displacement plot has been used to extract sensible values from stick/slip debond failures.

A change in failure mode was discovered during the impact testing in chapter 4. Adding 6 and 9 wt% CSR resulted in increased back face skin-core debonding. The unmodified and 3 wt% CSR panels experienced increased core cracking instead of this widespread debonding. The same transition has been revealed in isolated debonding tests in this chapter thus neatly explaining the unusual results of chapter 4. The SCB test specimens containing 6 and 9 wt% CSR experienced interface failure, whereas, the unmodified and 3 wt% CSR SCB test specimens experienced sub-interface failure in the core as the true interface in these specimens is tougher than the foam core.

Machining 1.5 mm grooves perpendicular to the crack direction in the surface of the foam core improves skin-core debond fracture energy by 50%. The grooves result in a resin coated channel at the interface which deflects the crack, inducing mixed mode fracture in the foam core and an increase in crack length, both of which contribute to an increase in fracture energy. The deeper 1.5 mm grooves were more effective than the 0.75 mm grooves.

When used in a composite sandwich structure, 0.75 mm 2.5 PHR aramid fibre-reinforced foam improves skin-core initiation and propagation fracture energy by 30% and 50% respectively. The same foam shows improved fracture energy in SENB testing and improved compressive properties as discussed in chapter 5. The same toughening mechanisms observed in the SENB specimens are also reported here, causing an improvement to the skin-core bond. The introduction of the fibres gives rise to extrinsic toughening mechanisms and the emergence R-curve behaviour.

The next chapter will present the second round of impact testing. The main discussion will surround the combining of the toughening mechanisms elucidated in this and the previous chapters to create an optimally damage resistant panel.

Chapter 8

Impact response with combined toughening mechanisms

8.1 Introduction

This chapter details an investigation into the impact response of CFRP composite sandwich structures employing a range of toughening mechanisms. Chapter 4 reveals that adding 3 wt% CSR to the skin matrix resin can reduce front skin delamination and back face deflection during an impact event. Chapter 4 also demonstrated that core cracking and skin-core debonding are the dominant damage types during the specific impact events studied in this research. Chapter 5 has demonstrated that adding 2.5 PHR 0.75 mm aramid fibres increases fracture energy and compressive properties of epoxy foam. Chapter 7 confirms that this increase in foam fracture energy results in an increased skin-core debond fracture energy for the aramid fibre reinforced foam core in a composite sandwich structure. Chapter 7 also reveals that machining grooves into foam cores results in an increased skin-core debond fracture energy.

The impact testing in this chapter aimed to combine these toughening mechanisms in composite sandwich structures to assess whether they would result in improved impact performance. The toughening mechanisms used are as follows:

- 3 wt% CSR modified matrix resin
- 2.5 PHR 0.75 mm aramid fibre-reinforced foam core

- 1.5 mm deep, 3 mm wide, 13 mm spacing grid of grooves

Eight types of panel containing the possible combinations of the above toughening mechanisms were manufactured. Two of each panel were manufactured, one panel was used to carry out a back face deflection test using 3D DIC similar to the test in Chapter 4. The second panel was used for a perforation test to measure the energy absorbed by the panel as a projectile passed through the center. The panels were manufactured using the method described in Section 4.2.

8.2 Results

Table 8.1 displays a summary of the data from the two sets of impact tests carried out, the deflection test and the perforation test. The left hand column describes the toughening modifications employed in the panel, 'Aramid-3-groove' refers to a panel with an aramid-reinforced foam core, 3 wt% CSR modified matrix resin, and grooves milled in the foam core as described previously. Figure 8.1 presents the maximum displacement during the displacement test and the energy absorbed during the perforation test of the control foam core panels as a bar chart. The displacements marked with an asterisk were taken from a section of the back face where some fibres had broken off. As a result, the DIC measurements were disrupted and interpolation was required to produce these values. The Aramid-0 panel resisted perforation during the perforation test. The velocity of the rebounded projectile was used to calculate how much energy was absorbed by the panel.

Table 8.1: Results of the impact testing of sandwich structures with combinations of toughening mechanisms

Panel modification	Maximum displacement [mm]	% change	Energy absorbed during perforation [J]	% change	% of projectile energy absorbed
Control-0	13.2*	-	309	-	74.2
Control-0-groove	12.4*	-6.6	314	1.8	74.7
Control-3	11.9	-10.0	326	5.5	78.2
Control-3-groove	11.1	-15.7	346	12.2	82.1
Aramid-0	9.7	-26.5	415†	34.3	98.9
Aramid-0-groove	9.7	-26.5	305	-1.2	73.0
Aramid-3	11.2*	-15.3	327	6.0	78.3
Aramid-3-groove	10.5	-20.6	422	36.8	99.8

* Slight damage to back face affected DIC measurement, some interpolation required.

† Projectile rebounded, rebound velocity measured for energy absorption calculation

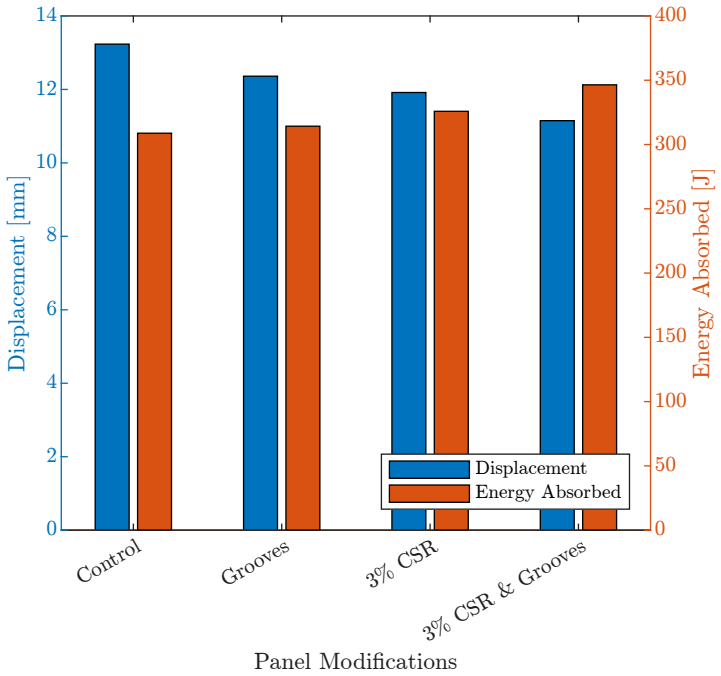


Figure 8.1: Bar chart displaying maximum displacement recorded during the displacement test and energy absorbed during the perforation testing of sandwich structures with a control foam core.

8.2.1 Displacement test

For the control foam core panels, it is clear that employing the different panel modifications improves the back face displacement. Adding grooves to the core improves back face displacement by 6.6%, while adding 3 wt% CSR improves back face displacement by 10%. The combination of these toughening mechanisms provides the most improvement over the control panel with a reduction of 15.7% for back face displacement. Figure 8.2 shows pictures of the cross sections of the control foam panels from the displacement test. The control-0 panel shows large skin-core debonding of both the front and rear skin. It also shows that the rear skin was damaged with broken fibres and delaminations on the site where the projectile impacted the rear skin. The control-0-groove and control-3 panels exhibit substantial core cracking and skin-core debonding. In the control-0-groove panel, the core cracks can be seen to initiate and terminate at a groove. In chapter 7, the grooves are shown to be lined with the matrix resin of the skin. The brittle matrix resin that lines these groove combined with the stress concentration of the groove is the reason for the locations of these cracks. In contrast, the control-3-groove panel does not exhibit any similar core cracking. Furthermore, in the zoomed image, it is clear that the grooves re-

main intact. The tougher resin has prevented any core cracks from initiating at the grooves. In addition, the skin-core debond on the back face can be seen to travel around the grooves as it did in the SCB testing in chapter 7. The grooves have had the intended effect of increasing the length of the debond and introducing multi-mode fracture thus increasing the absorbed energy and reducing the maximum back face deflection. This testing has shown that the maximum benefit of the grooves is achieved in conjunction with a tough resin.

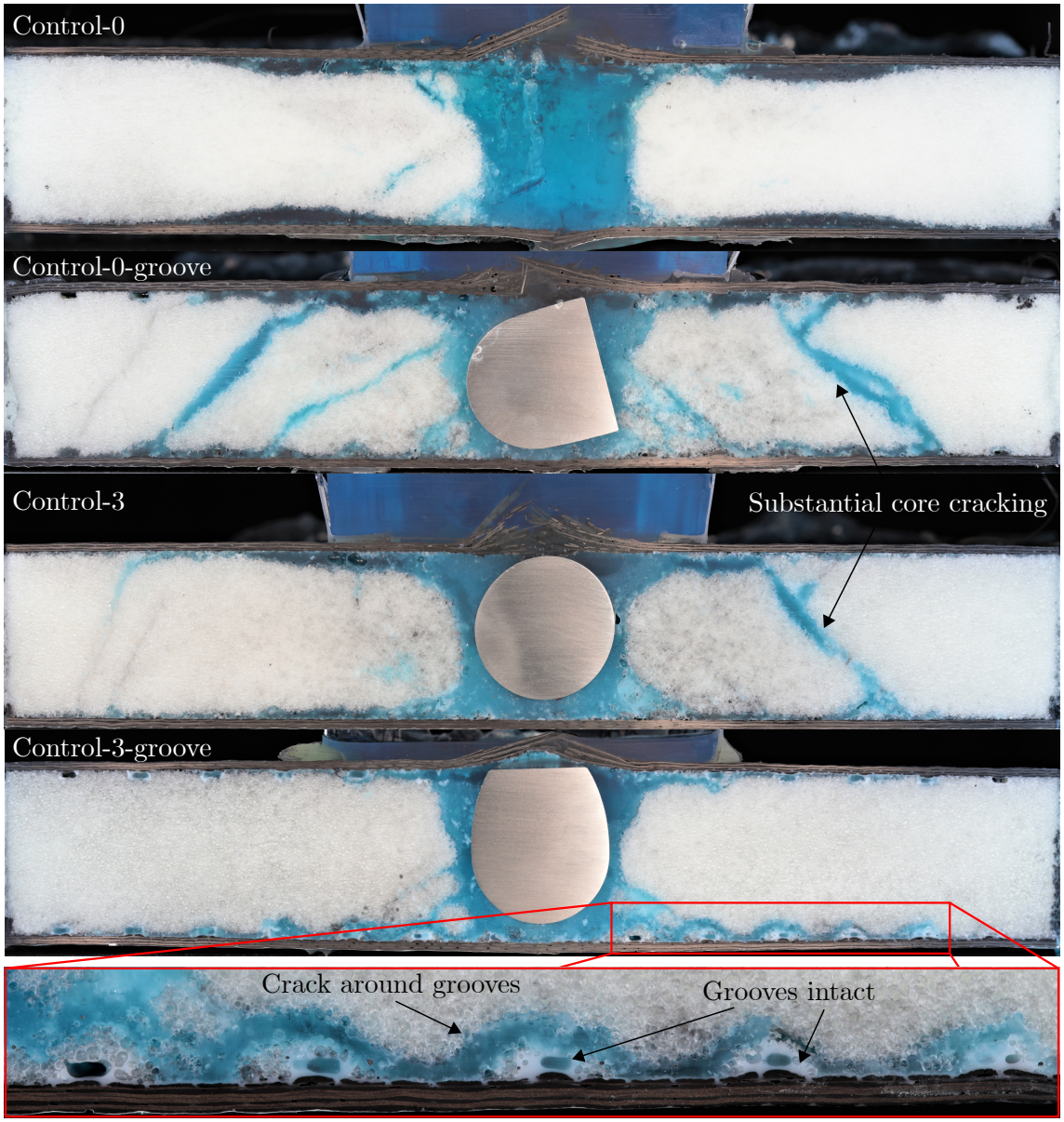


Figure 8.2: Control foam core sandwich structure cross sections from the displacement test.

All the aramid panels experienced the same or lower back face displacement than all the control panels. The addition of aramid to the core is the dominant panel mod-

ification in this research. The aramid-0 panel experienced 26.5% less displacement than the control panel, a significantly larger improvement than any other modification individually. Figure 8.3 shows pictures of the cross sections of the aramid foam panels from the displacement test.

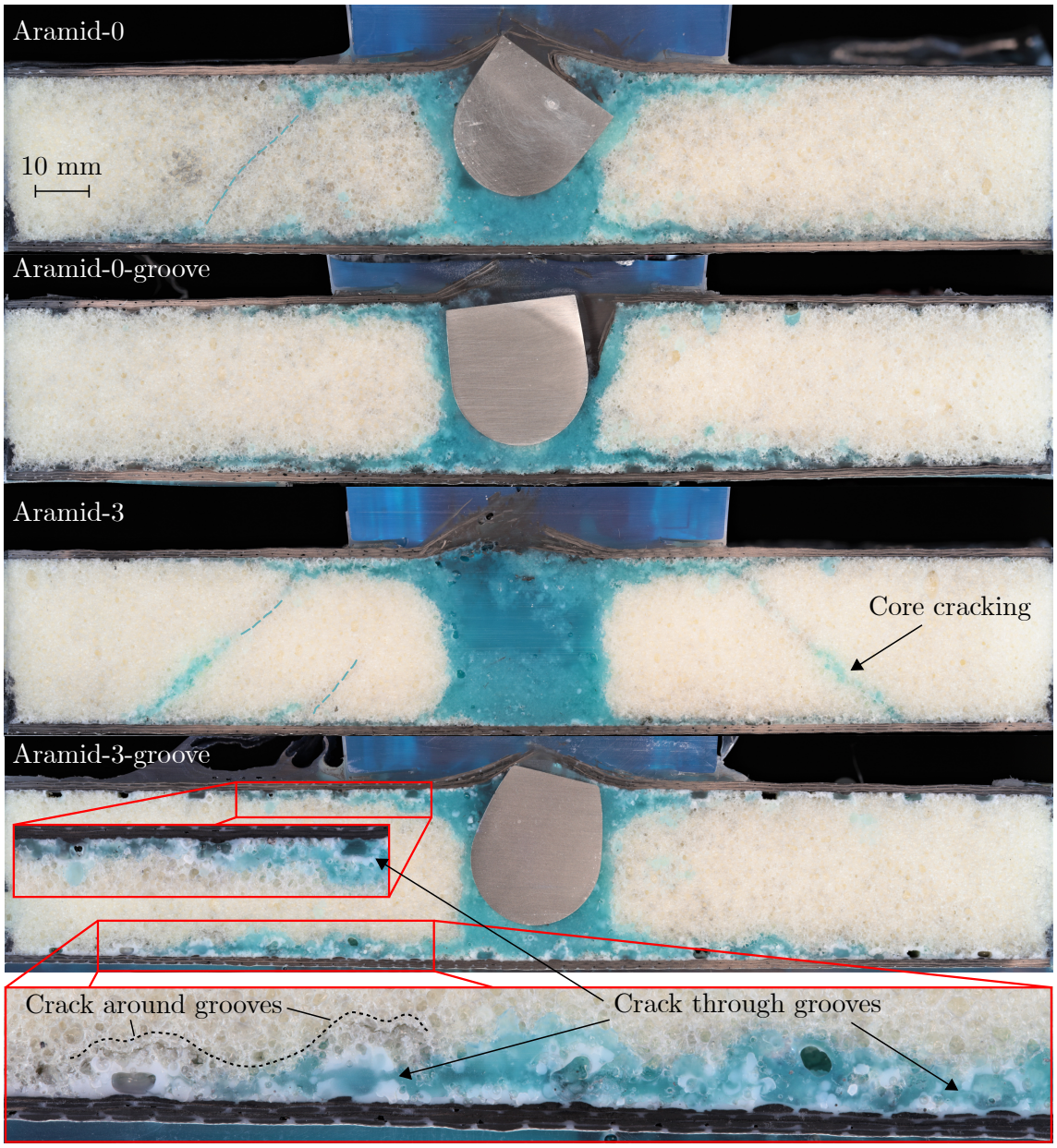


Figure 8.3: Aramid foam core sandwich structure cross sections from the displacement test.

The most notable difference when comparing these images to the control images in Figure 8.2 is that there is substantially less core cracking in the aramid foam. Both the grooved aramid panels do not show any core cracking. The aramid foam is tougher than the control foam as tested by SENB in chapter 5. The increased

foam toughness results in lower levels of core cracking in all the aramid foam core panels. The control panels have up to three full skin-to-skin core cracks on each side, however, the most seen in an aramid core is one. Where the grooves acted as initiation and termination points for core cracks in the control-0-groove panel, the aramid-0-groove panel does not exhibit the same behaviour. The tougher foam has resisted these cracks. In the control-3-groove panel the skin-core debond crack propagates around the grooves leaving the grooves intact. The zoomed image of the aramid-3-groove panel in Figure 8.3 shows the crack has travelled through the grooves and the toughened resin that lines them. In chapter 7 it is shown that aramid fibre-reinforcement improves the bond between the skin and core of a sandwich structure. This improved bond and the tougher foam results in the crack travelling through the grooves instead of around them. However, there is a secondary crack above the last broken groove in the zoomed image at the bottom of Figure 8.3.

Figure 8.4 exhibits the DIC displacement and calculated velocity over time for the aramid foam core panels. The shape of the plots is similar to the plots presented in chapter 4 for the previous impact tests. The points of front skin perforation and rear face contact are marked as green lines. The response of the panels is similar, though there are some small differences. The two 3 wt% panels experience larger maximum displacements. All the aramid panels exhibit similar extents of back face skin-core debonding. Chapter 7 explains that a lower strength resin results in a lower strength bond between the skin and the core. The 3 wt% resin has a lower UTS than the unmodified resin as tested in Chapter 4. The lower UTS results in a larger maximum displacement in the impact test here as less energy is expended in the skin-core debond compared to the unmodified resin.

8.2.2 Perforation test

For the control foam core panels, it is clear that the energy absorbed during perforation is improved by employing the different panel modifications. Adding grooves to the core improves energy absorbed by 1.8%, while adding 3 wt% CSR improves energy absorbed by 5.5%. The combination of these toughening mechanisms provides the most improvement over the control panel with an increase of 12.2% for energy absorbed. Figure 8.5 displays images of the cross sections of the perforated panels with control foam cores.

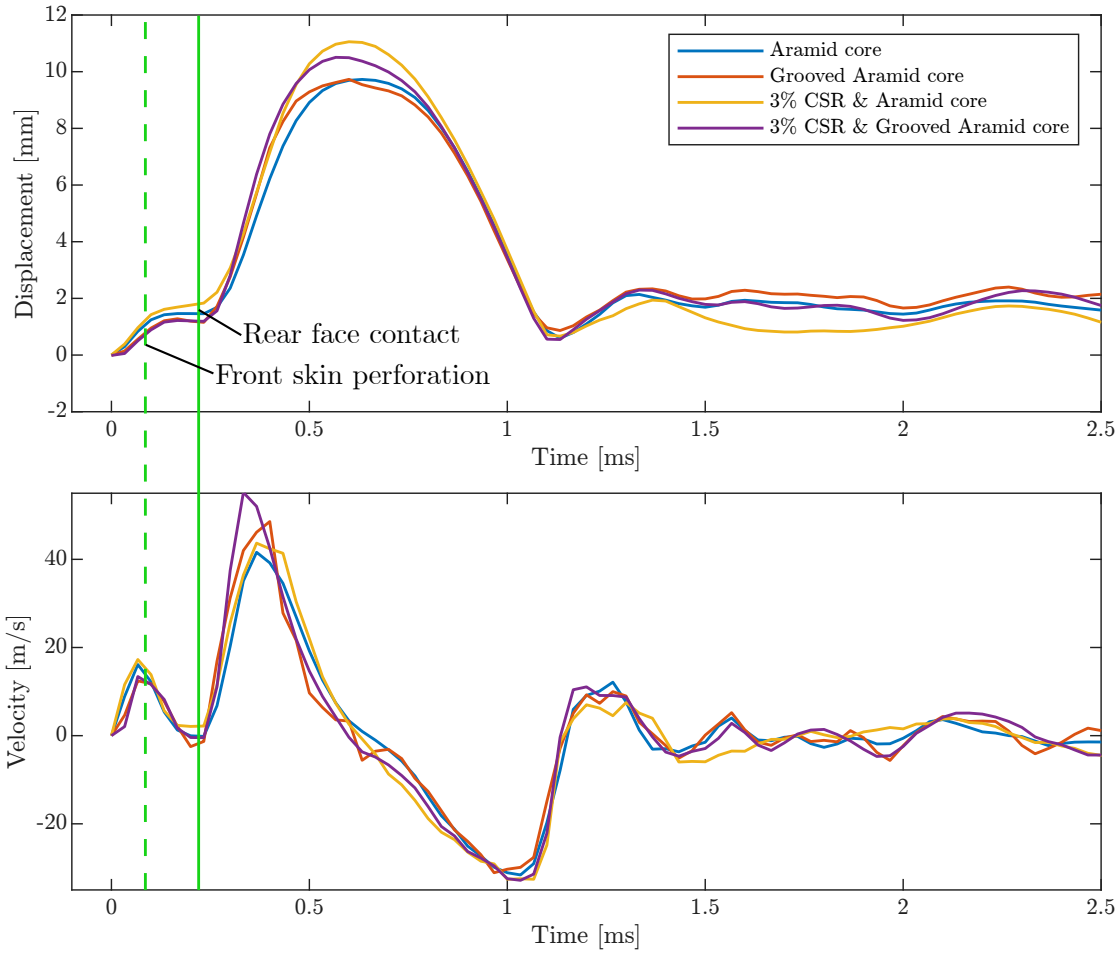


Figure 8.4: Centre point displacement and velocity versus time for sandwich structures with an aramid-reinforced foam core. The times of perforation and rear face contact are indicated by green lines.

All the perforated panels exhibit core cracking and skin-core debonding. Unfortunately, the center section of the control-0-groove panel coincides with a groove parallel to the section. As such, it is difficult to determine how much skin-core debonding there is. The two panels with unmodified matrices absorbed less energy during the perforation test. These two panels also exhibit less core cracking, with the 3 wt% panels having at least two full skin-to-skin cracks on each side of the projectile. The increased core cracking has caused an increase in the total energy absorbed during perforation. The toughening of the matrix skin induces these extra cracks. It is likely that the toughened rear skins provide more perforation resistance to the projectile and so impart a larger force on the core as the back face is peeled off. This results in more cracks within the core.

The energy absorbed during perforation of the aramid panels varies considerably.

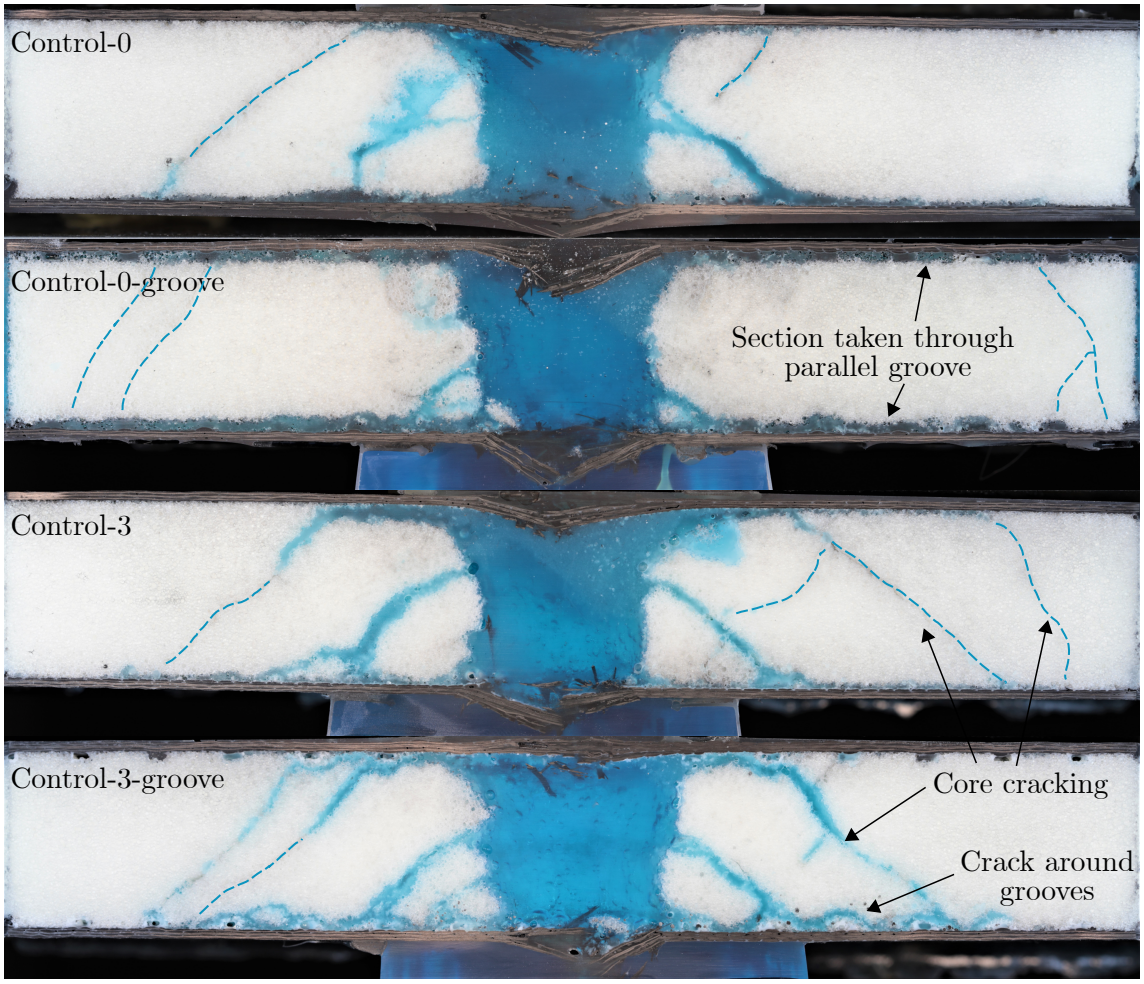


Figure 8.5: Control foam core sandwich structure cross sections from the perforation test.

The aramid-0 prevented the projectile from perforating it entirely and the aramid-3-groove panel absorbed 99.8% of the energy of the projectile. Whereas the aramid-0-groove panel only absorbed a similar amount of energy as the control-0 panel. Figure 8.5 displays images of the cross sections of the perforated panels with aramid foam cores. The most significant difference between these aramid panels and the control panels is the lack of core cracking in three out of the four panels. The increased fracture energy of the aramid core is the reason for this. As with the displacement test panels, the addition of aramid to the core is the dominant panel modification for the perforation test. Hassan and Cantwell [155] found a clear link between the perforation resistance of composite sandwich structures and the mode-II work of fracture of the core material. Furthermore, they found that the mode-II work of fracture could be up to thirty times greater than the mode-I equivalent and is a key energy absorbing damage mode in composite sandwich structures under impact loading.

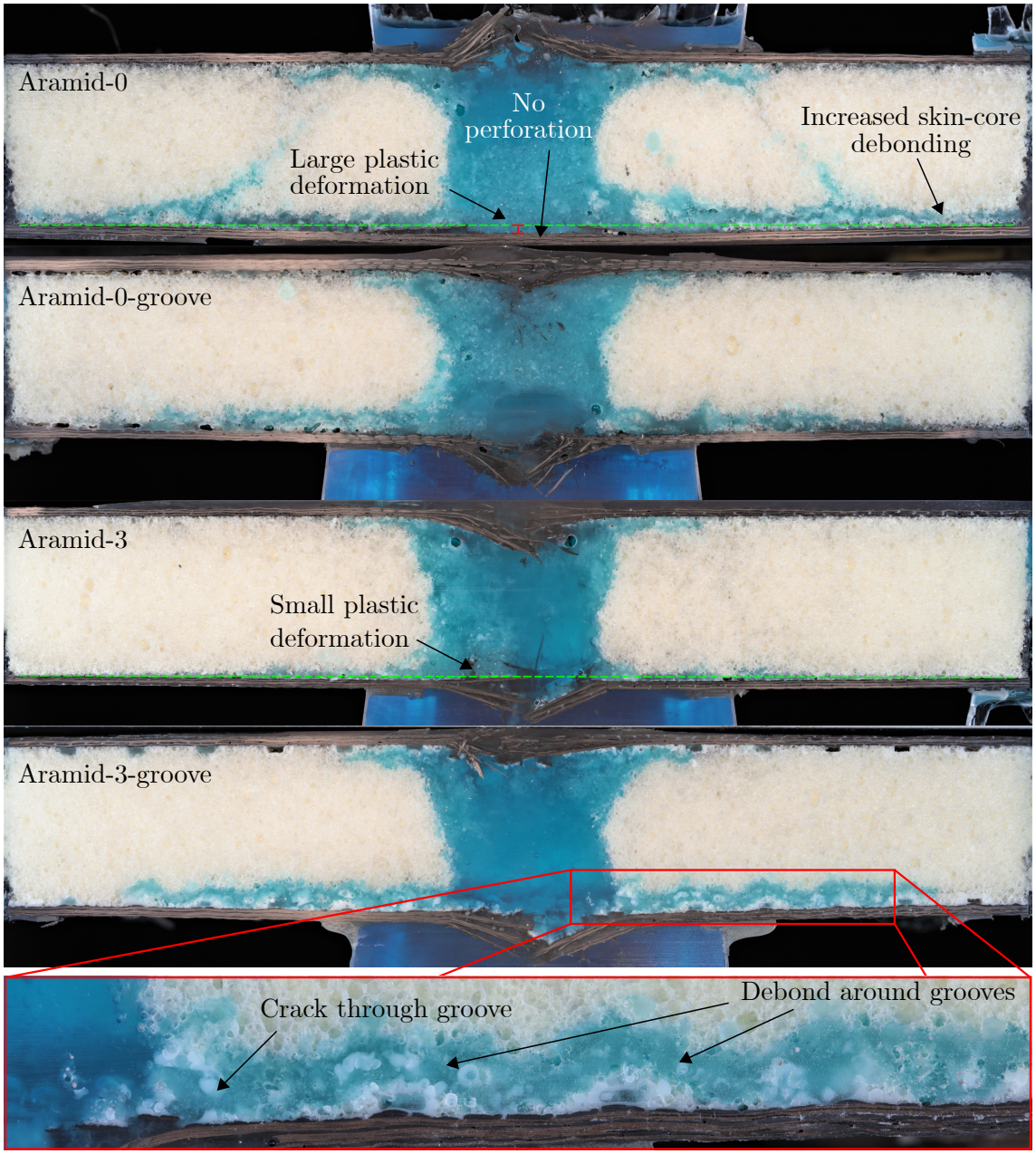


Figure 8.6: Aramid foam core sandwich structure cross sections from the perforation test. Note the Aramid-0 panel was not perforated by the projectile.

The aramid-0 prevented the projectile from perforating it, as a result, no energy could be absorbed during the perforation of the rear skin. It is likely that this perforation of the rear skin is a significant portion of the total energy absorbed. Goldsmith et al. [170] measured the perforation energy of carbon fibre epoxy laminates with a 12.7 mm steel projectile. They found the dynamic penetration energy of a 2.5 mm laminate to be 29 J. The skins in this research are approximately 1.8 mm

and the projectile was 24.9 mm and manufactured out of aluminium. Many factors contribute to the perforation energy which will be different when the laminate is connected to the rear of a sandwich structure. However, the order of magnitude of the energy can be assumed to be similar. This amount of energy is a significant portion of the projectile total energy, approximately 10%. As the rear skin is not perforated, the extent of the other damage types is increased to absorb the total energy of the projectile and rebound it. Figure 8.6 shows that almost the entire back face of the aramid-0 panel debonded during the test. Furthermore, this is the only aramid panel to exhibit any core cracking. This panel also has some plastic deformation of the rear skin.

The other panel to absorb a similar amount of energy was the aramid-3-groove panel. The projectile perforated the rear skin of this panel and so the extent of other damage types is reduced compared to the aramid-0 panel. The zoomed image shows the skin-core debond on the back face of this panel travelled through some grooves and around others leaving them intact. Both of these processes associated with the grooves absorb energy, however, these processes absorb more energy when the matrix resin is modified with 3 wt% CSR. The aramid-0-groove panel exhibits the same damage mechanisms as the aramid-3-groove, however, it absorbs significantly less energy due to the resin being unmodified.

The panel with the least damage, the aramid-3 panel, is also the panel that absorbed the least amount of energy from the projectile. There is less back face skin-core debonding in this panel and also very little plastic deformation. The order of damage events in this instance is critical in how much overall damage will occur and how much energy the panel will absorb. For example, if the rear skin is easily damaged and the projectile passes through without a high load being reached, the back face will not be levered off the core with as much force and less skin-core debonding will take place. Furthermore, if the load to initiate a skin-core debond is high, the rear skin will experience a higher force and be damaged more before skin-core debonding occurs. Skin-core debonding both absorbs energy and increases the compliance of the rear skin as the unsupported area increases, which will reduce the load and increase the energy absorbed perforating the rear skin. Cantwell and Morton [171] found that perforation energy increased with beam length for CFRP laminates under impact loading. On the other hand, if a skin-core debond is initiated at a low load, the skin will be allowed to deflect more and more energy will be absorbed through

the perforation of the rear skin and through the skin-core debonding. The initiation of the grooved panels during SCB testing in chapter 7 is the same as the other panels but the load then increases. This characteristic results in high values for perforation energy for both of the grooved panels. The ungrooved panels are polarised in that one absorbs a large amount of energy, the aramid-0 panel, while the aramid-3 panel absorbs much less energy. These panels have significantly differing amounts of skin-core debonding. The order of damage events in these panels are distinct, with one set of damage events leading to the projectile being stopped completely and the other allowing the projectile to pass through with 90 J of kinetic energy.

8.3 Concluding remarks

This chapter has investigated composite sandwich structures with various combinations of panel modifications designed to increase the impact performance of the panels. A number of important conclusions can be drawn from this work, which can be summarised as follows:

For the control foam core panels in the displacement tests, employing the grooves and 3 wt% CSR panel modifications reduced the maximum displacement. The combination of both of these panel modifications provides the best improvement over the control panel. Reinforcing the core with short cut aramid fibres is the dominant panel modification in this research. All of the aramid panels performed as well or better than the control foam panels. The aramid core caused less core cracking to occur. The machined grooves appear to toughen the interface in a similar manner to the SCB specimens tested in chapter 7, with skin-core debond cracks travelling around the grooves in the foam. However, adding aramid to the core caused some skin-core debond cracks to pass through the resin lined groves due to the increased fracture energy of the core and increased strength of the bond between the foam and the resin.

As with the displacement tests, the panel modifications improved the performance of the control foam core panels in the perforation tests. The combination of the grooves and the 3 wt% CSR was once again the best performing of the control foam core panels. Aramid reinforcement caused a significant improvement in some of the aramid foam core panels compared to the control panel. One of the panels resisted perforation while another absorbed 99.8% of the energy of the projectile.

The aramid foam core panels had no core cracking apart from the one panel that resisted perforation. The sequence of damage events was key in determining if a panel absorbed a large amount of energy and experienced a large amount of damage or absorbed less energy and had correspondingly less damage. Overall the panel modifications all provided some benefits over the control panel. However, the aramid foam cores provided the only significant improvement in impact performance. The modifications were chosen due to their performance in previous chapters detailing previous testing. The 3 wt% CSR resin has performed well in DCB testing and previous impact testing. The grooves performed well in SCB testing. The aramid fibre-reinforced cores performed well in SENB testing and SCB testing. This research shows that coupon testing of sandwich structure materials and interfaces can be used to chose materials and panel modification strategies to maximise the performance of a sandwich structure with some success.

The next chapter presents a series of carbon fibre-reinforced polymer laminate tensile tests. The effect of matrix modifiers on the laminate tensile properties will be discussed.

Chapter 9

Digital image correlation analysis of laminate tensile tests

9.1 Introduction

This chapter details an investigation into the effects of modifying the matrix resin of a CFRP laminate on its tensile properties. In chapter 4, CSR and silica nanoparticles were used to modify the properties of the matrix resin of composite sandwich structures. The aim of using CSR particles was to toughen the matrix resin which, in turn, toughens the laminates used as the skins of the sandwich structure. The silica nanoparticles were subsequently used to recover the stiffness of the matrix lost due to the use of soft CSR particles. This chapter will assess how the use of these particles affects the tensile properties of a cross-ply laminate. It is important to investigate any possible adverse effects of using toughenners in a laminate when designing a composite structure. The laminates tested in this chapter are the equivalent of combining both the top and bottom laminate skins of the sandwich structures detailed in chapter 4. A key aspect of this chapter is evaluating the usefulness of DIC as a non-contact strain measurement of the surface of the tensile specimens. The surface of composite laminates manufactured by infusion are frequently not flat due to the use of flow media and other consumables in the layup. This surface makes it difficult to apply strain gauges to measure strain accurately. Furthermore, clip gauge extensometers can slip into dips on the surface of the laminate giving erroneous strain readings during the test. DIC provides full-field strain for the specimen without contacting the surface. This chapter will explore how this full-field strain reveals other important information otherwise unavailable from the tensile testing

of laminates.

The laminates in this chapter are manufactured using the same seven resin formulations as in chapter 4. They were manufactured using the same infusion method as the sandwich structures, but without the core. The tabs used as the grip surface were a glass fibre reinforced epoxy material sourced from 'RG Composites'.

9.2 Results

9.2.1 Mechanical properties 0° and 90°

Table 9.1 displays a summary of the modulus values for the two principal directions of the laminates. Table 9.1 also reproduces from Table 4.1, the moduli of the bulk matrices used in the laminates. The failure of the samples has not been considered as the samples often failed at the tabs and were therefore invalid failures. For simplicity, the samples labeled 0° have fibres parallel to the test direction on the surface of the specimens, the fibres used in these samples also run the whole length of the carbon fibre roll used. Conversely, samples labeled 90° have fibres perpendicular to the test direction on the surface. A prediction for the laminate tensile modulus in either principal direction is also included. This principal laminate tensile modulus value was calculated using the rule of mixtures and inverse rule of mixtures as described by R. F. Gibson [172]. The longitudinal modulus of a lamina is calculated using the rule of mixtures as follows:

$$E_1 = E_\mathrm{f} v_\mathrm{f} + E_\mathrm{m}(1 - v_\mathrm{f}) \tag{9.1}$$

where E_f and E_m are the modulus of the fibre and matrix, respectively, and v_f is the fibre volume fraction. The transverse modulus of a lamina is calculated using the inverse rule of mixtures as follows:

$$\frac{1}{E_2} = \frac{v_\mathrm{f}}{E_\mathrm{f}} + \frac{1 - v_\mathrm{f}}{E_\mathrm{m}} \tag{9.2}$$

As the laminate is made up of orthogonal lamina, the principal laminate modulus, E_T, can be calculated using the rule of mixtures again without the need to resort

to classical laminate analysis.

$$E_{\mathrm{T}}(\mathrm{comp}) = E_1 v_1 + E_2(1 - v_1) \tag{9.3}$$

where v_1 is the proportion of lamina in the principal direction, 0.5 in this case. The value used for E_{f} is 250 GPa [173]. The fibre volume fraction was calculated by matching the predicted value with the highest measured value of modulus achieved in the mechanical testing. The reason for this is that the aim of providing the predicted values is to reveal the expected trend in the results, the absolute predicted values are of secondary importance in this regard. The resulting fibre volume fraction of 0.53 is reasonable for an infusion manufactured laminate [174].

Table 9.1: Tensile test results for the 0° and 90° samples.

wt% CSR	wt% SiO2	E_{T}(bulk) [GPa]	E_{T}(comp) 0° [GPa]	E_{T}(comp) 90° [GPa]	E_{T}(comp) Predicted [GPa]
0	0	2.96 ± 0.06	54.3 ± 2.7	56.1 ± 2.2	70.1
3	0	2.76 ± 0.02	60.4 ± 5.0	59.0 ± 3.0	69.8
6	0	2.73 ± 0.02	61.6 ± 1.0	58.0 ± 5.6	69.8
9	0	2.57 ± 0.02	70.1 ± 3.5	66.8 ± 3.0	69.6
3	5.9	3.02 ± 0.08	60.0 ± 4.5	62.3 ± 1.5	70.1
6	11.7	3.12 ± 0.07	64.4 ± 4.2	62.8 ± 1.5	70.3
9	17.2	3.16 ± 0.12	69.0 ± 1.7	65.0 ± 5.1	70.3

Figure 9.1 displays plots of laminate modulus versus wt% CSR for each sample in the 0° and 90° directions. The dashed lines represent the predicted moduli of the laminates based on the rule of mixtures models described. It is clear that the modulus of the matrix has very little effect on the predicted modulus of the corresponding laminate. The lower modulus, high wt% CSR, matrices produce predicted laminate modulus values only 0.7% lower than the control laminate, despite a 13% difference in matrix modulus. The measured modulus of the laminates shows that, for both directions, the addition of CSR to the matrix increases the tensile modulus of the laminate. This result is not intuitive and runs contrary to the expectations of the rule of mixtures model. The subsequent addition of silica has no additional effect on the laminate modulus.

In chapter 4 the CSR within the matrix is shown to increase the fracture energy of

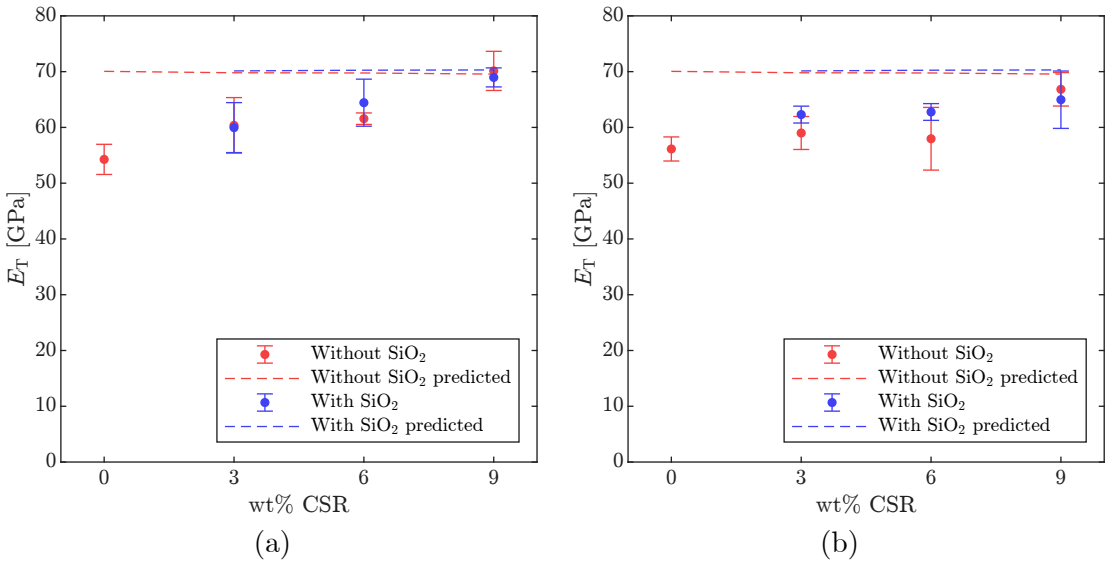


Figure 9.1: Tensile modulus versus wt% CSR. (a) 0° direction. (b) 90° direction.

both the bulk epoxy polymer and the composite laminates. It is known from SEM images in Figure 4.1 that CSR particles lie preferentially next to the fibres in the interphase region. The carbon fibre epoxy interphase region has been shown to be approximately 100-150 nm using a nanoscale dynamic mechanical imaging technique [175]. The CSR particles have an average diameter of 160 nm [40], as such, these particles could have a large influence on the properties of this interphase. Literature has shown that modifiying the interphase can improve laminate modulus by up to 20% as discussed in Section 2.7. The CSR in the matrix of the laminates tested here is reducing microcracking and enabling improved stress transfer between the matrix and the fibres. The limiting factor dominating the stiffness of a laminate is clearly the modulus of the fibres, however, this simply provides an upper bound. The composites in this chapter have very similar upper bound moduli as shown by the calculated values plotted in Figure 9.1. The tougher matrices with higher wt% CSR are able to achieve a modulus closer to this value due to less microcracking and improved stress transfer. Figure 9.2 (a) displays example stress versus strain plots for a control specimen and a 9 wt% CSR specimen. The difference in gradient and modulus is clear, while both specimens exhibit a linear response throughout the test. This suggests the presence of microcracks are as a result of manufacturing. The origin of these microcracks requires further investigation.

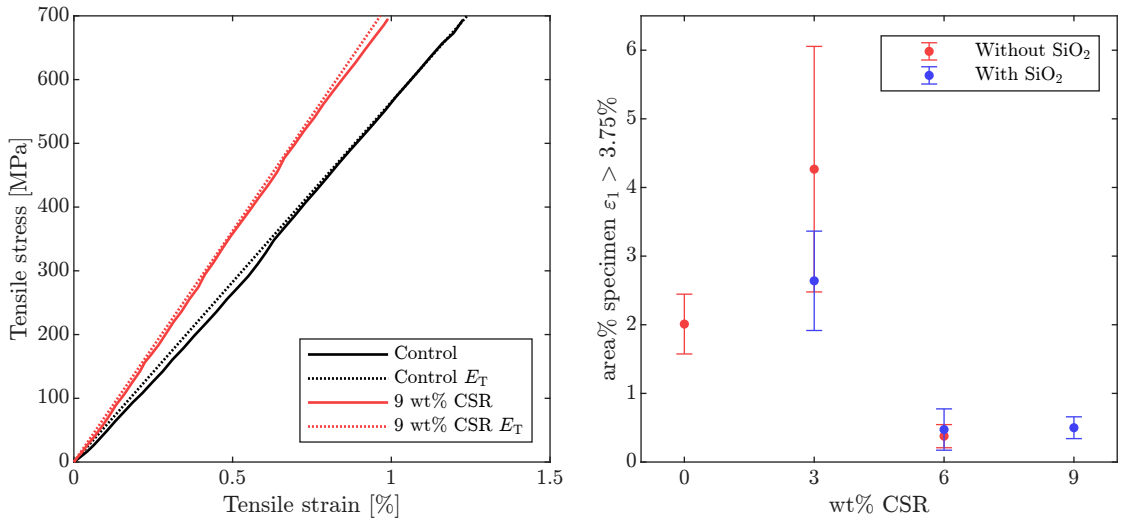


Figure 9.2: (a) Example stress versus strain data from the tensile testing of a control and a 9 wt% CSR sample, 0° direction. (b) Average percentage area of the 90° samples with a major strain over 3.75%.

9.2.2 Mechanical properties ± 45° in-plane shear

Table 9.2 summarises the results of the in-plane shear testing. Figure 9.3 (a) presents the shear modulus versus CSR wt% results for the laminates tested. Figure 9.3 (b) demonstrates how the 0.2% offset shear strength and the shear strength at 5% shear strain are calculated. The shear strength at 5% shear strain is reported according to recommendations in the ASTM standard [140]. Beyond this strain, fibre scissoring beyond 1.5° leads to an unacceptable violation of the assumption in the test method of a nominal ±45° laminate. Figure 9.4 displays both the 0.2% offset shear strength and the shear strength at 5% shear strain for the laminates tested.

Table 9.2: Tensile test results for the in-plane shear samples.

wt% CSR	wt% SiO_2	G_{12} [GPa]	G_{12} Predicted [GPa]	τ_{12} (0.2% offset) [MPa]	τ_{12} ($\gamma_{12} = 5\%$) [MPa]
0	0	2.81 ± 0.14	3.62	30.21 ± 3.15	49.03 ± 0.91
3	0	2.67 ± 0.17	3.38	31.55 ± 1.92	45.02 ± 0.50
6	0	3.10 ± 0.20	3.34	30.67 ± 1.13	46.85 ± 1.23
9	0	3.22 ± 0.08	3.15	29.08 ± 1.01	43.53 ± 0.99
3	5.9	3.19 ± 0.26	3.70	33.85 ± 33.85	49.11 ± 2.27
6	11.7	3.34 ± 0.18	3.82	33.40 ± 33.40	47.98 ± 1.05
9	17.2	3.21 ± 0.13	3.87	30.19 ± 30.19	45.80 ± 1.17

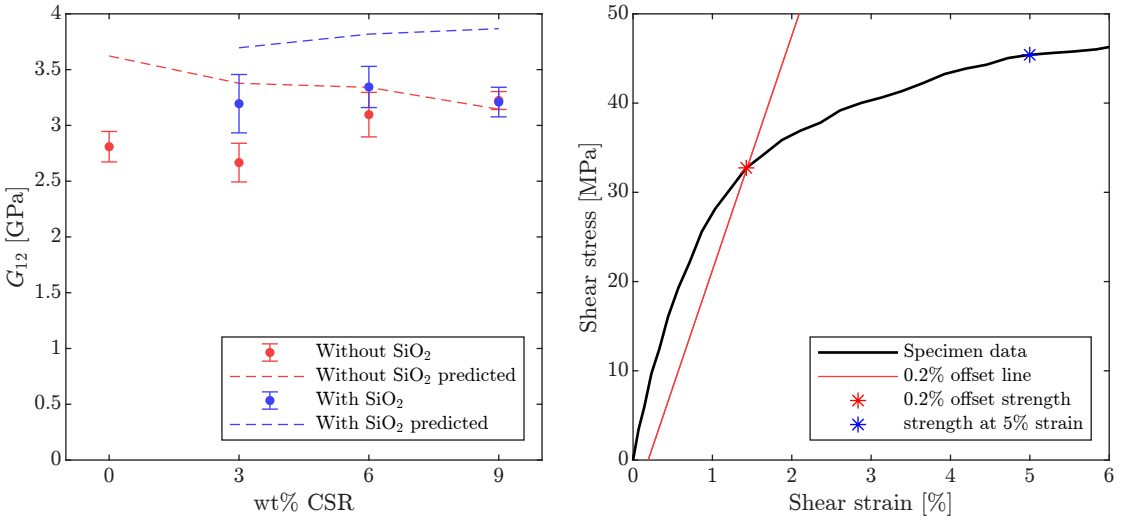


Figure 9.3: (a) Shear modulus versus wt% CSR, 45° direction. (b) Example shear stress versus shear strain including the 0.2% offset line and strength and the 5% strength.

The predicted values for shear modulus, G_{12}, are included in Table 9.2 and Figure 9.3 (a). The predicted shear modulus values are calculated using the matrix dominated cylindrical assemblage model described by Barbero [174] as follows:

$$G_{12} \cong G_{\mathrm{m}} \left(\frac{1 + v_{\mathrm{f}}}{1 - v_{\mathrm{f}}} \right) \tag{9.4}$$

where G_{m} is the shear modulus of the matrix calculated using the Young's modulus as follows:

$$G = \frac{E}{2(1 + \nu)} \tag{9.5}$$

where ν is the Poisson's ratio, taken here to be 0.33, similar to epoxies documented by Barbero [174].

It is clear that the addition of CSR into the laminate increases the shear modulus in a similar way to the 0° and 90° modulus values. However, unlike in the principal directions, the addition of silica does increase the shear modulus. From the bulk epoxy tensile results in chapter 4, it can be seen that the addition of silica increases the modulus of the CSR modified resins beyond that of the control resin. The shear modulus of the laminates is dominated by the shear modulus of the matrix. Hence,

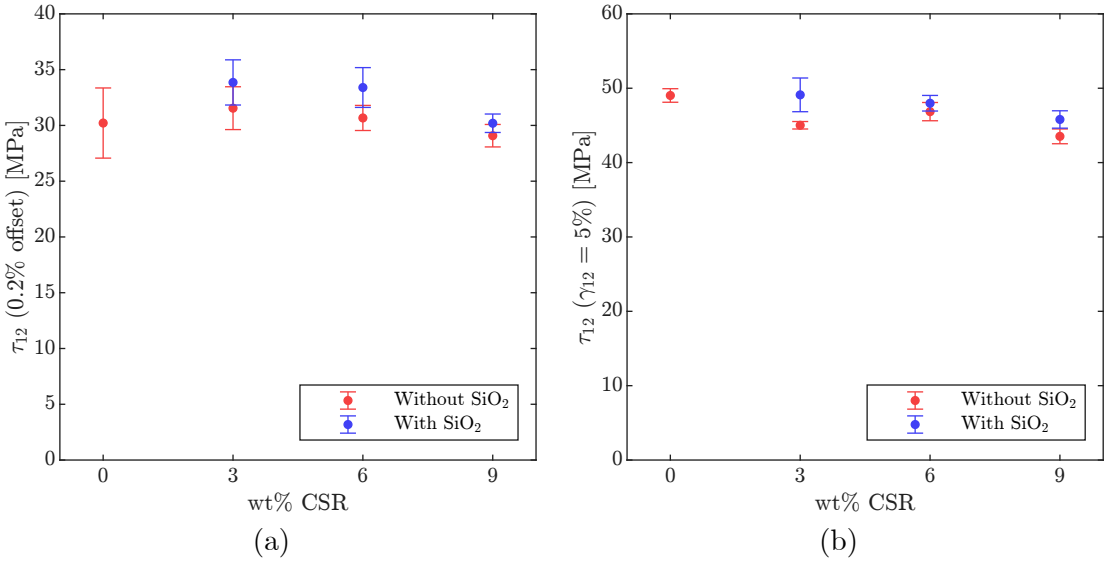


Figure 9.4: (a) Shear strength at a 0.2% offset versus wt% CSR, 45° direction. (b) Shear strength at a shear strain of 5% versus wt% CSR, 45° direction.

it is logical that the silica modified composite laminate samples have a higher shear modulus. The predicted values of shear modulus of the silica modified samples reflect this. Furthermore, the silica modified samples have higher values of 0.2% offset shear modulus and shear strength at 5% shear strain. It is surprising, however, that the solely CSR modified laminates have a higher shear modulus than the control laminate given the matrix dominated nature of this property. The tensile moduli of the matrices modified solely with CSR particles are lower than that of the control panel. As such, the predicted values of shear modulus of the laminates show a trend opposite to the experimentally measured values of the laminates. It is interesting to note that the predicted value of 9 wt% CSR modified shear modulus is close to the experimentally measured value while for laminates with a lower CSR content the discrepancy between measured and predicted values increases, with the model over predicting the modulus. It is likely that pre-existing microcracks are reducing the shear modulus of the laminates that have a low matrix toughness. The high toughness matrices are preventing these microcracks from affecting the moduli of the corresponding laminate and, as a result, achieve moduli closer to their predicted values.

9.3 DIC

DIC has been used throughout this chapter to measure strain. Foremost, DIC was used to construct virtual extensometers across the length of the specimens to

measure axial tensile strain. The use of DIC allowed the strain to be measured over a large gauge length of the sample, up to 80 mm, whereas a strain gauge typically measure strains over a small length. Considering the periodic nature of composite laminates, especially infusion manufactured laminates from stitched fabric containing tows, the strain across the sample will not be constant. As a result, measuring tensile strain over a large gauge length is preferable for an accurate and repeatable result. In addition to measuring simple tensile strain, DIC provides full field strain in any direction for the entire specimen. This strain is best visualised in a colour map such as the one shown at the top of Figure 9.5, where the major strain of the sample is shown over a range of 0-5%. When analysing the major strain of the samples, it became clear that the 0 and 3 wt% CSR exhibited a significant number of areas of high major strain than were observed in the 6 and 9 wt% CSR samples. Furthermore, these very high strain regions often correlated with small transverse cracks on the surface of the 90° laminates as displayed in Figure 9.6. The strain at which these cracks began to appear was at a local major strain of 3.75%. As a result, the major strain colour maps for the 90° samples were converted from a standard colour map to a binary colour map that differentiated areas above and below a major strain of 3.75% to allow for these areas to be measured. The globally applied tensile strain was 1.5% for all images, this strain allowed the samples to be directly compared as none of the samples had failed at this strain. Example binary colour maps are displayed in Figure 9.5. The percentage of the area of each specimen that was over the 3.75% threshold was calculated, these values are plotted in Figure 9.2 (b). It is clear that the 6 and 9 wt% CSR specimens exhibit less high strain areas and have a smaller surface area over the threshold strain.

A closer analysis of the 90° samples and the transverse cracks was carried out. Figure 9.6 is an example of an in depth analysis of an area containing transverse cracks in a 3 wt% CSR specimen. DIC colour maps of the specimen at varying zoom levels are presented, the top of the image concerns the specimen at a global strain of 1.5%. High strain regions are clear, within these areas, cracks are visible. It appeared that low strain regions were appearing adjacent to these cracks as the global strain increased. This is clear in the blue areas next to the cracked high strain regions. As a result, a section was taken through the specimen, a section allows numerical values of strain to be output along with the corresponding distance along the section. These strains are plotted in a graph of local strain versus distance along the section at 0.25% increments in global strain. The graph clearly shows

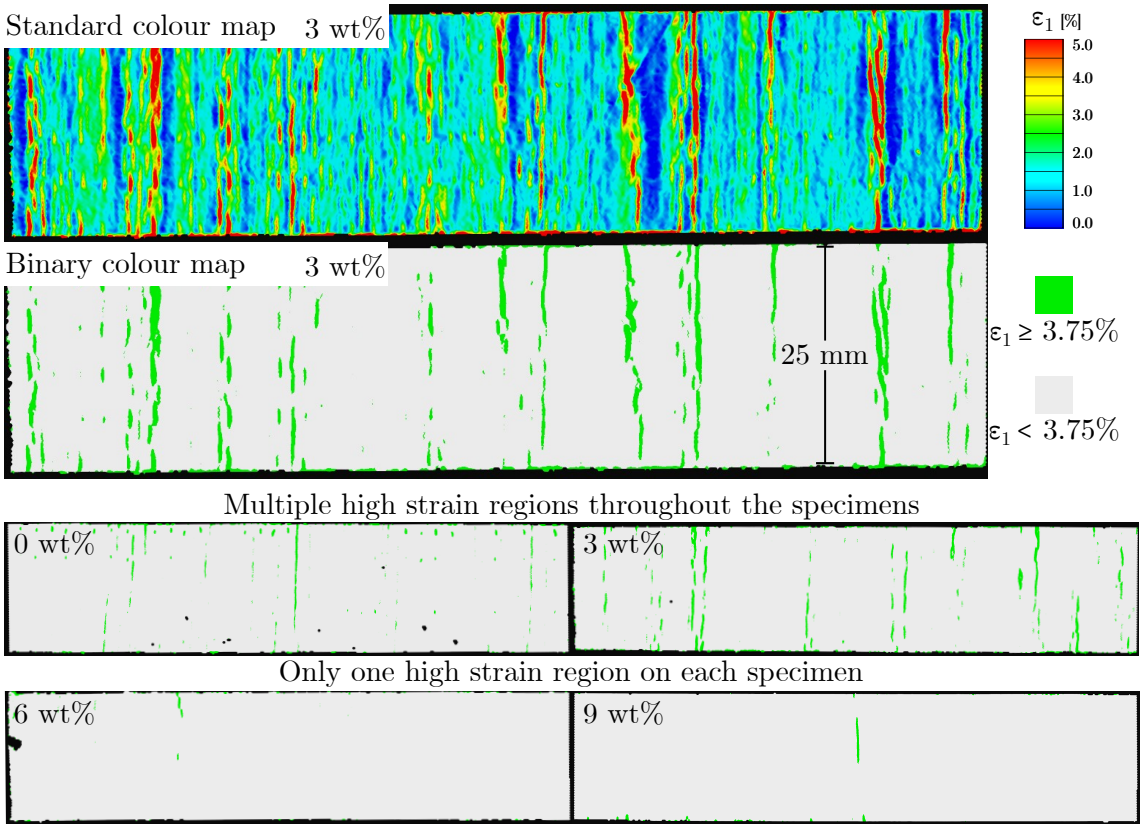


Figure 9.5: Example DIC of tensile specimens high strain region analysis at 1.5% global tensile strain. A standard colour map is shown followed by the corresponding binary colour map where the threshold strain is 3.75%. An example specimen from each wt% CSR is then shown. (Specimens and test direction are orientated horizontally across the page)

that the strain along the sample is initially constant with small deviations from the value of global strain, indicative of the composite nature of the laminate. As the globally applied strain increases beyond 0.75% the deviations in strain begin to increase along the section. Certain of these deviations increase preferentially to others, these are the locations of incipient microcracks. The strain at the crack sites reaches large values, the absolute value here is inconsequential as the material has already separated and so a local strain measurement is not valid but an artefact of the DIC measurement technique. An important observation from the graph is that either side of the high strain region, there are low strain regions significantly below the value of global strain. In fact, the strain can drop to zero or even register as negative in these regions. This reduction in stress is because the material next to it has failed and so is no longer effectively transferring stress along this surface ply, the region is stress shielded.

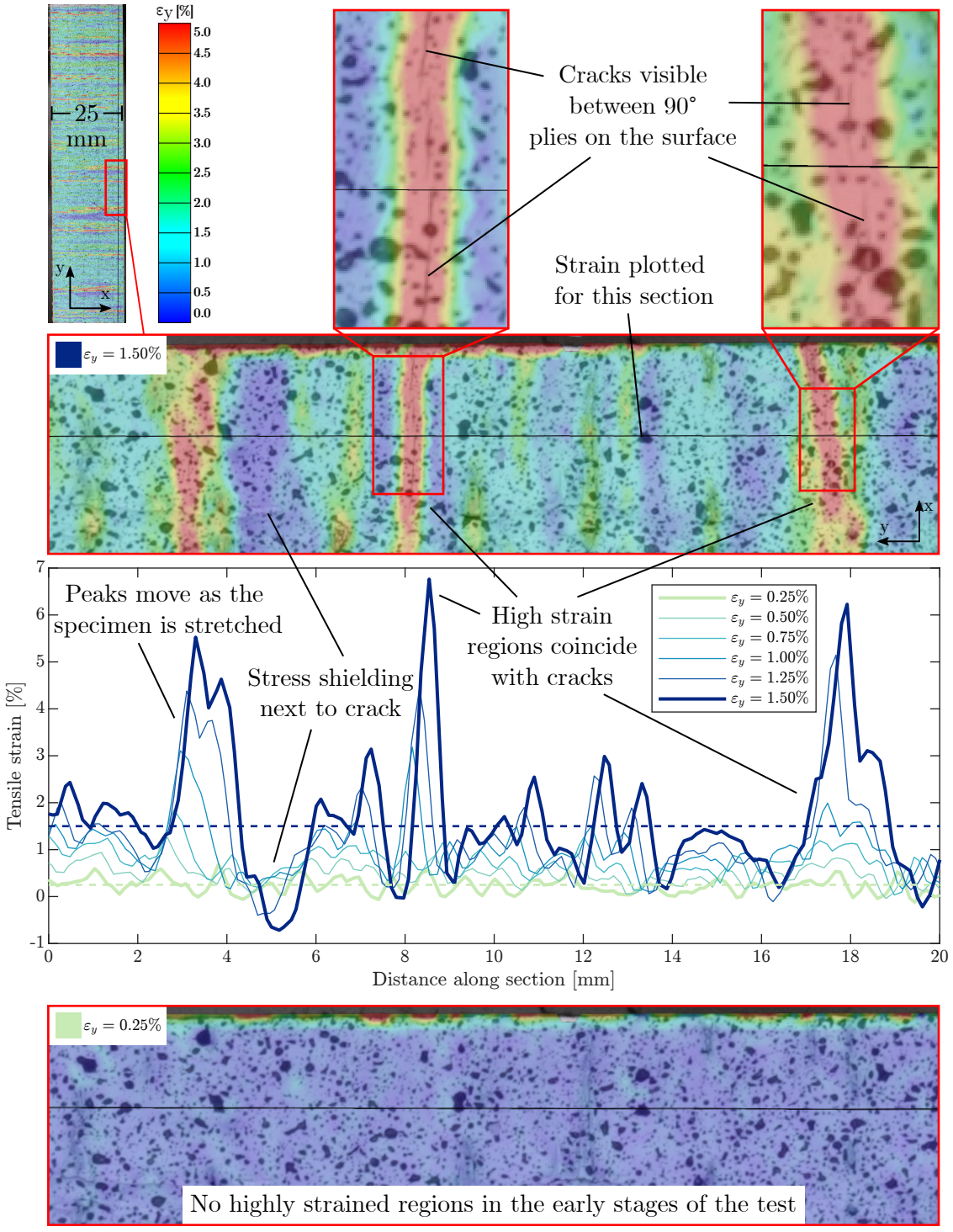


Figure 9.6: Example DIC analysis of a 3 wt% CSR tensile specimen with 90° tows on the surface. A standard colour map image is shown of the entire specimen showing where zoomed images are taken from. The black line on the colour maps represents a section where numerical values of strain have been output and plotted periodically at 0.25% increments of global tensile strain.

A similar analysis was carried out on a 90° specimen for each of the other CSR loadings. The section position was chosen to include areas of high strain and transverse cracks if they were present. For the 6 and 9 wt% CSR specimens, only one such region emerged in each specimen as seen in Figure 9.5. The resulting strain section plots are given in Figure 9.7. The differences between the specimens are clear, the 6 and 9 wt% CSR specimens exhibit one high strain region surrounded by smoother strain regions with strains similar to the globally applied strain. On the other hand, the control specimen has multiple high strain regions (and adjacent low strain, shielded, regions). The increased toughness of the highly CSR modified specimens reduces the extent of high strain regions and reduces the amount of transverse cracking. There is better stress transfer between matrix and fibre in the toughened composite laminates This explains the increase in modulus of the CSR modified samples as compared to the control sample.

The DIC of the 0° specimens also reveals interesting information beyond the global strain. Figure 9.8 includes a major strain colour map of a 0°, 3 wt% CSR specimen. For 0° samples, the fibres on the surface run parallel to the test direction. However, when the strain map is analysed by projecting the strain in the Z direction it is clear that the 90° tows below affect the strain in the 0° tows on top. The tows below cause undulations in the surface strain that have a spacing of 5 mm, the same spacing as the tows in the carbon fabric. High strain regions across the sample emerge similar to the high strain regions observed in the 90° samples previously. This implies that damage is initiating in the transverse ply below the surface. Damage in the transverse ply then causes cracks to appear between the 0° tows on the surface as seen in the zoomed images in Figure 9.8. The direction of the major strain in the detailed inset images show that the tows are separating as the microcracks form between them.

Figure 9.9 displays major strain colour maps for a 0°, 6 wt% CSR specimen. As in Figure 9.8, the 90° tows below the surface can be seen to affect the strain on the surface. The three colour maps correspond to the global strains labelled in the corner of each image. The final colour map is the last DIC image available prior to failure, an image of the failed specimen is included below. From the first colour map it is clear that one section of the gauge area experiences particularly high strains. Over the next two colour maps, one of the tows on the surface of the specimen begins to develop high strain regions and damage around it. The zoomed inset

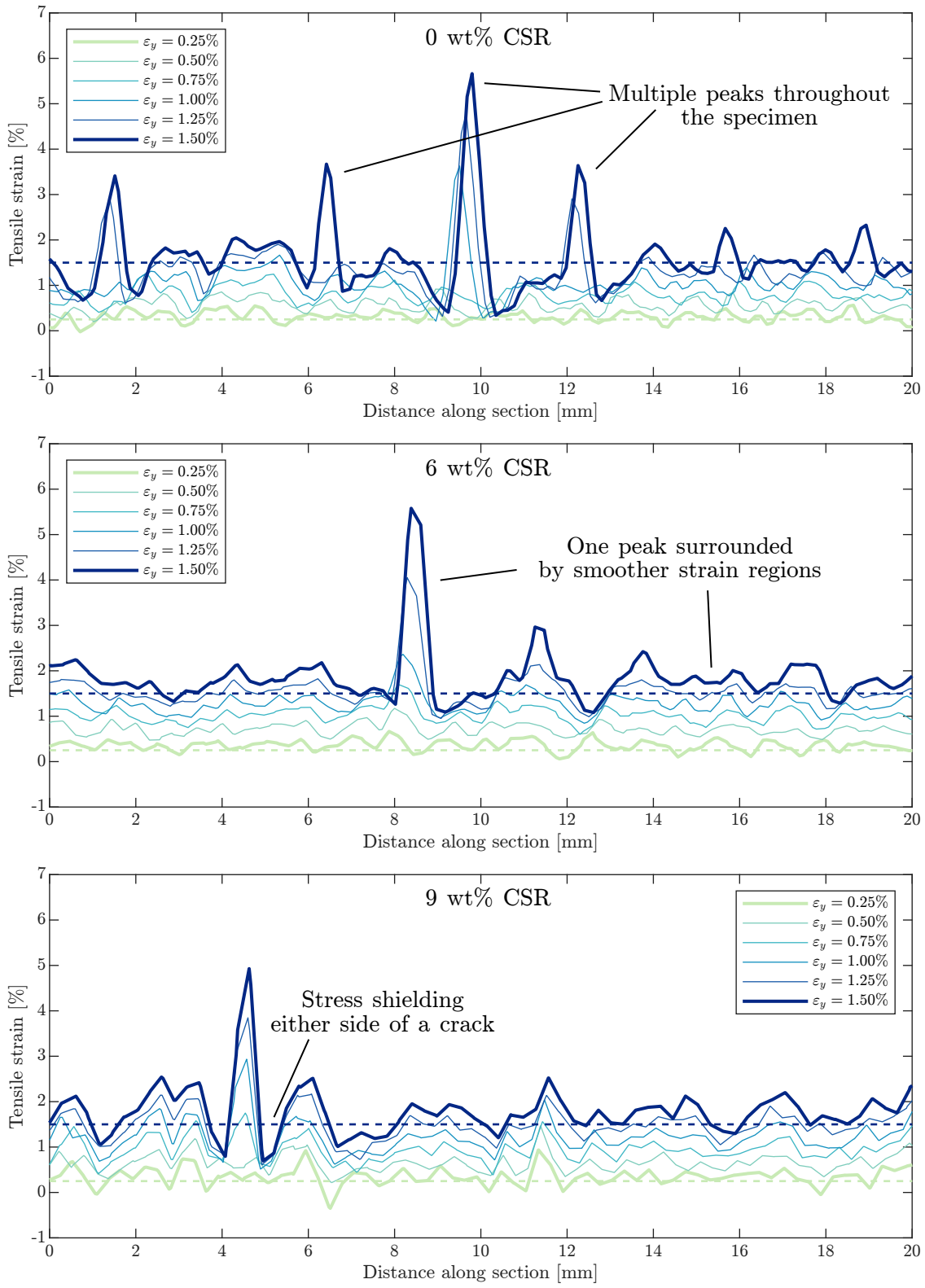


Figure 9.7: Example tensile strain graphs similar to the graph in Figure 9.6. The sections used to output the strain data were chosen to include a particularly high strain region. The strain is plotted periodically at 0.25% increments of global tensile strain.

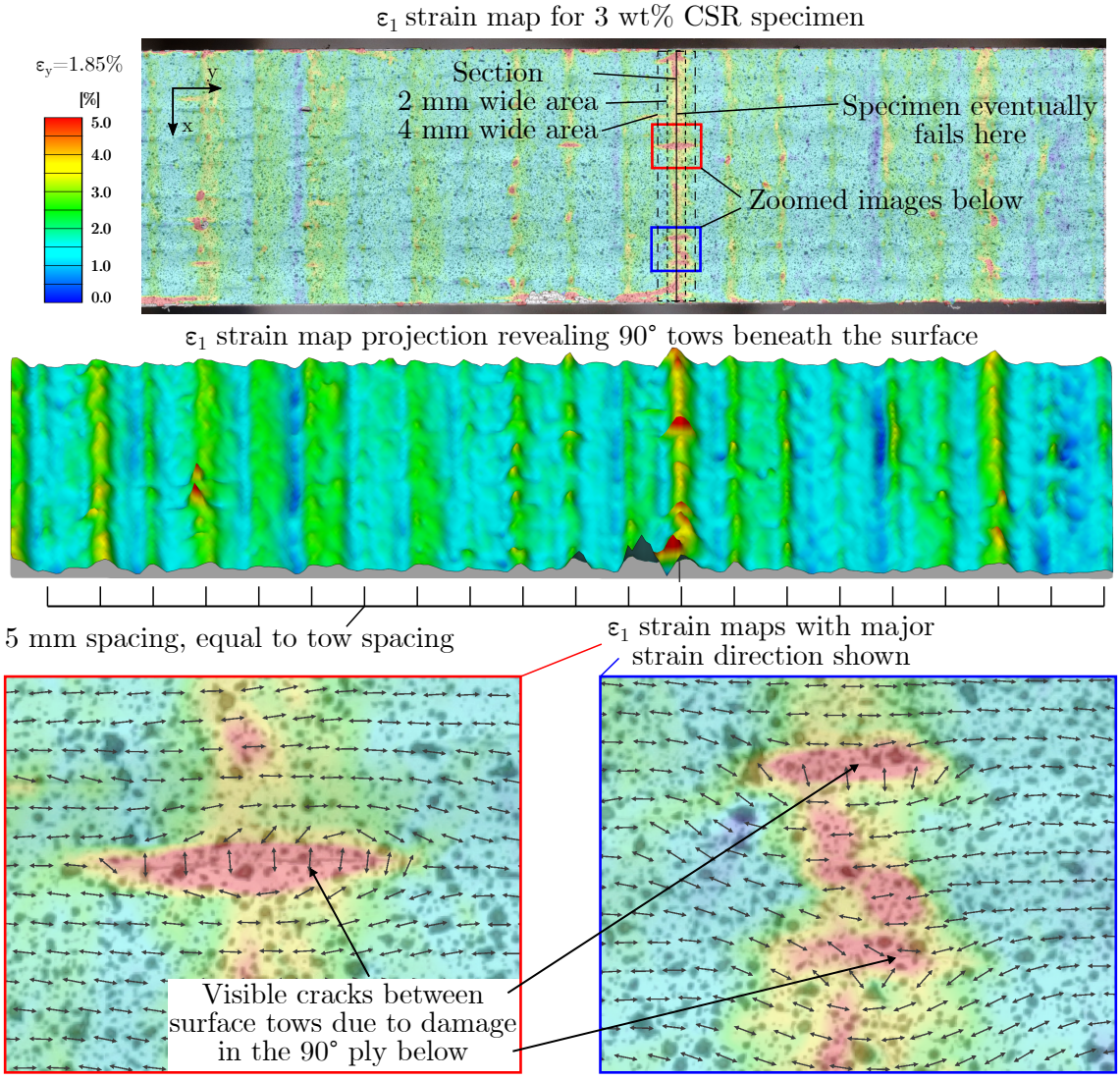


Figure 9.8: Example DIC analysis of a 3 wt% CSR tensile specimen with 0° tows on the surface. A standard colour map image is shown with the corresponding topographical projection below which reveals the position of the tows in the ply below. Zoomed images show cracks between tows on the surface due to damage in the ply below.

image shows the formation of microcracks along the tow. A stress shielded region can also be clearly observed immediately adjacent to the newly formed microcrack. This suggests that the tow is no longer loaded to its full capacity and has, in part, already failed as it is not transferring stress to the shielded blue area. The direction vectors of the major strain in the zoomed inset image clearly demonstrates that the tow is contracting as it is unloaded and pulling away from the surrounding loaded tows. Along this tow there is another high strain region at the other end of the specimen gauge area, this is likely where the tow has begun to fail at another location. The image of the failed specimen shows that the main failure of the laminate is located exactly where the original high strain section was recorded by

the DIC at a much earlier globally applied strain. Furthermore, it can be seen that the 0° tow that failed on the surface delaminated from the rest of the specimen. The DIC measurement technique has provided useful insight into the failure mechanisms that are not visible when simply using strain gauges to measure strain. The high strain damage regions are clear on the DIC full field strain map early in the loading when no difference can be ascertained in the global strain response.

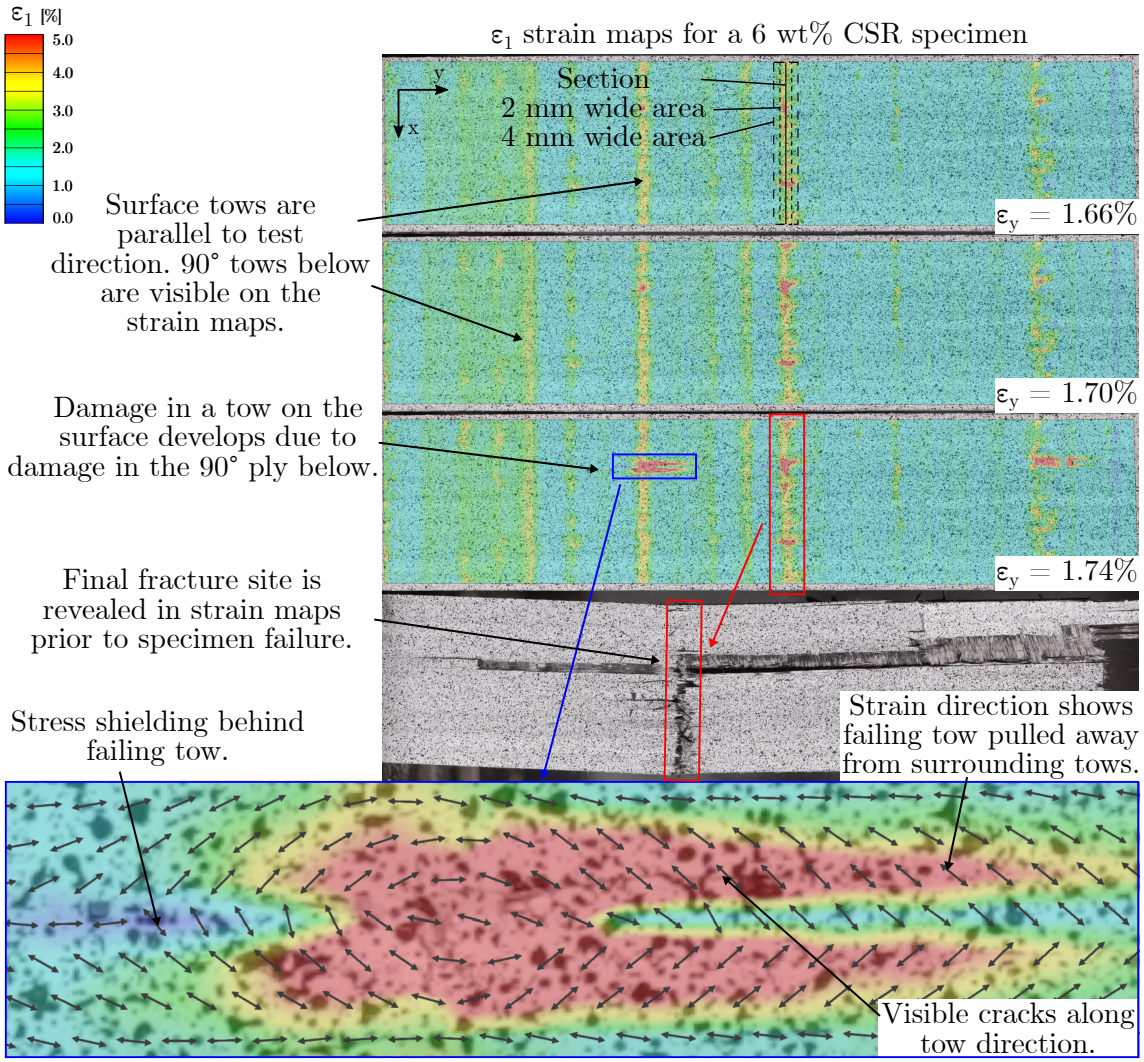


Figure 9.9: Example DIC analysis of a 6 wt% CSR tensile specimen with 0° tows on the surface. Standard colour map images are shown for three strains just prior to failure as severe damage development occurs. An image of the failed specimen is included. A zoomed image shows cracks along a failing tow on the surface and stress shielding.

On the first colour map in both Figure 9.8 and Figure 9.9 a section, a 2 mm area, and a 4 mm area have been highlighted. The tensile strain for these regions has been averaged and plotted against the sample tensile stress in Figure 9.10 along-

side the global tensile strain. In this respect they act as virtual strain gauges (or extensometers) with varying gauge lengths. The strain averaged over the different sized regions provides an insight into the onset of damage and the extent of the effect of the damaged region on the local modulus. Furthermore, it demonstrates how the measured value of strain tends towards the globally applied value of strain as the gauge length/area increases. In the 3 wt% CSR data in Figure 9.10 (a), the damaged section is immediately more compliant than the sample as a whole. This implies that there is some pre-existing damage in the sample prior to the test. At a stress of 350 MPa there is an inflection point where the damaged area becomes suddenly even more compliant. Interestingly, the damage area then becomes less compliant and the gradient (tangent modulus) increases throughout the remainder of the test. This is possibly due to local straightening of tows. In the 6 wt% CSR data in Figure 9.10 (b) the damage region is no more compliant than the sample as a whole at the beginning of the test. The inflection point for this specimen was observed at 600 MPa, a much higher stress than the 3 wt% CSR specimen. The increased matrix toughness of the 6 wt% CSR specimen prevents the damaged region from forming at lower stresses which is desirable. However, the compliance of the damaged region continues to increase throughout the remainder of the test until the specimen ultimately fails at the damage location.

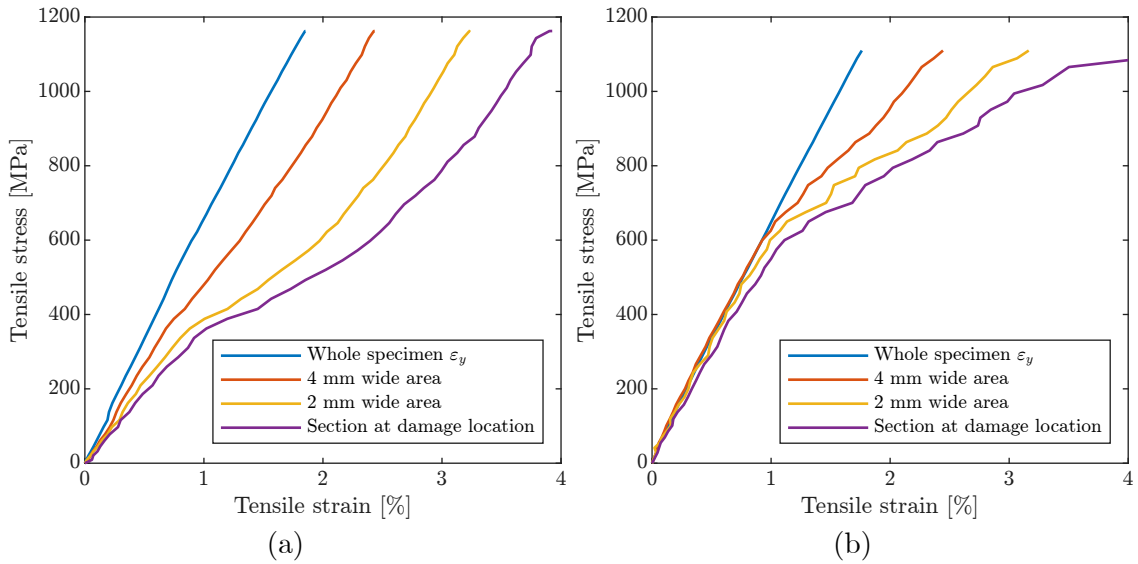


Figure 9.10: Example tensile stress versus strain graphs for the Section, 2 mm wide area, 4 mm wide area, and Whole specimen strain. (a) The 3 wt% CSR shown in Figure 9.8. (b) The 6 wt% CSR shown in Figure 9.9

9.4 Concluding remarks

This chapter has explored the use of digital image correlation for analysing simple laminate tensile tests. The laminate tensile tests were carried out to explore the effects of modifying the matrix of a CFRP laminate with CSR and silica nanoparticles. The tests reveal that CSR modification of the matrices increases the modulus of the laminates in the principal directions while the subsequent addition of silica has no additional effect. The highly modified 9 wt% CSR laminate achieved the highest modulus value, close to what would be expected based on the rule of mixtures calculations carried out. As less CSR was added, the modulus dropped due to the propagation of microcracks reducing the stress transfer between the matrix and the fibres. Literature has also shown that changing the interphase can affect the modulus of a laminate significantly. The transverse cracks became clear in DIC images as high strain regions and microscopic material separation even became visible. The areas of high strain were analysed and show that the 0 and 3 wt% CSR laminates exhibit far more areas of high strain and microcracking than the 6 and 9 wt% CSR laminates.

The in-plane shear tests revealed that the highly CSR modified panels exhibit higher shear modulus than the control panel. As with the tests in the principal direction, the shear modulus of the 9 wt% CSR laminate is close to the model predicted value. As less CSR is added to the laminate the measured value falls below the model predicted value. The addition of stiff silica particles increases the shear modulus as the shear modulus of the laminate is a matrix dominated property. The reason for the drop in modulus from the highly modified panels to the control is again due to the existence of microcracks in the matrix reducing the stress transfer between fibres and matrix. The differences in modulus are apparent from the beginning of the test. As a result, it it assumed that the cracks are present from the manufacturing process, either thermally or cure induced stresses. The highly CSR modified panels are better able to resist the formation and growth of process induced microcracks.

DIC has been used to analyse full field strain and extract strain data for sections and areas around damaged regions of the composite samples. The DIC has revealed the site of damage regions in the 90° tests in the form of transverse cracks. DIC is able to reveal the location of these damaged regions before any visible cracks are formed and significantly before ultimate failure of the sample. Analysing sec-

tions parallel to the test direction reveals low strain regions either side of transverse cracks, demonstrating the stress shielding in these regions. DIC reveals that the 6 and 9 wt% CSR laminates exhibit less high strain regions leading to visible cracks. For the 0° laminates, DIC reveals the location of the 90° tows below the surface in the form of undulations in strain. It is also clear from the DIC full field strain map that the damaged regions originate in the transverse ply below the surface in the 0° samples. The damage in the transverse ply below causes cracks to form between the 0° tows on the surface. When local axial strain is averaged over the damage region and plotted versus stress, inflection points become clear where damage either initiates or increases. This inflection point occurs at a higher stress in the 6 wt% CSR specimen than the 3 wt% CSR specimen.

The use of digital image correlation is a powerful tool revealing hitherto unreported micromechanisms of failure in ostensibly simple composite laminates.

Chapter 10

Conclusions and future work

10.1 Conclusions

Composite sandwich structures are used extensively across a wide range of industries for their high stiffness and strength-to-weight ratios. The brittle nature of these structures often prevents their full potential from being utilised. This thesis has investigated and improved the impact performance of carbon fibre-reinforced epoxy face sheet sandwich structures with epoxy foam cores.

The toughness of the core, the skin, and the skin-core bond have been improved. Alterations to improve the toughness of each of these components were conceived, applied, and tested in an isolated manner under static loading conditions. The most successful of these alterations were then utilised in full sandwich structures and tested under impact loading.

In addition, further studies were carried out to gain a more complete understanding of the materials used in this thesis. Epoxy foams were investigated over a range of densities, as a result, a transition in fracture performance has been identified. Architected polymers were studied with systematically varying bulk polymer properties. The outcome of this work has informed the design of toughened epoxy foams.

Tensile testing of composite laminates was carried out to investigate the effect of adding toughenners on the tensile properties of cross-ply laminates. Novel strain measurement techniques allowed micro cracks and small damage areas to be investigated. Toughenners were found to reduce the extent of these cracks and damage

areas. A detailed summary of the conclusions from each chapter are included in this section.

10.1.1 Impact response with toughened epoxy matrices

In this chapter the properties of CSR and silica modified bulk epoxies were characterised. The transfer of fracture performance from bulk polymer to CFRP laminate was analysed using DCB testing. Full sandwich structures were tested under impact loading and panel out-of-plane displacement and damage extent were measured and compared.

- The addition of CSR nanoparticles in the resin system used, caused a decrease in modulus similar to values anticipated by the Halpin-Tsai model. The silica nanoparticles increased the modulus past that of the unmodified system due to the use of a non-optimal silica density value during calculations. The addition of CSR caused a drop in UTS while silica nanoparticles had little additional effect. The modulus dropped from 2.96 ± 0.06 GPa to 2.57 ± 0.02 GPa at 9 wt% CSR. The UTS dropped from 73.1 ± 0.005 MPa to 51.8 ± 0.017 MPa at 9 wt% CSR and 17.2 wt% silica. The addition of CSR nanoparticles caused a significant increase in the fracture energies of bulk epoxy polymers while silica nanoparticles had a comparatively insignificant additional effect. The fracture energy increased from 188 ± 37 J/m^2 to 3459 ± 145 J/m^2 at 9 wt% CSR and 17.2 wt% silica.

- The use of CSR modified matrices was demonstrated to significantly enhance the Mode-I interlaminar fracture toughness of CFRP laminates. The transfer of toughness from the bulk epoxy polymers to the CFRP laminates in the form of initiation interlaminar fracture energies was limited due to space constraints between fibres. However, the steady-state propagation interlaminar fracture energies were enhanced through increasing CSR content as increased levels of fibre-bridging were induced. Interlaminar initiation and propagation fracture energies increased from 406 ± 61 J/m^2 and 996 ± 44 J/m^2 to 670 ± 44 J/m^2 and 1643 ± 72 J/m^2, respectively, at 9 wt% CSR and 17.2 wt% silica.

- A transition in failure mode in the impacted panels is clear between 3 and 6 wt% CSR. For 0 and 3 wt% CSR, increased core cracking occurs while for

6 and 9 wt% CSR, core cracking is replaced by large scale back face skin-core debonding. The interface appears tougher in the low CSR wt% panels, however, the energy of the projectile must be absorbed, and so increased core cracking is observed.

- The addition of 3 wt% CSR to the matrix of sandwich structures reduced back-face deflection and delamination within the front skin. Increasing to 6 and 9 wt% CSR caused increased deflection due to excessive drops in modulus and UTS outweighing toughening effects and rear face skin-core debonding. The subsequent addition of silica nanoparticles mitigated this drop in modulus and reduced deflection. Debonding failure occurring at the rear skin during impact has caused a higher back face deflection as the skin alone is less stiff than the skin with foam attached. Back face deflection reduced from 10.5 mm to 8.6 mm at 3 wt% CSR, it then increased to 11.2 at 9 wt% CSR. As a result of the findings in this project, it is likely that the optimal loading of CSR is 3 wt% to ensure skin and core remain attached whilst also providing some skin toughening benefits.

- It is likely that these results, such as the transition in failure mode between 3 and 6 wt% CSR are not widely applicable to any sandwich structure. The choice of resin infusion as a manufacturing process and the fact that the fracture toughness of the foam core is close to the interface toughness allowed this transition to occur. If a strong adhesive were used it is likely that sub-interface failure would be possible for all the matrix resins used in the current research. On the other hand, if a tougher or denser foam were used it is likely that interface failure would occur regardless of the properties of the matrix resin.

- The key findings are that mechanical properties can be tailored to dictate failure within the panel for a given impact event allowing maximum post-impact strength to be achieved. The toughness of all constituents and interfaces are important when considering the damage tolerance of a sandwich structure. If one element is toughened more than another, damage will be likely experienced in another element of the structure. An optimised structure will distribute damage in such a way as to maximise post-impact strength. It is considered that the techniques developed are very appropriate in optimising composite sandwich structures for transport, wind energy, and other applications.

10.1.2 Toughening of fibre-reinforced epoxy foam

In this chapter, low density fibre-reinforced epoxy foams containing short-cut carbon and aramid fibres were successfully synthesised for the first time in the literature. The effects of fibre type, length, and loading have been investigated. Compression and fracture properties were measured and compared to an unreinforced foam.

- Improvements in the fracture performance of epoxy foams have been achieved through the addition of these fibres. The incorporation of 5 PHR 0.75 mm aramid led to a maximum increase in fracture energy of 107% from 124 ± 13 J/m^2 to 256 ± 30 J/m^2.
- The main toughening mechanisms observed were fibre pull-out, fibre fracture and crack deflection and arrest.
- The addition of 2.5 PHR 0.75 mm aramid fibre and 0.6 mm carbon fibre both cause an increase in compressive yield strength of 10%, further additions cause a drop in strength.
- The addition of aramid fibre causes an increase in foam density of up to 16% from 175.1 ± 0.8 kg/m^3 to 203 ± 3.5 kg/m^3. Short carbon fibres only increased density up to 5% while 3 and 6 mm carbon fibres reduced the density of the as-blown foams by up to 2% due to large void formation.
- This investigation has deomonstrated that fibre reinforced epoxy foams can outperform their unreinforced counterparts with few drawbacks other than a slight increase in density and increased manufacturing complexity. There are more gains to be realised if longer fibres can be used to manufacture low density foams without large voids which reduce compressive strength. The presence of larger voids will also cause increased resin uptake during a resin infusion of skins or require more adhesive during bonded sandwich structure manufacture. For this reason, the most attractive option is to make use of short carbon and aramid fibres in epoxy foams.

10.1.3 Fracture properties of epoxy foam over a range of densities

This chapter details a systematic study of the effect of density on the fracture performance of epoxy foam. Material ranging from low-density foam to bulk polymer was investigated. The foam morphology was analysed and was linked to a transition in fracture properties. The compressive and tensile properties of the foam were also evaluated comprehensively.

- Eight foams were considered in this chapter with densities varying between 183-506 kg/m^3. The tensile and compressive modulus and strength were found to be reasonably well described by Gibson and Ashby models across their recommended validity ranges.

- Compressive yield strengths were measured between 2.33 ± 0.02 MPa and 17.34 ± 0.47 MPa. Compressive moduli varied between 86 ± 1 MPa and 516 ± 23 MPa.

- Tensile fracture strengths were measured between 1.67 ± 0.22 MPa and 14.23 ± 1.47 MPa. Tensile moduli varied between 113 ± 24 MPa and 936 ± 133 MPa.

- Fracture energy and toughness varied between 82 ± 15 J/m^2 and 931 ± 353 J/m^2, and 0.1 ± 0.01 MPa m$^{1/2}$ and 0.79 ± 0.12 MPa m$^{1/2}$, respectively.

- A critical foam density has been identified, above which the fracture energy is significantly higher than that of the base epoxy polymer. At densities lower than this, the fracture behaviour of the foam is consistent with the models proposed by Gibson and Ashby. The critical foam density for this epoxy polymer was identified as a relative density, ρ^*/ρ_s of 0.28. Notably, the transition from Gibson and Ashby behaviour to toughened behaviour occurs over a small density range.

- The data shows that the behaviour of the fracture toughness as a function of density, K^*_{Ic}, is well described by a sigmoidal function over the entire density range, including the fracture toughness of the bulk polymer.

- The relative density of the transition in fracture properties coincides with changes in foam morphology observed by SEM. Lower density foams below the transition in fracture toughness displayed evidence of a few large cells and

a wider cell size distribution. This wider cell size distribution appears to be the cause of the transition in fracture properties. Larger cell size distributions caused the premature failure of smaller cells at the crack front as larger cells are more compliant and do not carry a proportional amount of load. Larger cells also allow for cracks to propagate through low resistance paths within the foam. Interestingly, the tensile and compressive properties of the foam do not appear to be affected by cell morphology in the same way.

- It is proposed for applications where energy absorbing capabilities of the foam are critical, denser foams may be a more optimal choice, sacrificing a small gain in weight for a considerable gain in damage resistannce.

10.1.4 Skin-core debonding

In this chapter, the failure mode of skin-core debonding is isolated and analysed in detail. The SCB specimen was used to test this failure mode in a quasi static manner. The effect of matrix properties on the toughness of the skin-core bond was analysed. Two methods conceived to toughen this bond were evaluated. First, the machining of grooves in the foam core was tested. Second, the use of a fibre-reinforced foam was tested. Alongside standardised data reduction methods, a novel method of fitting test data to idealised fracture energy curves on a load versus displacement plot has been used to extract values from stick/slip debond failures.

- A change in failure mode was discovered during the impact testing in chapter 4. The same transition has been revealed in isolated debonding tests in this chapter. The panels containing 6 and 9 wt% CSR experienced interface failure, whereas, the unmodified and 3 wt% CSR panels experienced sub-interface core failure as the true interface in these panels is tougher than the foam core.

- Machining 1.5 mm grooves perpendicular to the crack direction in the surface of the foam core improves skin-core debond fracture energy by 50% from 170 ± 17 J/m^2 to 255 ± 47 J/m^2. The grooves result in a resin coated channel at the interface which deflects the crack, causing mixed mode fracture and an increase in crack length which both contribute to an increase in fracture energy. The deeper 1.5 mm grooves were more effective than the 0.75 mm grooves which measured a fracture energy of 194 ± 21 J/m^2.

- When used in a composite sandwich structure, 0.75 mm 2.5 PHR aramid fibre-reinforced foam improves skin-core initiation and propagation fracture energy by 30 and 50% from 231 ± 43 J/m^2 to 301 ± 52 J/m^2 and from 277 ± 38 J/m^2 to 416 ± 24 J/m^2, respectively. The same foam shows improved fracture energy in SENB testing and improved compressive properties in chapter 5. The same toughening mechanisms observed in the SENB specimens there are causing an improvement to the skin-core bond in this chapter. The introduction of the fibres gives rise to extrinsic toughening mechanisms and R-curve behaviour.

10.1.5 Impact response with combined toughening mechanisms

In this chapter, the most successful toughening mechanisms explored in the previous chapters were combined in sandwich structures. These sandwich structures were impact tested to evaluate the maximum performance increase the toughening mechanisms provided over the control. The three toughening mechanisms were, 3 wt% CSR toughened skin matrix, 2.5 PHR 0.75 mm aramid fibre-reinforced foam core, and 1.5 mm deep 3 mm wide 13 mm spacing grid of grooves in the foam core. A displacement test and a perforation test were carried out on each panel type.

- For the control foam core panels in the displacement tests, employing the grooves and 3 wt% CSR panel modifications reduced the maximum displacement from 13.2 mm to 12.4 mm and 11.9 mm, respectively. The combination of both of these panel modifications provides the best improvement over the control panel with a reduction to 11.1 mm.

- Reinforcing the core with short cut aramid fibres is the dominant panel modification in this research. All of the aramid panels performed as well or better than the control foam panels. The aramid core caused less core cracking to occur.

- The machined grooves appear to toughen the interface in a similar manner to the SCB specimens tested in chapter 7, with skin-core debond cracks travelling around the grooves in the foam. However, adding aramid to the core caused some skin-core debond cracks to pass through the resin lined groves due to the increased fracture energy of the core and increased strength of the bond between the foam and the resin.

- As with the displacement tests, the panel modifications improved the performance of the control foam core panels in the perforation tests. The combination of the grooves and the 3 wt% CSR was once again the best performing of the control foam core panels with an increase in energy absorbed from 309 J to 346 J.
- Aramid reinforcement caused a significant improvement in some of the aramid foam core panels compared to the control panel. One of the panels resisted perforation while another absorbed 99.8% of the energy of the projectile.
- The aramid foam core panels had no core cracking apart from the one panel that resisted perforation.
- The sequence of damage events was key in determining if a panel absorbed a large amount of energy and experienced a large amount of damage or absorbed less energy and had correspondingly less damage.

Overall the panel modifications all provided some benefits over the control panel. However, the aramid foam cores provided the only significant improvement to impact performance. The modifications were chosen due to their performance in previous chapters detailing previous testing. The 3 wt% CSR resin has performed well in DCB testing and previous impact testing. The grooves performed well in SCB testing. The aramid fibre-reinforced cores performed well in SENB testing and SCB testing. This research shows that coupon testing of sandwich structure materials and interfaces can be used to chose materials and panel modification strategies to maximise the performance of a sandwich structure with some success.

10.1.6 DIC of laminate tensile testing

This chapter detailed an investigation into the effects of modifying the matrix resin of a CFRP laminate on its tensile properties. Novel DIC strain measurement techniques revealed important information regarding microcracking and damage areas.

- The tensile tests revealed that CSR modification of the matrices increases the modulus of the laminates in the principal directions while the subsequent addition of silica has no additional effect.
- The modulus varied from 54.3 $\pm$ 2.7 GPa for the control laminate to 70.1 $\pm$ 3.5 GPa for a 9 wt% CSR laminate.

- The highly modified 9 wt% CSR laminate achieved a modulus value close to what would be expected based on the rule of mixtures calculations carried out.
- As less CSR was added, the modulus dropped due to the propagation of microcracks reducing the stress transfer between the matrix and the fibres. Literature has also shown that changing the interphase can affect the modulus of a laminate significantly.
- The transverse cracks became clear in DIC images as high strain regions and microscopic material separation even became visible. The areas of high strain were analysed and show that the 0 and 3 wt% CSR laminates exhibit far more areas of high strain and cracking than the 6 and 9 wt% CSR laminates.
- The in-plane shear tests revealed that the highly CSR modified panels exhibit higher shear modulus than the control panel. The values varied from 2.81 ± 0.14 GPa for the control laminate to 3.34 ± 0.18 GPa for a 6 wt% CSR 11.7 wt% silica laminate.
- Like the tests in the principal direction, the shear modulus of the 9 wt% CSR laminate is close to the predicted value. As less CSR is added to the laminate the measured value falls below the predicted value.
- The addition of stiff silica particles increases the shear modulus as the shear modulus of the laminate is a matrix dominated property.
- The reason for the drop in modulus from the highly modified panels to the control is again due to cracks in the matrix reducing the stress transfer between the fibres and the matrix.
- The differences in modulus are apparent from the beginning of the test. As a result, it it assumed that the cracks are present from manufacturing. The highly CSR modified panels are able to resist any growth in these cracks thus limiting the negative effects.
- DIC has been used to analyse full field strain and extract strain data for sections and areas around damage regions.
- The DIC has revealed the site of damage regions in the 90° tests in the form of transverse cracks. DIC is able to reveal the location of these damage regions before any visible cracks are formed.

- Analysing sections parallel to the test direction reveals low strain regions either side of transverse cracks, demonstrating the stress shielding of these regions.
- DIC reveals that the 6 and 9 wt% CSR laminates exhibit less high strain regions leading to visible cracks.
- For the 0° laminates, DIC reveals the location of the 90° tows below the surface in the form of undulations in strain. It is also clear from the DIC that the damage regions originate in the transverse ply below the surface in the 0° samples. The damage in the transverse ply below causes cracks to form between the 0° tows on the surface.
- When local axial strain is averaged over the damage region and plotted against stress, inflection points become clear where damage increases or initiates. This inflection point occurs at a higher stress in the 6 wt% CSR specimen than the 3 wt% CSR specimen.
- Overall the toughening of CFRP laminates increases the performance in tensile tests. Damage is delayed and the modulus is increased compared to the untoughened laminates.

10.1.7 Final remarks

The work presented in this thesis has shown that the impact performance of composite sandwich structures can be improved in a systematic manner.

The method shown here involved identifying damage types from early impact tests while modifying one aspect of the structure. In this case toughening the sandwich skin matrix was evaluated. It was realised that considering the performance of all the constituents and interfaces simultaneously is crucial to improving performance. Damage will occur elsewhere if one aspect of the structure is toughened disproportionately.

Once the damage types had been established, the areas where damage occurs could be modified. Having toughened the skin, the core and the skin-core interface remained to be improved. Following the realisation that the impact performance of the sandwich must be considered as a whole, it was decided to first isolate and im-

prove the individual components under static testing.

The core was improved through short-fibre reinforcement. Low density fibre reinforced epoxy foams were synthesised for the first time in the literature. SENB testing showed significant improvements. The skin-core bond was improved through the use of a fibre-reinforced foam and through the machining of grooves in the core. These improvements were all combined to achieve some improvements in the impact performance of the sandwich structures in the second round of impact testing. The short aramid fibre-reinforced core provided the only significant improvement in impact performance.

Throughout this thesis, further studies were carried out to gain a more complete understanding of the materials used. Epoxy foams were investigated over a range of densities, as a result, a transition in fracture performance has been identified. Tensile testing of composite laminates was carried out to investigate the effect of adding tougheners on the tensile properties. Novel strain measurement techniques allowed micro cracks and small damage areas to be investigated. Tougheners were found to reduce the extent of these cracks and damage areas. Architected polymers were studied with systematically varying bulk polymer properties. The outcome of this work has informed the design of toughened epoxy foams.

10.2 Recommendations for future work

Over the course of this project, some potential areas of future research have emerged, as well as some areas that could be studied further. These areas are discussed in this section.

- Testing sandwich structures with varying thicknesses and aspect ratios would usefully extend the work carried out in this thesis. Different sandwich thicknesses will require different toughening mechanisms, especially when considering groove depth.
- Extending the testing of the sandwich structures to include static tests such as three or four-point-bend testing. This testing would provide useful information regarding the effect of toughening mechanisms on damage limitation under static loading.

- Including post-impact strength testing of the sandwich structures such as edge-wise compression. A useful metric for assessing the damage resistance of a sandwich structure would be to measure the failure load of an impacted section.

- It was discovered in chapter 6 that a transition in fracture performance exists in the epoxy foam. The transition occurs at a higher density than the foams used in the sandwich structures in this research. It would be interesting to assess whether using a higher density foam, in order to benefit from this transition to a higher fracture energy, would be beneficial despite the increase in weight.

- Following on from the findings of chapter 5, foams reinforced with long fibres which do not contain large voids would likely perform very well. A method to manufacture these foams would need to be developed.

- In chapter 6 the morphology of the foam was linked to a transition in fracture performance. Lower density foams below the transition in fracture toughness displayed evidence of a few large cells and a wider cell size distribution. It would be interesting to develop a method to manufacture foams at similar densities with systematically varying cell size distributions. In this way the fracture performance of the foams may be improved for a given density.

- The research in chapter 6 resulted in the development of an empirical fit for the fracture energy of foam from low density to bulk polymer. However, it was not possible to manufacture foams to cover the full range of densities. A number of high density foams would need to be manufactured to ensure this fit accurately represents the full range of densities.

- The large thickness of the laminates tested in chapter 9 often resulted in the tabs failing in the grips before the specimens. This prevented the failure strength of the laminates from being evaluated. Thinner laminates would break at lower loads before the tabs failed and would enable failure strengths to be compared.

References

[1] G. Irven, A. Duncan, A. Whitehouse, D. Carolan, A. D. Fergusson, and J. P. Dear. Impact response of composite sandwich structures with toughened matrices. *Materials and Design*, 203:109629, 5 2021.

[2] G. Irven, D. Carolan, A. Fergusson, and J. P. Dear. Fracture performance of epoxy foam: Low density to bulk polymer. *Polymer*, 261:125420, 11 2022.

[3] G. Irven, D. Carolan, A. Fergusson, and J. P. Dear. Fracture performance of fibre-reinforced epoxy foam. *Composites Part B: Engineering*, 250:110433, 2 2023.

[4] G. Irven, D. Carolan, A. Fergusson, and J. P. Dear. Digital image correlation of cross-ply laminates in tension to reveal microcracking. *Composite Structures*, 319:117148, 9 2023.

[5] G. Irven, A. Whitehouse, D. Carolan, A. Fergusson, and J. P. Dear. Toughening of face-sheet core bonds in sandwich structures. *Engineering Fracture Mechanics*, 290:109498, 9 2023.

[6] G. Irven, A. Duncan, E. Rolfe, D. Carolan, A. D. Fergusson, and J. P. Dear. Impact response of composite sandwich structures with toughened epoxy matrices. In *International Conference on Composite Materials 22*, pages 1895–1906, Melbourne, 2019. Engineers Australia.

[7] F. C. Campbell. *Structural Composite Materials*. ASM International, Ohio, 2010.

[8] Boeing 787 Dreamliner. *www.boeing.com/commercial/aeromagazine*. 2021.

[9] SAAB Visby-class corvette. *www.saab.com/products/visby-class-corvette*. 2021.

[10] J. K. Paik and A. K. Thayamballi. *Ultimate limit state design of steel-plated structures*. John Wiley & Sons, Chichester, 2003.

[11] F . J. Plantema. *Sandwich Construction: The Bending and Buckling of Sandwich Beams, Plates and Shells*. Number 1. John Wiley and Sons Inc., New

York, 1966.

[12] H. G. Allen. *Analysis and Design of Structural Sandwich Panels*. Pergamon Press, Oxford, 1969.

[13] D. Zenkert. *An Introduction to Sanwich Contruction*. Engineering Materials Advisory Services, 1995.

[14] M. Kelly, H. Arora, A. Worley, M. Kaye, P. D. Linz, P. A. Hooper, and J. P. Dear. Sandwich Panel Cores for Blast Applications: Materials and Graded Density. *Experimental Mechanics*, 56(4):523–544, 4 2016.

[15] E. Rolfe, R. Quinn, G. Irven, D. Brick, J. P. Dear, and H. Arora. Underwater blast loading of partially submerged sandwich composite materials in relation to air blast loading response. *International Journal of Lightweight Materials and Manufacture*, 3(4):387–402, 12 2020.

[16] L. J. Gibson and M. F. Ashby. *Cellular Solids*. Cambridge University Press, 1997.

[17] C. A. Steeves and N. A. Fleck. Collapse mechanisms of sandwich beams with composite faces and a foam core, loaded in three-point bending. Part I: Analytical models and minimum weight design. *International Journal of Mechanical Sciences*, 46(4):561–583, 4 2004.

[18] C. A. Steeves and N. A. Fleck. Collapse mechanisms of sandwich beams with composite faces and a foam core, loaded in three-point bending. Part II: Experimental investigation and numerical modelling. *International Journal of Mechanical Sciences*, 46(4):585–608, 4 2004.

[19] E. Rolfe, C. Kaboglu, R. Quinn, P. A. Hooper, H. Arora, and J. P. Dear. High Velocity Impact and Blast Loading of Composite Sandwich Panels with Novel Carbon and Glass Construction. *Journal of Dynamic Behavior of Materials*, 4(3):359–372, 9 2018.

[20] V. Koissin, V. Skvortsov, S. Krahmalev, and A. Shilpsha. The elastic response of sandwich structures to local loading. *Composite Structures*, 63(3-4):375–385, 2 2004.

[21] V. Rizov and A. Mladensky. Mechanical behavior of composite sandwich structures subjected to low velocity impact - Experimental testing and finite element modeling. *Polymers and Polymer Composites*, 16(4):233–240, 2008.

[22] C. Kaboglu, L. Yu, I. Mohagheghian, B. R. K. Blackman, A. J. Kinloch, and J. P. Dear. Effects of the core density on the quasi-static flexural and ballistic performance of fibre-composite skin/foam-core sandwich structures. *Journal of Materials Science*, 53(24):16393–16414, 12 2018.

[23] N. Domun, C. Kaboglu, K. R. Paton, J. P. Dear, J. Liu, B. R. K. Blackman, G. Liaghat, and H. Hadavinia. Ballistic impact behaviour of glass fibre reinforced polymer composite with 1D/2D nanomodified epoxy matrices. *Composites Part B: Engineering*, 167:497–506, 6 2019.

[24] G. B. Chai and S. Zhu. A review of low-velocity impact on sandwich structures. In *Proceedings of the Institution of Mechanical Engineers, Part L: Journal of Materials: Design and Applications*, volume 225, pages 207–230, 2011.

[25] S. Abrate. *Impact on Composite Structures*, volume 108. Cambridge University Press, Cambridge, 1998.

[26] I. Baran and W. Weijermars. Residual bending behaviour of sandwich composites after impact. *Journal of Sandwich Structures and Materials*, 22(2):402–422, 2018.

[27] R. Bai, J. Guo, Z. Lei, D. Liu, Y. Ma, and C. Yan. Compression after impact behavior of composite foam-core sandwich panels. *Composite Structures*, 225:111181, 10 2019.

[28] Y. Chen, S. Hou, K. Fu, X. Han, and L. Ye. Low-velocity impact response of composite sandwich structures: Modelling and experiment. *Composite Structures*, 168:322–334, 2017.

[29] R. Nasirzadeh and A. R. Sabet. Study of foam density variations in composite sandwich panels under high velocity impact loading. *International Journal of Impact Engineering*, 63:129–139, 1 2014.

[30] X. Huo, H. Liu, Q. Luo, G. Sun, and Q. Li. On low-velocity impact response of foam-core sandwich panels. *International Journal of Mechanical Sciences*, 181:105681, 9 2020.

[31] D. Feng and F. Aymerich. Effect of core density on the low-velocity impact response of foam-based sandwich composites. *Composite Structures*, 239:112040, 5 2020.

[32] Y. Zhu and Y. Sun. Dynamic response of foam core sandwich panel with composite facesheets during low-velocity impact and penetration. *International Journal of Impact Engineering*, 139:103508, 5 2020.

[33] J. Zhou, M. Z. Hassan, Z. Guan, and W. J. Cantwell. The low velocity impact response of foam-based sandwich panels. *Composites Science and Technology*, 72(14):1781–1790, 9 2012.

[34] H. Wang, K. R. Ramakrishnan, and K. Shankar. Experimental study of the medium velocity impact response of sandwich panels with different cores. *Materials & Design*, 99:68–82, 6 2016.

[35] T. A. Anderson. An investigation of SDOF models for large mass impact on sandwich composites. *Composites Part B: Engineering*, 36(2):135–142, 3 2005.

[36] P. Feraboli and K. T. Kedward. A new composite structure impact performance assessment program. *Composites Science and Technology*, 66(10):1336–1347, 2006.

[37] B. L. Buitrago, C. Santiuste, S. Sánchez-Sáez, E. Barbero, and C. Navarro. Modelling of composite sandwich structures with honeycomb core subjected to high-velocity impact. *Composite Structures*, 92(9):2090–2096, 8 2010.

[38] N. K. Naik, P. Shrirao, and B. C. K. Reddy. Ballistic impact behaviour of woven fabric composites: Parametric studies. *Materials Science and Engineering A*, 412(1-2):104–116, 12 2005.

[39] D. Carolan, A. Ivankovic, A. J. Kinloch, S. Sprenger, and A. C. Taylor. Toughening of epoxy-based hybrid nanocomposites. *Polymer*, 97:179–190, 2016.

[40] D. Carolan, A. Ivankovic, A. J. Kinloch, S. Sprenger, and A. C. Taylor. Toughened carbon fibre-reinforced polymer composites with nanoparticle-modified epoxy matrices. *Journal of Materials Science*, 52(3):1767–1788, 2017.

[41] R. A. Pearson and A. F. Yee. Influence of particle size and particle size distribution on toughening mechanisms in rubber-modified epoxies. *Journal of Materials Science*, 26(14):3828–3844, 7 1991.

[42] F. Lu, W. J. Cantwell, and H. H. Kausch. The role of cavitation and debonding in the toughening of core-shell rubber modified epoxy systems. *Journal of Materials Science*, 32(11):3055–3059, 1997.

[43] J. Chen, A. J. Kinloch, S. Sprenger, and A. C. Taylor. The mechanical properties and toughening mechanisms of an epoxy polymer modified with polysiloxane-based core-shell particles. *Polymer*, 54(16):4276–4289, 7 2013.

[44] D. Quan and A. Ivankovic. Effect of core-shell rubber (CSR) nano-particles on mechanical properties and fracture toughness of an epoxy polymer. *Polymer*, 66:16–28, 6 2015.

[45] V. Cooper, A. Ivankovic, A. Karac, D. McAuliffe, and N. Murphy. Effects of bond gap thickness on the fracture of nano-toughened epoxy adhesive joints. *Polymer*, 53(24):5540–5553, 11 2012.

[46] A. J. Kinloch, S. J. Shaw, D. A. Tod, and D. L. Hunston. Deformation and fracture behaviour of a rubber-toughened epoxy: 1. Microstructure and fracture studies. *Polymer*, 24(10):1341–1354, 10 1983.

[47] A. F. Yee and R. A. Pearson. Toughening mechanisms in elastomer-modified epoxies - Part 1 Mechanical studies. *Journal of Materials Science*, 21(7):2462–

2474, 7 1986.

[48] Y. Huang and A. J. Kinloch. Modelling of the toughening mechanisms in rubber-modified epoxy polymers. *Journal of Materials Science*, 27(10), 1992.

[49] Y. Huang and A. J. Kinloch. Modelling of the toughening mechanisms in rubber-modified epoxy polymers - Part II A quantitative description of the microstructure-fracture property relationships. *Journal of Materials Science*, 27(10):2763–2769, 1 1992.

[50] R. A. Pearson and A. F. Yee. Toughening mechanisms in elastomer-modified epoxies - Part 2 Microscopy studies. *Journal of Materials Science*, 21(7):2475–2488, 7 1986.

[51] A. F. Yee, Dongming Li, and Xiaowei Li. The importance of constraint relief caused by rubber cavitation in the toughening of epoxy. *Journal of Materials Science*, 28(23):6392–6398, 12 1993.

[52] L. Marșavina and E. Linul. Fracture toughness of rigid polymeric foams: A review. *Fatigue and Fracture of Engineering Materials and Structures*, 43(11):2483–2514, 11 2020.

[53] W. Song, G. Konstantellos, D. Li, and K. Y. Lee. Short carbon fibre-reinforced epoxy foams with isotropic cellular structure and anisotropic mechanical response produced from liquid foam templates. *Composites Science and Technology*, 184, 11 2019.

[54] M. V. Alonso, M. L. Auad, and S. R. Nutt. Short-fiber-reinforced epoxy foams. *Composites Part A: Applied Science and Manufacturing*, 37(11):1952–1960, 11 2006.

[55] M. V. Alonso, M. L. Auad, and S. R. Nutt. Modeling the compressive properties of glass fiber reinforced epoxy foam using the analysis of variance approach. *Composites Science and Technology*, 66(13):2126–2134, 10 2006.

[56] T. C. Cotgreave and J. B. Shortall. Failure Mechanisms in Fibre Reinforced Rigid Polyurethane Foam. *Journal of Cellular Plastics*, 13(4):240–244, 7 1977.

[57] T. C. Cotgreave and J. B. Shortall. The mechanism of reinforcement of polyurethane foam by high-modulus chopped fibres. *Journal of Materials Science*, 12(4):708–717, 4 1977.

[58] T. C. Cotgreave and J. B. Shortall. The fracture toughness of reinforced polyurethane foam. *Journal of Materials Science*, 13(4):722–730, 1978.

[59] M. J. Carling. *Fracture Mechanics of Short Fibre Composites*. PhD thesis, Imperial College London, 1988.

[60] A. A. Desai, S. R. Nutt, and M. V. Alonso. Modeling of hybrid composite

foams. *Journal of Cellular Plastics*, 46(2):113–128, 3 2010.

[61] A. A. Desai, M. L. Auad, H. Hongbin Shen, and S. R. Nutt. Mechanical behavior of hybrid composite phenolic foam. *Journal of Cellular Plastics*, 44(1):15–36, 1 2008.

[62] H. Shen and S. R. Nutt. Mechanical characterization of short fiber reinforced phenolic foam. *Composites Part A: Applied Science and Manufacturing*, 34(9):899–906, 9 2003.

[63] H. Shen, A. J. Lavoie, and S. R. Nutt. Enhanced peel resistance of fiber reinforced phenolic foams. *Composites Part A: Applied Science and Manufacturing*, 34(10):941–948, 10 2003.

[64] S. T. Cholake, G. Moran, B. Joe, Y. Bai, R. K. Singh Raman, X. L. Zhao, S. Rizkalla, and S. Bandyopadhyay. Improved Mode I fracture resistance of CFRP composites by reinforcing epoxy matrix with recycled short milled carbon fibre. *Construction and Building Materials*, 111:399–407, 5 2016.

[65] A. R. Ravindran, R. B. Ladani, S. Wu, A. J. Kinloch, C. H. Wang, and A. P. Mouritz. The electric field alignment of short carbon fibres to enhance the toughness of epoxy composites. *Composites Part A: Applied Science and Manufacturing*, 106:11–23, 3 2018.

[66] M. Sakai, T. Miyajima, and M. Inagaki. Fracture toughness and fiber bridging of carbon fiber reinforced carbon composites. *Composites Science and Technology*, 40(3):231–250, 1 1991.

[67] J. K. Wells and P. W. R. Beaumont. The toughness of a composite containing short brittle fibres. *Journal of Materials Science*, 23(4):1274–1278, 4 1988.

[68] D. Hull and T. W. Clyne. *An Introduction to Composite Materials*. Cambridge University Press, 8 1996.

[69] N. J. Mills. *Polymer Foams Handbook: Engineering and Biomechanics Applications and Design Guide*. Butterworth Heinemann, 2007.

[70] L. Marșavina. Fracture mechanics of cellular solids. In *CISM International Centre for Mechanical Sciences, Courses and Lectures*, volume 521, pages 1–46. Springer, Vienna, 2010.

[71] L. Marșavina, D. M. Constantinescu, E. Linul, D. A. Apostol, T. Voiconi, and T. Sadowski. Refinements on fracture toughness of PUR foams. *Engineering Fracture Mechanics*, 129:54–66, 10 2014.

[72] A. McIntyre and G. E. Anderton. Fracture properties of a rigid polyurethane foam over a range of densities. *Polymer*, 20(2):247–253, 1979.

[73] D. Zenkert and J. Bäcklund. PVC sandwich core materials: Mode I fracture

toughness. *Composites Science and Technology*, 34(3):225–242, 1 1989.

[74] G. M. Viana and L. A. Carlsson. Mechanical Properties and Fracture Characterization of Cross-Linked PVC Foams. *Journal of Sandwich Structures & Materials*, 4(2):99–113, 8 2002.

[75] P. M. Stefani, A. T. Barchi, J. Sabugal, and A. Vazquez. Characterization of epoxy foams. *Journal of Applied Polymer Science*, 90(11):2992–2996, 12 2003.

[76] L. Wang, X. Yang, J. Zhang, C. Zhang, and L. He. The compressive properties of expandable microspheres/epoxy foams. *Composites Part B: Engineering*, 56:724–732, 1 2014.

[77] M. Jalalian, Q. Jiang, and A. Bismarck. Air Templated Macroporous Epoxy Foams with Silica Particles as Property-Defining Additive. *ACS Applied Polymer Materials*, 1(3):335–343, 3 2019.

[78] M. N. Bureau and V. Kumar. Fracture toughness of high density polycarbonate microcellular foams. *Journal of Cellular Plastics*, 42(3):229–240, 2006.

[79] Y. Huang and A. J. Kinloch. The toughness of epoxy polymers containing microvoids. *Polymer*, 33(6):1330–1332, 1 1992.

[80] N. H. Kim and H. S. Kim. Micro-void toughening of thermosets and its mechanism. *Journal of Applied Polymer Science*, 98(3):1290–1295, 11 2005.

[81] R. Bagheri and R. A. Pearson. The use of microvoids to toughen polymers. *Polymer*, 36(25):4883–4885, 1 1995.

[82] R. Bagheri and R. A. Pearson. Role of particle cavitation in rubber-toughened epoxies: 1. Microvoid toughening. *Polymer*, 37(20):4529–4538, 9 1996.

[83] R. Bagheri and R. A. Pearson. Role of particle cavitation in rubber-toughened epoxies: II. Inter-particle distance. *Polymer*, 41(1):269–276, 1 2000.

[84] Y. Liu, L. St-Pierre, N. A. Fleck, V. S. Deshpande, and A. Srivastava. High fracture toughness micro-architectured materials. *Journal of the Mechanics and Physics of Solids*, 143:104060, 10 2020.

[85] W. J. Cantwell and P. Davies. A test technique for assessing core-skin adhesion in composite sandwich structures. *Journal of Materials Science Letters*, 13(3):203–205, 1994.

[86] S. Prasad and L. A. Carlsson. Debonding and crack kinking in foam core sandwich beams-II. Experimental investigation. *Engineering Fracture Mechanics*, 47(6):825–841, 1994.

[87] W. J. Cantwell and P. Davies. A study of skin-core adhesion in glass fibre reinforced sandwich materials. *Applied Composite Materials*, 3(6):407–420, 1996.

[88] W. J. Cantwell, G. Broster, and P. Davies. The influence of water immersion on skin-core debonding in GFRP-balsa sandwich structures. *Journal of Reinforced Plastics and Composites*, 15(11):1161–1172, 8 1996.

[89] L. D. McGarva and B. T. Åström. Experimental investigation of compression moulding of glass/PA 12-PMI foam core sandwich components. *Composites Part A: Applied Science and Manufacturing*, 30(10):1171–1185, 10 1999.

[90] X. Li and L. A. Carlsson. The Tilted Sandwich Debond (TSD) specimen for face/core interface fracture characterization. *Journal of Sandwich Structures and Materials*, 1(1):60–75, 8 1999.

[91] X. Li and L. A. Carlsson. Elastic Foundation Analysis of Tilted Sandwich Debond (TSD) Specimen. *Journal of Sandwich Structures & Materials*, 2(1):3–32, 8 2000.

[92] A. Shipsha, M. Burman, and D. Zenkert. Interfacial fatigue crack growth in foam core sandwich structures. *Fatigue and Fracture of Engineering Materials and Structures*, 22(2):123–131, 1999.

[93] J. Ratcliffe and W. J. Cantwell. New test geometry for characterizing skin-core adhesion in thin-skinned sandwich structures. *Journal of Materials Science Letters*, 19(15):1365–1367, 8 2000.

[94] T. S. Gates and H. M. Herring. Facesheet Push-Off tests to determine composite sandwich toughness at cryogenic temperatures. In *19th AIAA Applied Aerodynamics Conference*, 2001.

[95] S. A. Smith and K. N. Shivakumar. Modified mode-I Cracked Sandwich Beam (CSB) fracture test. In *19th AIAA Applied Aerodynamics Conference*. American Institute of Aeronautics and Astronautics Inc., 2001.

[96] A. Ural, A. T. Zehnder, and A. R. Ingraffea. Fracture mechanics approach to facesheet delamination in honeycomb: Measurement of energy release rate of the adhesive bond. *Engineering Fracture Mechanics*, 70(1):93–103, 1 2003.

[97] K. N. Shivakumar and S. A. Smith. In Situ Fracture Toughness Testing of Core Materials in Sandwich Panels. *Journal of Composite Materials*, 38(8):655–668, 7 2004.

[98] E. H. Glaessgen, J. R. Reeder, D. W. Sleight, J. T. Wang, I. S. Raju, and C. E. Harris. Debonding Failure of Sandwich-Composite Cryogenic Fuel Tank with Internal Core Pressure. *Journal of Spacecraft and Rockets*, 42(4):613–627, 2005.

[99] K. Shivakumar, H. Chen, and S. A. Smith. An evaluation of data reduction methods for opening mode fracture toughness of sandwich panels. *Journal of*

Sandwich Structures and Materials, 7(1):77–90, 8 2005.

[100] C. Berggreen, B. C. Simonsen, and K. K. Borum. Experimental and numerical study of interface crack propagation in foam-cored sandwich beams. *Journal of Composite Materials*, 41(4):493–520, 5 2007.

[101] R. C. Østergaard and B. F. Sørensen. Interface crack in sandwich specimen. *International Journal of Fracture*, 143(4):301–316, 5 2007.

[102] J. G. Ratcliffe. Sizing a single cantilever beam specimen for characterizing facesheet-core debonding in sandwich structure. Technical report, NASA, 2010.

[103] J. G. Ratcliffe and J. R. Reeder. Sizing a single cantilever beam specimen for characterizing facesheet-core debonding in sandwich structure. *Journal of Composite Materials*, 45(25):2669–2684, 2011.

[104] Z. Suo and J. W. Hutchinson. Sandwich test specimens for measuring interface crack toughness. *Materials Science and Engineering A*, 107(C):135–143, 1 1989.

[105] D. Adams, J. Nelson, and Z. Bluth. *Development and Evaluation of Fracture Mechanics Test Methods for Sandwich Composites.* shorturl.at/mty67, FAA Technical Review, 2011.

[106] D. Adams, J. Nelson, Z. Bluth, and C. Hansen. Development and Evaluation of Fracture Mechanics Test Methods for Sandwich Composites. In *FAA JAMS Technical Review Meeting*, Baltimore, 2012.

[107] V. Gholami, F. Taheri-Behrooz, and B. Memar Maher. Fracture toughness and crack growth resistance of sandwich panels with grooved cores. *Journal of Sandwich Structures and Materials*, 24(3):1746–1767, 2 2022.

[108] T. Yokozeki and K. Iwamoto. Effects of core machining configuration on the debonding toughness of foam core sandwich panels. *Advanced Composite Materials*, 25(1):45–58, 1 2016.

[109] A. Truxel, F. Avileés, L. A. Carlsson, J. L. Grenestedt, and K. Millay. Influence of face/core interface on debond toughness of foam and balsa cored sandwich. *Journal of Sandwich Structures and Materials*, 8(3):237–258, 2006.

[110] Y. Hirose, H. Matsuda, G. Matsubara, F. Inamura, and M. Hojo. Evaluation of New Crack Suppression Method for Foam Core Sandwich Panel Via Fracture Toughness Tests and Analyses Under Mode-I Type Loading. *Journal of Sandwich Structures and Materials*, 11(6):451–470, 2009.

[111] X. Y. Miao, R. Lu, and X. Chen. Fracture behaviour of foam core sandwich structures with manufacturing defects using phase-field modelling. *Composite*

Structures, 274, 10 2021.

[112] Y. Hu, J. Zhu, J. Wang, and Y. Wu. Interfacial failure in stitched foam sandwich composites. *Materials*, 14(9):2275, 4 2021.

[113] J. M. Berthelot. Transverse cracking and delamination in cross-ply glass-fiber and carbon-fiber reinforced plastic laminates: Static and fatigue loading. *Applied Mechanics Reviews*, 56(1):111, 2003.

[114] K. W. Garrett and J. E. Bailey. Multiple transverse fracture in 90° cross-ply laminates of a glass fibre-reinforced polyester. *Journal of Materials Science*, 12(1):157–168, 1 1977.

[115] J. E. Bailey, P. T. Curtis, and A. Parvizi. On the transverse cracking and longitudinal splitting behaviour of glass and carbon fibre reinforced epoxy cross ply laminates and the effect of Poisson and thermally generated strain. *Proc R Soc London Ser A*, 366(1727):599–623, 1979.

[116] R. Talreja. Damage Mechanics and Fatigue Life Assessment of Composite Materials. *International Journal of Damage Mechanics*, 8(4):339–354, 10 1999.

[117] R. Talreja, S. Yalvac, L. D. Yats, and D. G. Wetters. Transverse Cracking and Stiffness Reduction in Cross Ply Laminates of Different Matrix Toughness. *Journal of Composite Materials*, 26(11):1644–1663, 7 1992.

[118] S. Subramanian, J. J. Lesko, K. L. Reifsnider, and W. W. Stinchcomb. Characterization of the fiber-matrix interphase and its influence on mechanical properties of unidirectional composites. *Journal of Composite Materials*, 30(3):309–332, 2 1996.

[119] M. S. Madhukar and L. T. Drzal. Fiber-Matrix Adhesion and Its Effect on Composite Mechanical Properties: II. Longitudinal (0°) and Transverse (90°) Tensile and Flexure Behavior of Graphite/Epoxy Composites. *Journal of Composite Materials*, 25(8):958–991, 7 1991.

[120] M. S. Madhukar and L. T. Drzal. Fiber-Matrix Adhesion and Its Effect on Composite Mechanical Properties: I. Inplane and Interlaminar Shear Behavior of Graphite/Epoxy Composites. *Journal of Composite Materials*, 25(8):932–957, 7 1991.

[121] P. W. Manders, T. W. Chou, F. R. Jones, and J. W. Rock. Statistical analysis of multiple fracture in 0°/90°/0° glass fibre/epoxy resin laminates. *Journal of Materials Science*, 18(10):2876–2889, 10 1983.

[122] J. Tong, F. J. Guild, S. L. Ogin, and P. A. Smith. On matrix crack growth in quasi-isotropic laminates—I. Experimental investigation. *Composites Science and Technology*, 57(11):1527–1535, 1 1997.

[123] J. W. Lee and I. M. Daniel. Progressive Transverse Cracking of Crossply Composite Laminates. *Journal of Composite Materials*, 24(11):1225–1243, 11 1990.

[124] P. W. M. Peters. The Strength Distribution of 90° Plies in 0/90/0 Graphite-Epoxy Laminates. *Journal of Composite Materials*, 18(6):545–556, 11 1984.

[125] A. Parvizi and J. E. Bailey. On multiple transverse cracking in glass fibre epoxy cross-ply laminates. *Journal of Materials Science*, 13(10):2131–2136, 1978.

[126] A. S. D. Wang and F. W. Crossman. Initiation and Growth of Transverse Cracks and Edge Delamination in Composite Laminates Part 1. An Energy Method. *Journal of Composite Materials*, 14(1):71–87, 1 1980.

[127] F. W. Crossman, W. J. Warren, A. S. D. Wang, and G. E. Law. Initiation and Growth of Transverse Cracks and Edge Delamination in Composite Laminates Part 2. Experimental Correlation. *Journal of Composite Materials*, 14(1):88–108, 1 1980.

[128] F. W. Crossman and A. S. D. Wang. The Dependence of Transverse Cracking and Delamination on Ply Thickness in Graphite/Epoxy Laminates. In *Damage in Composite Materials: Basic Mechanisms, Accumulation, Tolerance, and Characterization*, pages 118–118. ASTM International, 100 Barr Harbor Drive, PO Box C700, West Conshohocken, PA 19428-2959, 2009.

[129] A. S. D. Wang, P. C. Chou, and S. C. Lei. A Stochastic Model for the Growth of Matrix Cracks in Composite Laminates. *Journal of Composite Materials*, 18(3):239–254, 5 1984.

[130] W. W. Feng, K. L. Reifsnider, G. P. Sendeckyj, T. T. Chiao, G. L. Rodericks, W. W. Stinchcomb, L. de Vore, and A. S. D. Wang. Fracture Mechanics of Sublaminate Cracks in Composite Materials. *Journal of Composites Technology and Research*, 6(2):45, 2010.

[131] J. A. Nairn. The Strain Energy Release Rate of Composite Microcracking: A Variational Approach. *Journal of Composite Materials*, 23(11):1106–1129, 11 1989.

[132] A. S. D. Wang, N. N. Kishore, and C. A. Li. Crack development in graphite-epoxy cross-ply laminates under uniaxial tension. *Composites Science and Technology*, 24(1):1–31, 1 1985.

[133] F. J. Guild, S. L. Ogin, and P. A. Smith. Modelling of 90° Ply Cracking in Crossply Laminates, Including Three-Dimensional Effects. *Journal of Composite Materials*, 27(7):646–667, 7 1993.

[134] N. Laws and G. J. Dvorak. Progressive Transverse Cracking In Composite Laminates. *Journal of Composite Materials*, 22(10):900–916, 10 1988.

[135] ISO 527-1. *Plastics-Determination of tensile properties*. International Organization for Standardization, Geneva, Switzerland, 2012.

[136] ASTM D1623-17. *Standard Test Method for Tensile and Tensile Adhesion Properties of Rigid Cellular Plastics*. American Society for Testing and Materials, West Conshohocken, USA, 2017.

[137] ASTM D695-15. *Standard Test Method for Compressive Properties of Rigid Plastics*. American Society for Testing and Materials, West Conshohocken, USA, 2015.

[138] J. G. Williams and C. Gamonpilas. Using the simple compression test to determine Young's modulus, Poisson's ratio and the Coulomb friction coefficient. *International Journal of Solids and Structures*, 45(16):4448–4459, 8 2008.

[139] ASTM D1621-16. *Standard Test Method for Compressive Properties Of Rigid Cellular Plastics*. American Society for Testing and Materials, West Conshohocken, USA, 2016.

[140] ASTM D3518-18. *Standard Test Method for In-Plane Shear Response of Polymer Matrix Composite Materials by Tensile Test of a ± 45° Laminate*. American Society for Testing and Materials, West Conshohocken, USA, 2018.

[141] ASTM D5045-14. *Standard Test Methods for Plane-Strain Fracture Toughness and Strain Energy Release Rate of Plastic Materials*. American Society for Testing and Materials, West Conshohocken, USA, 2014.

[142] A. Pugna, R. Negrea, E. Linul, and L. Marșavina. Is fracture toughness of pur foams a material property? A statistical approach. *Materials*, 13(21):1–13, 10 2020.

[143] E. E. Saenz, L. A. Carlsson, and A. M. Karlsson. In situ analysis of fatigue crack propagation in polymer foams. *Engineering Fracture Mechanics*, 101:23–32, 3 2013.

[144] ISO 15024. *Fiber-reinforced plastic composites-Delamination of mode I interlaminar fracture toughness for unidirectional reinforced materials*. International Organization for Standardization, Geneva, Switzerland, 2001.

[145] ASTM 3039-17. *Standard Test Method for Tensile Properties of Polymer Matrix Composite Materials*. American Society for Testing and Materials, West Conshohocken, USA, 2017.

[146] GOM Correlate 2020. *www.gom.com/en/products/gom-suite/gom-correlate-pro*.

[147] D. Incerti, T. Wang, D. Carolan, and A. D. Fergusson. Curing rate effects on the toughness of epoxy polymers. *Polymer*, 159:116–123, 12 2018.

[148] J. C. Halpin. Stiffness and Expansion Estimates for Oriented Short Fiber Composites. *Journal of Composite Materials*, 3(4):732–734, 1969.

[149] J. C. Halpin and J. L. Kardos. The Halpin-Tsai equations: A review. *Polymer Engineering & Science*, 16(5):344–352, 5 1976.

[150] W. M. Haynes. *CRC Handbook of Chemistry and Physics*. CRC Press, 92 edition, 2011.

[151] S. Sprenger. Nanosilica-toughened epoxy resins. *Polymers*, 12(8):1777, 8 2020.

[152] A. Bajpai, B. Wetzel, A. Klingler, and K. Friedrich. Mechanical properties and fracture behavior of high-performance epoxy nanocomposites modified with block polymer and core–shell rubber particles. *Journal of Applied Polymer Science*, 137(11):48471, 3 2020.

[153] Y. L. Liang and R. A. Pearson. Toughening mechanisms in epoxy-silica nanocomposites (ESNs). *Polymer*, 50(20):4895–4905, 9 2009.

[154] B. B. Johnsen, A. J. Kinloch, R. D. Mohammed, A. C. Taylor, and S. Sprenger. Toughening mechanisms of nanoparticle-modified epoxy polymers. *Polymer*, 48(2):530–541, 1 2007.

[155] M. Z. Hassan and W. J. Cantwell. The influence of core properties on the perforation resistance of sandwich structures - An experimental study. *Composites Part B: Engineering*, 43(8):3231–3238, 12 2012.

[156] K. T. Faber and A. G. Evans. Crack deflection processes-II. Experiment. *Acta Metallurgica*, 31(4):577–584, 4 1983.

[157] P. Walstra. *Principles of Foam Formation and Stability*. Springer, London, 1989.

[158] M. S. Rajput, M. Burman, J. Köll, and S. Hallström. Compression of structural foam materials – Experimental and numerical assessment of test procedure and specimen size effects. *Journal of Sandwich Structures and Materials*, 21(1):260–288, 2019.

[159] D. Carolan, A. Mayall, J. P. Dear, and A. D. Fergusson. Micromechanical modelling of syntactic foam. *Composites Part B: Engineering*, 183:107701, 2 2020.

[160] M. F. Ashby. Mechanical Properties of Cellular Solids. *Metallurgical transactions. A, Physical metallurgy and materials science*, 14 A(9):1755–1769, 1983.

[161] S. K. Maiti, M. F. Ashby, and L. J. Gibson. Fracture toughness of brittle cellular solids. *Scripta Metallurgica*, 18(3):213–217, 1984.

[162] L. Wang, X. Yang, T. Jiang, C. Zhang, and L. He. Cell morphology, bubbles migration, and flexural properties of non-uniform epoxy foams using chemical foaming agent. *Journal of Applied Polymer Science*, 131(23), 12 2014.

[163] S. Kirkpatrick. The nature of percolation 'channels'. *Solid State Communications*, 12(12):1279–1283, 6 1973.

[164] S. Kirkpatrick. Percolation and Conduction. *Rev. Mod. Phys.*, 45(4):574–588, 1973.

[165] J. K. W. Sandler, J. E. Kirk, I. A. Kinloch, M. S. P. Shaffer, and A. H. Windle. Ultra-low electrical percolation threshold in carbon-nanotube-epoxy composites. *Polymer*, 44(19):5893–5899, 9 2003.

[166] S. He, D. Carolan, A. D. Fergusson, and A. C. Taylor. Toughening epoxy syntactic foams with milled carbon fibres: Mechanical properties and toughening mechanisms. *Materials and Design*, 169:107654, 5 2019.

[167] L. J. Gibson and M. F. Ashby. Mechanics of Three-Dimensional Cellular Materials. *Proceedings of The Royal Society of London, Series A: Mathematical and Physical Sciences*, 382(1782):43–59, 1982.

[168] M. F. Kanninen. An augmented double cantilever beam model for studying crack propagation and arrest. *International Journal of Fracture*, 9(1):83–92, 3 1973.

[169] I. K. Partridge and D. D. R. Cartié. Delamination resistant laminates by Z-Fiber® pinning: Part I manufacture and fracture performance. *Composites Part A: Applied Science and Manufacturing*, 36(1):55–64, 1 2005.

[170] W. Goldsmith, C. K. H. Dharan, and H. Chang. Quasi-static and ballistic perforation of carbon fiber laminates. *International Journal of Solids and Structures*, 32(1):89–103, 1 1995.

[171] W. J. Cantwell and J. Morton. Impact perforation of carbon fibre reinforced plastic. *Composites Science and Technology*, 38(2):119–141, 1 1990.

[172] R. F. Gibson. *Principles of Composite Material Mechanics*. CRC Press, Boca Raton, 4th edition, 2016.

[173] Hyosung Advanced Materials. *www.hyosungadvancedmaterials.com*. 2020.

[174] E. J. Barbero. *Introduction to Composite Materials Design*. CRC Press, 2nd edition, 2010.

[175] Y. Gu, M. Li, J. Wang, and Z. Zhang. Characterization of the interphase in carbon fiber/polymer composites using a nanoscale dynamic mechanical imaging technique. *Carbon*, 48(11):3229–3235, 9 2010.

[176] H. Neuber. *Theory of notch stresses: principles for exact calculation of*

strength with reference to structural form and material. USAEC Office of Technical Information, vol. 4547 edition, 1961.

[177] M. Creager and P. C. Paris. Elastic field equations for blunt cracks with reference to stress corrosion cracking. *International Journal of Fracture Mechanics*, 3(4):247–252, 12 1967.

[178] D. Carolan, P. Alveen, A. Ivanković, and N. Murphy. Effect of notch root radius on fracture toughness of polycrystalline cubic boron nitride. *Engineering Fracture Mechanics*, 78(17):2885–2895, 12 2011.

[179] J. G. Berryman. Random close packing of hard spheres and disks. *Physical Review A*, 27(2):1053–1061, 1983.

[180] J. Feder. Random sequential adsorption. *Journal of Theoretical Biology*, 87(2):237–254, 11 1980.

[181] A. P. Thompson and E. D. Glandt. Random sequential adsorption in porous solids. *Journal of Colloid And Interface Science*, 146(1):63–68, 10 1991.

[182] D. Carolan. *Personal Communication.* 2021.

[183] B. D. Lubachevsky and F. H. Stillinger. Geometric properties of random disk packings. *Journal of Statistical Physics*, 60(5-6):561–583, 9 1990.

Appendix A

Fracture performance of architected polymers

A.1 Introduction

It has been previously established in chapter 4 that the fracture toughness of the foam core of a sandwich structure is important as a key energy dissipating mechanism under impact loading scenarios. Furthermore, it has also been demonstrated that the addition of CSR greatly improves the fracture performance of a bulk epoxy polymer. Chapter 5 focused on improving the fracture performance of epoxy foam using short fibre reinforcement. Chapter 6 described the relationship between fracture performance and foam density. The current chapter builds on this research further and details a systematic study on the effect of density and bulk material toughness on the fracture performance of epoxy foam-like structures. These structures consist of holes in a polymer plate. These could be referred to as 2D foams, quasi-2D foams or architected polymers [84]. The advantage of this approach is that microstructural variables such as inter-void distance, the distribution of inter void distances, and volume fraction can be precisely controlled and related back to the fracture performance of the architected structure.

Bulk epoxy plates with holes drilled in to mimic the structure of a foam on a 2D plane will be the focus of the research in this chapter. The central theme of this chapter is uncovering how the mechanical and fracture properties of the bulk material affect the fracture performance of the 2D foam structure.

A.2 Materials & Manufacturing

A commercially sensitive epoxy based resin formed the basis of the materials investigated in this chapter. This resin was similar to the one used to manufacture the foams in Chapter 5 with some modifications to prevent the resin from foaming when mixed with the hardener. Bulk epoxy plates were manufactured using this resin formulation. The resin was first degassed in a vacuum. A stoichiometric amount of the curing agent was then added, mixed, and degassed a second time. Bulk polymer panels were cast by carefully pouring the resin mixture into moulds to produce either 3 mm, 8 mm, or 14 mm thick plates from which test specimens could be machined. The plates were initially cured at 40 °C for 10 h, followed by a 12 h post-cure at 70 °C.

Some polymer plates were prepared as described in Chapter 3 for standardised bulk polymer tensile and SENB testing. Standardised SENB testing was conducted on samples both 8 mm and 14 mm in thickness. The larger samples enabled DIC strain measurements to be made more accurately. Non-standardised SENB testing was also carried out on bulk polymer plates. These tests required a 2 mm diameter hole to be drilled as the start of the crack. This mimics the effect of a crack beginning in a void in a foam. A CNC machine, Haas tool room mill, was used to drill these holes in the centre of the samples. Further configurations of holes were drilled ahead of the crack using a CNC machine which will be described in more detail later in this chapter.

A.2.1 Hole arrangements

A variety of hole configurations were tested using SENB specimens. As described by Liu et al. [84], the two mechanisms that will govern the fracture behaviour of these materials are crack blunting and hole-hole interaction. The holes effectively blunt the crack-tip, i.e., increase the crack tip radius, and would be expected to result in an increase in apparent fracture energy as compared to a sharp crack [176–178]. Throughout the remainder of this chapter, the term apparent fracture energy will be used to describe the energy dissipated in any structure containing a machined hole, but calculated via the standard approach [141], while the term critical fracture energy is reserved for the material property as measured from a sharp crack. The analysis of all Single Edge Notch Bending (SENB) results presented in this section assumes the existence of a sharp crack, in line with traditional fracture mechan-

ics methodologies. However, it's important to note that this may not fully reflect the actual behaviour of the samples that have been prepared with machined holes. These holes represent blunt, rather than sharp, crack initiators. For future analyses, a more accurate reflection of the material response could be obtained by employing a blunt crack analysis approach. To isolate the effect of crack blunting, specimens with one hole as the crack tip were machined as shown in Figure A.1 (a), to allow the effect of the 2 mm diameter hole crack tip to be compared to a sharp crack in a standardised SENB. Hole-hole interaction and spacing will affect the space available ahead of the crack tip for plastic deformation and other damage dissipation mechanisms to occur. Thin ligaments will likely fail in simple tension, while the presence of sufficiently thick ligaments ahead of the crack tip will allow plastic deformation to occur and will result in an increase in apparent fracture energy. Additionally, in order to systematically investigate the effect of hole-hole interaction, samples containing holes with a hole-hole spacing of between 2.5 mm and 7 mm were machined immediately ahead of the initial crack tip, as shown in Figure A.1 (a).

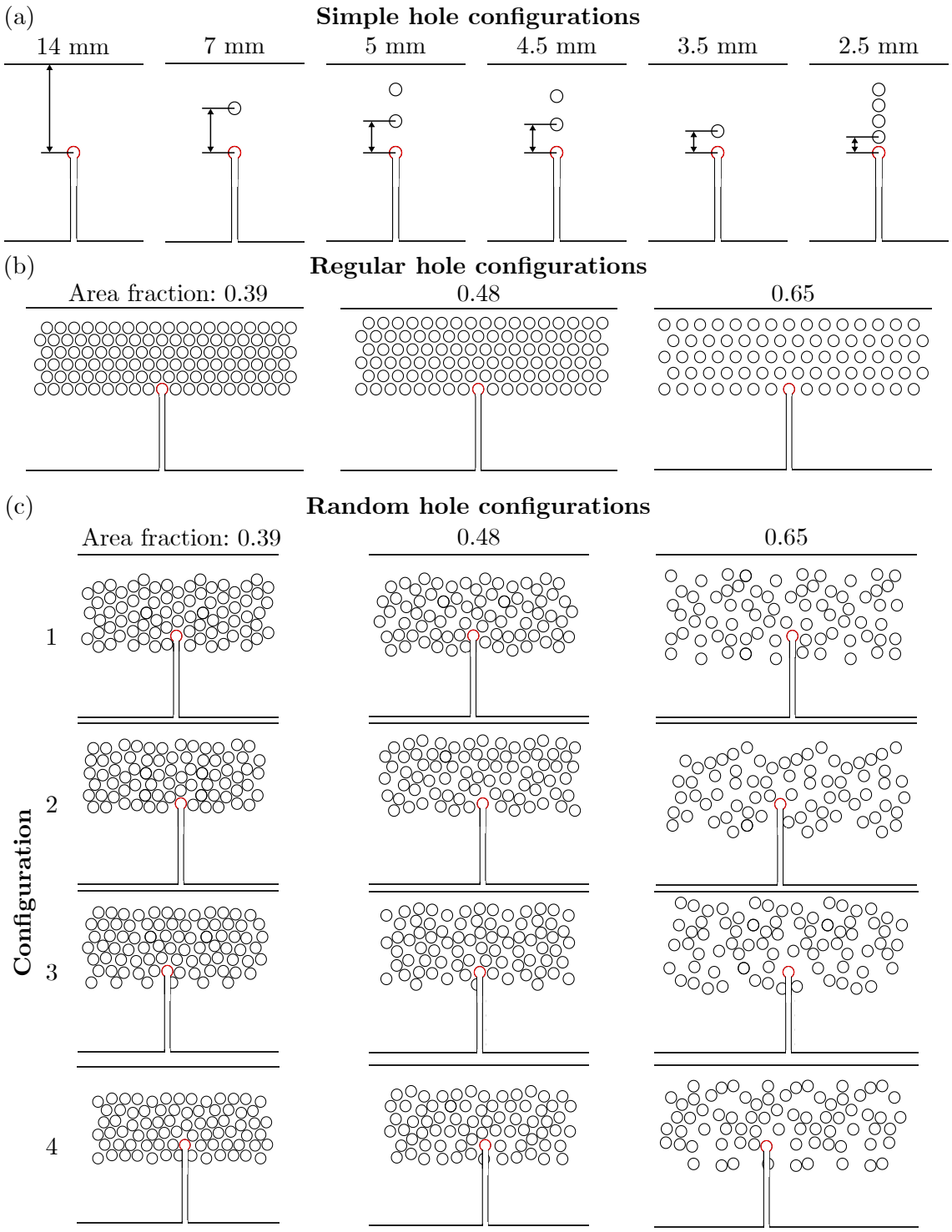


Figure A.1: Hole configurations drilled into bulk epoxy material for SENB testing. Simple hole configurations followed by regular arrays and random arrays of holes. Area fraction values represent the proportion of bulk material remaining.

The main purpose of this research was to further understand the effectiveness of using a toughened bulk material as the base resin with which to manufacture a foam. As a result, it was necessary to investigate arrays of holes. An array of holes surrounding the crack tip will provide a different response to a simple line of holes even if the hole diameter and ligament thicknesses are the same in both cases. The array of holes will significantly increase the local compliance around the potential crack path. Hole arrangements were drilled in a limited area ahead of the crack tip as this significantly reduced the machining time of the specimens. Restricting the machining area to ahead of the crack tip changes the global compliance of the specimens compared to if the holes were drilled across the whole specimen. As a result, these samples can only be compared to each other and absolute values of apparent fracture energy have no wider meaning outside of this comparison. Regular hexagonal arrangements of holes were machined at various area fractions. These regular arrangements are presented in Figure A.1 (b). Area fraction is used in this research as the arrangements of holes are 2D. Area fraction refers to the proportion of bulk material remaining after machining in the area where holes have been drilled. Area fraction is equal to volume fraction and relative density for the machined area. The lowest area fraction theoretically possible for a hexagonal arrangement is 0.093, this would result in a ligament thickness of 0 mm. The calculation for this theoretical minimum, based on the diagram in Figure A.2, is as follows:

$$\text{Area of the triangle, } A_{\mathrm{T}} = \frac{\sqrt{3}D^2}{4} \tag{A.1}$$

$$\text{Area of circle within the triangle, } A_{\mathrm{C}} = \frac{\pi D^2}{8} \tag{A.2}$$

$$\text{Area fraction} = \frac{A_{\mathrm{T}} - A_{\mathrm{C}}}{A_{\mathrm{T}}} \tag{A.3}$$

$$\text{Area fraction} = \frac{2\sqrt{3} - \pi}{2\sqrt{3}} \approx 0.093 \tag{A.4}$$

A series of preliminary machining tests, adjusting drill feed rate and rotational speed, revealed that a minimum ligament thickness of 0.1 mm was required to ensure the ligaments remained intact after the machining operation. This practical, manufacturing limit was imposed for all subsequent arrangements of holes throughout the remainder of the work.

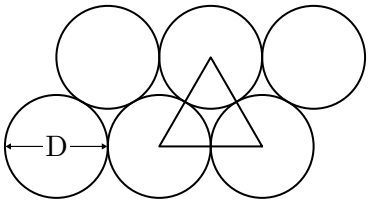


Figure A.2: Schematic of hexagonal circle packing.

Real foams contain voids that are not regularly arranged or of a consistent size and shape. Thus, to best imitate a foam, random arrangements of holes were prepared at various area fractions. The random arrangements will contain ligaments of varying thicknesses for a given area fraction. A high area fraction structure can theoretically contain small ligaments as well as large ligaments, while a low area fraction structure, cannot contain overly thick ligaments as the interparticle distance is necessarily small. Carolan [159] addresses this in research considering glass microsphere syntactic foams of varying density.

The lowest area fraction possible for the randomly close-packed (RCP) limit on a 2D plane is ≈ 0.18 [179]. This limit increases to ≈ 0.20 when the minimum ligament thickness constraint of 0.1 mm is implemented for an array of 2 mm diameter holes. One method of achieving a random array of holes on a 2D plane is to use random sequential adsorption (RSA). However, several authors have reported a minimum achievable area fraction on a 2D plane of ≈ 0.45 using RSA [180, 181]. In order to achieve a lower area fraction and imitate foams at practically useful densities, a more sophisticated method of arranging the holes was required. A proprietary script developed by Dr. Carolan [182] based on a molecular dynamics approach, first introduced by Lubachevsky and Stillinger, can achieve hole densities up to the RCP limit [159, 179, 183]. This script was used to produce four arrangements of holes for each of the three area fractions (0.39, 0.48, 0.65) outlined in Figure A.1. The script outputs the x, y coordinates and radii, r, within a unit square with periodic boundary conditions imposed. These squares can then be scaled and repeated three times to cover the entire region of interest ahead of the crack tip in the SENB specimen. The initial crack tip was chosen from the middle square as one of the holes closest to the bottom edge and close to the middle of that edge. Thus the initial crack tip always lay within a hole.

A.3 Results

The tensile and fracture properties of the bulk epoxy polymers used in this chapter are summarised in Table A.1. As seen in chapter 4, the addition of CSR nanoparticles to the epoxy resin was found to greatly increase the toughness of the bulk resin. In addition, the CSR has resulted in a drop in both modulus and ultimate tensile strength. How the differences in these bulk polymer properties will affect the SENB results of the samples with machined holes will be the focus of the remainder of this chapter.

Table A.1: Tensile properties and fracture energy of the bulk polymers used in this chapter.

wt% CSR	E_t [GPa]	UTS [MPa]	G_{Ic} [J/m^2]
0	3.84 ± 0.08	96.8 ± 0.7	268 ± 23
3	3.81 ± 0.05	94.2 ± 0.8	768 ± 104
10	2.97 ± 0.10	61.6 ± 0.6	3608 ± 107

A.3.1 Simple holes

The apparent fracture energies associated with the first load drop of the simple holes SENB tests are presented in Figure A.3.

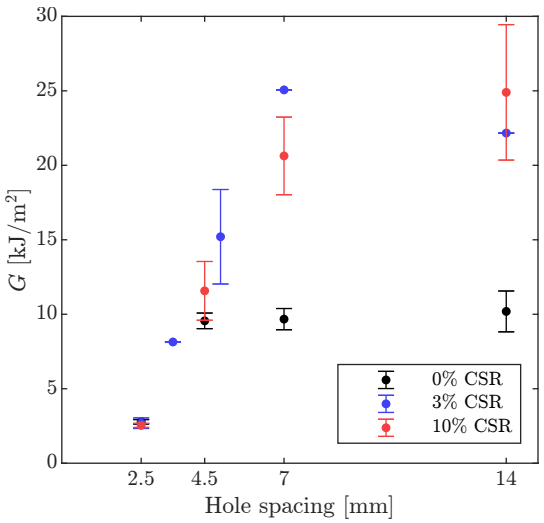


Figure A.3: Fracture energy versus hole spacing for SENB samples with simple hole arrangements ahead of the starting hole. 14 mm spacing represents a sample with no further holes drilled in addition to the crack starting hole.

The apparent fracture energy for the samples with 14 mm spacing (no additional holes ahead of the crack) for the epoxy polymers modified with 3 and 10 wt% CSR is more than twice the value of the apparent fracture energy of the corresponding untoughened sample. Figure A.4 displays full field strain, ϵ_x, colour-maps for the region ahead of the crack of the one hole samples calculated using the last DIC image taken immediately prior to failure. It it clear from the colour-maps that the toughened epoxy polymers modified with 3 and 10 wt% CSR particles undergo significantly more plastic deformation than the untoughened sample. The area of the toughened specimens that is coloured red, and so is above 3% strain in the x-direction, is significantly larger than the corresponding high strain area of the untoughened specimen. This observation is confirmed when the numerical values for the opening strains, ϵ_x, along the section ahead of the crack tip, indicated by the black lines in Figure A.4, are extracted and plotted in Figure A.5. From Figure A.5, it can be seen that the DIC computed strains in the toughened specimens reach higher values than the strain in the untoughened specimen at the crack tip. Furthermore, the epoxy polymer modified with 10 wt% CSR particles reaches a much higher maximum strain than either of the epoxy polymers modified with 0 and 3 wt% CSR particles. The addition of 10 wt% CSR has increased the fracture energy of the bulk material as highlighted by SENB test results of the samples with a sharp precrack detailed in Table A.1. Furthermore, the modulus of the material is reduced due to the addition of the rubber particles. The combination of these changes in bulk material properties causes the large increase in apparent fracture energy of the one hole epoxy polymer structure modified with 10 wt% CSR particles. The difference between the apparent fracture energy of the epoxy polymers modified with 3 and 10 wt% CSR particles is small, however, the difference in the maximum opening strain reached at the crack tip is significant. The reduction in tensile strength, due to the addition of 3 wt% CSR particles is small relative to the unmodified polymer, while the drop in tensile strength due to the addition of 10 wt% CSR particles is much larger. As a result, compared to the epoxy polymer modified with 10 wt% CSR particles, the fracture loads achievable in the epoxy polymer modified with 3 wt% CSR particles are larger but the maximum displacement of the crosshead during the SENB test is lower. This results in a similar fracture energy for the two toughened one hole samples despite the large differences in the fracture and tensile properties of the bulk material.

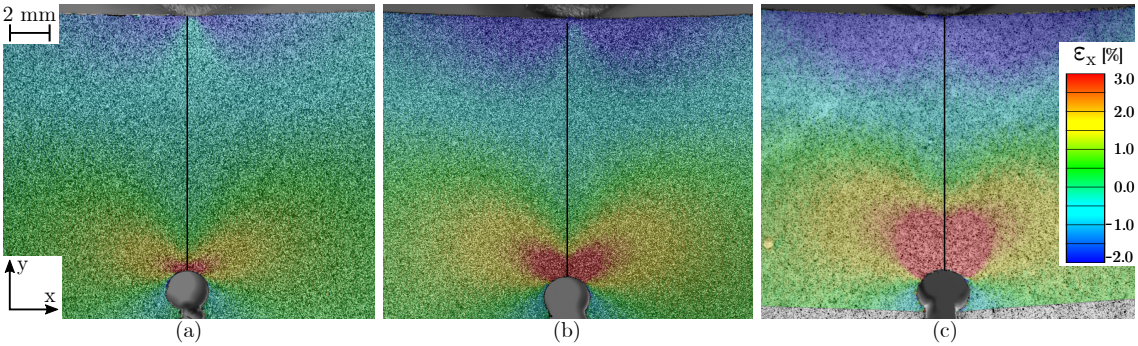


Figure A.4: DIC strain colour-map of SENB samples with no further holes drilled (14 mm spacing). (a): 0% CSR (b): 3% CSR (c): 10% CSR.

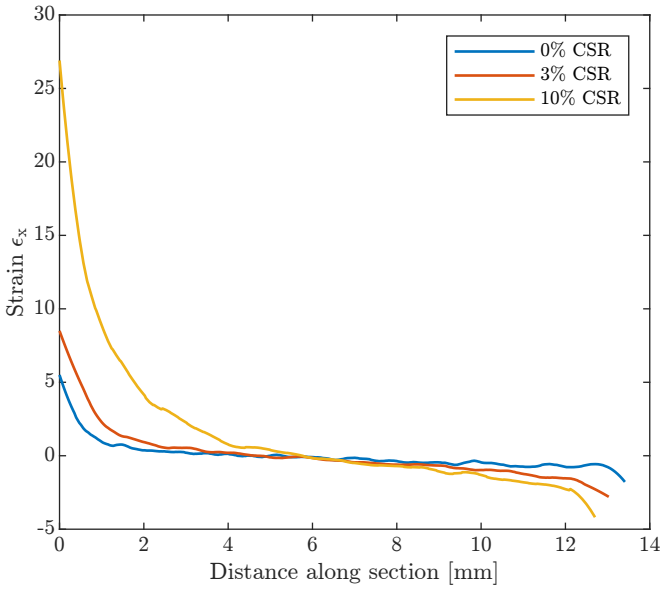


Figure A.5: ϵ_x versus distance along the section for SENB samples with no further holes ahead of the crack tip.

The 7 mm hole spacing geometries behave in a similar manner to the single hole geometries. In fact, the 7 mm geometries produce a materially similar result to the one hole geometries. The ligament thickness of 5 mm (7 mm spacing - 2×1 mm radius of the holes) is large enough such that the opening strain is essentially zero, i.e. far-field, at the subsequent hole as the sample fails and so the presence of the second hole has no influence on the fracture behaviour at the first hole. This can be clearly seen seen when analysing the full field strain, ϵ_x, colour-maps in Figure A.6. The strain at the second hole is approximately zero.

The fracture energy for the samples with 2.5 mm hole spacing are all approximately 2.5 kJ/m^2. The dominant factor in this test is the ligament thickness between the holes, the fracture properties of the bulk material have little additional effect. The

0.5 mm ligament restricts the growth of the high strain area significantly. This is evident in the full field strain, ϵ_x, colour-maps in Figure A.7 where there are no clear differences between the samples. The toughness of the bulk material has no effect on this geometry as the differences in the high strain area ahead of the crack tip observed in the single hole geometry do not have sufficient space to be fully realised. The apparent fracture energy values recorded from this geometry are simply the result of the first ligament failing in tension, with all subsequent ligaments failing rapidly thereafter. In fact, the epoxy polymer modified with 10 wt% CSR particles recorded a slightly lower value of apparent fracture energy than either of the geometries modified with 0 and 3 wt% CSR particles. This is due to the lower tensile strength of the bulk material.

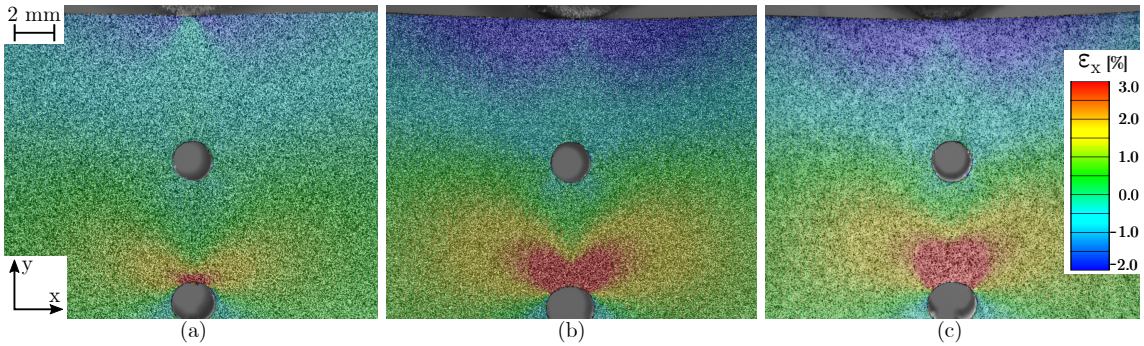


Figure A.6: DIC strain colour-map of SENB samples with 7 mm spacing between hole centres. (a): 0% CSR (b): 3% CSR (c): 10% CSR.

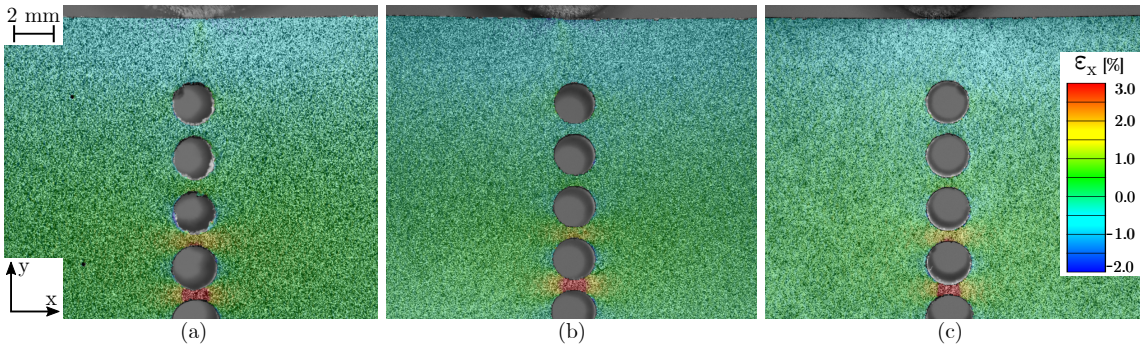


Figure A.7: DIC strain colour-map of SENB samples with 2.5 mm spacing between hole centres. (a): 0% CSR (b): 3% CSR (c): 10% CSR.

Figure A.8 displays the full field strain, ϵ_x, colour-maps for the region ahead of the crack of standard SENB specimens with a sharp crack. The strain distribution was calculated using the last DIC image taken immediately prior to failure. The difference between the strains ahead of the single hole specimens in Figure A.4 and

the sharp crack specimens in Figure A.8 is clear. The blunt hole allows for more plastic deformation to develop ahead of the crack compared to the sharp crack in the standardised test. This difference is most substantial when comparing the untoughened specimens. The high strain region ahead of the sharp crack untoughened polymer specimen is imperceptible with the resolution and field of view of the DIC in this image. However, the high strain region for the untoughened sample is clearly visible in Figure A.4. The red, apparent high strain regions visible alongside the initial crack in Figure A.8 are artefacts of the DIC measuring technique. The DIC is simply measuring the paint splitting as the initial crack opens.

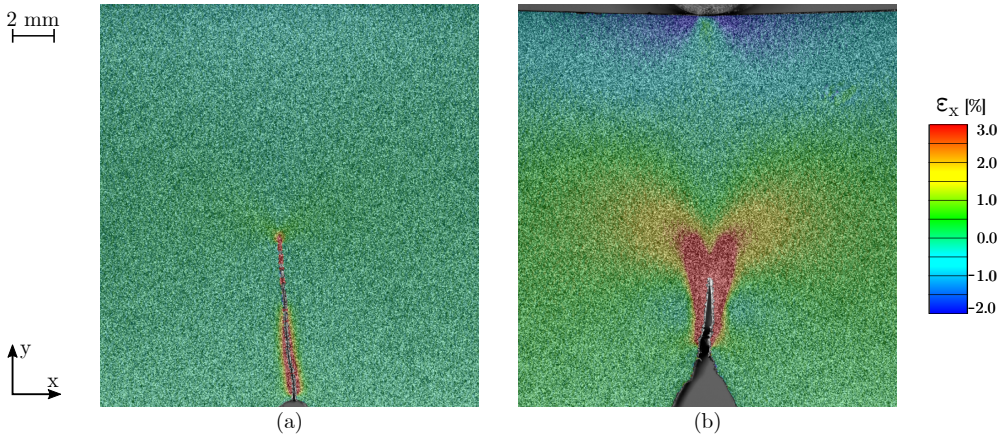


Figure A.8: DIC strain colour-map of SENB samples with sharp cracks. (a): 0 wt% CSR (b): 10 wt% CSR.

A.3.2 Regular arrays

Figure A.9 presents the apparent fracture energy results of the SENB tests of geometries manufactured with regular arrays of holes ahead of the crack tip. The result presented in Figure A.9 (a) is the apparent fracture energy measured as the energy dissipated up to the first observed drop in load in the load-displacement trace. The second result presented in Figure A.9 (b) is the total energy dissipated by the sample. This is measured up to when either the sample completely fails or all the thin ligaments between holes have failed and the only remaining intact material is the thick section at the top of the specimen where the loading pin makes contact. Finally, the value of total energy dissipated minus the apparent fracture energy dissipated up to the first load drop is presented in Figure A.9 (c). This allows an examination of the ability of the regular arrays to 'trap' the crack and inhibit further crack propagation throughout the geometry. Figure A.10 displays load versus displacement curves for

the SENB testing of the unmodified epoxy polymer and the epoxy polymer modified with 10 wt% CSR particles for each area fraction tested. The difference between the total and apparent fracture energy is clear when analysing the load versus displacement curves. The specimens manufactured with the unmodified epoxy polymer all fail completely after the peak load is reached. This failure behaviour is independent of area fraction. Thus, the total energy dissipated and the apparent fracture energy at the first drop in load of these specimens is equal. In the epoxy polymer modified with 10 wt% CSR particles, the crack is arrested at subsequent holes for the geometries with an area fraction of 0.39 and 0.48. In these geometries the load drops sequentially as the crack progresses through the structure. The total energy dissipated up to final failure is larger than the apparent fracture energy, as clearly shown in Figure A.9.

However, for the maximum area fraction of 0.65, no crack arrest between subsequent holes is observed and the geometries fail catastrophically after first failure. In this case there is no difference between the apparent fracture energy at first load drop and the total energy dissipated by the structure.

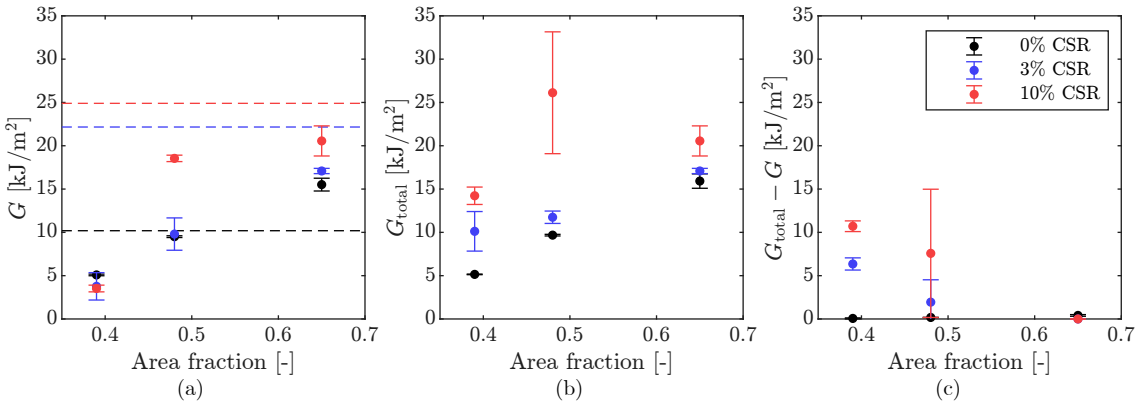


Figure A.9: Fracture energy versus area fraction for SENB samples with regular arrays of holes. (a) Apparent fracture energy measured up to the first load drop. The dashed lines represent the apparent fracture energy of samples with one hole (14 mm spacing). (b) Total fracture energy measured up to final ligament failure. (c) Total fracture energy minus the apparent fracture energy at first load drop.

In the 0.39 area fraction geometries, with correspondingly thin ligaments of epoxy between holes, the untoughened samples record a higher apparent fracture energy and peak load than the geometries manufactured with toughened epoxy polymers. The tensile strength of the untoughened epoxy polymer is higher than either of the

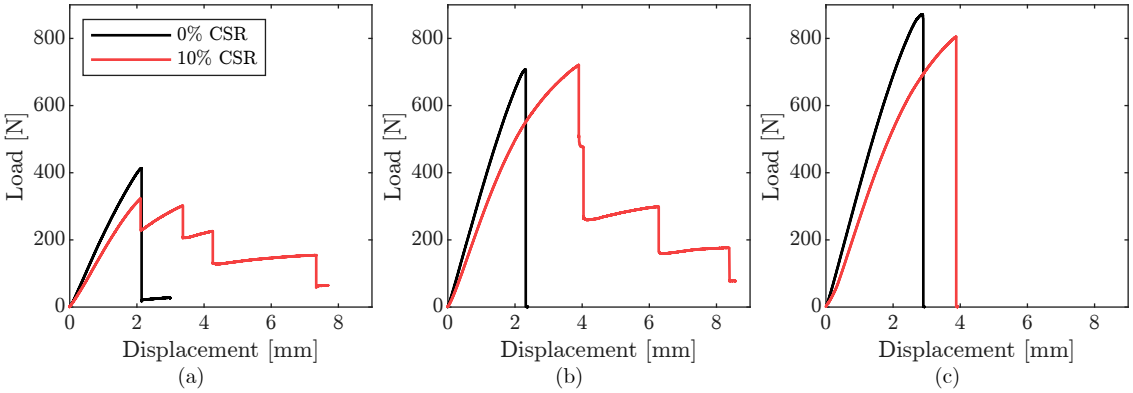


Figure A.10: Load versus displacement for the SENB testing of 10 wt% CSR and 0 wt% CSR samples with regular arrays of holes. (a): Area fraction 0.39 (b): Area fraction 0.48 (c): Area fraction 0.65.

CSR modified epoxy polymers and the thin ligaments, as explained for the simple hole arrangements, do not allow for the large high strain regions to develop. The full development of these high strain regions are necessary for the toughened structures to outperform the untoughened structures. Once the first ligament has failed, the untoughened structures are unable to arrest the crack due to the brittle nature, i.e. low critical fracture energy, of the bulk material from which they are manufactured. On the other hand, the toughened epoxy polymers are able to arrest the crack in this geometry, hence the total energy dissipated is greater than the apparent fracture energy at first load drop, as presented in Figure A.9 (c). Figure A.11 and Figure A.12 display full field opening strain, ϵ_x colour-maps for the region ahead of the initial crack tip for the 0.39 and 0.65 area fraction regular geometries. Again, each of these images has been calculated using the last DIC image taken immediately prior to failure. Figure A.13 and Figure A.14 plot the opening strain along the section ahead of the crack in the 0.39 and 0.65 area fraction regular geometries. The gaps in the lines plotted on these graphs correspond to hole locations where no strain is recorded. The differences in both the full-field strains, Figure A.11, and section strains, Figure A.13, between individual test samples for the 0.39 area fraction specimens are small, i.e. the behaviour of the structure is similar regardless of the bulk material. The untoughened sample records a slightly higher strain at the crack tip, i.e. 0 mm distance along the section, than the toughened samples. This is due to the higher tensile strength of the bulk material, however the strain distributions are similar and do not depend on the properties of the bulk polymer.

Once the geometry of the regular array specimens is increased to an area fraction

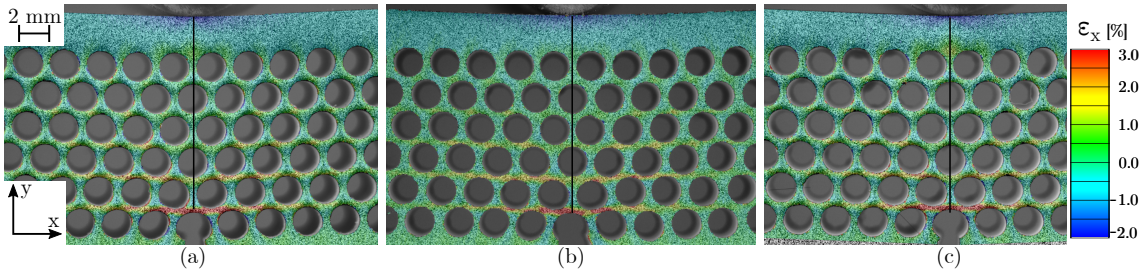


Figure A.11: DIC strain colour-map of SENB samples with regular arrays of holes, 0.39 area fraction. (a): 0% CSR (b): 3% CSR (c): 10% CSR

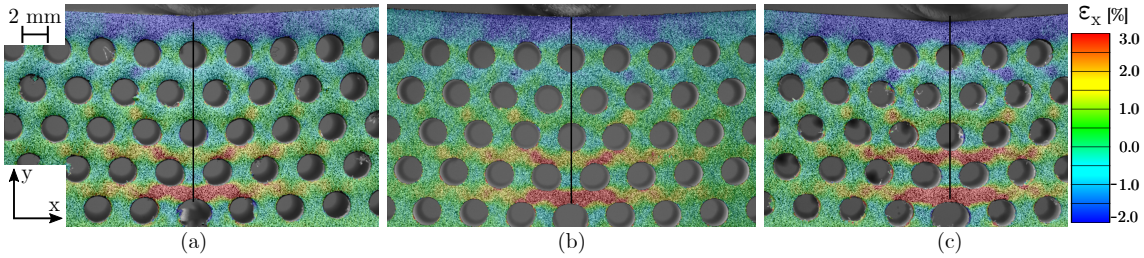


Figure A.12: DIC strain colour-map of SENB samples with regular arrays of holes, 0.65 area fraction. (a): 0% CSR (b): 3% CSR (c): 10% CSR

of 0.48, differences in fracture behaviour between the samples begin to be revealed. The epoxy polymer modified with 10 wt% CSR particles achieves both a significantly higher apparent fracture energy at first load drop and a total dissipated energy than the same geometry manufactured with either unmodified epoxy polymer or epoxy polymer modified with 3 wt% CSR. The ligament thickness between neighbouring holes is greater than in the 0.39 area fraction structures, and so the tougher bulk material has sufficient space to produce the desired toughening effects within the array of holes. Clearly then, there is a substantial difference between the total energy dissipated and the apparent fracture energy for the geometries manufactured with nano-toughened polymers, demonstrating that crack arrest is still taking place as the crack propagates from hole to hole. Crack arrest is also clearly evident in the load versus displacement plot in Figure A.10 (b).

The ligament thickness between holes in the 0.65 area fraction specimens is now large enough for both the toughened materials to outperform the geometry manufactured from the unmodified material. The dashed lines on Figure A.9 represent the apparent fracture energy value of the samples with a single hole at the crack tip. It is of interest to note that the unmodified, 0.65 area fraction sample reaches a larger apparent fracture energy value than the corresponding one hole sample. On the other hand, the toughened samples do not reach the same apparent fracture

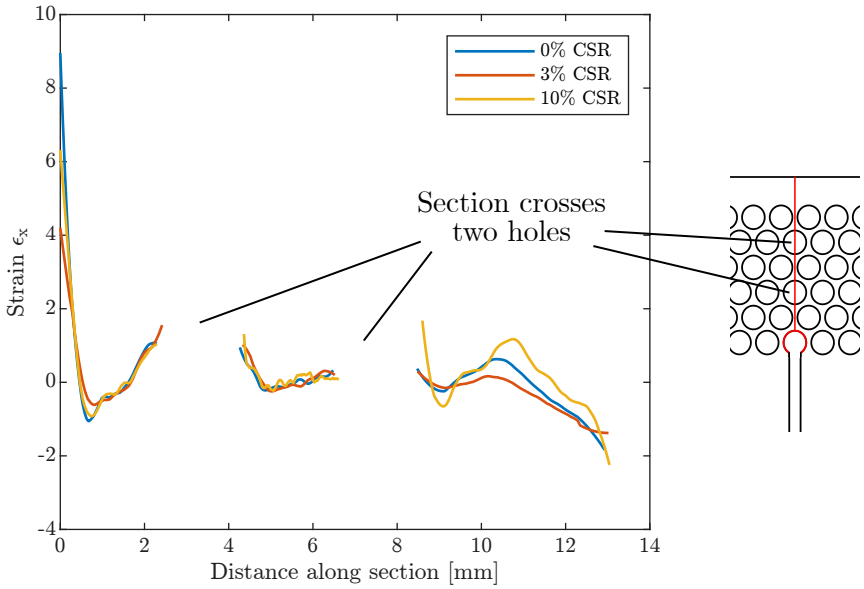


Figure A.13: ϵ_x versus distance along the section for SENB samples with a regular array of holes, 0.39 area fraction.

energy as the corresponding single hole samples made of the same polymers. The unmodified, 0.65 area fraction sample has ligaments between successive holes with a thickness sufficient to allow the full load to be reached, similarly to the corresponding single hole geometry. However, the compliance of the 0.65 area fraction sample is greater than that of the single hole sample. Since the apparent fracture energy is proportional to compliance, the observed apparent fracture energy of the multi hole array structure is greater. The toughened 0.65 area fraction samples do not have sufficient space ahead of the crack tip for the full high strain region to develop as completely as in the single hole geometries. As a result the recorded apparent fracture energy is lower than the single hole counterparts. The differences between the samples with regard to the opening strain ahead of the crack tip is made clear in Figure A.12 and Figure A.14. The strain in the 10 wt% CSR, 0.65 geometries reaches 40%, while the 3 and 0 wt% CSR geometries reach only 22% and 17%, respectively. The high strain values at the notch tip allow the 10 wt% geometries to reach a higher displacement before failure than the 0 wt% CSR geometry as highlighted in the load versus displacement graph in Figure A.10 (c). The measured apparent fracture energy is higher for the geometry manufactured from the toughened material as a result. Interestingly, after the initial load drop, the crack is not arrested in any 0.65 area fraction samples. The release of stored elastic strain energy is too high for the ligaments following the crack to arrest the propagating crack and stop it progressing through the entire sample.

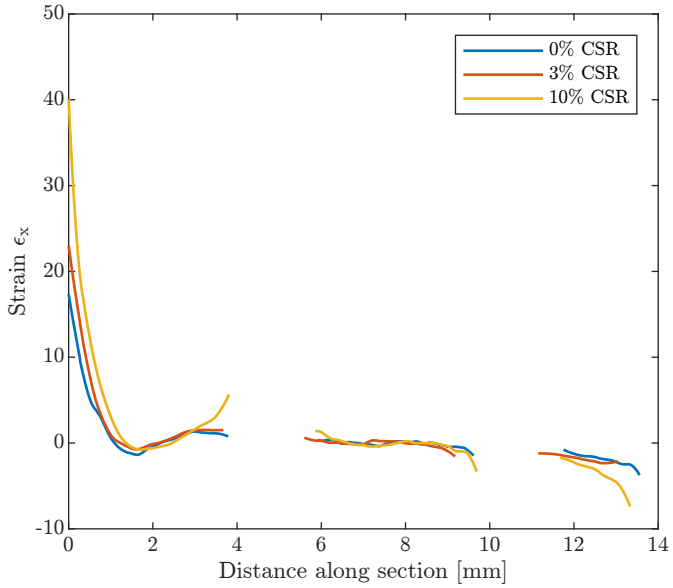


Figure A.14: ϵ_x versus distance along the section for SENB samples with a regular array of holes, 0.65 area fraction.

A.3.3 Random arrays

Figure A.15 presents the average apparent, total and, total - apparent fracture energy for the SENB structures with random arrays of holes for each area fraction. There is little difference between the geometries manufactured with either the unmodified or CSR modified epoxy when considering the apparent fracture energy at first load drop. The 10 wt% CSR structures outperform the other structures by a small margin, however, the uncertainty is large due to the random nature of the hole arrangements. As expected, the 0.39 area fraction structures recorded the lowest apparent fracture energy values. As discussed at the beginning of this chapter, in order to achieve the low area fraction the holes must have a low interparticle distance [159]. It follows that there is insufficient space in the array for any large ligaments to be present. As a result, the distribution of hole-to-hole ligament thicknesses is smaller than in the higher area fraction structures. Consequently, the lower area fraction arrangements are more similar to regularly arranged structures than the higher area fraction structures and achieve fracture energies closer to the regular geometries. This is clearly demonstrated in Figure A.16, which presents the individual results from each hole configuration and the corresponding regular results as dashed lines. The results of the 0.39 area fraction random geometries are reasonably comparable to the regular results. The standard deviation in the 0.39 area fraction results is also smaller due to the reduction in the range of geometrically allowable

ligament thicknesses.

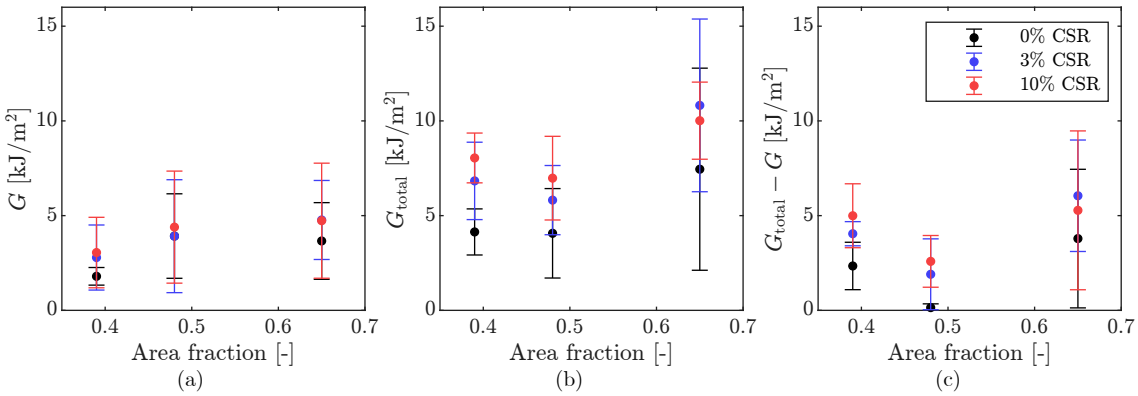


Figure A.15: Fracture energy versus area fraction for SENB samples with random arrays of holes. (a) Fracture energy measured up to the first load drop, apparent fracture energy. (b) Total fracture energy measured up to final ligament failure. (c) Total fracture energy minus the apparent fracture energy.

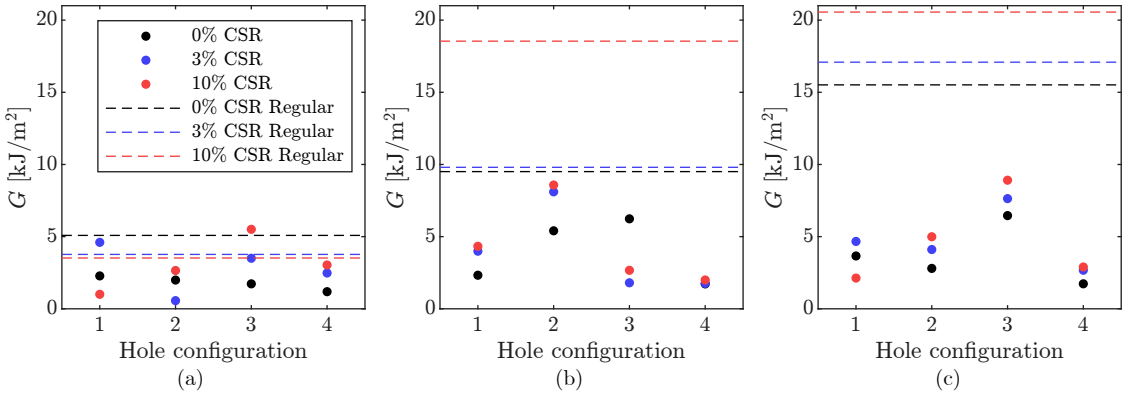


Figure A.16: Fracture energy versus area fraction for SENB samples with random arrays of holes showing the value for individual hole configurations. Dashed lines represent the values for regular arrays of holes. (a) Area fraction 0.39 (b) Area fraction 0.48 (c) Area fraction 0.65

The 0.48 and 0.65 area fraction geometries measure similar apparent fracture energy values which are, on average, higher than for the 0.39 area fraction geometries. The 0.48 and 0.65 area fraction geometries apparent fracture energy values are considerably below the values measured for the corresponding regular geometries. It is clear from the images of the random arrays in Figure A.1 that some thin ligaments of polymer between adjacent holes are present in all random arrays. The apparent fracture energy values are measured at the first load drop. This load drop in the random samples is invariably caused by a thin ligament breaking in the vicinity of the

high strain region ahead of the crack tip. The ligaments in the regularly arranged geometries are of constant thickness and so there are no thin ligaments to cause this premature failure. A consequence of thin ligaments leading to early failure, is that the crack is often subsequently arrested by the presence of a thicker ligament elsewhere in the structure. This point is made clear when the difference between the total energy dissipated and the apparent fracture energy values at first load drop are compared. At an area fraction of 0.65, this value is zero for all regularly arranged structures. However, for the random geometries at the same area fraction, this value is substantial and often larger than the apparent fracture energy value. This reveals that more energy is absorbed after the first failure in these samples.

The thin ligaments that initially fail are not always directly adjacent to the initial crack. An example of this phenomenon can be observed in Figure A.17 where the hole arrangement 3, 0.65 area fraction, 0 wt% CSR structure is pictured. There are three images, immediately before and after the initial load drop, and then after the final load drop. The two ligaments that failed during the initial load drop, labelled with a black 'A', are much thinner than the thick ligaments surrounding the initial crack tip. They can be seen to be experiencing high strain before failure in image 1 of the series. The load versus displacement curve in Figure A.18 (a) reveals that, after the initial load drop, the sample continued to a higher load and displacement until one of the thick ligaments connected to the main crack broke. As a result, this sample recorded a significant difference between the apparent fracture energy and the total fracture energy. The different resin systems do not always fail in the same way for the same hole arrangement. The corresponding 10 wt% CSR structure did not experience the same initial failure at the same thin ligament as the 0 wt% CSR structure.

In hole arrangement 1 at 0.65 area fraction, the 10 wt% CSR structure experienced several load drops as the crack was arrested several times. The 0 wt% CSR structure failed catastrophically once the first ligament fractured as shown in Figure A.19. In this case, the 10 wt% CSR structure recorded a significant difference between the total and apparent fracture energy. The initial failure of the thick ligament at the crack tip substantially increases the compliance of the structure which allows large deformation to occur after the first failure. The several subsequent instances of small load drops, sequential ligament failures, also leads to a high total fracture energy.

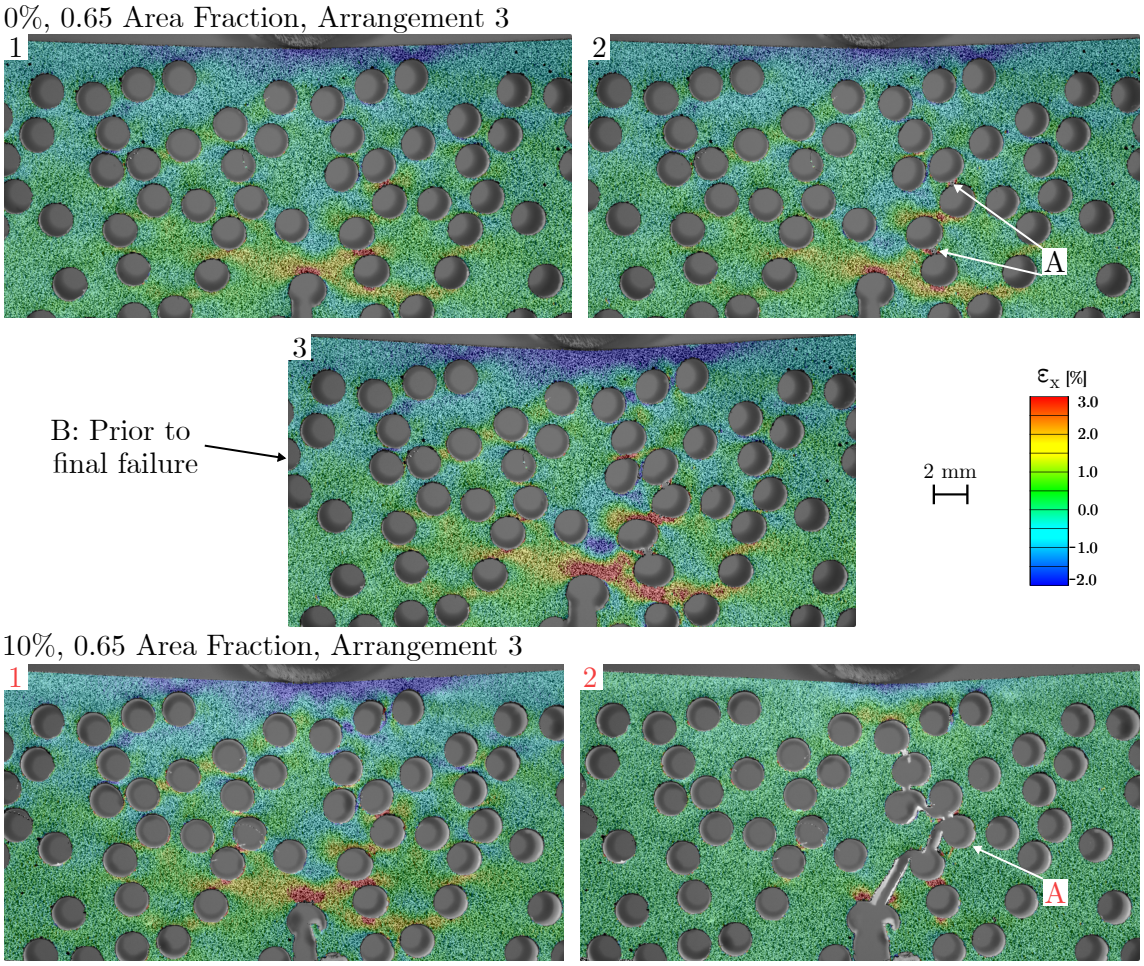


Figure A.17: DIC strain colour-maps of random SENB samples. 0.65 area fraction arrangement 3. Top three images: 0 wt% CSR. Bottom two images: 10 wt% CSR. Letters correspond to load drops in Figure A.18 (a)

However, the 0 wt% CSR structure, with the same hole arrangement, reached a higher peak load and recorded a higher apparent fracture energy but there was no subsequent arrest of the crack.

The premature failure of the random samples compared to the regular samples provides a comparison to the transition in fracture performance of epoxy foams described in chapter 6. In chapter 6, a large distribution in cell size was linked to a correspondingly low fracture toughness of the low density foams. Large compliant cells provide little support to adjacent small cells, which fail first at the crack tip, leading to the complete failure of the sample. Fracture models based on a regular cell structure cannot capture this behaviour [161]. In this chapter, a large distribution of ligament thicknesses, specifically the existence of small ligaments in a dense material, cause premature failure compared to a regular structure of the same density.

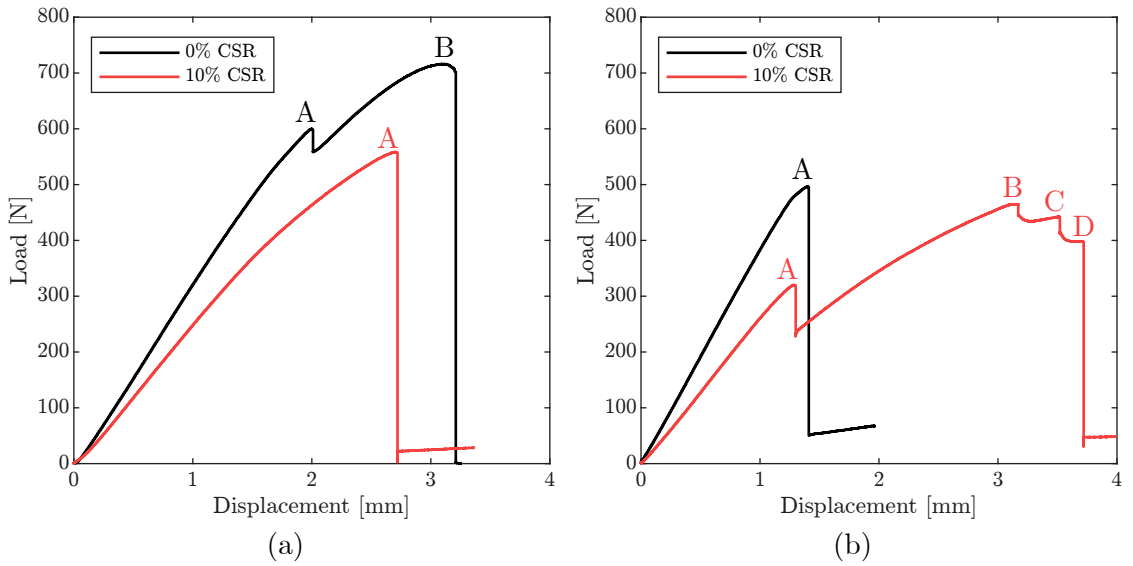


Figure A.18: Load versus displacement for the SENB testing of 10 wt% CSR and 0 wt% CSR samples with 0.65 area fraction. (a) Arrangement 3 (b) Arrangement 1.

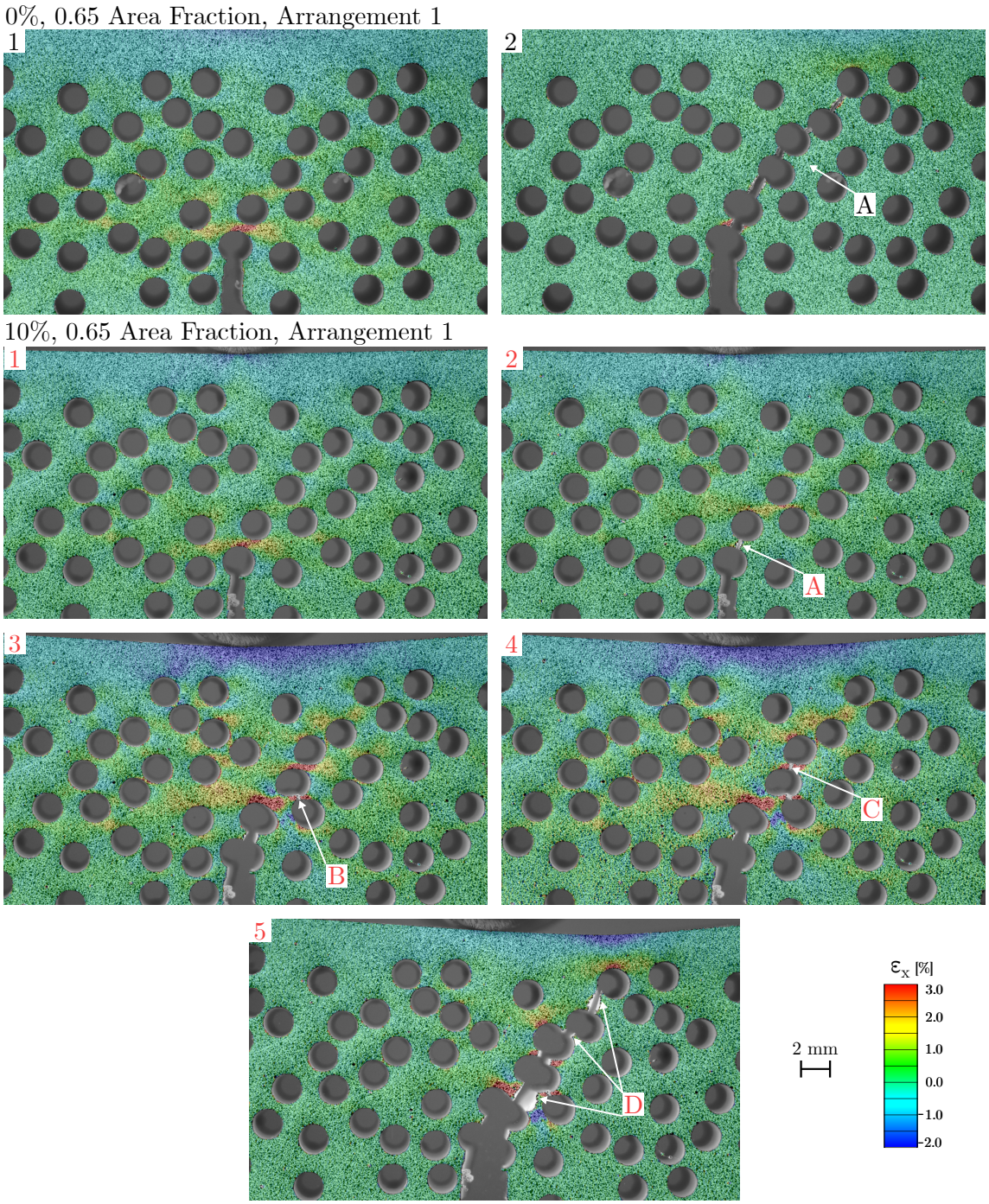


Figure A.19: DIC strain colour-maps of random SENB samples. 0.65 area fraction arrangement 1. Top two images: 0 wt% CSR. Bottom five images: 10 wt% CSR. Letters correspond to load drops in Figure A.18 (b).

A.4 Concluding remarks

In this chapter, multiple arrangements of holes drilled into bulk epoxy polymer plates have been tested via SENB. The aims were to investigate the effect of hole blunting, hole-hole interaction, and bulk material properties. The main outcomes can be summarised as follows.

2 mm diameter holes significantly blunt a crack in all the bulk epoxy polymers measured in this research, leading to large increases in measured fracture performance. This is not the critical fracture energy and we have referred to this as apparent fracture energy. The most significant difference is noted for the untoughened bulk epoxy where the ratio between the apparent fracture energy of the geometry with a 2 mm hole and the critical fracture energy of the sharp crack standardised geometry is the greatest. When analysing structures with a single line of holes ahead of the initial crack, the level of hole-hole interaction depends on the bulk polymer critical fracture energy. The untoughened sample reveals no difference in fracture behaviour between geometries with a hole spacing of 4.5 mm and 14 mm. The untoughened samples do not develop a large enough high strain region ahead of the crack tip such that it is affected by the 4.5 mm hole. The toughened samples develop large enough high strain regions ahead of the crack tip such that their complete development is constrained by the presence of a hole in this region. The toughened samples require a hole spacing of 7 mm to reach their maximum apparent fracture energy. The 2.5 mm hole spacing limits the high strain region of both the untoughened and toughened epoxy polymers. Fracture is governed simply by tensile failure of the first ligament. The untoughened sample has the highest ultimate tensile strength and so records the highest apparent fracture energy.

In regular arrays of holes, the same mechanisms as in the simple holes can be observed. For low area fraction geometries with correspondingly thin ligaments between holes, the stronger, low fracture energy, unmodified bulk polymer outperforms the weaker, high fracture energy, modified bulk polymers. As the area fraction increases and the ligaments between holes become thicker, the tougher polymers begin to outperform the untoughened polymer. The thicker ligaments provide more space for the toughened polymers to develop high strain regions ahead of the crack. This results in an increase in the measured apparent fracture energy. Furthermore, the high toughness polymers are able to arrest the crack at the next hole once the first

failure has occurred. This leads to the total fracture energy up to complete failure being greater than for the untoughened polymer which does not arrest cracks in the same manner.

In random arrays of holes, the lower the area fraction, the lower the variation in interparticle distance. Consequently, there is a narrow range of ligament thicknesses at the low area fraction. This results in the measured apparent fracture energy of the randomly arranged structures being close to the measured value for the corresponding regular arrangement of holes. On the other hand, the high area fraction samples have a wider range of geometrically allowable ligament thicknesses. The thin ligaments fail early and cause the random arrangements to have significantly lower measured apparent fracture energies than the corresponding regular hole arrangements. There is also a high standard deviation for these samples due to the larger range in ligament thicknesses. However, the random arrangements often have the ability to arrest the crack several times after first failure, whereas the high area fraction regular arrangements cannot. As a result, the random arrangements can record higher total fracture energy dissipated than the corresponding regular arrangements of holes.

Overall this study has shown that using a toughened bulk material in a foam is not likely to result in an improved apparent fracture energy. The drop in tensile strength of the bulk material as a result of adding a rubber toughener causes a reduction in performance for a low density material structure. The benefits of using a toughened polymer are not realised in the small ligaments that exist in these low density materials. The lack of space precludes the growth of high strain regions ahead of a crack tip, thus eliminating any energy absorbing advantage.